NASA/TM–2014-218169

Impact Testing and Simulation of Composite Airframe Structures

Karen E. Jackson, Justin D. Littell, Lucas G. Horta, and Martin S. Annett
Langley Research Center, Hampton, Virginia

Edwin L. Fasanella
National Institute of Aerospace, Hampton, Virginia

Michael D. Seal II
Analytical Mechanics Associates, Inc., Hampton, Virginia

February 2014

NASA STI Program . . . in Profile

Since its founding, NASA has been dedicated to the advancement of aeronautics and space science. The NASA scientific and technical information (STI) program plays a key part in helping NASA maintain this important role.

The NASA STI program operates under the auspices of the Agency Chief Information Officer. It collects, organizes, provides for archiving, and disseminates NASA's STI. The NASA STI program provides access to the NASA Aeronautics and Space Database and its public interface, the NASA Technical Report Server, thus providing one of the largest collections of aeronautical and space science STI in the world. Results are published in both non-NASA channels and by NASA in the NASA STI Report Series, which includes the following report types:

- TECHNICAL PUBLICATION. Reports of completed research or a major significant phase of research that present the results of NASA Programs and include extensive data or theoretical analysis. Includes compilations of significant scientific and technical data and information deemed to be of continuing reference value. NASA counterpart of peer-reviewed formal professional papers, but having less stringent limitations on manuscript length and extent of graphic presentations.

- TECHNICAL MEMORANDUM. Scientific and technical findings that are preliminary or of specialized interest, e.g., quick release reports, working papers, and bibliographies that contain minimal annotation. Does not contain extensive analysis.

- CONTRACTOR REPORT. Scientific and technical findings by NASA-sponsored contractors and grantees.

- CONFERENCE PUBLICATION. Collected papers from scientific and technical conferences, symposia, seminars, or other meetings sponsored or co-sponsored by NASA.

- SPECIAL PUBLICATION. Scientific, technical, or historical information from NASA programs, projects, and missions, often concerned with subjects having substantial public interest.

- TECHNICAL TRANSLATION. English-language translations of foreign scientific and technical material pertinent to NASA's mission.

Specialized services also include organizing and publishing research results, distributing specialized research announcements and feeds, providing information desk and personal search support, and enabling data exchange services.

For more information about the NASA STI program, see the following:

- Access the NASA STI program home page at *http://www.sti.nasa.gov*

- E-mail your question to help@sti.nasa.gov

- Fax your question to the NASA STI Information Desk at 443-757-5803

- Phone the NASA STI Information Desk at 443-757-5802

- Write to:
  STI Information Desk
  NASA Center for AeroSpace Information
  7115 Standard Drive
  Hanover, MD 21076-1320

NASA/TM–2014-218169

Impact Testing and Simulation of Composite Airframe Structures

Karen E. Jackson, Justin D. Littell, Lucas G. Horta, and Martin S. Annett
Langley Research Center, Hampton, Virginia

Edwin L. Fasanella
National Institute of Aerospace, Hampton, Virginia

Michael D. Seal II
Analytical Mechanics Associates, Inc., Hampton, Virginia

National Aeronautics and
Space Administration

Langley Research Center
Hampton, Virginia 23681-2199

February 2014

Available from:

NASA Center for AeroSpace Information
7115 Standard Drive
Hanover, MD 21076-1320
443-757-5802

Table of Contents

List of Figures

List of Tables

List of Acronyms

AATD – Aviation Applied Technology Directorate
ANOVA – Analysis of Variance
ASTM – American Society for Testing and Materials
CFC – Channel Filter Class
CPU – Central Processing Unit
DAS – Data Acquisition System
FRF – Frequency Response Functions
ft – unit of length, foot or feet
g – unit of acceleration, ratio of measured or predicted acceleration to the acceleration of gravity
Hz – Hertz
in – unit of length, inch
IRIG – Inter-Range Instrumentation Group
kHz – unit of frequency, kilo Hertz
ksi – unit of pressure, kilo pounds per square inch
LandIR – Landing and Impact Research
lb – unit of force, pound
LSTC– Livermore Software Technology Corporation
LV – Laser Vibrometer
mils – 1/1000 of an inch
min – unit of time, minute
MPC – Magnitude-Phase-Comprehensive
ms – unit of time, millisecond (1/1000 of a second)
mV – unit of voltage, millivolt or 1/1000 of a volt
MTS – Materials Testing System
NASA – National Aeronautics and Space Administration
NDE – Nondestructive Evaluation
PSD – Power Spectral Density
psi – unit of pressure, pounds per square inch
RSVVP – Roadside Safety Verification and Validation Program
SAE – Society of Automotive Engineering
SARAP – Survivable Affordable Repairable Airframe Program
SGC – Sprague & Geers Comprehensive
SGM – Sprague & Geers Magnitude
SGC – Sprague & Geers Comprehensive
SMP – Symmetric Multiprocessing
SOCIT - System Observer Controller Identification Toolbox
SPC – Single Point Constraint
SRW – Subsonic Rotary Wing
SVD – Singular Value Decomposition
s – unit of time, second
TVA – Technology Validation Article
US – United States
VPV – Virtual Prototype and Validation

Impact Testing and Simulation of Composite Airframe Structures

Karen E. Jackson, Justin D. Littell, Lucas G. Horta, Martin S. Annett
NASA Langley Research Center
Hampton, Virginia

Edwin L. Fasanella
National Institute of Aerospace (NIA)
Hampton, Virginia

Michael D. Seal
Analytical Mechanics Associates, Inc.
Hampton, Virginia

1.0 ABSTRACT

Dynamic tests were performed at NASA Langley Research Center on composite airframe structural components of increasing complexity to evaluate their energy absorption behavior when subjected to impact loading. A second objective was to assess the capabilities of predicting the dynamic response of composite airframe structures, including damage initiation and progression, using a state-of-the-art nonlinear, explicit transient dynamic finite element code, LS-DYNA. The test specimens were extracted from a previously tested composite prototype fuselage section developed and manufactured by Sikorsky Aircraft Corporation under the US Army's Survivable Affordable Repairable Airframe Program (SARAP). Laminate characterization testing was conducted in tension and compression. In addition, dynamic impact tests were performed on several components, including I-beams, T-sections, and cruciform sections. Finally, tests were conducted on two full-scale components including a subfloor section and a framed fuselage section. These tests included a modal vibration and longitudinal impact test of the subfloor section and a quasi-static, modal vibration, and vertical drop test of the framed fuselage section. Most of the test articles were manufactured of graphite unidirectional tape composite with a thermoplastic resin system. However, the framed fuselage section was constructed primarily of a plain weave graphite fabric material with a thermoset resin system. Test data were collected from instrumentation such as accelerometers and strain gages and from full-field photogrammetry.

A primary objective of the research program was to assess the capability of LS-DYNA for predicting damage initiation and progression of composite airframe structures subjected to crash loading. Finite element models of the composite specimens were developed and impact simulations were performed. The properties of the composite material were represented using both a progressive in-plane damage model (Mat 54) and a continuum damage mechanics model (Mat 58) in LS-DYNA. Test-analysis comparisons of time history responses and the location and type of damage are presented for each test article. In addition, multi-dimensional model calibration techniques were applied to the subfloor and fuselage section models in an attempt to reconcile differences between test (photogrammetry data) and analytical predictions. Major findings of this research program are listed, as follows.

(1) Dynamic testing of composite airframe components and full-scale articles demonstrated many different modes of structural deformation and material failure behaviors including global/local buckling, debonding, material crushing, brittle fracture, layer splitting, and delamination.

(2) Photogrammetry proved useful in providing or augmenting more traditional test data.

(3) Laminate characterization testing and simulations were conducted as a means of developing and calibrating the baseline material models.
(4) In general, simulations that were performed using Mat 54 did a poor job in replicating the impact responses of the components and the subfloor. The Mat 54 models tended to fail catastrophically in a brittle fashion, absorbing little kinetic energy. The fuselage section proved an exception. The Mat 54 model was able to predict the location and amount of damage to the fuselage section, even matching the kinematics of the floor following separation from the sides of the fuselage structure.
(4) Simulations performed using Mat 58 to represent the composite material demonstrated generally good comparison with test data; however, the level of comparison was highly dependent on the ERODS parameter, which defines the ultimate strain for element deletion.
(5) Neither material model was capable of predicting delamination failure.
(6) Multi-dimensional calibration techniques were applied to both the composite subfloor and fuselage section models to assess model deficiencies and uncertainties, to evaluate parameter importance, and to compute required model changes needed to better reconcile test and predictions. Results from the vibration test of the composite fuselage section indicated that the model needed to have the modulus reduced by 27% from the baseline value. However, results using impact data suggested an increase in modulus. These two findings are inconsistent; however, both are supported by experimental data. These conflicting results highlight the inadequacy of the existing models to be predictive under different loading conditions. Although, comparisons of the observed global behavior with analytical predictions are reasonable, attempts to use the analytical models to predict other test conditions will likely fail.

2.0 INTRODUCTION

In 2008, the Survivable Affordable Repairable Airframe Program (SARAP) Virtual Prototype and Validation (VPV) Program was initiated between Sikorsky Aircraft Corporation and the United States (US) Army Aviation Applied Technical Directorate (AATD). The objectives of the program were to validate technology advances in design processes, structural efficiency, crashworthiness, materials and manufacturing processes, and reparability of rotorcraft airframe structures. Specific objectives of the SARAP VPV program included a 25% weight reduction, 40% recurring and 40% non-recurring cost reduction, maintaining crashworthiness, and repairable structure as compared to a 2002 metallic baseline. The comprehensive SARAP VPV program, which is described in Reference 1, included identification, review and evaluation of various design, analysis, material, and manufacturing technologies. As part of this program, a prototype Technology Validation Article (TVA) was constructed that was representative of the center section of a production Black Hawk helicopter, which is a metallic design.

Following detailed design, manufacturing, and assembly, a full-scale vertical impact test of the TVA was performed at the Landing and Impact Research (LandIR) facility at the National Aeronautics and Space Administration (NASA) Langley Research Center in August 2008. A post-test photograph of the TVA is shown in Figure 1. The purpose of the test was to evaluate the performance of a “tilting roof” concept, patented by Sikorsky Aircraft Corporation, that was intended to dissipate the kinetic energy of high mass items, such as the rotor transmission, during a crash event [1]. The tilting roof concept required controlled and predictable failures of the roof

structure with energy absorption accomplished using aluminum crush tubes.

Figure 1. Post-test photograph of the SARAP TVA following the 2008 vertical drop test.

Post-test inspection of the TVA indicated that damage was primarily limited to the roof area, with little or no damage found in the subfloor, or the forward framed fuselage section. Following the test, the TVA was moved to AATD, located at Ft. Eustis, VA. In 2010, NASA Langley obtained the residual SARAP hardware for testing under the NASA Subsonic Rotary Wing (SRW) crashworthiness research program. In May 2011, NASA and Sikorsky signed a Space Act Agreement [2] allowing for cooperation between the two organizations to pursue common research interests, including: composite material and airframe structural testing under dynamic loading; development of accurate and robust material models to predict aircraft structural response using LS-DYNA; and, validation of analytical models through test-analysis correlation.

Six different types of test specimens of varying complexity were extracted from the SARAP residual hardware for testing. Laminate characterization testing was conducted in tension and compression. In addition, dynamic impact tests were performed on several components, including I-beams, T-sections, and cruciform sections. Finally, several tests were conducted on two full-scale components including a subfloor section and a framed fuselage section. These tests included a modal vibration and longitudinal impact test of the subfloor section and a quasi-static, modal vibration, and vertical drop test of the framed fuselage section. Most of the test articles were manufactured of graphite unidirectional tape composite with a thermoplastic resin system. However, the framed fuselage section was constructed primarily of a plain weave graphite fabric material with a thermoset resin system.

Since its inception in 2006, the SRW crashworthiness research program has focused on improved prediction of rotorcraft crashworthiness, addressing topics such as occupant modeling and injury prediction, multi-terrain impact simulation, model validation studies that focused on probabilistic analysis, and development of system-integrated simulation models [3]. Recently, the research program was refocused to assess current analytical capabilities used to predict crashworthiness of composite airframe structures. Thus, obtaining the SARAP residual hardware was fortuitous and allowed testing of fairly simple coupons, more complex components, and complex built-up airframe structures for the purpose of model validation. One objective of the research program

was to assess the capability of LS-DYNA [4, 5], a commercial nonlinear, explicit transient-dynamic finite element code, for predicting damage initiation and progression of composite airframe structures subjected to crash loading.

Finite element models were developed to represent each of the test articles and simulations were conducted using LS-DYNA. Within LS-DYNA, two composite material models were evaluated: MAT_ENHANCED_COMPOSITE_DAMAGE (Mat 54), a progressive failure model that uses the Chang-Chang failure criterion to simulate ply-by-ply failure and property degradation and MAT_LAMINATED_COMPOSITE_FABRIC (Mat 58), a continuum damage mechanics model for representing unidirectional tape and fabric composite materials. Sikorsky provided the material property values for Mat 54, whereas properties for Mat 58 were determined by assessing literature data, by comparing with similar Mat 54 values, and by using a trial and error process in which laminated coupons were simulated under both tensile and compressive loading.

The level of agreement between test and analysis was determined through comparisons between experimental and analytical time history responses and comparisons between observed structural deformation, damage initiation, and failure with predicted behavior. No specific metrics were defined for quantifying test-analysis comparisons, in part because no acceptable metrics have been established as standards. However, multi-dimensional model calibration techniques were applied to both the composite subfloor and fuselage section models to assess model deficiencies and uncertainties, to evaluate parameter importance, and to compute required model changes needed to better reconcile test and predictions.

The report contains several major sections including Experimental Testing, Model Development and Test-Analysis Comparisons, Discussion of Results, Concluding Remarks, References, and Appendix A. Non-Destructive Evaluation (NDE). The general approach in documenting results is to start with simple coupons, then progress to more complicated components, and to end with the full-scale structures.

3.0 EXPERIMENTAL TESTING

This section of the report describes the experimental program that was conducted using residual hardware obtained from the post-drop-test SARAP TVA. There are eight subsections including a description of the test specimens and a summary of results from: Nondestructive Evaluation (NDE); laminate characterization testing; dynamic crush testing of two I-beams, two T-sections, and two cruciform sections; a longitudinal impact test of a subfloor section; and, a vertical drop test of a framed fuselage section.

3.1 Specimen Descriptions

The SARAP residual hardware arrived at NASA in excellent shape. Care was taken to determine the most appropriate use for each portion of the residual hardware to optimize the data generated. Specimens were chosen such that the hardware could be tested from the coupon level all the way to full-scale impact testing. The final layout provided six different types of specimens, with a potential for a future seventh specimen. A depiction of the SARAP residual hardware utilization is shown in Figure 2.

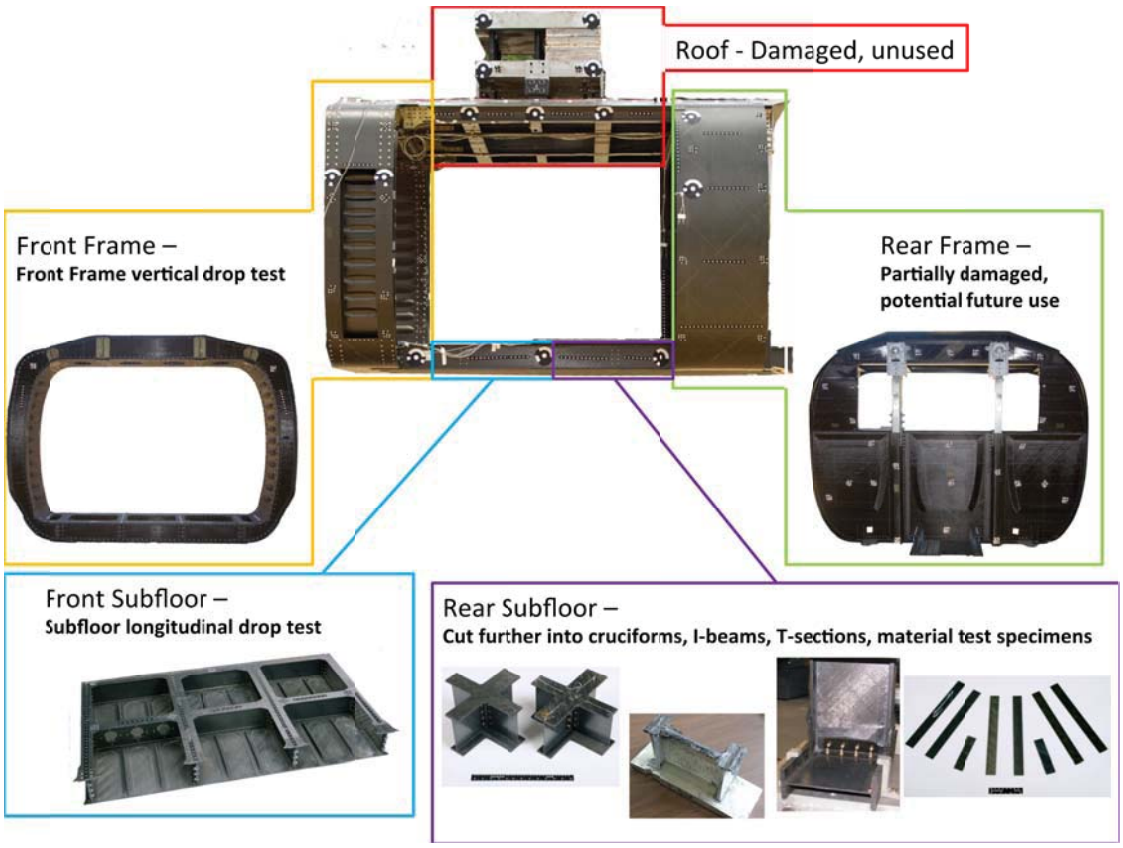

Figure 2. SARAP residual hardware utilization.

It should be noted that the SARAP TVA was constructed primarily of thermoplastic unidirectional graphite tape composite material that was cured using both autoclave and in situ techniques. However, the framed fuselage sections on either end of the TVA were constructed primarily of thermoset plain weave graphite fabric material.

3.2 Nondestructive Evaluation (NDE)

Since the TVA had been previously subjected to a fairly severe vertical impact test condition, it was necessary to evaluate the structural integrity of the test specimens cut from the original fuselage section. Two Nondestructive Evaluation (NDE) methods were used to assess the smaller coupons and components: baseline ultrasonic C-scanning and single sided flash thermography. Results of these inspections are described in Section 9.0 Appendix A. In general, some areas of possible damage were identified for the larger components (I-beams, T-sections, and cruciform sections) and these were noted in the resulting scanned photographs. However, no specific identifiable flaws were found. Consequently, these specimens were subsequently tested, as described in the present report. No attempt was made to perform NDE of the large subfloor section or the framed fuselage section.

3.3 Laminate Characterization Testing

As mentioned previously, the SARAP TVA was constructed primarily of both thermoplastic unidirectional graphite tape and thermoset plain weave graphite fabric composite materials.

Laminate property characterization testing was performed for both types of materials. It should be noted that the fabric material was only used in the framed fuselage section. All other specimens were constructed of unidirectional tape material.

3.3.1 Unidirectional Tape

Quasi-static tests were conducted on laminated coupons extracted from three separate areas on the rear SARAP subfloor. Areas on the floor base, the floor T-stiffeners, and the I-beam webs were the main areas of interest. The coupons were used to evaluate mechanical properties for specific regions on the SARAP test article, and to determine potential differences in the laminate properties due to processing, installation, or fabrication. The locations of the coupon extractions are shown in Figure 3.

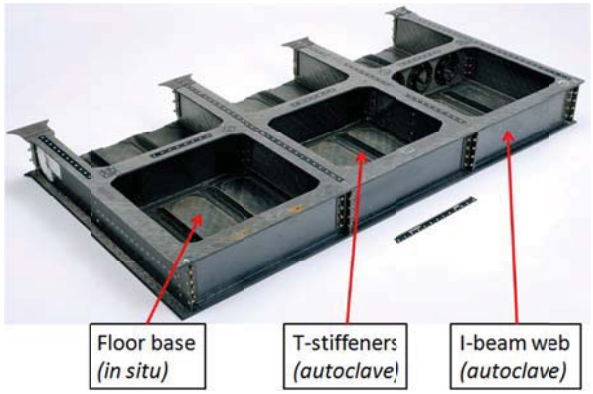

Figure 3. Laminate coupon extraction locations with identified fabrication methods.

Testing was conducted in accordance with American Society for Testing and Materials (ASTM) standards including ASTM D3039 [6] for tensile specimens and ASTM D3410 [7] for compression specimens. Tensile specimen dimensions were 10-in. x 1-in., with an unsupported gage length of 6-in. Compressive specimen dimensions were 6-in. x 1-in., with an unsupported gage length of 2-in. A photograph of sample extracted coupon specimens is shown in Figure 4.

Figure 4. Sample set of extracted coupon specimens.

All tests were conducted using a Materials Testing System (MTS) quasi-static load machine operated in displacement control. Both load and displacement values generated from the

machine were recorded, along with full-field strain photogrammetric measurements. Stress was computed by dividing the recorded load by the original cross-sectional area. Strain data were obtained from photogrammetry for four discrete points located at four distinct areas on the surface of the specimen. Strain data were checked by dividing the photogrammetric displacement data, collected at two discrete points located 0.5-in. apart, by the original separation distance. This method mimics traditional extensometer readings. All specimens were first scanned using NDE techniques to check for possible defects that might be present following the prior TVA drop test. No signs of internal damage were discovered and the specimens were deemed suitable for static testing. See Section 9.0 Appendix A for NDE results.

A total of seven laminated coupons fabricated of thermoplastic unidirectional graphite tape material were tested in tension. Two coupons were cut from I-beams on the rear subfloor, one was cut from a T-stiffener and four were extracted from the floor. Tensile testing was conducted at a displacement rate of 0.05 in/min. Table 1 summarizes the results, using averages ± standard deviations in the data, where possible.

Table 1. Quasi-Static Tension Results.

Coupon from rear subfloor	**Manufacture Process**	**Failure Strain (%)**	**Maximum stress (ksi)**	**Modulus (msi)**
I-beam	Autoclave	1.04 ± 0.03	71 ± 4.2	6.8 ± 0.1
T-stiffener	Autoclave	1.12	68	6.1
Floor	In situ	0.95 ± 0.03	59 ± 1.3	6.1 ± 0.1

Due to the small sample size, statistical measurements could not be performed on the coupons extracted from the T-stiffeners. As indicated in Table 1, the I-beam coupons had slightly higher moduli than the T-stiffener or the floor coupons. It also shows that the floor coupons had slightly lower failure strains and lower maximum stresses, indicating that they are the weakest laminates tested, but not by a large amount. The data also suggests that the manufacturing methods may factor into the laminate response, as the floor coupons show a much lower failure strain and maximum stress than coupons taken from the other two locations. For visualization, representative data sets are plotted in Figure 5 for laminated coupons taken from different locations.

The data plotted in Figure 5 reinforces the data shown in Table 1. The blue I-beam coupon data follows a slightly steeper slope than the other two curves, while the floor coupon response (green curve) shows a slightly softer response.

Due to limited availability, only coupons removed from the floor section were tested in compression. A total of six coupons were tested at a quasi-static displacement rate of 0.05 in/min. Table 2 summarizes the results.

Results show that the failure strain and the maximum stress at failure of the composite floor coupons in compression are approximately half of the corresponding property values in tension. The average modulus is slightly higher for the compressive coupons, but the scatter in the data suggests that the modulus is the same in compression as it is for tension. Sample compressive stress-strain curves are plotted in Figure 6.

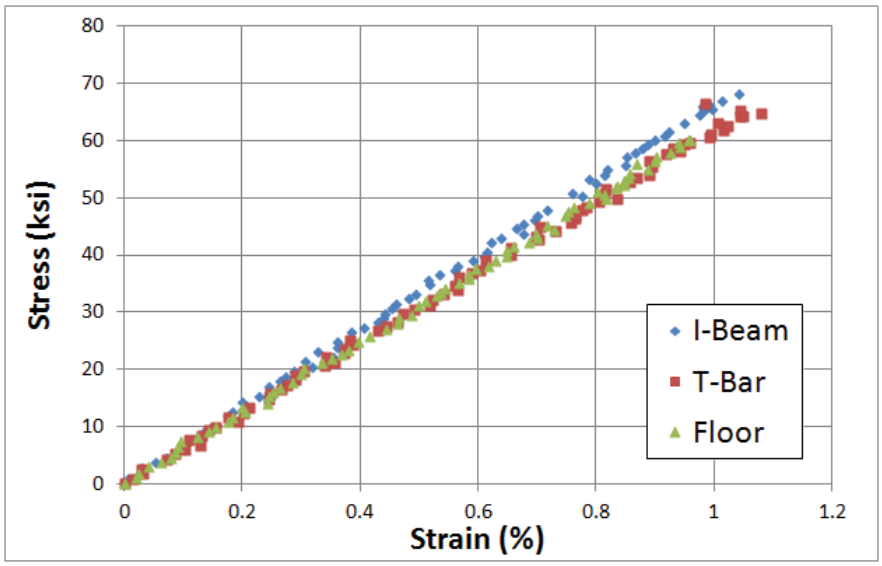

Figure 5. Tensile stress-strain curves for laminated coupons taken from three different locations.

Table 2. Quasi-Static Compression Results.

Coupon extracted from	Manufacturing Process	Failure Strain (%)	Maximum stress (ksi)	Modulus (msi)
Floor	In situ	0.49 ± 0.05	34.6 ± 2.5	6.3 ± 0.2

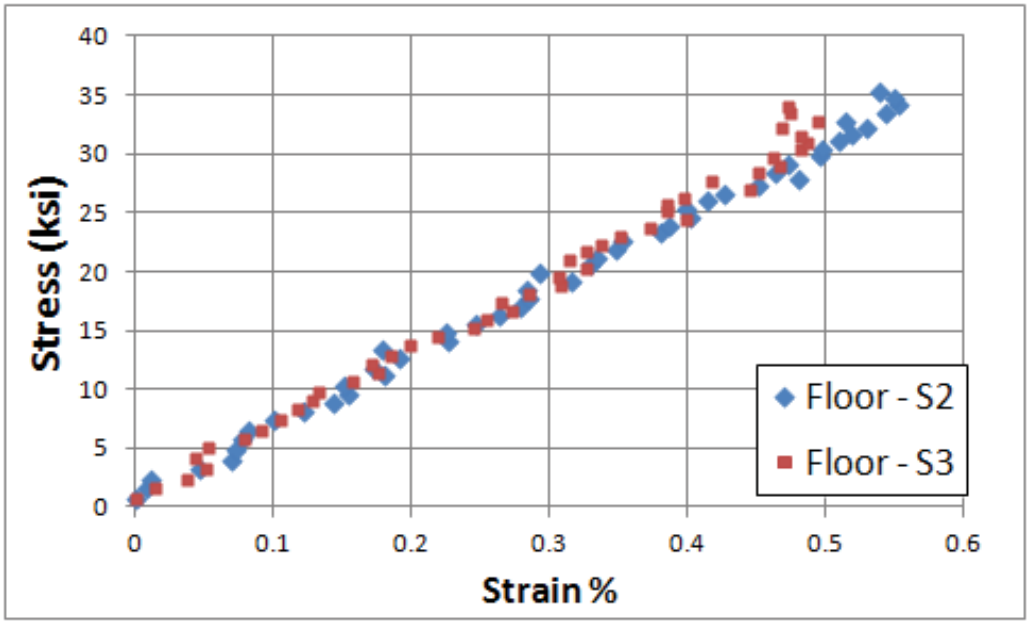

Figure 6. Compressive stress-strain curves of laminated floor coupons fabricated of unidirectional tape.

3.3.2 Plain Weave Fabric

Tensile and compressive properties of laminated coupons constructed of plain weave graphite fabric material were conducted. These specimens were removed from undamaged portions of the longitudinal I-beam webs in the subfloor of the rear fuselage section. No NDE examinations

were performed; however, the specimens showed no visible signs of damage. Only eight coupons were tested. Specimens were 1-in. wide, 10-in. long and 0.12-in. thick. The unsupported gage length in tension was 6-in.

As with the unidirectional tape coupons, all tests were conducted using a MTS quasi-static load test machine operated in displacement control at a rate of 0.05-in/min. Both load and displacement values from the test machine were recorded, along with full-field strain photogrammetric measurements.

Four coupons were tested in tension and the stress-strain data are plotted in Figure 7(a). Based on analysis of the data, the average Young's modulus was 8.173e+6-psi, the tensile strength of the composite laminate was 99,147-psi, and the strain-to-failure was 1.2%. Likewise, four specimens were tested in compression and the stress-strain data are plotted in Figure 7(b). Based on data averaging, the Young's modulus was 7.0e+6-psi, the compressive strength was 47,300-psi, and the compressive strain-to-failure was 0.64%. Note that the compression specimens were less than half the length of the tensile coupons, with an unsupported gage length of 2-in. Finally, it is important to note that these properties are for fabric laminates, not fabric material.

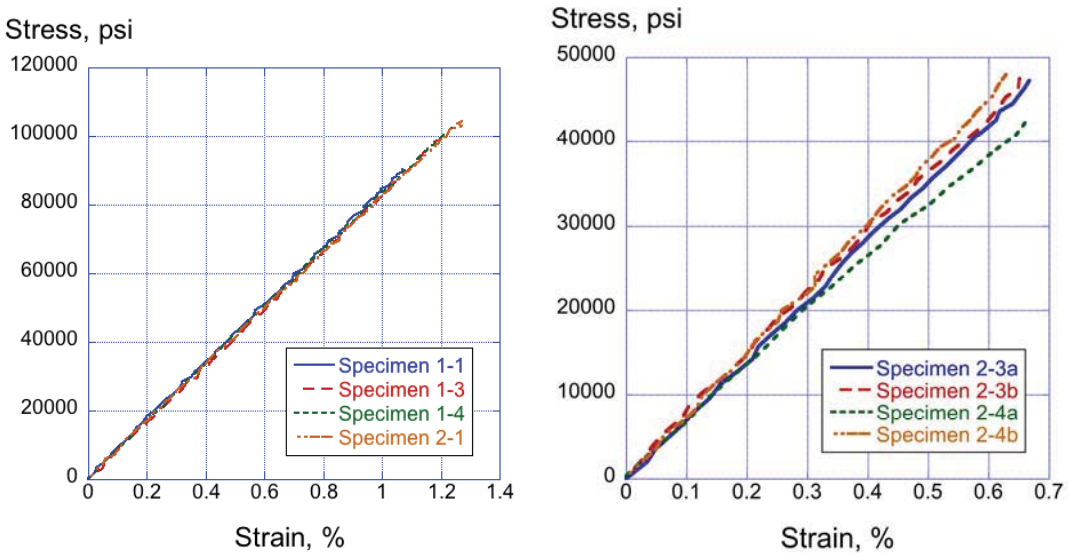

(a) Tension. (b) Compression.

Figure 7. Fabric coupon responses to tensile and compressive loading.

3.4 Dynamic Crush Testing of Two I-Beam Specimens

The component test series began with a pair of tests on the SARAP I-beam floor supports. Two I-beam specimens were extracted from interior regions of the SARAP TVA rear subfloor. The test articles were 4.56-in. tall, 6.2-in. wide, and potted into a rigid foundation such that the main axis of the I-beam was oriented vertically. Corner notches were cut into the upper ends of the web to initiate specimen crushing and to reduce peak accelerations upon initial contact with the drop mass. Two vertical tests were conducted at drop heights of 4- and 8-ft using a 14-ft vertical drop tower. Instrumentation included two accelerometers on the drop mass and a stochastic speckle pattern for use with full-field strain photogrammetry on the web of the specimen. The

drop mass weight was 204.8 lbs. A labeled schematic and photograph of an I-beam specimen are shown in Figure 8.

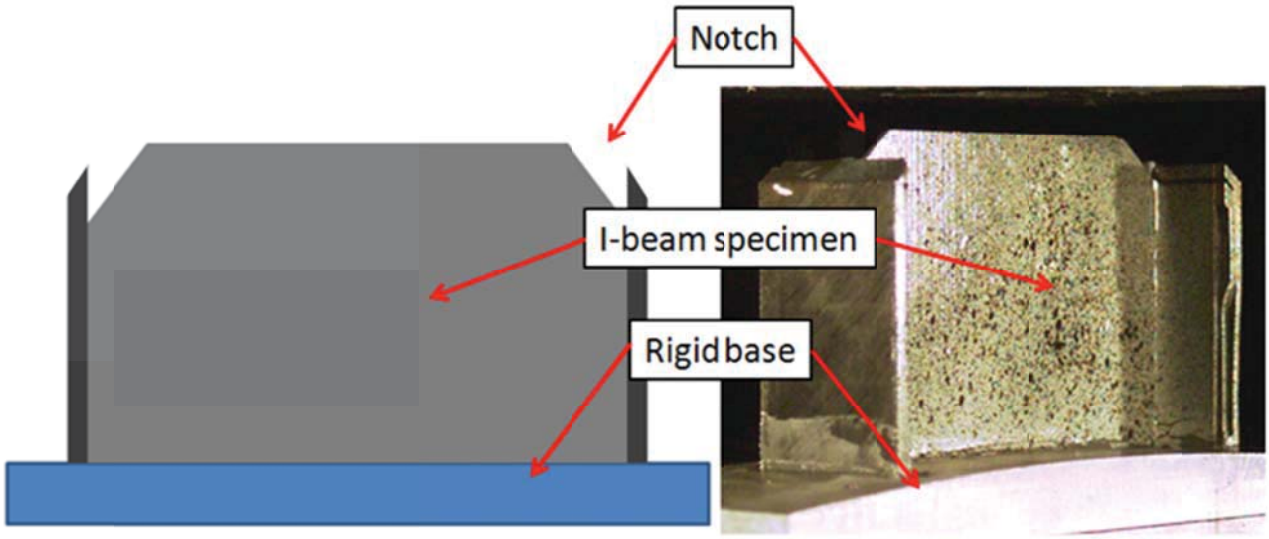

Figure 8. I-beam specimen configuration.

Test data were collected using a National Instruments Data Acquisition System (DAS) at 25-kHz sampling rate with a 13.675-kHz antialiasing filter. This DAS system and sampling rate were used to collect data for all component tests including the I-beams, T-sections, and cruciform sections.

3.4.1 I-Beam Test at 4-ft Drop Height

The impact velocity for the 4-ft drop test was 189.6-in/s. An image sequence is shown from the front face of the specimen in Figure 9.

The upper left image in Figure 9 shows the specimen 1-ms before impact. The upper right image shows the specimen 1-ms after impact. At this time, the drop mass has begun crushing the upper edge of the web, and has just contacted the outer flanges, which were approximately 1/16-in. shorter than the web. At 5-ms after impact, the top portion of the I-beam web is crushing, with many of the composite layers delaminating and subsequently bending locally at the top of the web. The side flanges have begun to crush, but are not exhibiting significant amounts of delamination. At 10-ms after impact, material crushing and delamination from both the web and flanges can be seen. This time also corresponds to the approximate time of maximum displacement of the impact mass.

The measured acceleration responses from two accelerometers on the drop mass are plotted in Figure 10. The acceleration was filtered with a Butterworth low-pass filter, with a cut-off frequency of 1,000-Hz. Following initial impact, the drop mass acceleration exhibits peaks of 125- and 113-g occurring at approximately 6- and 7-ms, respectively. Following the peak, the acceleration drops to zero and remains at zero following a small rebound. The lack of a substantial rebound of the drop mass indicates that very little elastic energy was stored in the specimen. As shown in Figure 11, the maximum crush displacement of the drop mass was 0.85-in., as determined from photogrammetric data analysis. This plot also shows the displacement

time histories obtained from double integration of the two accelerometers located on the drop mass. These curves are in close agreement; however, the photogrammetry data is generally considered more accurate due to the fact that acceleration data may contain large offsets or drifts.

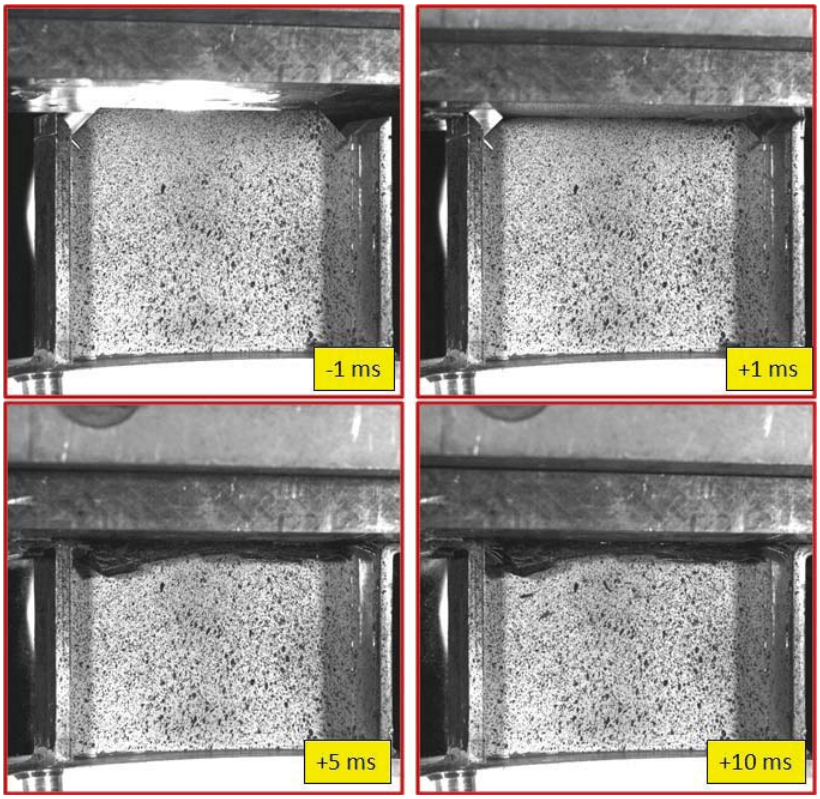

Figure 9. Image sequence of the I-beam 4-ft drop test.

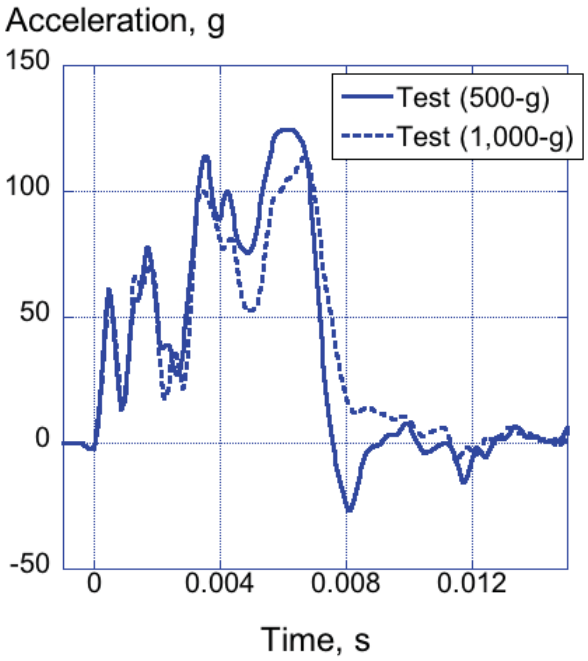

Figure 10. Drop mass acceleration from the 4-ft I-beam test.

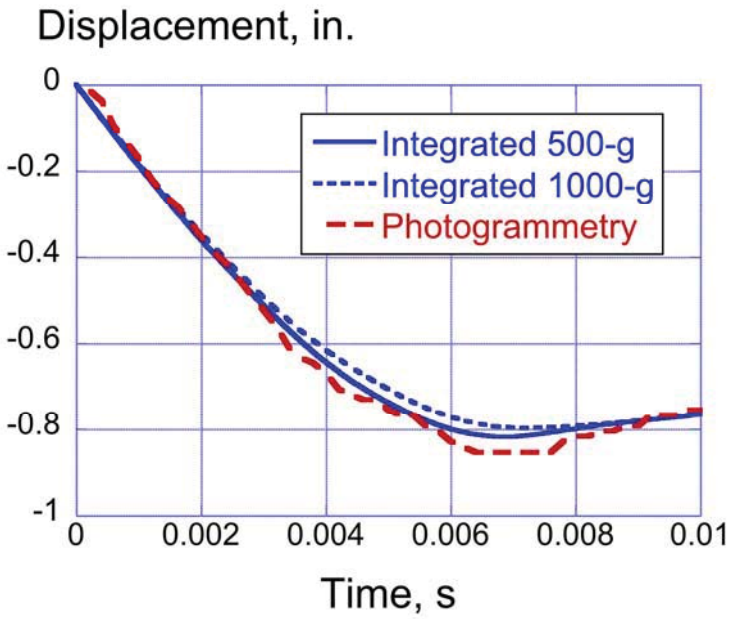

Figure 11. Drop mass crush displacement from the 4-ft I-beam test.

The photogrammetric data were next examined. The front web was filmed and sampled at 15 kHz. Compressive strains at two distinct times during the crushing sequence are shown in Figure 12. The compressive strain at 1-ms after impact, which occurs on the upward side of the acceleration curve is shown in Figure 12(a). The stress wave can be seen in the specimen by noting that, near the top where the drop mass is touching the specimen, strains are between -0.8 and -1.0 percent. The corners appear to have slightly larger strains, which could potentially be due to an uneven surface at the free edge of the specimen. However, the fixed end of the specimen exhibits between 0.0 and -0.2% strain, indicating that the stress wave has not travelled through the specimen and the strain is not fully developed at the fixed end.

The image shown in Figure 12(b) shows the compressive strain at 7.2-ms after impact, or, more specifically, the time of maximum acceleration. Layer delaminations and bending interfere with viewing of the uppermost edge of the crush front, so strains cannot be resolved up to the edge. However, by comparison of the two images, much of the middle region of the specimen that once exhibited -0.5% strain (in green) is now closer to 0.0% strain (in orange). The entire visible portion of the strain data on the specimen is exhibiting this low 0.0% value. These results indicate that the strain has become localized in the crush front. This finding is confirmed by examining the videos and pictures post-test. Visual inspections show that the majority of the specimen away from the crush front has stayed intact. Almost all of the damage has occurred at the crush front, and it is best characterized by layer delamination and bending with large amounts of material crushing.

A photograph of the specimen post-test is shown in Figure 13. The photogrammetric measurements are confirmed when looking at the failure patterns. The impact surface shows signs of ply delamination, material crushing, and localized bending, while the bottom of the specimen, which is fixed into the rigid base, exhibits no failure.

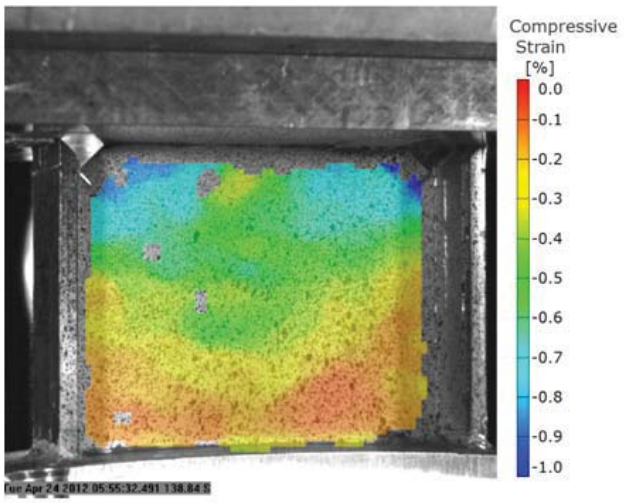

(a) Time = 1-ms.

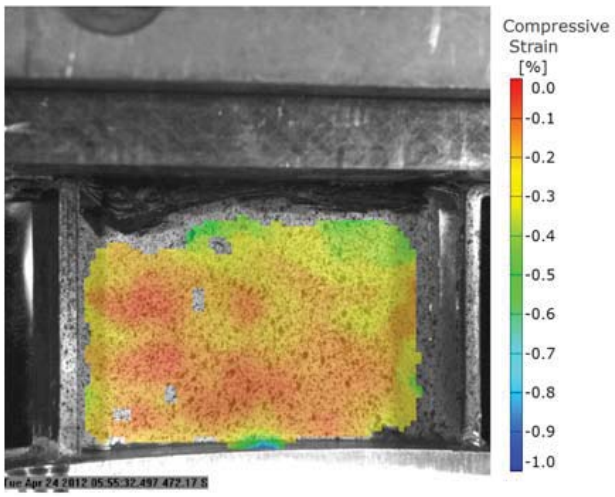

(b) Time=7.2-ms.

Figure 12. Compressive strain at 1-ms and 7.2-ms after impact of the I-beam.

Figure 13. Post-test photograph of the I-beam tested at 4-ft drop height.

3.4.2 I-Beam Test at 8-ft Drop Height

The impact velocity for the 8-ft drop test was 265.2 in/s. Image sequences are shown from the front face of the specimen in Figure 14. The upper left image in Figure 14 shows the specimen 1-ms before impact. The upper right image shows the specimen 1-ms after impact. At this time, the drop mass has begun crushing the edge of the web section, and has just contacted the flanges, which were approximately 1/16-in. shorter than the web. At 5-ms after impact, the top portion of the I-beam web is exhibiting localized bending and delamination with many of the layers splitting due to the impact on the free edge. The side flanges are also exhibiting severe delaminations. At 10-ms after impact, material crushing from both the web and flanges can be seen, by noting that the entire web of the specimen is blocked from the image view by localized bending of composite layers. This time also corresponds with the approximate time of the maximum displacement of the drop mass. The acceleration response, as measured from the drop mass, is shown in Figure 15. The acceleration was filtered with a low-pass Butterworth filter, with a cut-off frequency of 1,000-Hz.

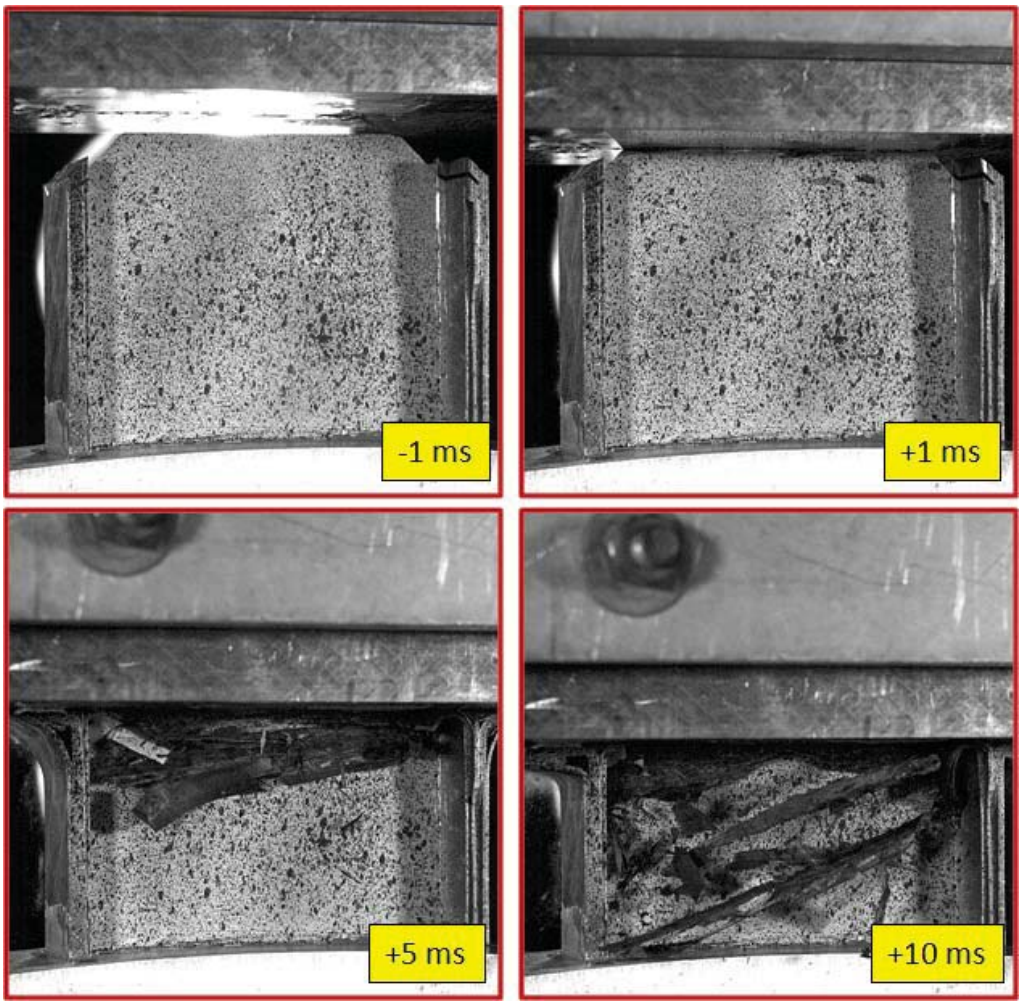

Figure 14. Image sequence of the 8-ft I-beam test.

Even filtered, the drop mass acceleration contains a number of oscillations. Between initial impact and 5-ms, the acceleration increases to a peak of 128-g. After 5-ms, the acceleration exhibits two subsequent peaks of 115- and 105-g, before decreasing to zero. The maximum crush displacement of the drop mass is 1.75 inches, as measured by both photogrammetry and double integration of the acceleration response. This value is more than double the displacement of the 4-ft test. The crush displacement response is shown in Figure 16. A small rebound is evident in the displacement curve, which indicates that very little elastic energy was released.

The photogrammetric data were next examined. The front web was filmed and sampled at 15-kHz. Compressive strains at two distinct times during the crush sequence are shown in Figure 17. The compressive strain at 1-ms after impact, which occurs during the increasing portion of the acceleration curve, is shown in Figure 17(a). The stress wave can be seen in the specimen at this time. The specimen is exhibiting large strain levels near the top, which are shown in blue. The bottom fixed portion of the specimen is yellow and orange in color, indicating that the strains at this location are between 0.0 and -0.3%. The corners appear to have slightly larger strains, which could potentially be due to an uneven surface at the top.

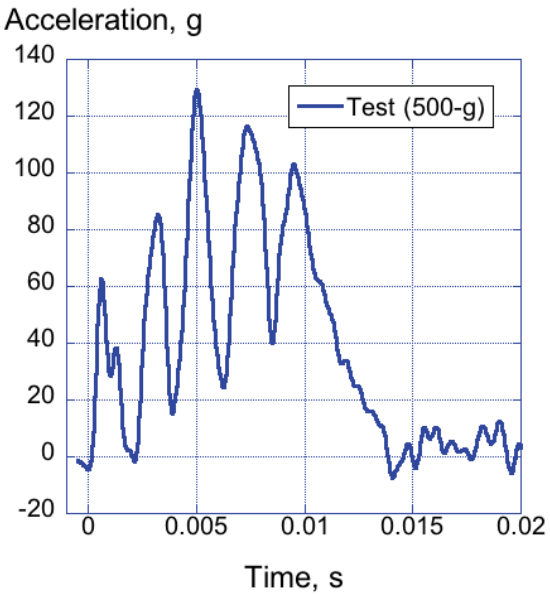

Figure 15. Drop mass acceleration from the 8-ft I-beam test.

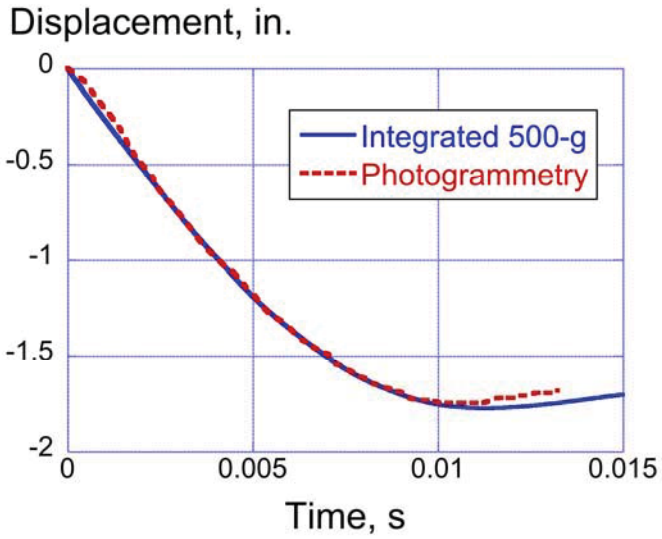

Figure 16. Drop mass crush displacement from the 8-ft I-beam test.

Unfortunately, photogrammetric data at 10-ms after impact do not exist due to the large amount of ply delamination, material crushing, and localized bending, which interferes with viewing of the web. The image shown in Figure 17(b) shows the compressive strain data at 5-ms after impact, which is close to the time of peak acceleration. Debris at the uppermost edge of the specimen interferes with viewing of the crush front, so strains cannot be resolved up to the edge. However, a defined crush front is still visible by noting the transition from high compressive strain in blue near the crush front to low compressive strain near the base. The post-test specimen is shown in Figure 18.

The photogrammetric measurements are again confirmed when looking at the failure patterns. Even though the specimen crushed approximately double the amount of the 4-ft specimen, the

deformation patterns are the same. Large amounts of ply delamination, localized bending, and material crushing are evident toward the upper (impact) end of the specimen. In contrast, the bottom of the specimen, which is fixed into the rigid base, exhibits no failure.

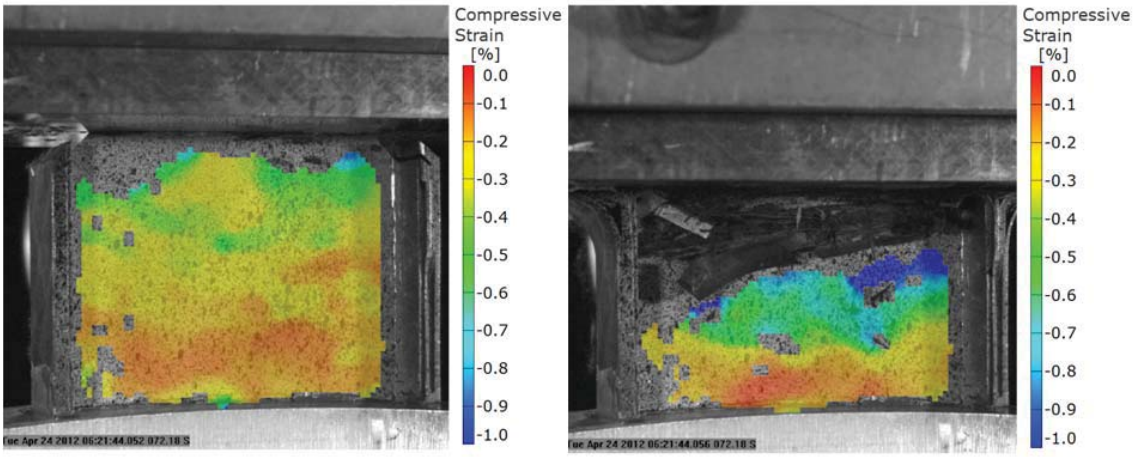

(a) Time = 1-ms. (b) Time = 5-ms.

Figure 17. Compressive strain at 1-ms and 5-ms after impact

Figure 18. Post-test I-beam specimen following 8-ft drop test.

3.5 Dynamic Crush Testing of Two T-Section Specimens

Two T-section specimens were extracted from the SARAP TVA rear subfloor, at the location where a lateral I-beam terminates at the edge of a longitudinal I-beam. At this termination point, the two I-beam sections on the floor were fastened together using doublers. When extracted, these specimens resembled a T shape. Two drop tests were conducted on the T-sections using a 14-ft vertical drop tower, such that the lateral I-beam portion of the specimen is oriented in the vertical direction. This orientation ensures that initial contact with the large drop mass occurs at the end of the vertical flanges and web. The longitudinal I-beam of the T-section was placed in a horizontal orientation, and used to support the vertical I-beam. The side flanges of the horizontal I-beams were clamped in four places to a large base fixture, which was fixed. A small aluminum bar (approximately 1-in. x 1-in. by 5.56-in.) was placed between the two inner flanges

of the horizontal I-beam and located in the center of the specimen, just beneath the vertical web. The bar was intended to react the compressive load applied to the vertical web to promote crushing rather than global buckling of the specimen. The specimens were impacted vertically to determine crush behavior, failure mechanisms, and energy absorbing characteristics of the vertical I-beam of the T-section. Accelerometers were mounted to the drop mass and the vertical I-beam web was also painted with a stochastic speckle pattern to collect full-field photogrammetric data. The drop mass weight was 204.8 lbs. A picture of a T-section specimen in the test setup is shown in Figure 19. The overall dimensions of the specimen were: 9-in. tall, 6.2-in. wide, and 13-in. long.

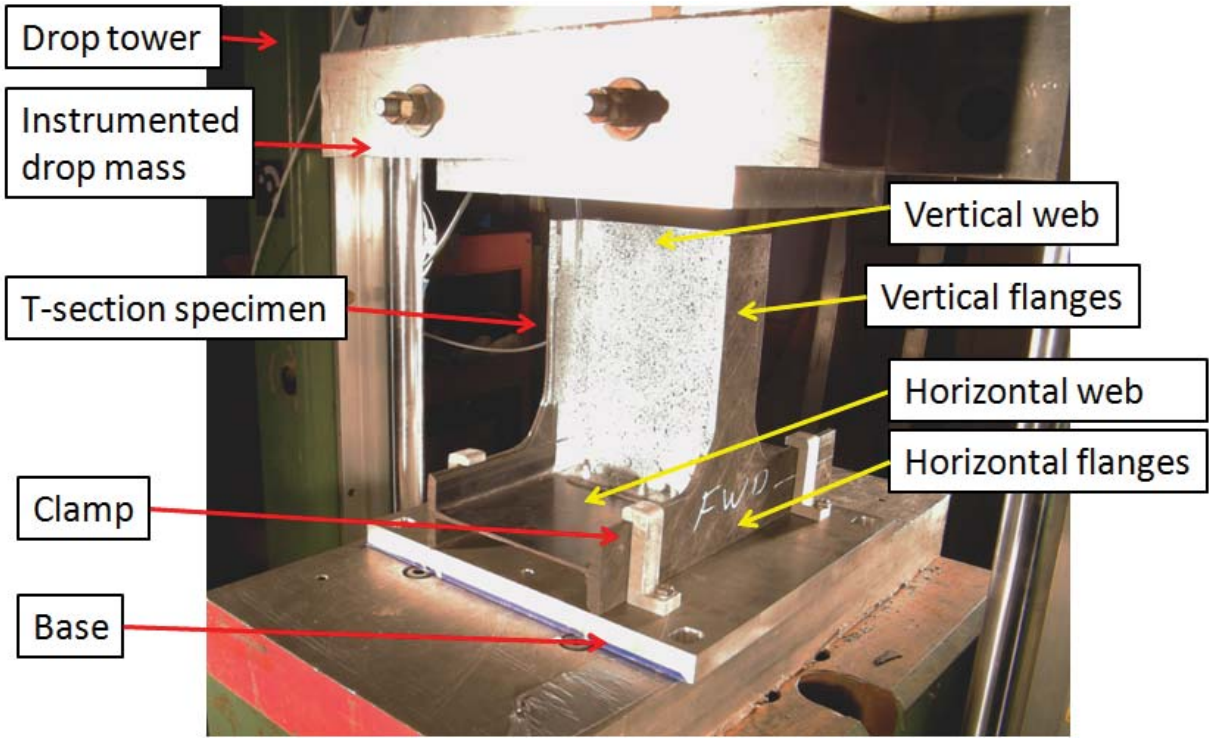

Figure 19. T-section test set-up.

3.5.1 T-Section Test at 2-ft Drop Height

The first T-section test was conducted for a drop height of 2-ft. At this height, the drop mass obtained an impact velocity of 134.9-in/s. An image sequence taken from the rear, opposite side of the pattern, is shown in Figure 20. The top left image is 1-ms before impact. The top right image shows the specimen 1-ms after impact, which indicates buckling of the vertical I-beam flanges near the transition regions connecting them to the horizontal I-beam flanges. The bottom left image shows this buckling progressing to where there are also large delaminations between the layers on the flange. The bottom left image also shows buckling at the bottom of the web, near the doublers fastening the two webs together. The bottom right image shows the drop mass at maximum displacement. The acceleration response recorded from an accelerometer on the drop mass is shown in Figure 21. The acceleration trace was filtered using a low-pass Butterworth filter with a cut-off frequency of 1,000-Hz.

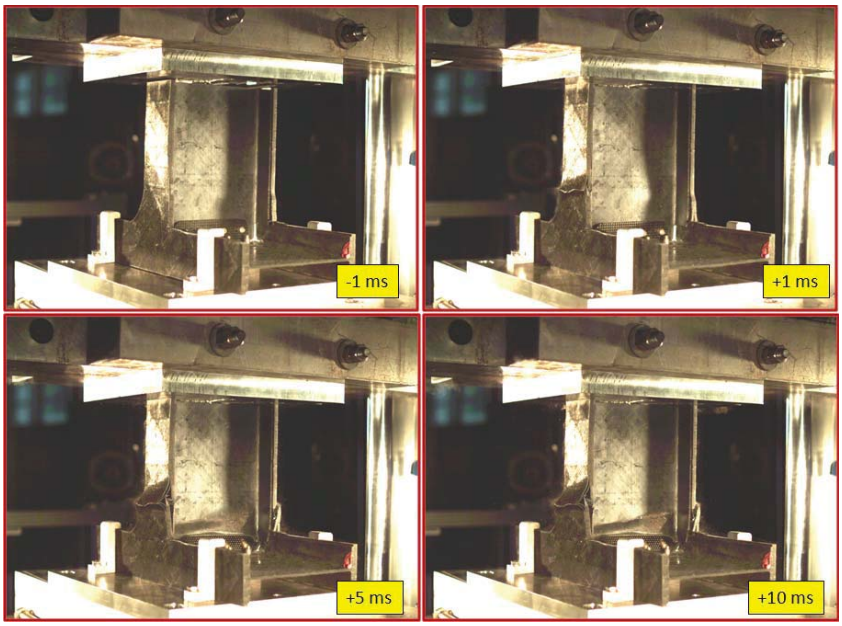

Figure 20. Image sequence of the T-section test at 2-ft drop height.

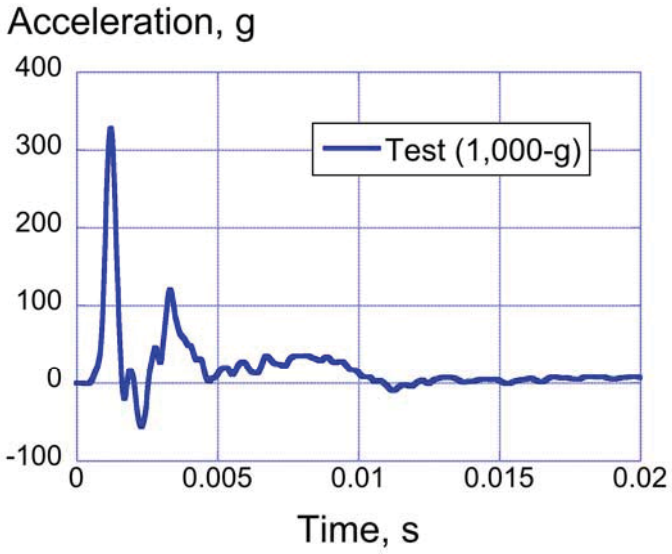

Figure 21. Drop mass acceleration from the 2-ft T-section test.

The drop mass acceleration shows a large initial spike peaking at 325-g at approximately 1-ms after initial impact. This initial spike represents first contact between the drop mass and the specimen. Unlike the previous I-beams, the T-sections did not have a trigger to initiate crushing. Thus, the initial spike represents the peak load before specimen failure. This peak is followed by a second peak of 114-g at 3.2-ms after impact. After 10-ms, the drop mass has reached its maximum crush displacement, and the acceleration trace shows no significant acceleration after this point. The maximum crush displacement, as measured by photogrammetry, was 0.44 inches, as shown in Figure 22. This plot also shows the displacement response obtained by double integration of the acceleration data. The integrated acceleration response shows a higher maximum crush displacement of 0.48-in. A considerable rebound is evident in Figure 22

indicating that a significant amount of energy was stored and released during the impact event.

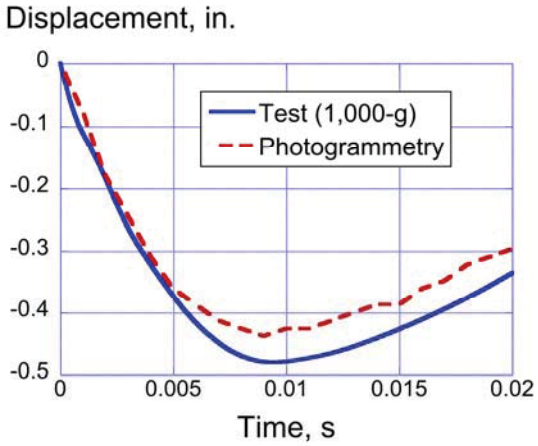

Figure 22. Impact mass crush displacement from the 2-ft T-section test.

The photogrammetric data are next examined. Cameras were used to film the front web of the T-section, sampling at 10-kHz. Two fringe plots are shown in Figure 23 at 1-ms after initial impact.

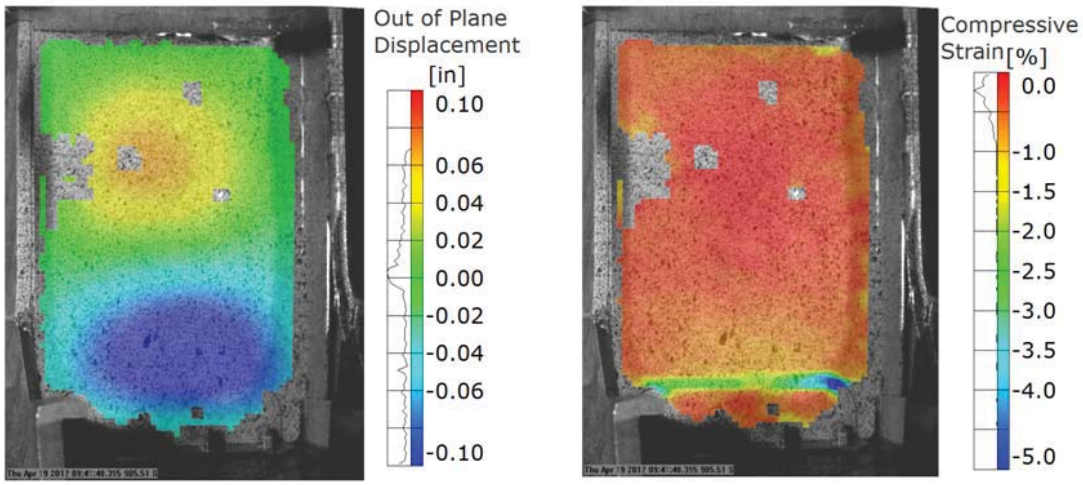

(a) Out-of-plane displacement. (b) Compressive strain.

Figure 23. Photogrammetric results for 2-ft drop test of the T-section, 1-ms after impact.

The photogrammetric data shows large amounts of out-of-plane motion in the specimen web. The top portion of the vertical web, shown in Figure 23(a), exhibits displacement toward the camera view, while the lower portion of the specimen exhibits out-of-plane displacement away from the camera view. This behavior looks like an "oil canning" mode of motion. Compressive strain on the surface of the specimen is shown in Figure 23(b). Note that the majority of the web is exhibiting low or nearly zero strain. However, the web/doubler junction exhibits large variations in strain, as indicated by the blue-green region near the bottom of Figure 23(b). Combining the two data sets, the conclusion can be reached that the web exhibits considerable out-of-plane motion; however, the primary failure mode is crushing near the base of the web at

the doubler region and delamination of the vertical flanges. This finding is confirmed by examining the videos and pictures post-test. Photographs of the post-test specimen are shown in Figure 24.

(a) Front view. (b) Rear view.

Figure 24. Post-test photographs of the 2-ft T-section test specimen.

The post-test photographs shown in Figure 24 confirm photogrammetric data for failure. Both the front and back views show a distinct failure line running horizontally right above the doubler on the web. Furthermore, these photographs show composite layer delamination and localized bending of the vertical flanges, near the transition region between vertical and horizontal. This evidence supports the conclusion that the specimen failed through crushing near the boundary edges and delamination of the vertical flanges.

3.5.2 T-Section Test at 4-ft Drop Height

A second T-section drop test was conducted at a higher impact velocity. The 204.8-lb drop mass was released from a height of 4-ft, producing an impact velocity of 192-in/s. An impact sequence is shown in Figure 25.

The upper left image in Figure 25 shows the specimen 1-ms before impact. The upper right image shows the specimen 1-ms after impact. By this time, the vertical flanges have failed completely above the fillet. At 5-ms after the impact, the vertical I-beam has separated from the horizontal I-beam and the energy of the drop mass is crushing the web of the vertical I-beam into the doubler region. At 20-ms after impact, the impact mass has reached maximum crush displacement. The lower right image shows failure of the vertical I-beam's web, flange and doubler region. The acceleration response, as measured from the drop mass, is plotted in Figure 26. As with the 2-ft test, the acceleration curve was filtered using a low-pass Butterworth filter with a cut-off frequency of 1,000-Hz.

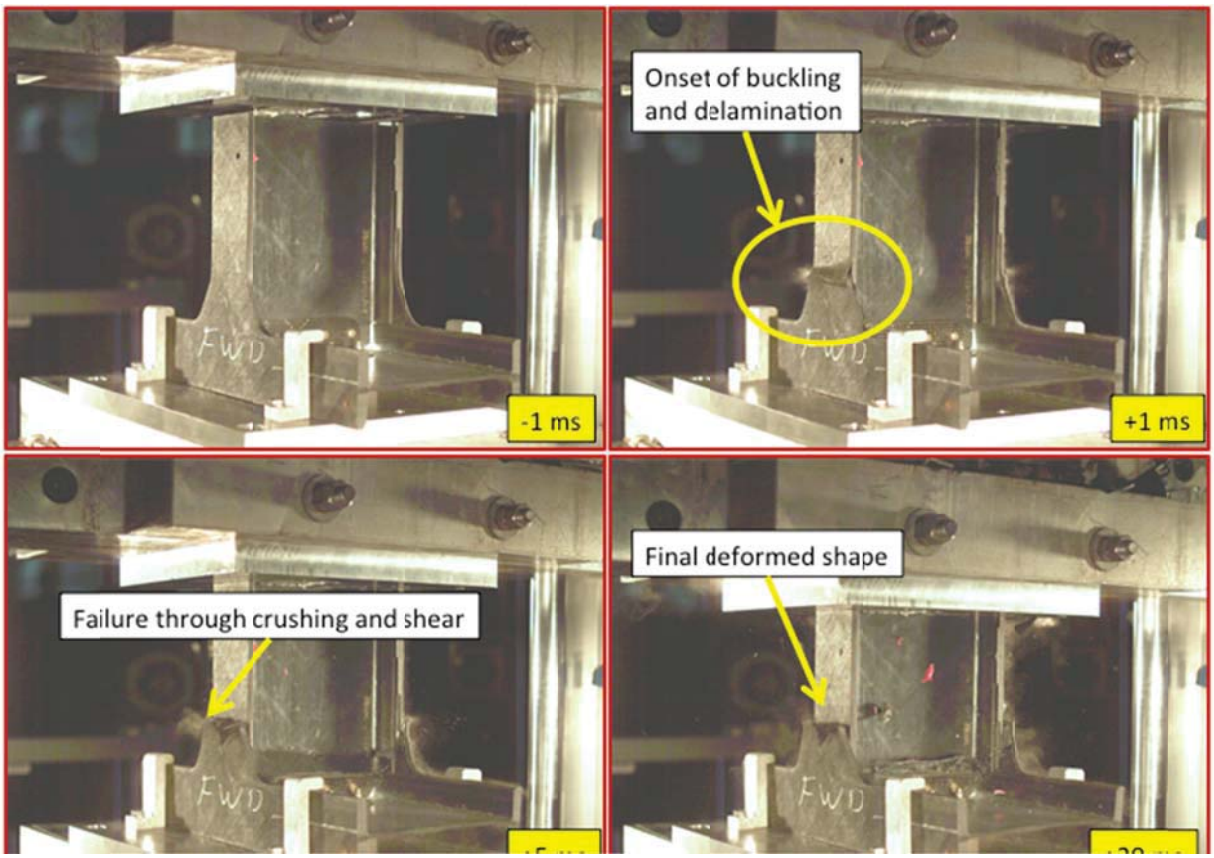

Figure 25. Image sequence of the 4-ft T-section test.

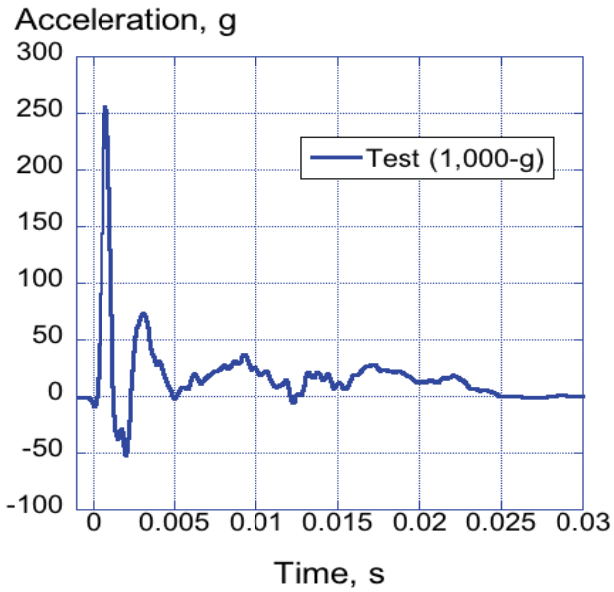

Figure 26. Drop mass acceleration of the 4-ft T-section test.

The drop mass acceleration shows a large spike of 254-g occurring 1.3-ms after initial impact. This initial spike occurs as the drop mass impacts the specimen. This peak is followed by a second peak of 71-g at 3.5-ms after impact. At 25-ms, the drop mass has reached maximum

crush displacement, and the acceleration trace shows no significant acceleration after this point. The maximum vertical displacement of the drop mass is 1.63 inches, as measured by photogrammetry. The maximum value as determined by double integration of the acceleration data is 1.67-in. Both displacement curves are shown in Figure 27.

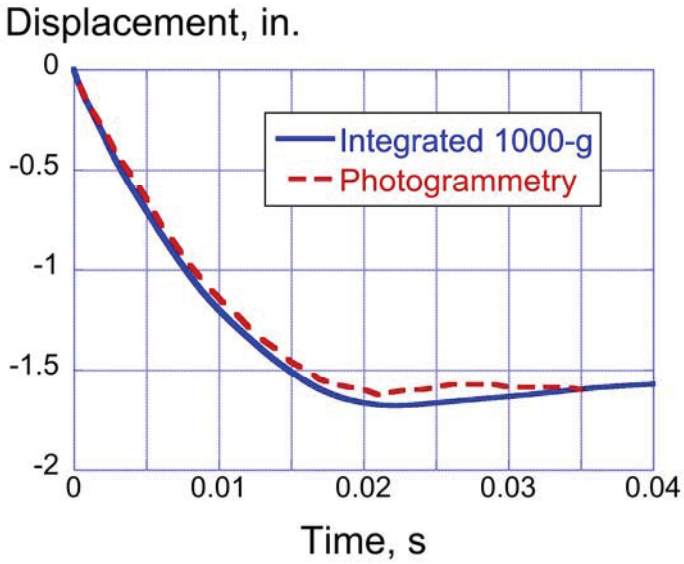

Figure 27. Drop mass crush displacement of the 4-ft T-section test.

The photogrammetric data are next examined. Cameras were used to film the front web of the T-section, sampling at 10-kHz. Because of the faster impact velocity, the two fringe plots are shown at 0.5-ms after initial impact in Figure 28.

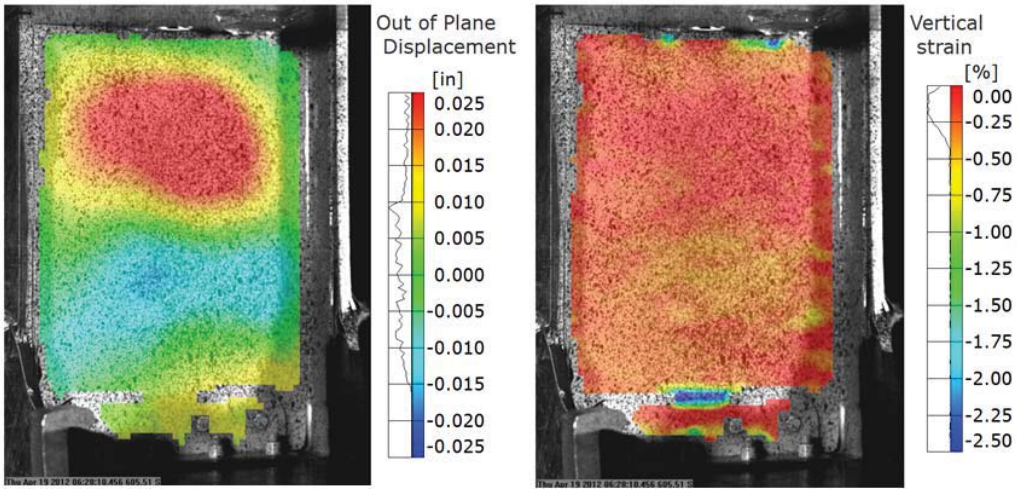

(a) Out-of-plane displacement. (b) Compressive strain.

Figure 28. Photogrammetry results for 4-ft T-section drop test, 0.5-ms after impact.

As with the lower velocity impact test, the photogrammetry data again shows large amounts of out-of-plane motion in the vertical web of the specimen. The out-of-plane behavior resembles an "oil canning" mode of motion with opposite out-of-plane displacement on the top and bottom

separated by a zero datum in the middle. A contour plot of compressive strain on the surface of the specimen is shown in Figure 28(b). The majority of the web is exhibiting low (between 0 and -0.25%) compressive strain. However, as with the lower velocity test, the web/doubler junction exhibits large variations in strain, as indicated by the blue-green region near the bottom of Figure 28(b). Combining the two data sets, the conclusion can be reached that the web exhibits considerable out-of-plane motion; however, primary failures occur near the base of the web at the doubler region and at the vertical flanges located just above the fillets. Unlike the previous lower velocity test, delaminations of the vertical flanges created a complete line of fracture, separating the vertical flange into two parts. This separation allowed the upper flange to become wedged inside the lower structure. This data is confirmed by examining the videos and pictures post-test, as shown in Figure 29.

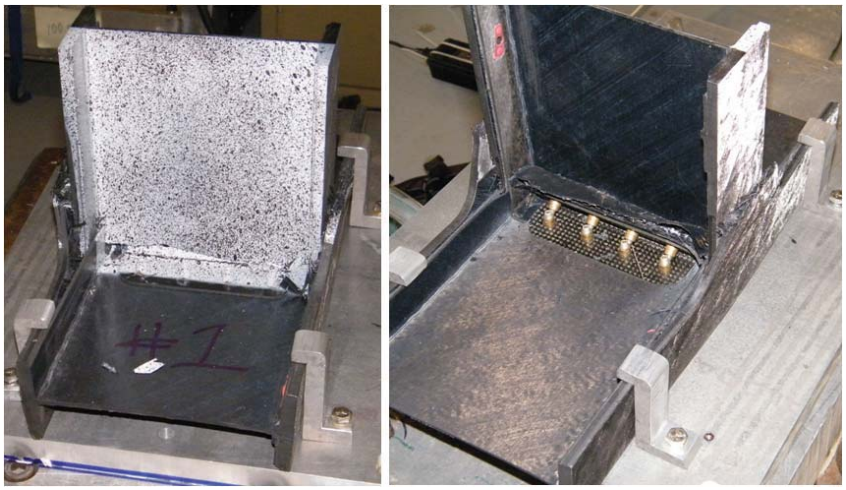

(a) Front view. (b) Rear view.

Figure 29. Post-test photographs of the T-section following the 4-ft test.

The photogrammtric data are confirmed by examining the post-test photographs shown in Figure 29. Both the front and back views show complete failure of the doubler region between the vertical and horizontal I-beam webs. Furthermore, it shows a complete shear failure of the composite layers on the vertical flanges, near the transition region between vertical and horizontal. This evidence supports the conclusion that the specimen failed near the boundary edges, at the fasteners, and at regions of transition in the geometry. These two T-section tests proved to be less of a demonstration of a pure material failure, but rather an examination of the influence of test constraints and boundary conditions.

3.6 Dynamic Crush Testing of Two Cruciform Sections

Two cross-shaped cruciform sections located at the junctions of the longitudinal and lateral I-beams were extracted from the post-test SARAP TVA rear subfloor. These components were designated cruciform sections. The length of each quadrant was approximately 6 in., which made the entire specimen a 12-in. by 12-in. cross. Each cruciform was approximately 6 in. tall. A photograph of one cruciform test specimen is shown in Figure 30.

Figure 30. Photograph of a cruciform section test specimen.

Two vertical drop tests were conducted on identical cruciform specimens. The specimens were impacted using a 14-ft vertical drop tower to determine their crush behavior, failure patterns and mechanisms, and energy absorbing characteristics for two different impact velocity conditions. During the test, the top flange was impacted by the drop mass, while the bottom flange remained fixed. The cruciform sections were instrumented with fifteen strain gages mounted on the I-beam webs located around the various quadrants, with nine outboard gages located near the free edge of the web and six inboard gages located near the intersections of the webs. Two quadrant faces were painted with a stochastic speckle pattern to collect full-field photogrammetric data. A picture of the cruciform in the drop tower is shown in Figure 31.

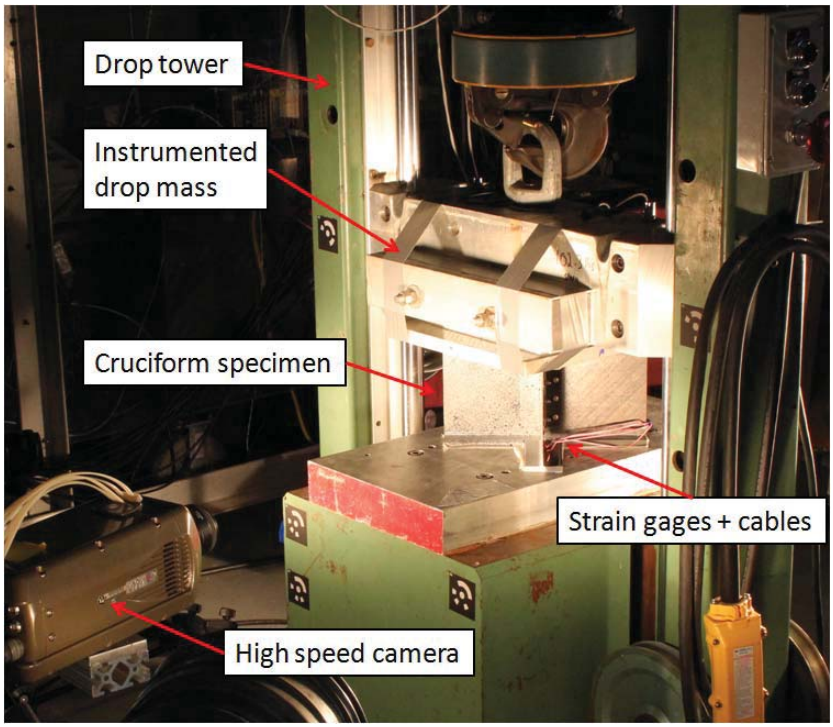

Figure 31. Photograph of the cruciform test setup.

The drop mass weight was 215 lbs. Two tests were conducted, one from a drop height of 4-ft and one from a drop height of 8-ft. Strains were measured from the strain gages and from full-field photogrammetric techniques. Accelerometers were mounted on the drop mass to measure the impact acceleration responses.

3.6.1 Cruciform Section Test at 4-ft Drop Height

The first specimen was impacted at a velocity of 192.5-in/s. An image series of the impact is shown in Figure 32. The upper left image shows the cruciform specimen immediately before impact. The left side of the picture shows the unpainted region and locations of strain gages on the cruciform. The right side of the picture shows one of the painted faces of the cruciform. Also note that there is an edge of a face of the cruciform perpendicular to the camera view in the middle of the image. The upper right image shows the cruciform immediately following impact. The three visible faces of the cruciform are wavy, as noticed by the reflections in the light patterns. At this time, the maximum acceleration has occurred. At 2-ms after impact, the lower left picture shows the first signs of failure. The webs have split near the bottom of the cruciform. At 15-ms after impact, the lower right image shows the drop mass at the time of maximum crush depth. At this time, the cruciform webs exhibit signs of large deformations and global buckling. Crushing in the lower webs is still present; however, by this time the web layers have delaminated along the free edges due to the large amounts of deformation present.

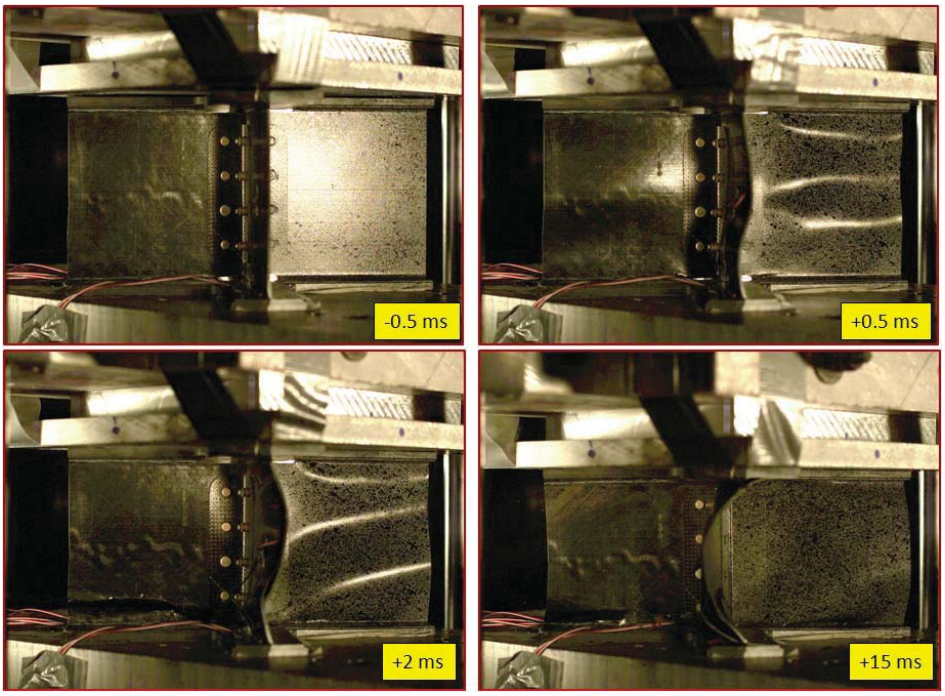

Figure 32. Image sequence of cruciform crush during the 4-ft drop test.

The acceleration time history responses, as measured from two accelerometers on the drop mass, are plotted in Figure 33. The data are filtered with a low-pass Butterworth filter with a 1,000-Hz cut-off frequency. The peak acceleration is 540-g and occurs 1.2-ms after impact. The extremely high initial spike can be attributed to the lack of a “trigger” or intentional defect designed into the specimen whose main function is to minimize initial peak loads and to initiate

crushing. In addition to the lack of a trigger mechanism, the high spike can also be attributed to the fact that the cruciform has a much higher cross-sectional area than previous test specimens. Finally, the acceleration stabilizes between 50- to 60-g and eventually enters a gradual decay starting at 10-ms and ending at rest approximately 20-ms after impact.

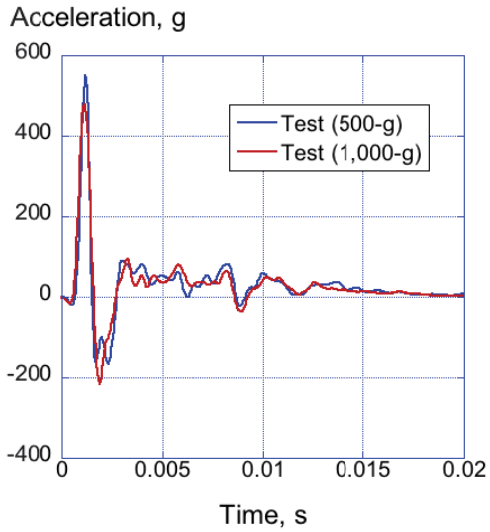

Figure 33. Drop mass accelerations from the 4-ft cruciform test.

The majority of the strain gages that were applied to the test article immediately debonded upon impact. Consequently, strain gage data were not examined. However, strain fields from the photogrammetric data were evaluated, as shown in Figure 34. For both images in the figure, two quadrant faces of the cruciform are visible. These faces are separated by the untracked doubler region near the intersection of the two quadrants.

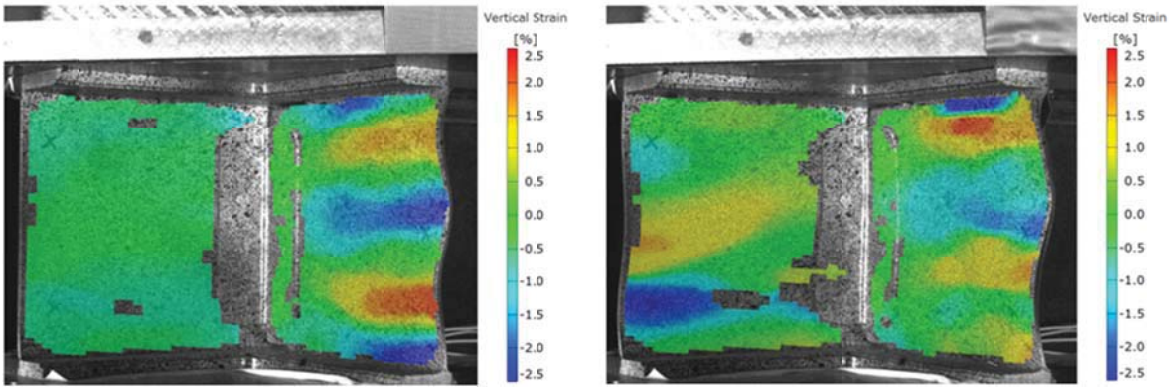

(a) Time=0.4-ms. (b) Time = 0.65-ms.

Figure 34. Vertical strain field at 0.4-ms and 0.65-ms after impact.

The vertical strain field at approximately 0.4-ms after impact is shown in Figure 34(a). The image clearly shows approximately zero strain in the left quadrant and alternating regions of +2.5% and -2.5% strain on the right. This behavior indicates that the drop mass did not impact the cruciform uniformly. The right side of the specimen exhibits large deformation, global buckling, and crushing, but no crushing is evident on the left side. Also note that the edge view

of the right quadrant is visible in the image. The alternating areas of high and low strain correspond to the waviness in the wall of the quadrant. Positive strain indicates out-of-plane tension, which occurs from bending of the wall toward the cameras, while negative strain indicates the opposite. The specimen is shown at approximately 0.65-ms after impact in Figure 34(b). Portions of the cruciform walls have begun to debond, which are indicated by the areas of high and low strain. The impact has begun to crush the left quadrant of the specimen and the low strain area near the lower left corner is an early indication of web crushing, which was seen in post-test inspections. The alternating areas of high and low strain near the top of the right quadrant indicate that a delamination failure has occurred. This failure can be seen by looking at the edge of the right quadrant in the image. Other areas of the specimen are exhibiting high strain; however, these areas have not quite failed. The majority of the onset of failures occurs around the time of the peak load, seen at 0.91-ms after the initial impact.

Displacement data were computed from photogrammetric measurements taken from the high-speed cameras and by double integration of the acceleration data obtained from two accelerometers on the drop mass. Values of maximum crush displacement range from 0.97- to 1.1-in., as indicated in Figure 35. The maximum displacement occurs approximately between 10- and 15-ms after initial impact. A photograph of the post-test specimen is shown in Figure 36.

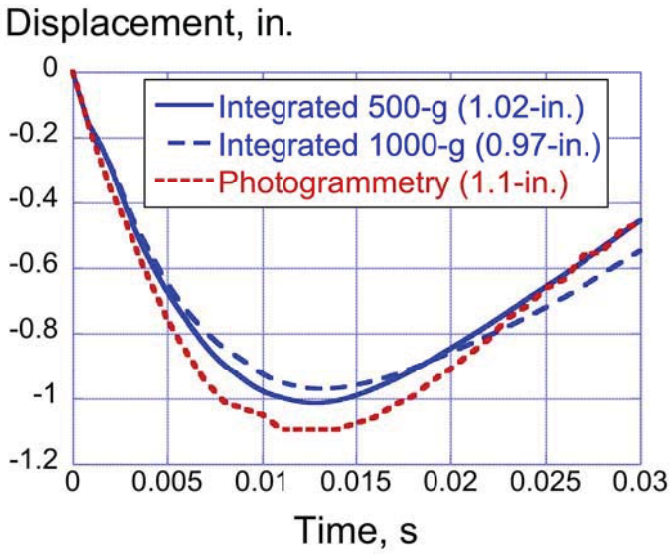

Figure 35. Crush displacement of the 4-ft drop of a cruciform section.

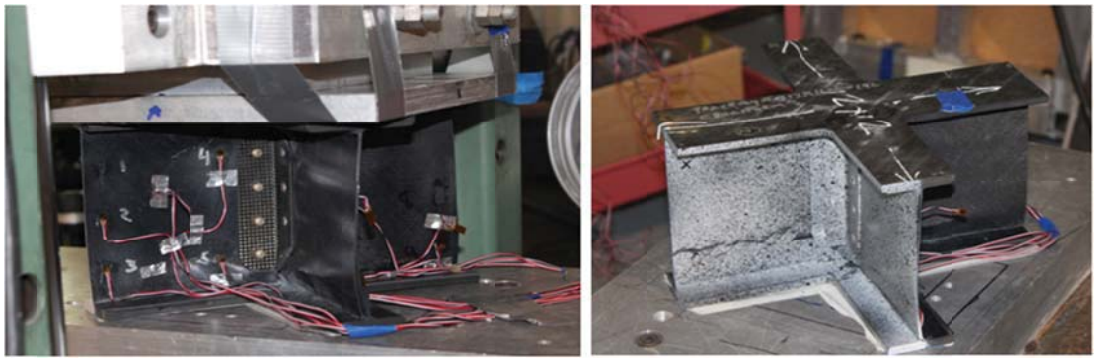

Figure 36. Post-test images of cruciform specimen following 4-ft drop test.

The failure near the bottom of the specimen is clearly shown in both images in Figure 36. The early onset of this failure was the same as that tracked through photogrammetric techniques. The delamination seen on the right side of the photogrammetric results seems to be absent from the right image in Figure 36. When the drop mass was removed from the specimen, the wall appeared to spring back to an almost pre-test condition. The separations from the delamination were visible when the mass was resting on the cruciform; however, the damage seemed to close up when the mass was removed. Both the base and impact flanges of the specimen were undamaged. This finding confirms that the energy absorbed from the cruciform specimen came primarily from global buckling, crushing, and delamination of the web sections.

3.6.2 Cruciform Section Test at 8-ft Drop Height

A second cruciform specimen was tested at an increased velocity of 268.6-in/s. An image sequence of the impact is shown in Figure 37. The image in the upper left of Figure 37 shows the specimen immediately before impact. This view is similar to the previous cruciform view: it shows one cruciform quadrant on the left side, one on the right side and an edge of one face in the middle, perpendicular to the camera view. The upper right image shows the specimen 1-ms after impact. At this time, failure has already occurred through crushing on the left side quadrant, and delamination in the perpendicular face. The lower left image shows the cruciform 2-ms after impact. Failures are present in all three visible quadrants. Finally, the lower right image in Figure 37 shows the cruciform 15-ms after impact at which point the drop mass has reached maximum crush displacement. Acceleration responses from two accelerometers mounted to the drop mass are plotted in Figure 38. These curves were filtered using a low-pass Butterworth filter with a cut-off frequency of 1,000-Hz.

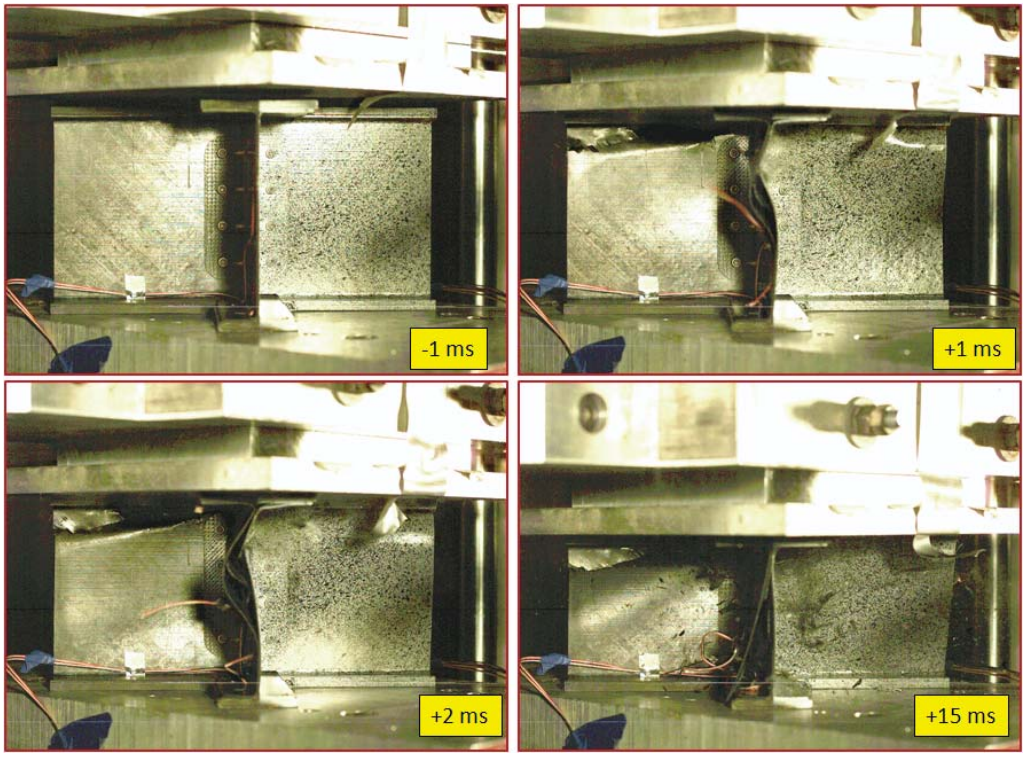

Figure 37. Image sequence of cruciform crush during the 8-ft drop test.

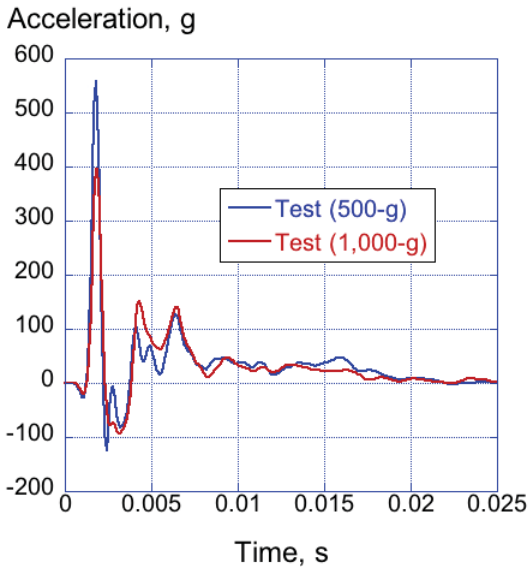

Figure 38. Drop mass acceleration from the 8-ft cruciform test.

Maximum accelerations ranged from 400- to 550-g and occurred at a time of 1.2-ms after initial impact. Two smaller peaks ranging in magnitude from 100- to 145-g occurred after the initial spike. Following these two smaller peaks, the acceleration stabilizes at approximately 40-g and remains at that level for approximately the next 10-ms. At 17-ms after impact, the acceleration response decays and reaches zero at 20-ms. This acceleration response is very similar to the cruciform test which was conducted at a lower impact velocity. Even though the energy is two times greater in this case, both specimens required approximately the same peak acceleration to initiate failure and similar trends are observed in the acceleration time histories after initial failure. However, the extra kinetic energy is absorbed through specimen crushing, as evidenced by the higher maximum displacement of the drop mass, shown in Figure 39.

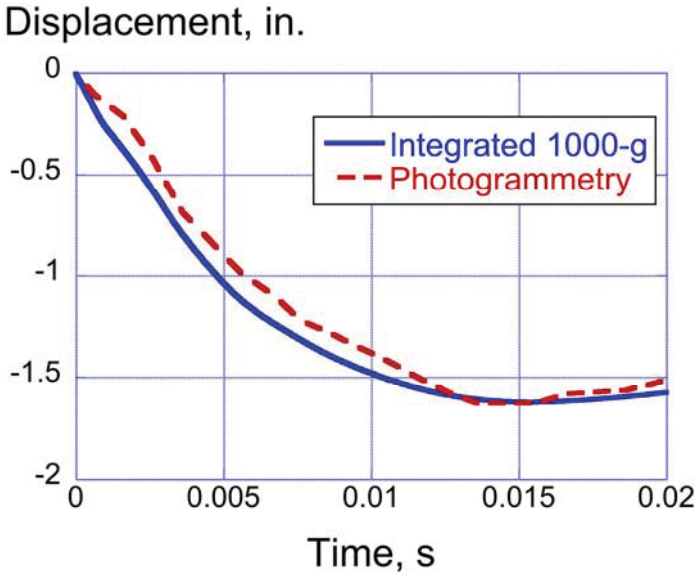

Figure 39. Crush displacement of the 8-ft cruciform test.

A maximum average crush displacement of 1.64-in. was determined by averaging the values obtained from photogrammetric target tracking using the high-speed cameras and from double integration of the accelerometer data, as shown in Figure 39. This value is higher than that obtained during the lower velocity impact (1.64-in. maximum crush for the 8-ft drop compared with 1.07-in. maximum crush for the 4-ft drop).

The photogrammetric measurements were of limited success for this test. The photogrammetric test settings used speeds much lower than the first test due to equipment availability. This slower speed, along with motion blurring which occurred due to the slower shutter speed only allowed for a partial strain map to be investigated. A fringe plot of strain, at approximately 0.5-ms after initial impact, is shown in Figure 40. The portion of the image that lacks the strain field is blurred from deformations happening in these areas. However, the strain map does show that approximately -0.3% far field strain occurs on the specimen surface during impact. Finally, the specimen is shown in post-test photographs in Figure 41.

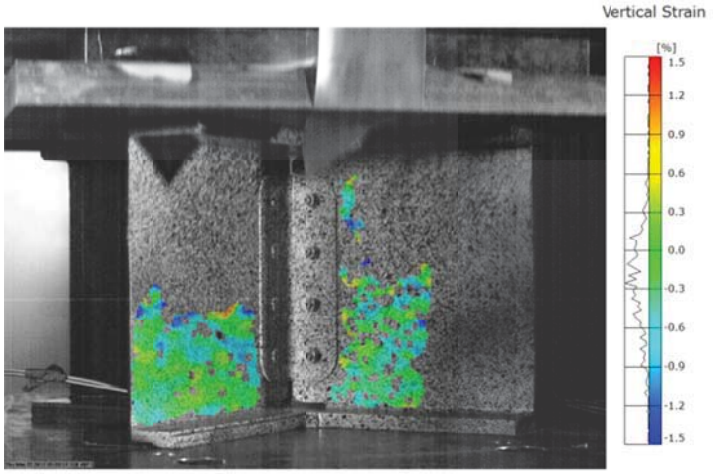

Figure 40. Vertical full-field strain map of the cruciform specimen during the 8-ft drop test.

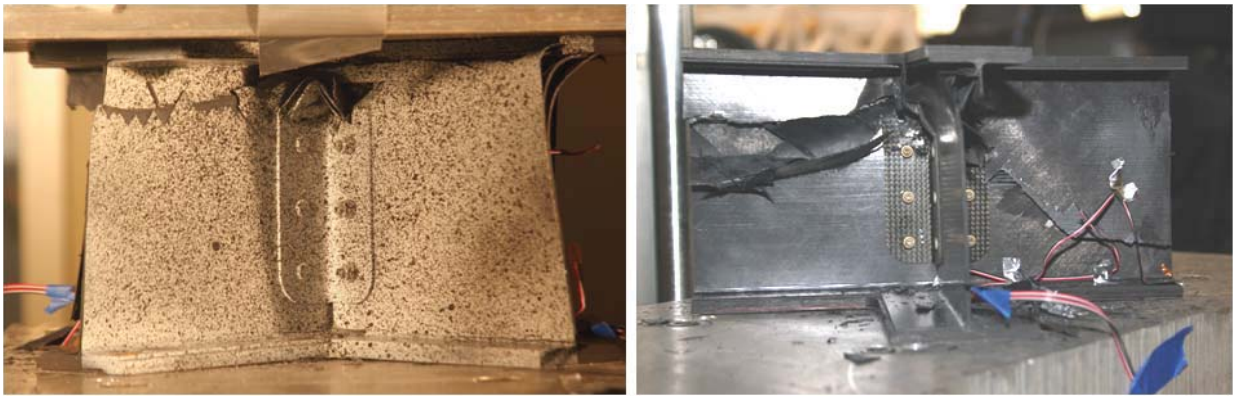

Figure 41. Post-test images of cruciform specimen following the 8-ft drop test.

As shown in the photographs of Figure 41, massive failure is evident throughout the specimen. Large areas of debonding and ply delamination are observed in all four quadrants. A noticeable crush front is observed near the top of the specimen. Also, part of the doubler region, which is the strongest part of the entire specimen, has failed. Due to the large amount of damage in the

specimen, it was possible to remove entirely the top flange away from the rest of the specimen due to the failures near the crush front. The greater amount of damage in this test, as compared with the previous 4-ft drop test, is attributed to the higher kinetic energy associated with the 8-ft drop test condition.

3.7 Testing of the Subfloor Section

A fairly large subfloor section was removed intact from the post-test SARAP TVA, with the intent of conducting a longitudinal impact test. The location of the removed subfloor section is highlighted in Figure 42. A longitudinal test was conducted to replicate a horizontal impact of a helicopter with a large amount of forward velocity into a rigid wall, which is one of the test conditions specified in the military crashworthiness requirement MIL-STD-1290A(AV) [8]. This test condition is infrequently evaluated; however, given that the subfloor was available, the longitudinal impact test was planned and conducted. To replicate this test condition, the subfloor section was positioned vertically and crushed dynamically using the 70-ft vertical drop tower located at the LandIR facility. The impact occurred such that the subfloor specimen remained stationary while a large instrumented portal frame drop mass was released from a height of 91-inches and impacted the specimen at a nominal velocity of 22-ft/s (264-in/s). The subfloor section test article is shown in Figure 43 in a vertical configuration.

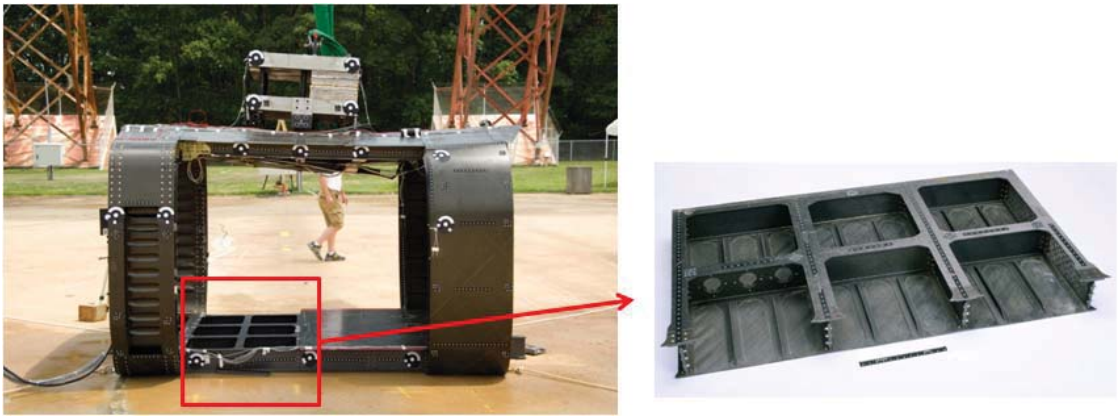

Figure 42. SARAP subfloor test article location.

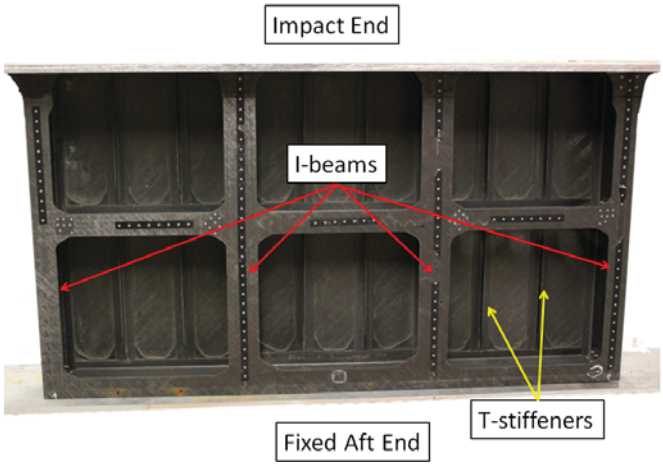

Figure 43. SARAP subfloor test article.

The subfloor I-beams were instrumented at various locations with 12 strain gages. A stochastic speckle pattern was painted onto the base (smooth, skinned side of the subfloor) and the I-beams for use with photogrammetric imaging techniques. The bottom of the specimen was potted to achieve a fixed condition on the aft end. The impact end was free, but attached to a flat plate, which would provide a large flat surface for the drop mass to impact. A photograph of the subfloor after potting, instrumenting, and painting is shown in Figure 44. A green circle in Figure 44 represents a strain gage mounted to the I-beam flange in the location noted. A yellow circle represents a strain gage mounted to the I-beam web in the location noted. Overall dimensions of the test article were: 35-in. tall, 62-in. wide, and 6-in. deep.

3.7.1 Modal Testing

A modal test was performed on the composite subfloor in position while under the 70-ft vertical drop tower at NASA's LandIR facility prior to the scheduled impact test. Analysts involved with the project were interested in performing a modal test with the 4,279-lb-impact mass resting on top of the test article in order to estimate the first plunging mode. A photograph of the test set-up is shown in Figure 45. From the bottom to the top, the test set-up consisted of concrete blocks, two aluminum plates, composite subfloor, aluminum impact mass, and orange portal frame.

Figure 44. Pre-test photograph of the subfloor section highlighting strain gage locations.

Accelerometers were mounted to the test article at selected locations. Eighteen accelerometers were mounted in the X-axis (normal to the test article floor surface) using wax. Following the first set of tap tests with an impact hammer at several locations, the accelerometers were rotated to the Z-axis (vertical) and all taps were repeated. An overall view of the test article with accelerometers mounted in the Z-axis is shown in Figure 46.

Taps were performed at four seleted locations on the test article with a 1-lb hammer, as depicted in Figure 47. Each location was tapped six times and the results were averaged to obtain Power Spectral Density (PSD), Frequency Response Functions (FRF), and coherence data. After

obtaining poor results with the 1-lb hammer, additional datasets were obtained with a 3-lb hammer at two locations in the Z-axis. The 1-lb hammer was used to excite with ~30 lb peak forces in the X-axis and ~100 lb peak forces in the Z-axis, and the 3-lb hammer increased the forces in the Z-axis to ~200 lb peak.

Figure 45. Modal test setup.

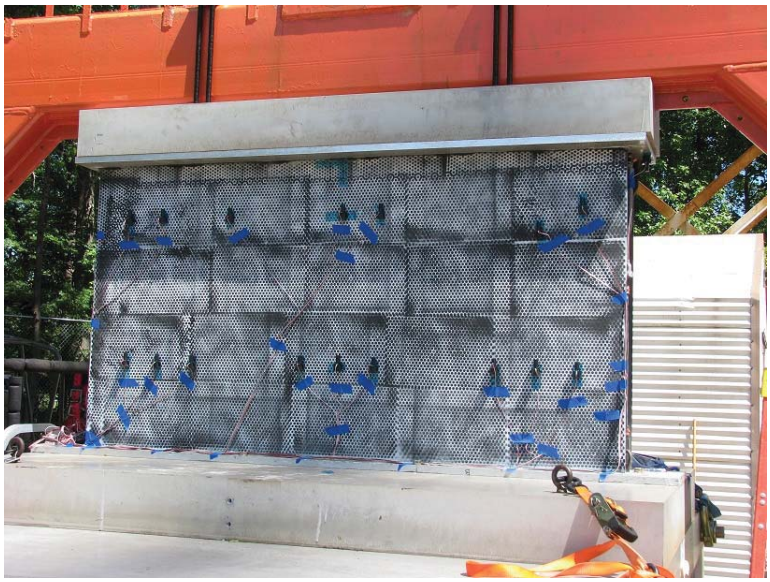

Figure 46. Accelerometers mounted on subfloor test article.

FRF and coherence results are shown in Figures 48 and 49. A reciprocity check between the X-axis excitation locations is shown in Figure 48. Poor coherence below 120 Hz indicates that the measurement results cannot be trusted below that frequency. The FRFs indicate that reciprocity is satisfied for these measurements above 120 Hz, but the peaks are not well defined and are noisy. A similar reciprocity check is shown in Figure 49 for the Z-axis excitation locations with the 3-lb hammer, with the frequency resolution reduced from 0.5 Hz to 2.0 Hz. While the coherence of these measurements is improved, they are still noisy and reciprocity is not exhibited.

Figure 47. Tap excitation in vertical direction.

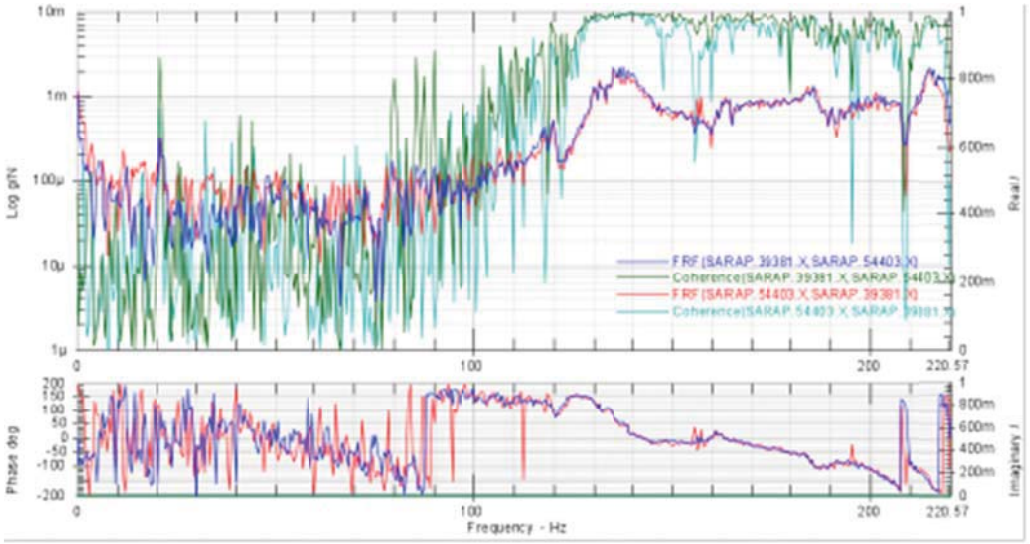

Figure 48. Horizontal axis reciprocity check.

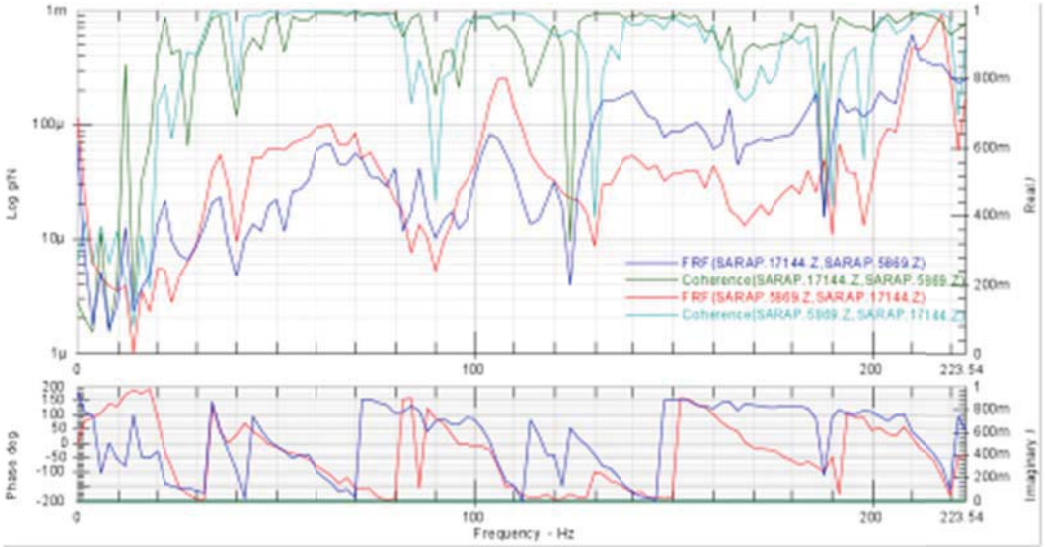

Figure 49. Vertical axis reciprocity check.

The reasons behind the poor measurement results could not be effectively diagnosed and fixed due to the limited amount of time allotted for the modal test. Improvements in coherence with higher force inputs suggest that exciting the structure with more energy, such as with a modal test shaker, would have been an appropriate follow-up step to obtain better measurements. However, this approach was beyond the scope of the "simple" modal test that was agreed upon. Attempts to use experimental modal analysis methods on the measurements resulted in complex mode estimates and poor agreement between measured and regenerated FRF curves. Unfortunately, none of the mode shape estimates obtained were satisfactory enough to present without being misleading.

3.7.2 Subfloor Impact Test Results

The longitudinal impact test of the subfloor was conducted on June 27, 2012. Photogrammetric tracking targets were placed on the portal frame such that velocities and impact angles could be obtained. Aluminum honeycomb stops were placed underneath the portal frame feet to serve as safety barriers should a test anomaly occur. A picture of the test set-up with the test article under the 70-ft drop tower is shown in Figure 50. The weight of the test article including the portal frame drop mass was 5,100-lbs, and the impact condition was nominally 22-ft/s (264-in/s). The specimen was crushed to failure.

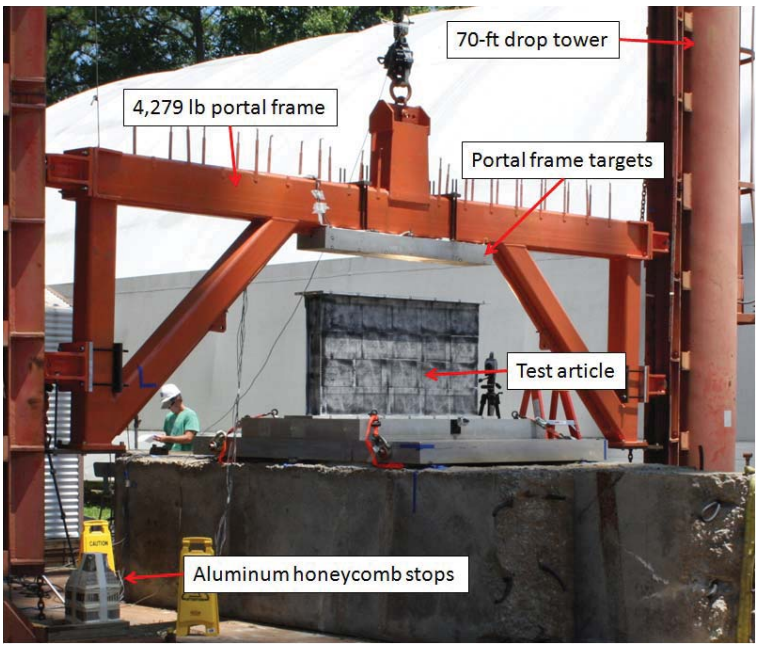

Figure 50. Subfloor longitudinal impact test set-up.

Image sequences of the test are shown in Figures 51 and 52. These images show the time history of the subfloor failure. The upper left pictures show the specimen immediately before impact. The upper right pictures show the specimen at 3-ms after impact. In these pictures, the T-stiffeners, which are attached to the subfloor base between the supported I-beam flanges on the floor, have already debonded from the test article. These pictures also show the first indication of I-beam crushing. The lower left pictures are taken at 6-ms after the impact and show the I-beam sections post failure. The lower right pictures show the specimen 25-ms after initial

impact. In these pictures, the specimen has completely failed and the residual I-beam components are absorbing energy through debonding, shearing or crushing.

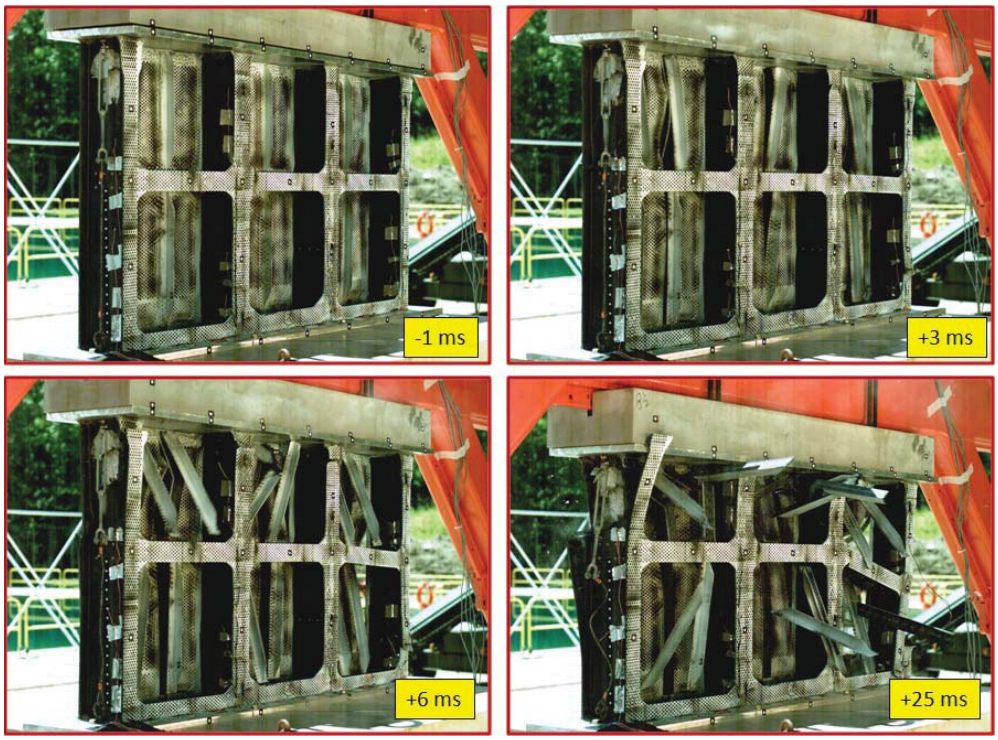

Figure 51. North east camera view of subfloor deformation.

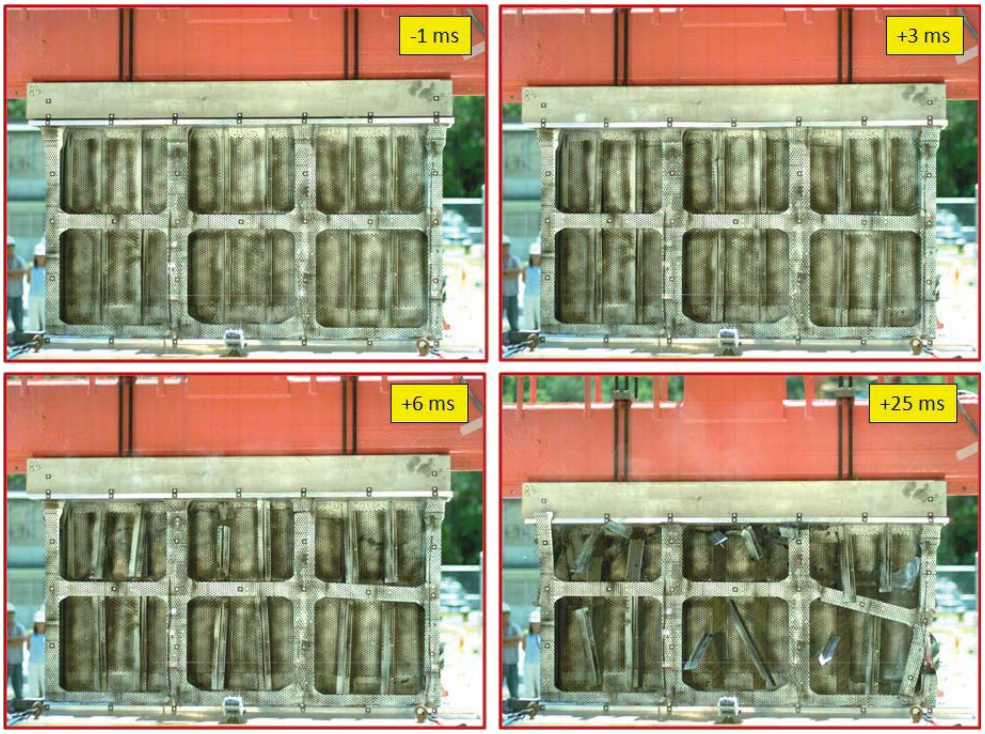

Figure 52. North camera view of subfloor deformation.

Five accelerometers were mounted on the portal frame drop mass, three of which were oriented in the vertical direction and two were oriented in the two normal directions to the vertical. The vertical accelerometers ranged between 750- and 2000-g while the upper range of the normal accelerometers was 200-g. The sample rate for the accelerometers was 25 kHz using the T-DAS Pro DAS. The results from the accelerometers were inconclusive. Of the three vertical accelerometers used, two accelerometers (750- and 2000-g maximum range) immediately failed upon first contact between the drop mass and the test article. The center accelerometer recorded an acceleration time history, but after further inspection, a large unexplained offset was present in the data immediately after first contact. Because of this anomaly, data from this accelerometer were not used. Strain gages were intended to provide load path information during impact. However, the results were also inconclusive since most of the strain gages debonded upon first contact of the portal frame and the test article.

Photogrammetric imaging was conducted only on the base (skinned) side of the test article due to camera malfunctions on the open side. The base side was filmed at 600 x 800 resolution at 10 kHz, which captured the motion of the drop mass, along with the strain field around the bottom of the specimen. Through examination of the high-speed video and the photogrammetric data, the majority of the damage and failure occurred in the first 1- to 6-ms after impact. The velocity time history of the drop mass was determined based on photogrammetric data analysis and is plotted versus time in Figure 53(a). Vertical red lines are included in the plot to highlight the time of initial impact, the time at which the portal impacts the honeycomb stops, and the time of motion stop. The time duration between initial impact and contact with the honeycomb stops is important to the analytical correlation study. The data shown in Figure 53(a) was obtained by differentiating photogrammetric displacement data, which can produce a noisy response. Consequently, the photogrammetric velocity response was filtered using a Society of Automotive Engineering (SAE) Channel Filter Class (CFC) 60-Hz low-pass filter, as shown in Figure 53(b).

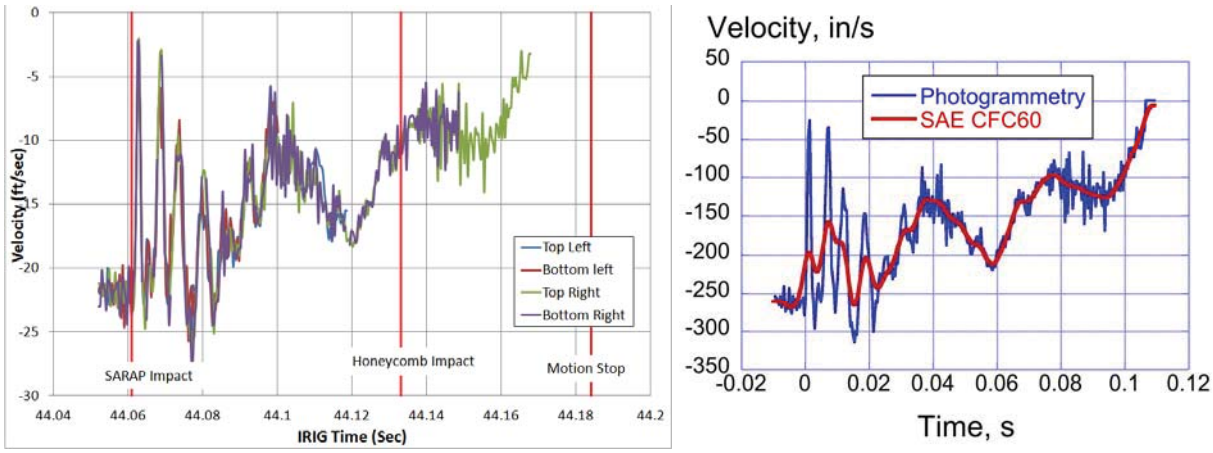

(a) Velocity data from photogrammetry. (b) Velocity data filtered.

Figure 53. Drop mass velocity responses from photogrammetric measurements of the subfloor.

The velocity at impact was 21.98-ft/s (263.76-in/s). The curves plotted in Figure 53(a) represent four different tracked targets on the drop mass. All four show good agreement, which gave further confidence in the photogrammetric results. The velocity curves show an almost linear trend with some slight oscillations as they approach the time of honeycomb impact. Kinematic

equations were used to determine the average acceleration during this time period by dividing the change in velocity over the change in time. With this method, the average acceleration between initial and honeycomb impact is approximately 4.9-g. The data ends partially between the honeycomb impact and the motion stop because the targets being tracked on the drop mass fell out of the camera view and were obstructed by the base of the subfloor at this time. The motion stop datum was determined qualitatively by examining the high-speed videos.

The displacement of the drop mass was also measured using the photogrammetric techniques to investigate crush displacement of the test article, as plotted in Figure 54. The displacement response shows that the subfloor crushed approximately 13 inches before the honeycomb stops engaged, which occurred at 0.071-s. The displacement of the subfloor base was next examined using full-field strain photogrammetric techniques. Out-of-plane displacement is shown in Figure 55. Note that the lower left portion of the base could not be tracked.

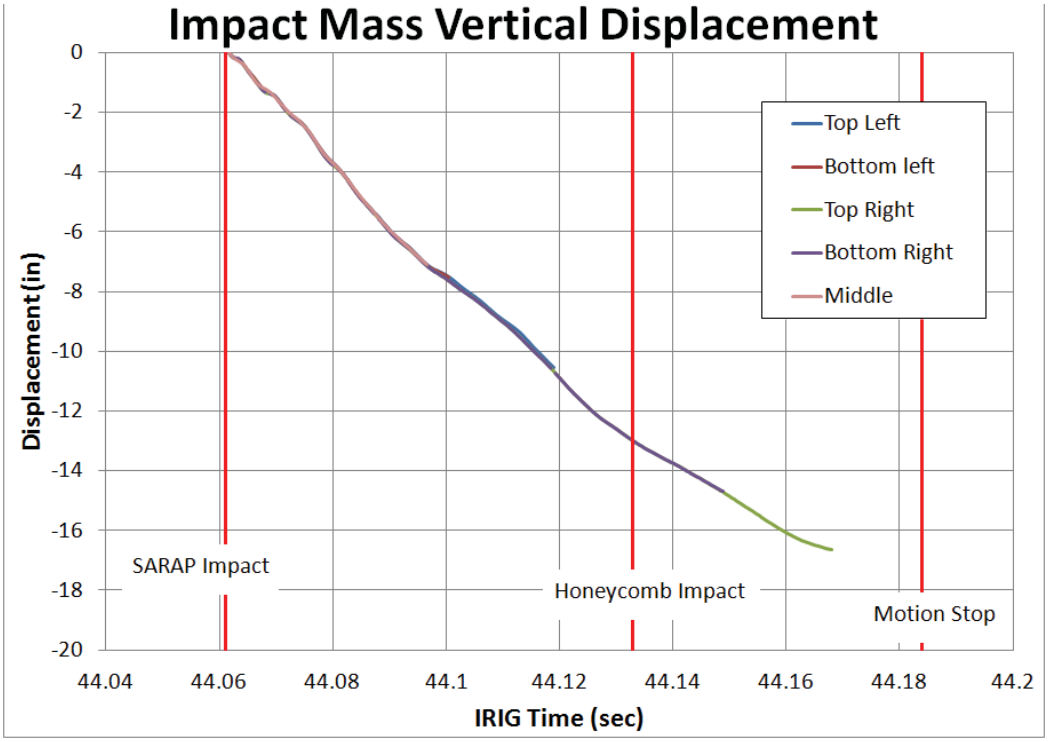

Figure 54. Drop mass vertical displacement of the subfloor.

The out-of-plane displacement at 1.2- and 5-ms after impact are shown in Figures 55(a) and (b), respectively. The large green areas are the areas on the base between the I-beam structural members, which are only supported by post-bonded stiffeners. However, due to the immediate failure of the post-bonded T-stiffeners, the areas between the I-beams are unsupported. The structure between the areas of green corresponds to the locations of the I-beams on the test article. The displacement shows an "oil-canning" mode of motion until 5-ms when a shear failure near the top of the base causes it to crush instead of deform. The failure shape can be observed by examining the top of the tracked region in Figure 55(b). Note the convex shaped curve, above which data is not tracked. The strains in the specimen were very low, as shown in Figure 56.

At 1.2-ms after impact, the subfloor base is intact and exhibits a strain variation between -0.4 and -1.0%, as shown in Figure 56(a), indicating that the subfloor is absorbing the initial impact energy by deforming. No clear pattern occurs which quantifies the differences in straining between the unsupported base and the supported I-beam sections. The failure location near the top of the base does begin to show by noting the large blue horizontal lines near the top, indicating that the strain is approximately -1% in compression. However, at 5-ms after impact, the average full-field strain ranges from 0 to -0.2%, as shown in Figure 56(b). This result indicates that the impact has progressed past structural deformation and moved toward material failure.

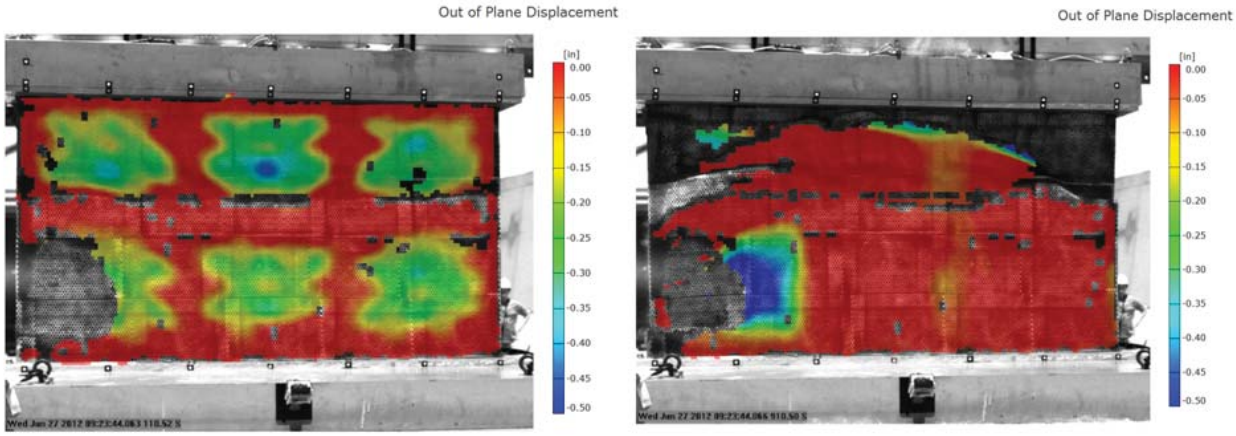

(a) Time = 1.2-ms. (b) Time = 5-ms.

Figure 55. Out-of-plane displacement in the subfloor test article at 1.2- and 5-ms after impact.

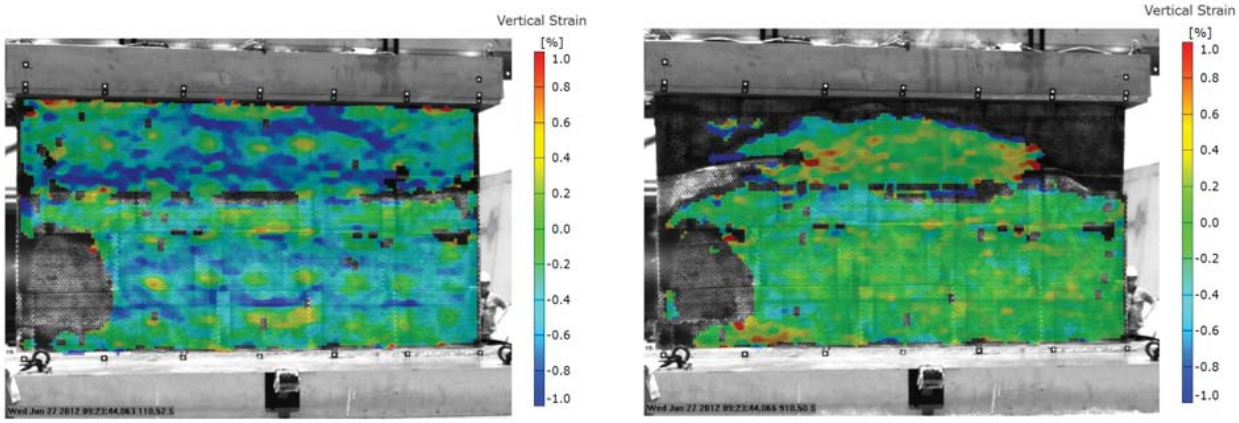

(a) Time = 1.2-ms. (b) Time = 5-ms.

Figure 56. Vertical strain in the subfloor test article at 1.2- and 5-ms after impact.

The test article was damaged beyond repair from the impact. Photographs of the specimen are shown in Figure 57 immediately after the impact. The open side of the subfloor specimen, shown in Figure 57(a), shows that two of the I-beams actually crushed to absorb the impact energy and two of the I-beam flanges delaminated from the I-beam webs to absorb energy. The photograph of the base side of the subfloor section, shown in Figure 57(b), shows that the unsupported section of the base of the floor remained relatively intact. However, the base separated from the

I-beams, evidence of which is supported from the displacement and strain data. The photograph of Figure 57(b) also indicates that there was a large shear failure near the top of the base of the subfloor.

(a) Open subfloor deformation. (b) Base (skinned) side deformation.

Figure 57. Post-test photographs of the subfloor.

Further inspections showed that the T-stiffeners debonded cleanly off of the subfloor base and contributed almost no energy absorption. A photograph showing a portion of the base in which both the T-stiffeners and the I-beam flanges have come apart from the base section (circled) is shown in Figure 58(a). The largely intact T-stiffeners, which debonded immediately upon impact, were collected and are shown post-test in Figure 58(b).

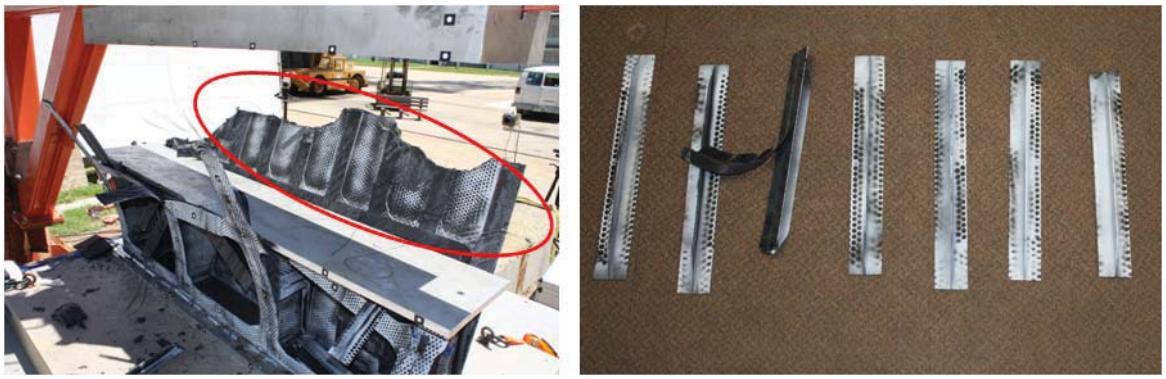

(a) Subfloor open side failures. (b) Post-test collected T-stiffeners.

Figure 58. Post-test subfloor stiffener behavior.

3.8 Testing of the Framed Fuselage Section

This section of the report describes modal, quasi-static, and impact testing of the forward framed fuselage section that was extracted from the post-test SARAP TVA. The extraction location is depicted in Figure 2. The fuselage section dimensions were: 17-in. deep, 69-in. tall, and 97-in. wide. The height of the subfloor was 6-in. NDE was not performed on the test article; however, some areas of localized delamination were present near the top right-side outer skin. Epoxy was inserted into the delaminated area during attachment of the upper mass. Two nondestructive tests were performed including modal vibration and quasi-static testing, prior to vertical drop testing of the fuselage section.

3.8.1 Modal Testing

Modal testing of the SARAP forward fuselage section concentrated on extracting two critical modes that were identified by pre-test analysis as important contributors to the fuselage impact response (the 4th vibration mode at 73-Hz and the 8th mode at 144-Hz). From the pre-test analysis, it was also determined that supporting the fuselage at two points underneath the floor would not constrain these two critical modes and therefore this configuration was selected for the modal test. A montage of pictures from the modal test is shown in Figure 59. A front-left view of the entire fuselage test section is shown in the center of Figure 59. Close-up photographs of the left, right, top, and floor accelerometers are shown including a view of the bottom support. For all testing PCB Piezotronics Model T333B42 accelerometers were used with nominal sensitivity of 500 mV/g. For excitation, a PCB Piezotronics 086D20 impact hammer with a hard tip was used with an in-line load cell to measure the input force. Because only nine accelerometers were available, testing was conducted by sections (i.e., left, top, etc.). For each data set, the fuselage was hit with the impact hammer in all 3 directions. Although most of the accelerometers were placed to measure accelerations normal to the inner surface of the fuselage, 1 to 2 accelerometers were placed to measure the out-of-plane accelerations (i.e. x-direction). Acceleration data were collected from 0- to 256-Hz with a frequency resolution of 0.5-Hz. A total of 34 acceleration measurements were obtained.

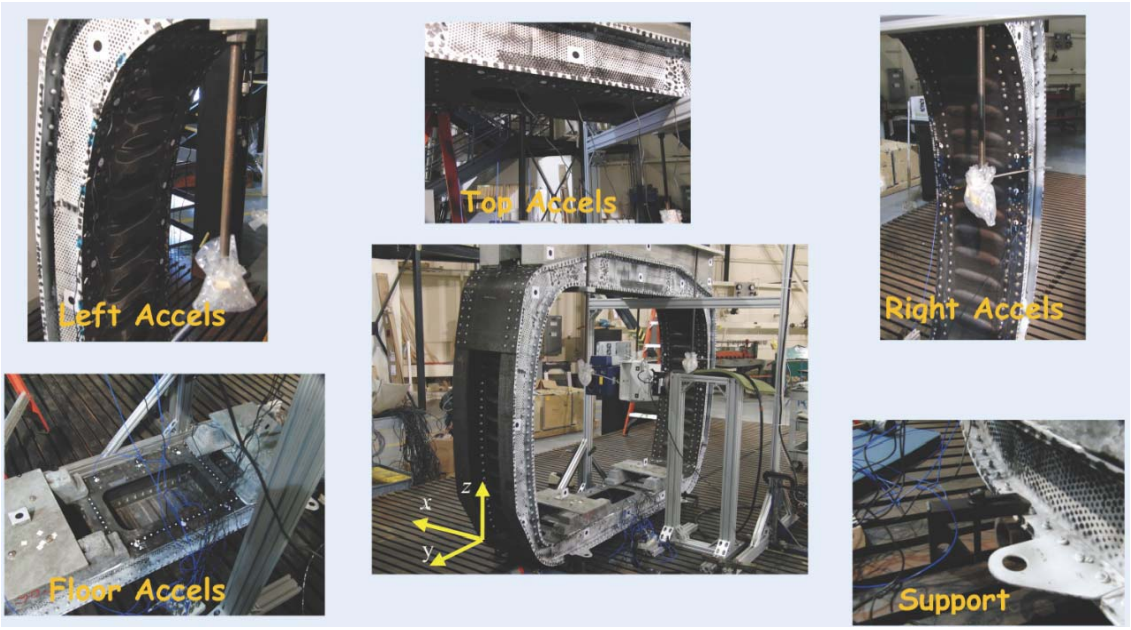

Figure 59. Montage of composite fuselage test section undergoing modal testing.

Because the modal test is nondestructive, it is a convenient way to collect data for an initial assessment of the LS-DYNA model. During the drop test, only certain vibration modes play a role in the test article deformation. To determine what vibration modes need to be targeted, an impact simulation was conducted and the time histories were decomposed into time-invariant impact shapes. Then, the impact shapes were compared to the vibration modes of the structure using orthogonality. Only vibration modes with high orthogonality values were targeted during the modal test. Based on this procedure, only two vibration modes were deemed important for impact: the 4th vibration mode at 73 Hz and the 8th mode at 144 Hz. The mode at 144 Hz is

primarily the fuselage floor moving in the vertical direction, whereas the mode at 73 Hz involves motion of the entire cross section.

For modal testing, the fuselage section was simply supported at the bottom. The fuselage section is shown in Figure 60 prior to modal testing. In the modal test configuration, the test article weighed 1,610-lb, including 368-lb for the fuselage section, 423.5-lb for the floor ballast, and 818.5-lb for the upper ballast. Two different tests were conducted: 1) the first test used a Laser Vibrometer (LV) to measure velocity at different points inside the fuselage due to an excitation from an overhead shaker positioned to impart loads in the vertical direction, and 2) the second test used an impact hammer and accelerometers. Based on model predictions, the bandwidth for the modal test was from 10- to 250-Hz. Data from the LV was collected at 38 locations on the top, bottom, and both sides of the fuselage. However, all data from the LV only measured velocity perpendicular to the laser head and therefore no forward/backward motion of the fuselage was recorded. In contrast, 34 accelerometers were also placed at top, bottom, and both sides; however, in this case, 2 accelerometers were also placed to measure forward/backward motion. In addition, the hammer tests included hits in all 3 directions while measuring acceleration. Data sets from tests using a shaker with an LV system and data using accelerometers with an impact hammer were both analyzed. Surprisingly, data with the LV system resulted in mode shapes that were inconsistent with the acceleration data and the LS-DYNA model. For this reason, results using the LV data will not be presented and efforts to use this dataset were dropped.

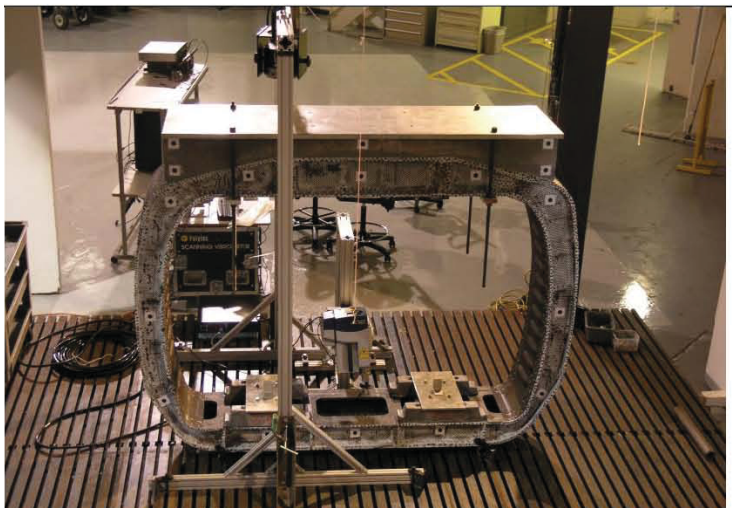

Figure 60. Modal test set-up for composite fuselage test section.

Frequency response functions from the vibration tests with 34 accelerometers were analyzed using the MATLAB® SOCIT (System Observer Controller Identification Toolbox) [9] and the Frequency Domain Identification Toolbox [10]. Frequency data were analyzed to determine the experimental mode shapes and frequencies used to compare with analysis. The results of this analysis are reported in Section 4.6.3 of this report.

3.8.2 Static Testing

Prior to static and impact testing, the fuselage section was modified to include ballast mass and

instrumentation. Due to the slanted roof line of the test article, two 5.5-in. wide, 84-in. long aluminum wedge shaped blocks were mounted via epoxy to the top of the north (rear) and south (front) edges of the test article to create a flat surface. An aluminum plate was then fastened onto the two wedges to tie them together. The two wedges and plate were known as the upper ballast mass. Once together, the entire fixture was clamped to the top of the portal frame. The portal frame also included an aluminum impact mass, which was installed for the previous subfloor test. This impact mass remained attached to the portal frame to provide extra accelerometer mounting locations as well as adding extra ballast weight. The extra mass, plates and wedges were all needed to achieve the appropriate clearance for the test article to fit within the portal frame's bracing legs and also to increase the total drop mass to 5,884 lbs. Ballast mass was added to the floor in the form of four 100-lb lead weights to simulate seats and occupants. A photograph of the test article is shown in Figure 61.

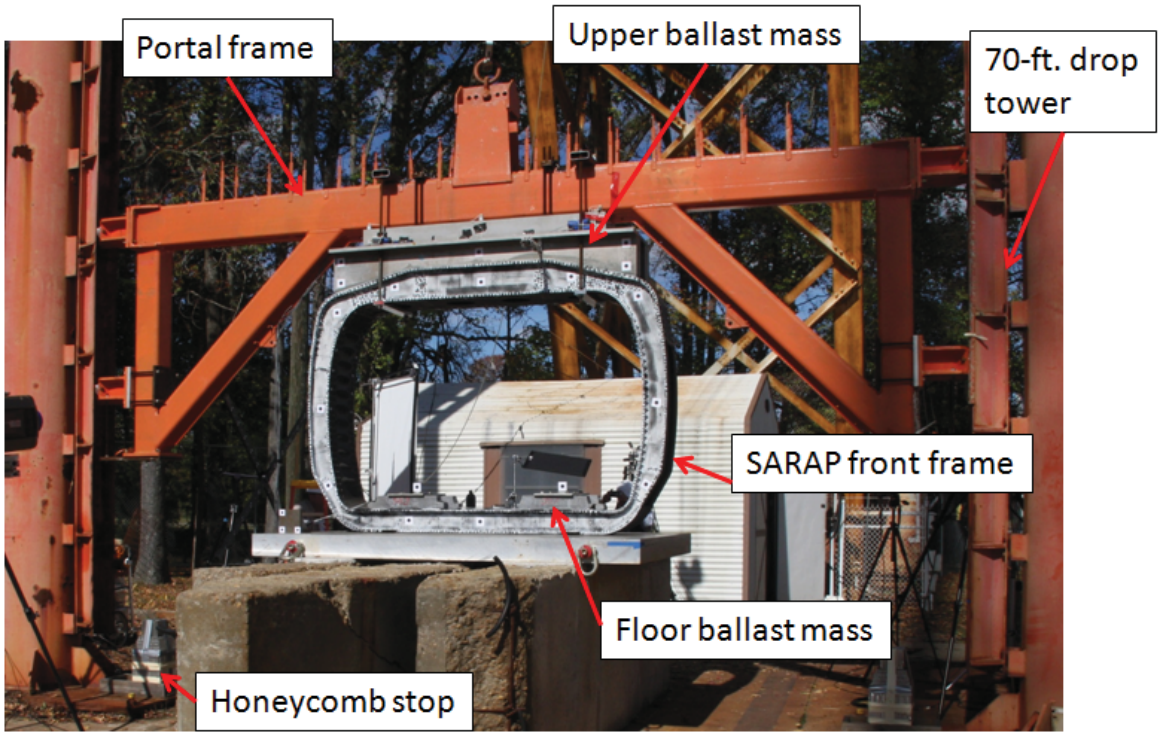

Figure 61. Pre-test photograph of the framed fuselage section in test position (south view).

Prior to static testing, a stochastic speckle pattern was painted on both sides of the fuselage section for collecting full-field photogrammetric data. The static test was first conducted on the test article to determine vertical deflection while in the test condition. The applied static load was the overhead mass used for the impact test. The static test was conducted by raising the portal frame a slight amount such that the test article was approximately 1-in. off of the ground and the weight of the overhead ballast mass was offloaded. Then, a set of images was acquired from both sets of photogrammetric cameras in this unloaded state. Next, the test article was then lowered back onto the impact surface such that the entire overhead ballast mass was being supported by the test article. Finally, a second set of images was acquired with both photogrammetric cameras. The images were then loaded into the photogrammetry software, compared, and deflections were computed.

Three data sets were used to determine the test article deflection for the static test. The three data sets were the north face stochastic pattern and both the north and south face target locations. The south face stochastic pattern was too small for the south cameras to analyze. The discrete target locations analyzed on both the south and north faces are depicted in Figure 62. The differences in the purely vertical positions for the targets located on each of the faces, along with a column for the lateral motion of the targets located on the sides of the test article are shown in Table 3.

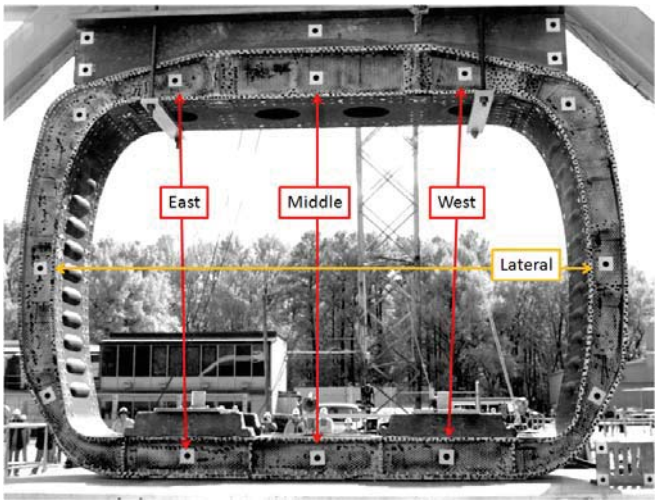

Figure 62. Discrete tracked target locations used for deflection measurements during the fuselage section static test (north view).

Table 3. Target Deflection for the Static Test of the Fuselage Section.

Camera view	**East deflection (mil)**	**Middle deflection (mil)**	**West deflection (mil)**	**Lateral deflection (mil)**
South	59.9	57.6	48.3	6.4
North	52.7	68.6	54.1	14.1

The average for all of the deflections was approximately 56.9 mils, while the standard deviation was 7.0-mil. It should be noted that the resolution of the photogrammetric system in this configuration was approximately 5-mil, and thus the spread in the data can be partially attributed to the resolution. However, there are also potential physical causes for discrepancies in the data. Two major factors noted were the possibility of misalignment in attaching the test article to the portal frame and the addition of a layer of composite underneath the north face of the test article. This additional layer was most likely added during the original fabrication of the frame section to help support the subfloor. When the framed fuselage section was cut away from the TVA for the facilitation of this test series, the extra layer remained. The addition of this layer did make the test article slightly asymmetric and caused the north side to be loaded slightly higher than the south side.

The full-field north side photogrammetric data confirms the results in Table 3. Horizontal and vertical displacement maps from the north side of the test article are shown in Figure 63.

Though individual values were not examined from the displacement fields, general trends were noted. The maximum horizontal displacement of the right edge, depicted in Figure 63(a), shows approximately 15- to 18-mils of displacement, whereas the centerline shows almost no horizontal displacement. The vertical displacement map is shown in Figure 63(b). The bottom of the test article was selected as the data reference plane and, as such, this region of the test article showed very little displacement. Starting at this almost zero datum, the displacement increased from the bottom to the top and reached a maximum of approximately 50 mils at the top of the test article. Due to imaging issues, the data on the left side of the test article spanning up to the upper left corner was deemed suspect and not included in the analysis.

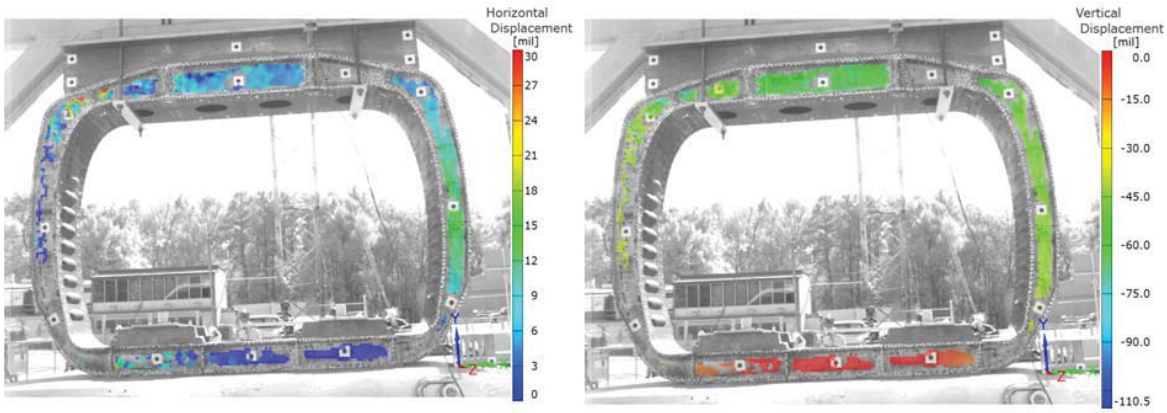

(a) Horizontal. (b) Vertical.

Figure 63. Horizontal and vertical displacement fields on the north face of the fuselage section.

3.8.3 Impact Testing

The framed fuselage section was drop tested using the 70-ft. vertical drop tower at the LandIR facility. The test article was attached to the drop tower portal frame, raised to a nominal height of 91-in. and dropped to achieve a nominal 22-ft/s (264-in/s) velocity. The total drop weight, which included the portal frame, the upper ballast mass, lower floor ballast mass and the test article was 5,884 lbs. Instrumentation was limited to seven accelerometers at locations on the portal frame and two accelerometers on the lead weights on the test article floor. The sample rate for the accelerometers was 25 kHz using the T-DAS Pro DAS. Photogrammetric data were acquired from both sides of the test article. Sampling rate for the south photogrammetric cameras was 10-kHz, while the sampling rate for the north photogrammetric cameras was 1-kHz. The main purpose of the south cameras was to measure the impact conditions along with time histories for displacement and velocity through the discrete targets, while the north cameras were to capture full-field deformations of the test article through analysis of the stochastic speckle pattern. However, the targets and the stochastic pattern were applied to both sides in an attempt to collect extra data, if possible. Aluminum honeycomb was placed underneath both portal legs to stop the portal frame should a test anomaly occur. The impact test set-up is depicted in Figure 61.

The measured impact velocity was 20.75-ft/s (249-in/s) and the total vertical crush of the test article was 7.25-in., as measured from photogrammetric data analysis. The pitch angle at impact was 0.42° leaning towards the south, and the roll angle was 0.29° leaning towards the west, as determined from the photogrammetric data. Failure occurred at the floor through shearing and

brittle fracturing from the sides near the lower corners. Delaminations occurred near the crush front on the lower sides. An image sequence of the test is shown in Figure 64 from the southeast view and in Figure 65 from the north view. Note that the honeycomb stops did not engage during the test.

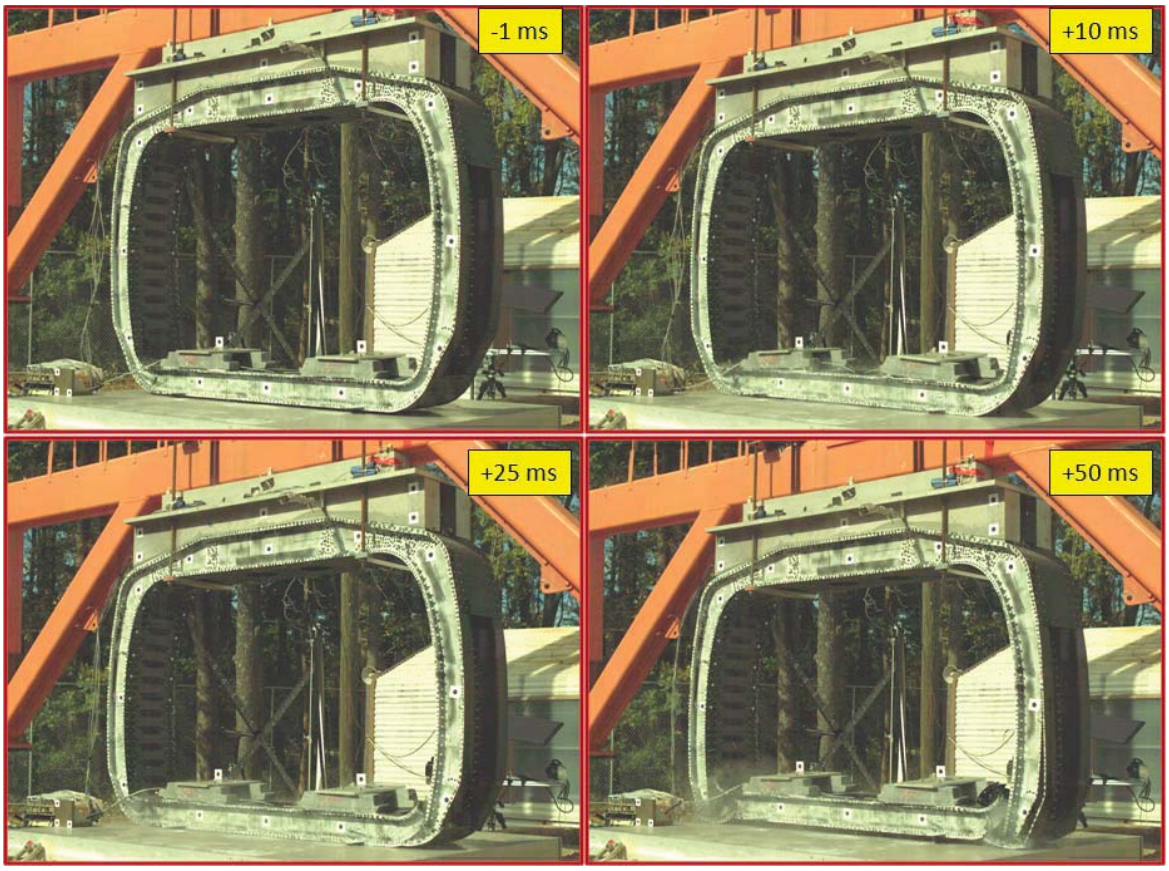

Figure 64. Image sequence of the fuselage section drop test from the southeast camera.

Four still images extracted from the high-speed videos are shown in Figures 64 and 65. The first image in the upper left shows the test article immediately before impact. The upper right image shows the specimen 10-ms after impact. At this time, the bottom of the test article has contacted the ground and the sides have bowed out. Localized failure due to shear and buckling of the individual layers has begun; however, the test article has largely retained its structural integrity. The lower left pictures show the test article 25-ms after impact. At this point in time, large-scale failures due to shearing and brittle fracturing in the floor structure were present in the lower corners. The lower right images show the test article 50-ms after impact. The floor structure has completely broken away from the rest of the test article. During the time history of the impact, the floor structure rebounds before coming to rest skewed toward the southwest corner of the test article. Photographs of the southeast and northwest corners of the test article are shown in Figure 66 during floor separation.

Acceleration responses from the five accelerometers mounted on the portal frame and drop mass are similar, so only a representative acceleration response is plotted. Similarly, the accelerations from the two accelerometers located on the floor ballast mass are similar to each other, but

different from the other five, so only one of the floor accelerations is examined. Thus, there are two distinct acceleration responses from the test. The portal frame, drop mass, and upper test article represent the first, while the floor of the fuselage section represents the second. The acceleration responses from accelerometers located on the middle of the portal drop mass and on the lower floor ballast mass are shown in Figure 67 as representative traces for both locations. The raw acceleration curves at both locations were filtered using a low-pass Butterworth filter with cut-off frequencies of 300- and 1,000-Hz. The lower filter frequency was needed to capture the underlying pulse, due to the large amount of oscillations in the data.

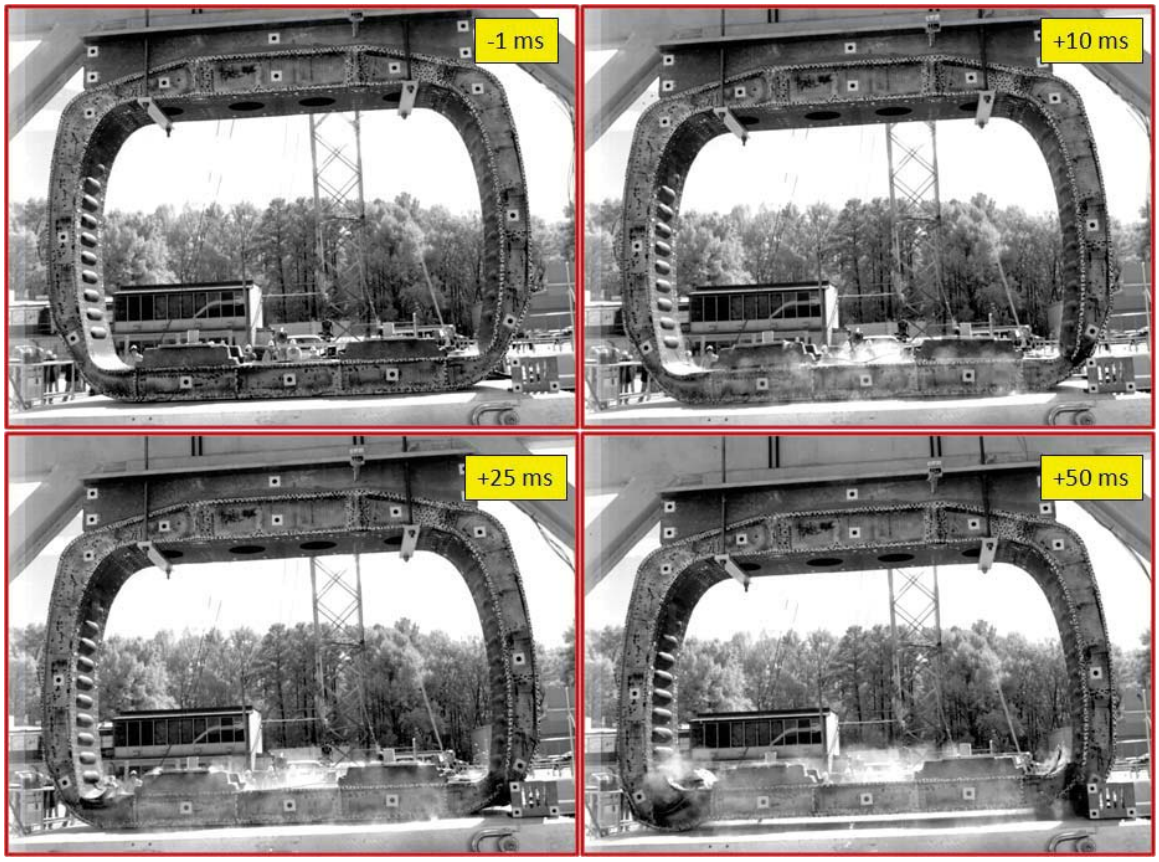

Figure 65. Image sequence of the fuselage section drop test from the north camera.

Based on the 300-Hz filtered data, the portal frame exhibited an oscillatory acceleration response, achieving an initial 100-g peak for the first 1-ms of the response, then immediately plunging to approximately -100 g. Thereafter, the response oscillated at 26-Hz around a mean value of 2.6-g starting after 30-ms. Based on the 300-Hz data, the floor acceleration, shown in Figure 67(b), also exhibited a very large spike of 475-g during the first 1-ms of impact. This large acceleration resulted from the initial impact of the test article with the ground. After the initial spike, three subsequent acceleration peaks of 60-, 47- and 57-g occurred at times of 15-, 30-, and 38-ms, respectively. These peaks all occurred during the dip in the drop mass acceleration. After the four initial acceleration spikes, the floor accelerations settled out and eventually decayed to zero by 0.05-s. At this point, the 26-Hz oscillation arises in the upper drop mass acceleration. The 26-Hz oscillation mode was attributed to the portal frame legs flexing during the impact.

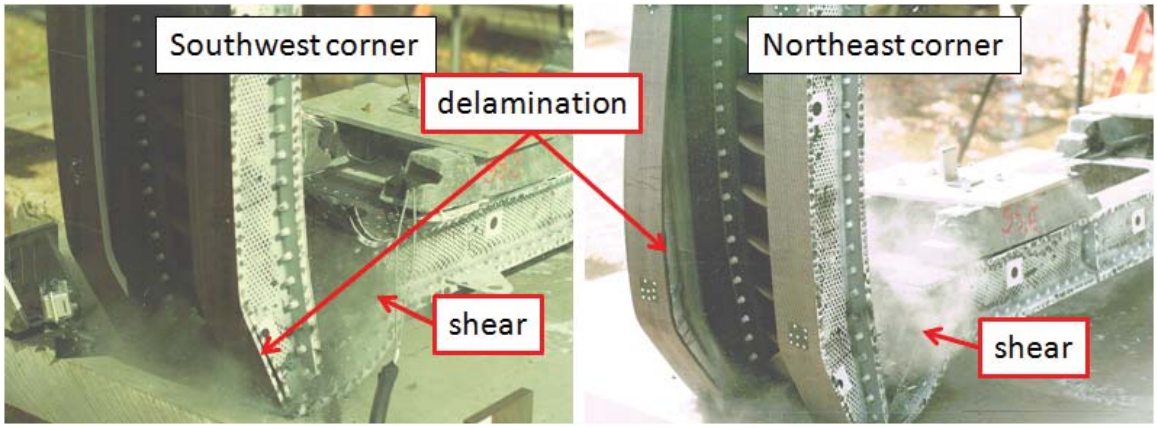

(a) Southwest view. (b) Northeast view.

Figure 66. Close up views of floor failures that occurred during the fuselage section impact test.

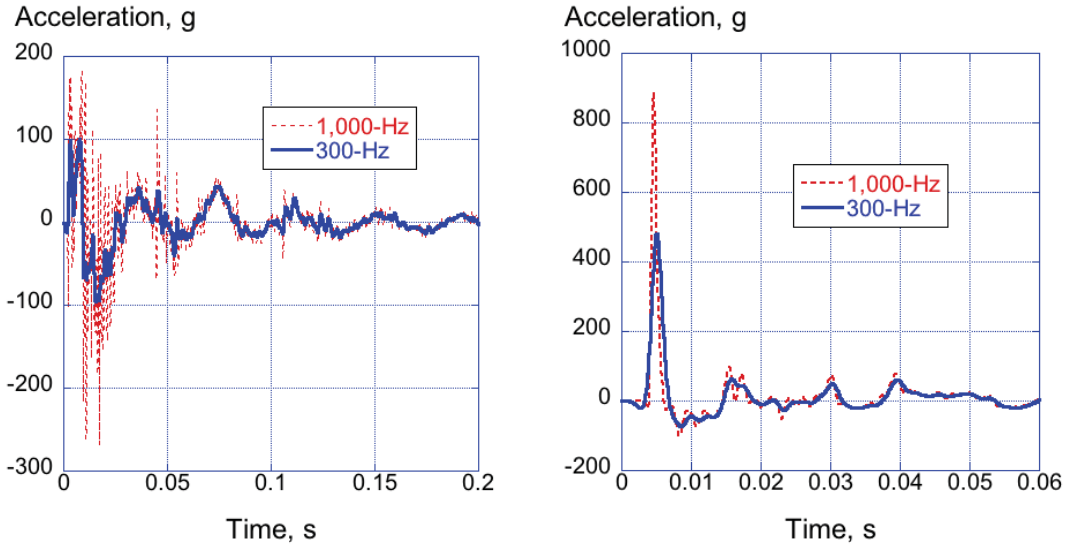

(a) Portal frame acceleration. (b) Floor acceleration.

Figure 67. Portal frame drop mass acceleration and floor acceleration.

The south face photogrammetric data was next examined for the velocity time histories, shown in Figure 68. The differentiated photogrammetric data shows two distinct velocity traces, which are similar to what was seen with the acceleration data. Before impact, the traces overlay, reaching a maximum of 20.75-ft/s. Immediately after impact, the curves diverge. While the first visible evidence of failure at the floor occurred at approximately 5-ms after impact, the curve for the test article floor suggested that the beginning of separation between the floor and the rest of the test article occurred almost immediately after impact. The floor velocity goes positive between 20- and 160-ms, indicating a velocity in the upward direction, which also agreed with the test videos. The test videos showed that the west side of the floor rebounded over 22-in. Meanwhile, the other curve, which represents the response of the portal frame and upper mass, showed a gradual decrease from the impact velocity toward zero. There were still noticeable oscillations in the portal frame and upper test article data after impact. These oscillations were

absent from the floor data because the floor separated from the rest of the test article early in the impact event. However, after 160-ms, the two curves began their convergence toward zero, which was an indication that the impact event had concluded.

Full-field photogrammetric data was captured from the north side of the test article only. The vertical strain on the test article is shown at 5- and 33-ms after impact in Figures 69(a) and (b), respectively. These two particular times were chosen to examine the structural deformation before failure (5-ms) and after failure (33-ms) of the test article. Due to debris interfering with the camera view during the impact, the floor deformation was not tracked.

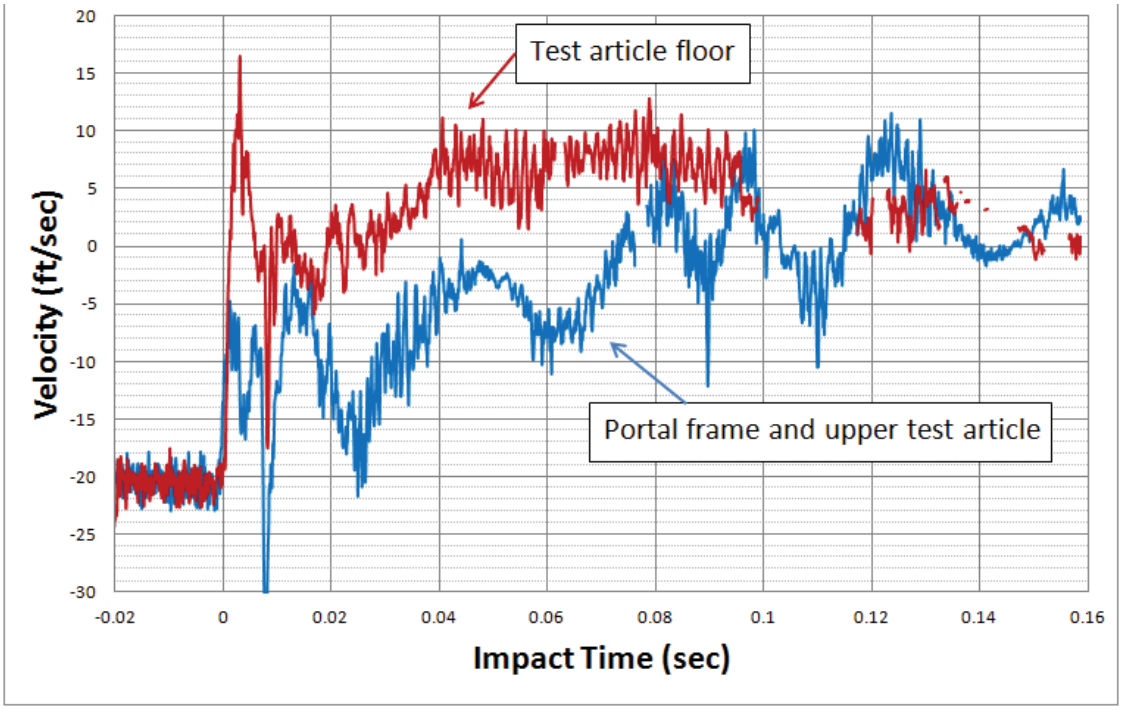

Figure 68. Velocity responses from photogrammetry of the fuselage section floor and portal frame.

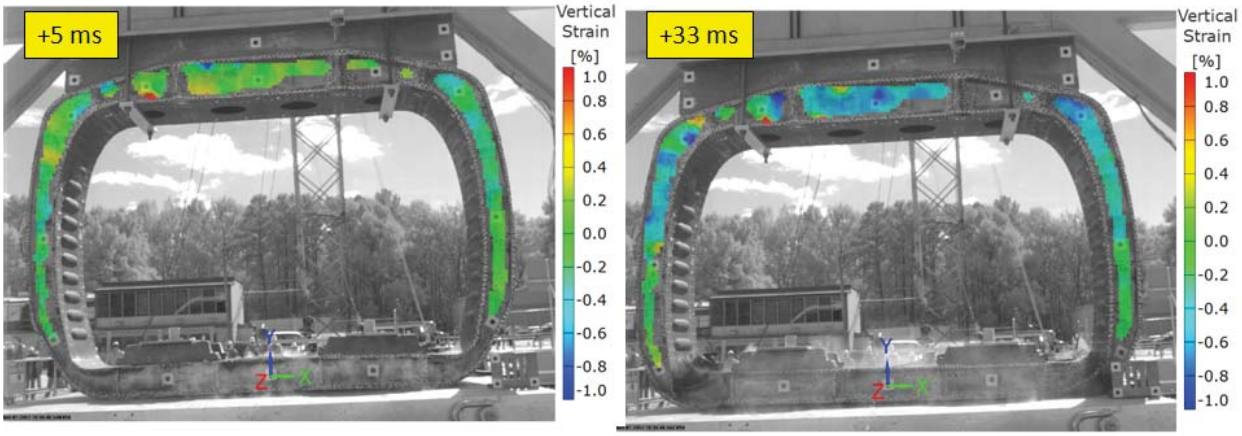

(a) Time = 5-ms. (b) Time = 33-ms.

Figure 69. Vertical strain fringe plots at 5-ms and 33-ms after fuselage section impact.

Care must be taken when interpreting the strain results, as the low resolution in the data allows for potentially invalid and misinterpreted data due to edge effects in the pattern. An example is the area of red (>1% strain) near the upper left corner of the test article. This data is invalid because the software is grouping the deformation data from the flange with the deformation data from the web. The data is physically nonsensical and must be ignored. However, after examining the remainder of the test article, the results show that both tensile and compressive strain were present at 5-ms. The majority of the tracked locations on the top of the test article show a tensile strain, while the sides of the test article show compressive strain in the 0 to -0.2% range. At 33-ms after impact, the results show more compressive strain near the top of the test article than near the bottom, where the failures occurred. The top strains approach -0.4 to -0.6% in compression, while strains near the floor failures hover around 0.0%. This finding indicates that the bottom sides of the test article have become unloaded due to the failure of the floor. However, the data resolution as acquired from photogrammetry is one data point every 5/8-in., and the data sampling rate is 1-kHz, which are both low to capture any highly localized behavior which develops during composite failures, and thus these areas of highly localized strain that develop quickly before failure are not captured. Instead, photogrammetric data represent more of an overall structural deformation, which is intended to acquire and display macro-level results for use with computer modeling correlations.

The framed fuselage section came to rest shortly after impacting the surface. A post-test photograph is shown in Figure 70.

Figure 70. Post-test photograph of the framed fuselage section test article.

After the test, the fuselage section was examined thoroughly for locations of failure. The lower sides were damaged beyond repair due to the large amounts of buckling, folding and

delaminations that occurred near the impact. The floor, despite being heavily damaged near the edges where it detached from the sides, appeared to be undamaged near the middle and under the lower ballast mass. Post-test photographs of the test article are shown in Figures 71-73. The upper portion of the test article was in excellent shape after the test. This undamaged condition was most likely due to the rigidization of this area when attaching the aluminum wedges over the outer I-beam flanges.

Figure 71. Post-test location of the front frame floor (overhead view).

Figure 72. Post-test photographs showing the floor separation locations.

Figure 73. Post-test photograph showing the interior of the floor.

4.0 MODEL DEVELOPMENT AND TEST-ANALYSIS COMPARISONS

A primary objective of this project is to evaluate the capabilities of the commercial nonlinear, explicit transient dynamic code, LS-DYNA [4, 5], for simulating the impact response of composite airframe structures, focusing on the prediction of damage initiation and progression leading to ultimate failure. This section of the report will document the material model development and provide test-analysis comparisons for: laminate characterization tests; dynamic crush tests of I-beam, T-section, and cruciform section components; the longitudinal impact test of the subfloor section; and, the vertical drop test of a two-frame fuselage section.

Finite element models were developed to represent each of the test articles and simulations were conducted using LS-DYNA. Two composite material models were evaluated: MAT_ENHANCED_COMPOSITE_DAMAGE (Mat 54), a progressive failure model that uses the Chang-Chang failure criterion to simulate ply-by-ply failure and property degradation and MAT_LAMINATED_COMPOSITE_FABRIC (Mat 58), a continuum damage mechanics model for representing unidirectional tape and fabric composite materials. Sikorsky provided the material property values for Mat 54, whereas properties for Mat 58 were determined by assessing literature data, by comparing with similar Mat 54 values, and using a trial and error process in which laminated coupons were simulated under both tensile and compressive loading.

The level of agreement between test and analysis was determined through comparisons between experimental and analytical time history responses and comparisons between observed structural deformation, damage initiation, and failure with predicted behavior. Several correlation metrics are available for use in quantifying the level of agreement between two curves as part of the validation process of a numerical model. These include the Roadside Safety Verification and Validation Program (RSVVP) [11, 12] that allows pre-processing of two curves, including filtering, phasing, and timing adjustments, etc. Sixteen different metrics are included that are classified into 3 categories: (1) magnitude-phase-comprehensive (MPC) metrics, (2) single-value metrics, and (3) analysis of variance (ANOVA) metrics. This methodology was applied successfully in Reference 13. An MPC metric was developed by Sprague and Geers [14, 15], which provides a measure of the "goodness of fit" between two curves. Three parameters are calculated over a specified time interval: Sprague and Geers Magnitude (SGM), Sprague and Geers Phase (SGP), and Sprague and Geers Comprehensive (SGC), which is a combination of magnitude and phase. Generally, a value of less than 40 for SGM, SGP, or SGC is considered passing the criteria.

No specific metrics were defined for quantifying test-analysis comparisons, as presented in this report, in part because the impact dynamics community at large has not established acceptable standards. Consequently, the level of test-analysis agreement is determined by visual inspection of the time history responses. However, multi-dimensional model calibration techniques were applied to both the composite subfloor (see Section 4.5.4) and fuselage section (see Section 4.6.6) models to assess deficiencies and uncertainties, to evaluate parameter importance, and to compute required model changes needed to better reconcile test and predictions.

4.1 Material Model Development and Comparison with Laminate Property Data

4.1.1 Description of Mat 54 Material Model

The LS-DYNA material property designated MAT_ENHANCED_COMPOSITE_DAMAGE or (Mat 54) [5], was selected for evaluation in this study. Mat 54 material properties were obtained from existing finite element models, provided by Sikorsky. This material model is used to represent orthotropic materials, such as composite laminates fabricated of unidirectional tape material, and should be limited to thin shell construction. Composite lamination theory is used to determine ply stresses and strains in the laminate. Two different failure criteria can be specified including Chang-Chang [16, 17] or Tsai-Wu [18], by setting the CRIT parameter to 54 for Chang-Chang, or 55 for Tsai-Wu in the Mat 54 card. For all of the Mat 54 simulations presented in this document, CRIT was set to 54. The Chang-Chang failure criterion is a progressive in-plane damage model that accounts for three in-plane failure modes: matrix cracking, fiber-matrix shearing, and fiber breakage. The nonlinear shear stress-strain behavior is based on the theory described in References 19 and 20. For fiber failure and/or fiber-matrix shearing, the level of property degradation within the damaged area depends on the size of damage predicted by the fiber failure criterion [21]. Note that most progressive failure models are strength-based. When the strength of a ply within the laminate is exceeded, the properties are degraded. Progressive failure is achieved through ply-by-ply failure within the laminate. Once all plies in the laminate have failed, the element is deleted. Mat 54 input parameters are defined in Table 4; however, specific input values are not included to protect Sikorsky data rights.

Mat 54 incorporates a set of model-specific parameters that influence material failure behavior, but that cannot be measured in a laboratory. Some of these parameters include TFAIL, SOFT, ALPH, YCFAC, FBRT, BETA, and EFS, as defined in Table 4. If utilized, these parameters must be determined through analytical calibration studies, or by trial and error. Reference 22 provides an excellent description of these parameters, along with the results of parametric studies showing how changes in these parameters can influence model responses.

Several different Mat 54 models were defined and used in finite element models of the SARAP residual hardware. For example, two Mat 54 models were based on autoclave and in situ properties of unidirectional graphite tape materials. However, since the autoclave and in situ properties were so similar, only the autoclave properties were used in simulations of all test articles, with one exception. The fuselage section model introduced three new Mat 54 material models, used to represent both thermoplastic unidirectional graphite tape and thermoset plain weave graphite fabric materials. Note that fabric materials were only used in the fuselage section model. All other models used the autoclave Mat 54 properties. The Mat 54 property values for thermoplastic tape and thermoset fabric composites that were provided by Sikorsky are considered baseline properties and they were not changed for any of the simulations conducted.

4.1.2 Description of Mat 58 Material Model

MAT 58 is a continuum damage mechanics material model based on the Matzenmiller-Lubliner-Taylor theory [23] and is intended for use with shell elements to simulate composite tape laminates and woven fabrics. The model requires input of material properties in tension, compression, and shear to define stress-strain behavior within the lamina or laminate. The user specifies the in-plane elastic modulus and Poisson's ratio in two primary directions, designated A

and B in LS-DYNA. Maximum strength values in tension, compression, and shear are also specified at corresponding strain values. A representation of the stress-strain curve for in-plane tension is illustrated in Figure 74. The tensile response is initially linear elastic with the modulus specified by EA. Stress increases nonlinearly until XT, the maximum strength, is reached. The nonlinear portion of the response is defined internally by LS-DYNA based on a continuum damage mechanics theory [23]. Once XT is reached, the stress is reduced based on the "stress limiting" factor SLIMT1, and is then held constant at the reduced value until elements reach a strain specified by the ERODS parameter in the material model, at which point the elements are deleted and removed from the solution. Through the appropriate selection of the SLIM parameters and ERODS, it is possible to incorporate plastic-like behavior in the model and avoid pre-mature element failure. Similar stress-strain responses are defined for in-plane compression and shear. Reference 24 provides an excellent description of continuum damage mechanics based composite failure models and gives an excellent assessment of Mat 58 for predicting energy absorption of composite materials. Additional information on this material model can also be found in Reference 5.

Table 4. Mat 54 Material Model Parameter Definitions.

Property Description	Symbol
Density	RO
Longitudinal Young's modulus	EA
Transverse Young's modulus	EB
Poisson's ratio, BA	PRBA
Shear modulus, AB	GAB
Shear modulus, BC	GBC
Shear modulus, CA	GCA
Material axes option	AOPT
Max matrix strain, for element deletion	DFAILM
Max shear strain for element deletion	DFAILS
Time step size criteria for element del.	TFAIL
Shear stress parameter for nonlinear term	ALPH
Softening reduction factor for material strength in the crash front	SOFT
Softening for fiber tensile strength	FBRT
Reduction factor for comp fiber strength after matrix comp failure	YCFAC
Max strain for fiber tension	DFAILT
Max strain for fiber comp	DFAILC
Effective failure strain	EFS
Longitudinal comp strength, psi	XC
Longitudinal tensile strength, psi	XT
Transverse comp strength, psi	YC
Transverse tensile strength, psi	YT
Shear strength, psi	SC
Failure criteria (54-Chang)	CRIT
Weighting factor for shear in fiber	BETA

A literature search was conducted and several references [25-27] were found that contained fairly detailed material property data for AS4/PEEK, which is a commonly used thermoplastic

composite material. A listing of material properties based on literature data is provided in Table 5. In the table, tensile properties were found in Reference 25, compression properties were found in Reference 26, and shear properties were found in Reference 27. This data is included for comparative purposes only.

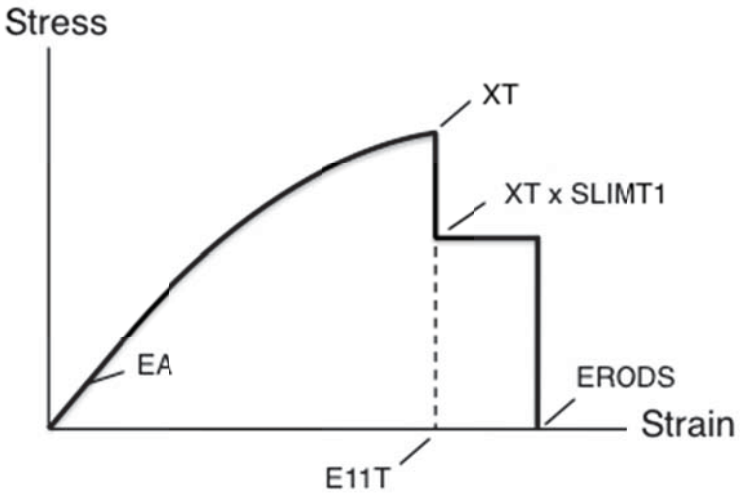

Figure 74. Typical in-plane tension stress-strain curve used for material within Mat 58.

Table 5. AS4/PEEK Material Properties from Literature [20-22].

Symbol, Units	Property Definition	Literature values
E11, psi	Tensile modulus in the fiber direction	20.198E06
E22, psi	Tensile modulus transverse to the fiber direction	1.466E06
PR12	Poisson's Ratio in the 1-2 direction	0.33
G12, psi	Shear modulus in the 1-2 direction	0.84E06
XT, psi	Tensile strength in the fiber direction	326,925
XC, psi	Compressive strength in the fiber direction	179,053
YT, psi	Tensile strength in the transverse direction	13,320
YC, psi	Compressive strength in the transverse direction	25,538
SS, psi	Shear strength	12,000
E11T, %	Tensile failure strain in the fiber direction	1.55
E22T, %	Tensile failure strain in the transverse direction	1.15
E11C, %	Compression failure strain in the fiber direction	0.4
E22C, %	Compression failure strain in the transverse direction	3.75
GMS, %	Shear failure strain	5.0

Mat 58 input values, which are defined in Table 6, were determined based on data from the literature search, from comparison with similar Mat 54 property values, and from test-analysis comparisons of coupon specimens. Simple finite element models were developed to generate analytical predictions for comparison with tension and compression test data. Using this approach, it was possible to calibrate the material properties using reverse engineering based on comparison with laminate test data. However, it should be noted that not all parameters in Mat

58 can be determined through laboratory testing, especially the SLIM parameters and ERODS. These parameters must be based on calibrating the simulation results to best match the test data. Finally, it should be noted that, once the baseline Mat 58 properties were established, they were not changed for any of the simulations conducted. However, separate parameters studies were performed to study the influence of variations in ERODS, the parameter that controls element deletion; and in strength values XT, XC, and E11T. As with Mat 54, actual property values for Mat 58 are not included in Table 6 to protect Sikorsky data rights.

Table 6. Mat 58 Material Model Property Definitions.

Material Property Description, units	**Symbol**
Density, lb-s^2/in^4	RO
Young's modulus longitudinal direction, psi	EA
Young's modulus transverse direction, psi	EB
Poisson's ratio in the BA direction	PRBA
Stress limit of nonlinear portion of shear curve, psi	TAU1
Strain limit of nonlinear portion of shear curve, in/in	GAMMA1
Shear modulus in the AB direction, psi	GAB
Shear modulus in the BC direction, psi	GBC
Shear modulus in the CA direction, psi	GCA
Min stress factor for limit after max stress (fiber tension)	SLIMT1
Min stress factor for limit after max stress (fiber compression)	SLIMC1
Min stress facto for limit after max stress (matrix tension)	SLIMT2
Min stress factor for limit after max stress (matrix compression)	SLIMC2
Min stress factor for limit after max stress (shear)	SLIMS
Material axes option (=0.0 locally orthotropic)	AOPT
Time step for automatic element deletion	TSIZE
Maximum effective strain for element layer failure	ERODS
Softening reduction factor for strength in the crash front	SOFT
Failure surface type	FS
Strain at longitudinal compressive strength, in/in	E11C
Strain at longitudinal tensile strength, in/in	E11T
Strain at transverse compressive strength, in/in	E22C
Strain at transverse tensile strength, in/in	E22T
Strain at shear strength, in/in	GMS
Longitudinal compressive strength, psi	XC
Longitudinal tensile strength, psi	XT
Transverse compressive strength, psi	YC
Transverse tensile strength, psi	YT
Shear strength in the A-B plane, psi	SC

4.1.3 Comparison of Tensile Laminate Response with Simulation (Unidirectional Tape)

The in-plane tension model is shown in Figure 75. The 1-in. x 1-in. tension model contains approximately 300 quadrilateral shell elements. Single Point Constraints (SPCs) were applied to fully constrain the left edge nodes, i.e. translations and rotations about the x-, y-, and z-axes were fixed. In addition, an SPC was defined to fix translations and rotations for the right edge nodes,

except that translation in the x-direction was allowed. The right edge nodes were assigned a BOUNDARY_PRESCRIBED_MOTION_SET specifying that at the termination time (0.3 seconds) the maximum x-displacement is 0.03-inches, which corresponds to a maximum strain in the x-direction of 3%. The fairly long termination time of 0.3 seconds ensured that quasi-static loading was applied and that the kinetic energy of the simulation was minimal.

A unidirectional graphite tape laminate was simulated using the tension model shown in Figure 75. A local material direction was specified for this laminate such that 0°-layers were oriented in the x-direction. The ply orientations were input using the PART_COMPOSITE card in LS-DYNA with a total laminate thickness of 0.096-inches. The baseline Mat 54 and Mat 58 unidirectional tape material models were assigned. The tensile model was executed using the default Belytschko-Tsay shell element formulation (ELFORM=Type 2). Output from the model included SPC forces in the x-direction for the left edge nodes, which were summed and then divided by the cross-sectional area to obtain an average stress. Strain was obtained by scaling the time response. Models were executed using LS-DYNA Symmetric Multi Processing (SMP) Version 971 R6.0.0 with double precision and required up to 78 minutes of Central Processing Unit (CPU) on a single processor for an end time of 0.3 seconds.

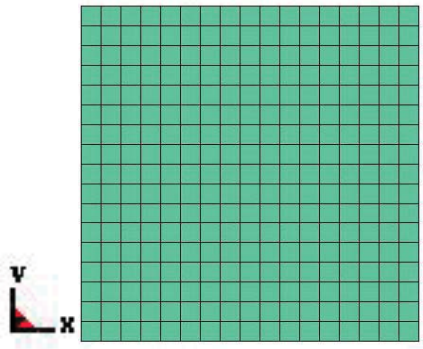

Figure 75. Finite element model used for simulating in-plane tensile loading.

Comparisons of experimental and analytical stress versus strain responses are shown in Figures 76(a) and (b) for Mat 54 and Mat 58 material models, respectively. For Mat 54, the predicted response is slightly stiffer than the test and both curves are essentially linear elastic to failure. However, the Mat 54 analytical response under predicts the experimental tensile strength and the strain-to-failure. For example, the test coupon fails at a tensile strain of 0.0107-in/in and at a tensile strength of 73,400-psi, whereas the model fails at a lower strain of 0.007-in/in and at a lower stress of 53,056-psi. Following failure, the laminate no longer has load-bearing capability. One explanation for the premature failure in the Mat 54 model is that DFAILM is set at a very low value. As indicated in Reference 22, DFAILM, which is the maximum strain in the matrix, must be greater than or equal to the maximum value of YT/EB or YC/EB. In this case, the minimum value was selected to provide a conservative response.

For Mat 58, the model matches the stiffness of the test response well; however, the strength of the laminate is over predicted. The Mat 58 model obtains maximum strength at a strain of 0.016-in/in and a stress of 93,600-psi. Based on the fact that SLIMT1 is set at a high value (close to 1.0), the value of stress at failure is maintained in the elements until the strain corresponding to the value of ERODS is achieved. Note that since element deletion produces holes in the model

resulting in stress concentrations, it is prudent to keep ERODS as high as possible to prevent numerical problems and subsequent pre-mature failure of the model.

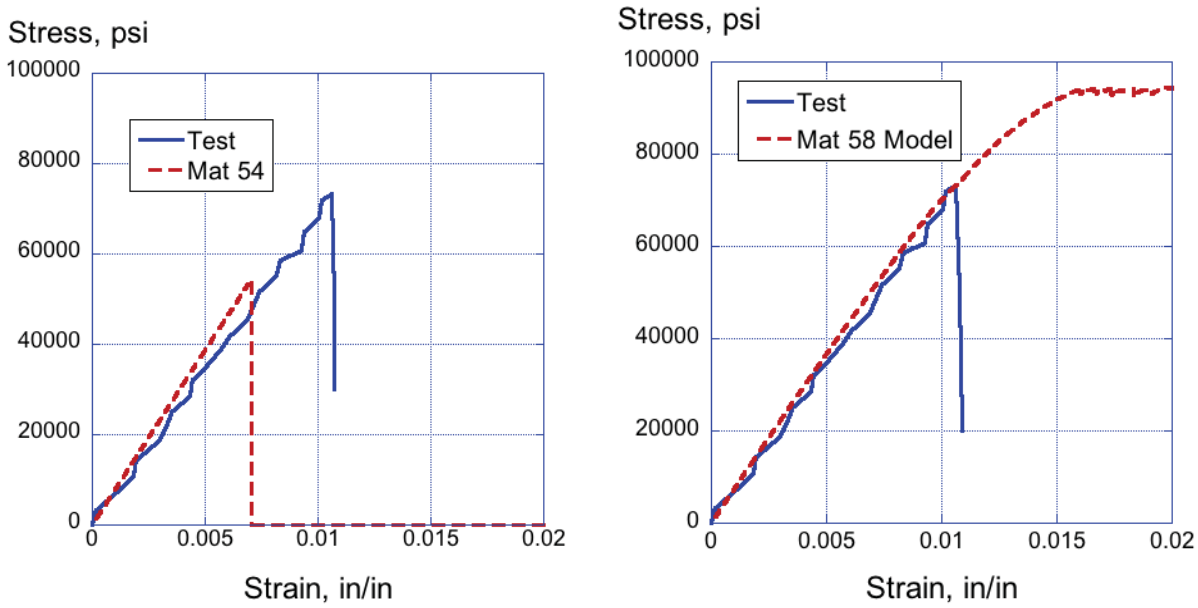

(a) Mat 54 autoclave properties. (b) Mat 58 properties.

Figure 76. Comparison of Mat 54 and Mat 58 tensile stress-strain responses with test data.

To improve the Mat 58 comparisons with the tensile test results, two parametric studies were conducted. In the first, the values of XC, XT, and E11T were reduced. XC was reduced by 25%; XT was reduced by 25%; and, E11T was reduced by 35%. This Mat 58 model is designated the reduced strength model. Predictions from this model are plotted in Figure 77(a) with the tensile test data, as well as the predicted response from the baseline Mat 58 model. The reduced strength model accurately predicts the value of tensile strength; however, due to the large value of ERODS, the stress level is maintained. A second study was conducted to determine the influence of changes to the ERODS parameter. Simulations were conducted using the baseline Mat 58 material model for unidirectional tape material; however, ERODS was varied between 0.01 and 0.05 in increments of 0.01. In the baseline Mat 58 material model, a high value of ERODS was specified. The results of the ERODS parameter study, shown in Figure 77(b), indicate that best agreement with test data is for an ERODS value between 0.02 and 0.03.

4.1.4 Comparison of Compressive Laminate Response with Simulation (Unidirectional Tape)

The in-plane compression model is shown in Figure 78. This model has a height of 1-in. and a width of 0.5-in. The reduced width, as compared with the tension model, was needed to minimize the tendency of the model to buckle out-of-plane during the simulations. The compression model contains 50 quadrilateral shell elements. The compression models were executed using the default Belytschko-Tsay shell element formulation (ELFORM= Type 2). SPCs were applied to fix the left edge nodes. In addition, SPCs were used to fix translations and rotations for the right edge nodes, except that translation in the x-direction was allowed. The BOUNDARY_PRESCRIBED_MOTION_SET card was defined for the right edge nodes

specifying that at the termination time (0.3 seconds) the maximum x-displacement is -0.015-inches, which corresponds to a maximum x-direction strain of -3%. As before, the fairly long termination time of 0.3 seconds ensured that quasi-static loading was applied and that the kinetic energy of the simulation was minimal.

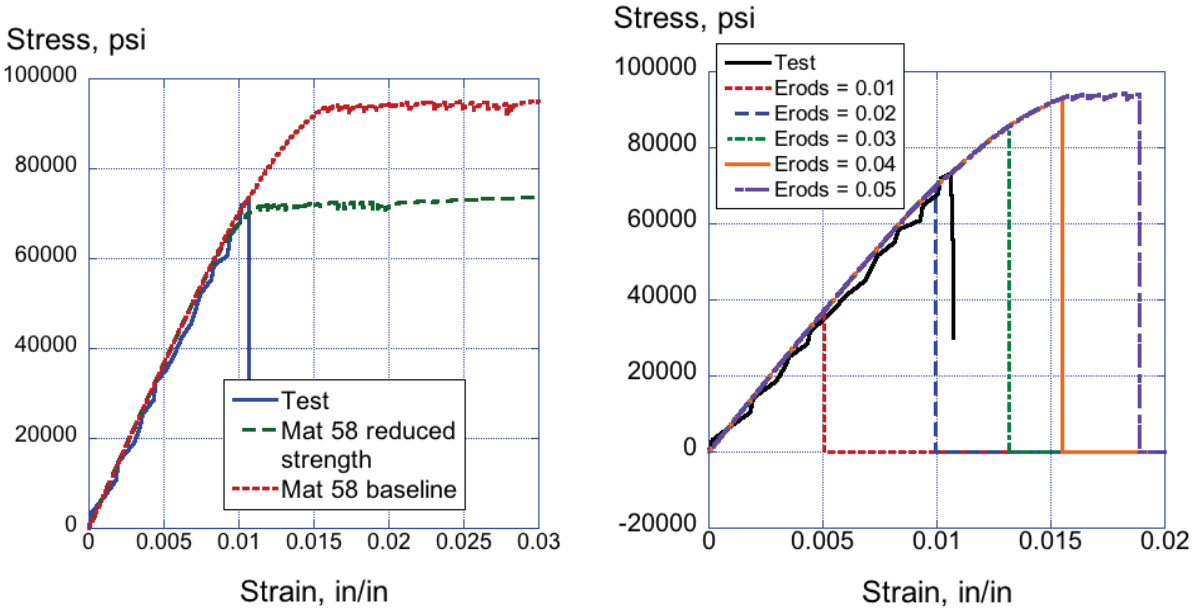

(a) Reduced strength model. (b) ERODS study results.

Figure 77. Results of two Mat 58 parameter studies on the tensile laminate response.

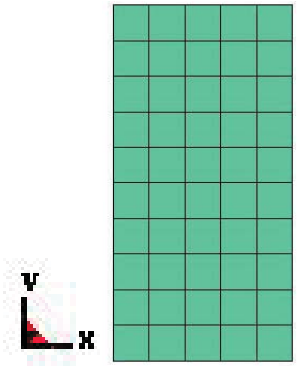

Figure 78. Finite element model used for simulating in-plane compressive loading.

As with the tensile loading case, a unidirectional graphite tape laminate was simulated. A local material direction was specified for this laminate such that 0°-layers were oriented parallel to the x-axis. The ply orientations were input using the PART_COMPOSITE card with a total laminate thickness of 0.096-inches. In the first simulation, the Mat 54 unidirectional tape material model representing the autoclave fabrication technique was assigned. In the second, Mat 58 properties for unidirectional graphite tape material were assigned. Output from the compression model included SPC forces in the x-direction for the left edge nodes, which were summed and then divided by the cross-sectional area to obtain an average stress. Strain was obtained by scaling the time response. The model was executed using LS-DYNA SMP Version

971 R6.0.0 with double precision and required 13 minutes of CPU on a single processor for an end time of 0.3-s.

Comparisons of experimental and analytical stress versus strain responses are shown in Figures 79(a) and (b) for Mat 54 and Mat 58 material models, respectively. For the Mat 54 simulation, the predicted response exhibits a linear elastic response to failure. Note that the compression data deviates from linearity at a low value of strain. However, the analytical curve over predicts both the failure stress and strain-to-failure of the test coupon. As with the tension model, when failure occurs in compression, the laminate loses the capability to carry load.

As shown in Figure 79(b), the Mat 58 model matches the initial stiffness of the test response well. However, the test response deviates from linearity very early and fails at a strain of 0.0055-in/in and at a stress of 33,900-psi. The model exhibits a linear elastic response and reaches maximum strength at a strain of 0.0066-in/in and a stress of 48,500-psi. At that point, the stress at "failure" is reduced by the SLIMC1 factor, which leads to the observed stair step response. Elements are removed from the model once a strain corresponding to the value of ERODS is achieved.

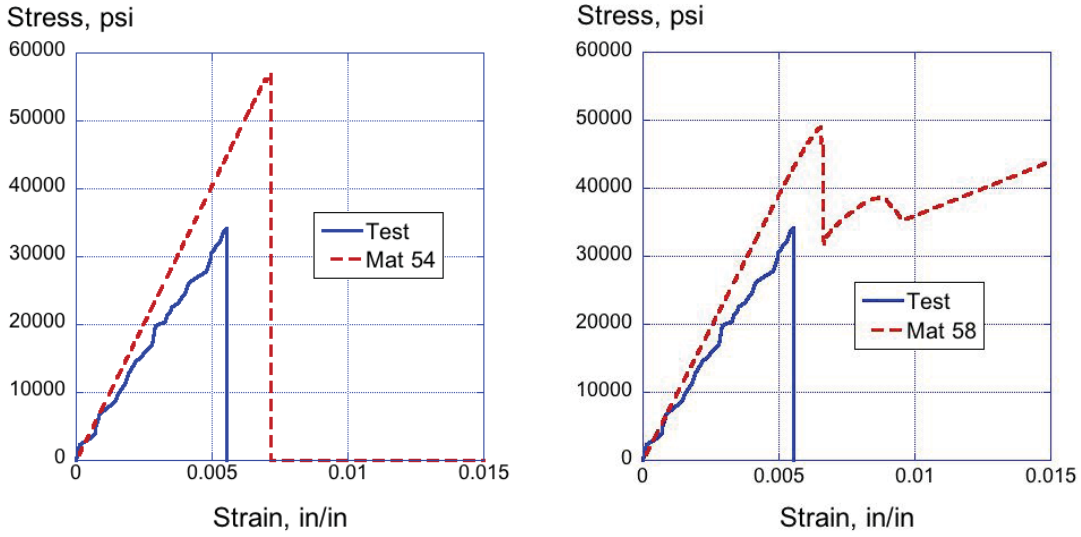

(a) Mat 54 properties. (b) Mat 58 properties.

Figure 79. Comparison of compression stress-strain responses.

As with the tensile loading case, two separate parametric studies were performed including the Mat 58 reduced strength model, in which XC, XT, and E11T were lowered; and the ERODS variation study. Results are shown in Figures 80(a) and (b), respectively. The reduced strength model matched the stiffness of the current Mat 58 material model; however, both models were stiffer than the test, which deviated from linearity at low strain values. However, the reduced strength model achieves maximum strength at a significantly lower stress (36,667-psi) and lower strain (0.005-in/in) than the baseline Mat 58 model, which initially fails at a stress of 48,750-psi and a strain of 0.0066-in/in. This change is attributed to the 25% reduction in XC, the longitudinal compressive strength in Mat 58. The ERODS parameter variation shows that best agreement with test is obtained using a low value of ERODS of 0.01.

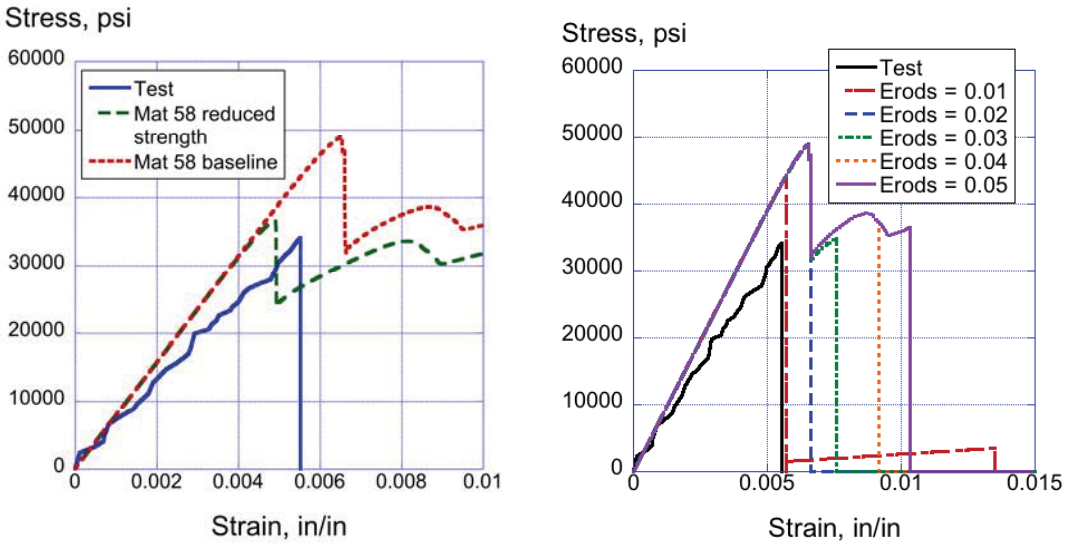

(a) Reduced strength model. (b) ERODS variation study results.

Figure 80. Results of two Mat 58 parameter studies on the compressive laminate response.

4.1.5 Comparison of Tensile Laminate Response with Simulation (Fabric)

The finite element model, shown in Figure 75, was modified to represent fabric material. The modifications included changing the total laminate thickness to 0.12-in., and changing the laminate stacking sequence to match the test specimen. In addition, the material models for Mat 54 and Mat 58 were updated to reflect the fabric construction. All other model details remained the same, as described in Section 4.1.3.

Predicted stress-strain results are shown in Figures 81(a) and (b) for Mat 54 and Mat 58, respectively, compared with the average tensile response of the fabric coupons. The Mat 54 response exhibits excellent agreement with the stiffness of the tensile data; however, the strength is under predicted. The model fails at approximately 75,000-psi and 0.0085-in/in strain, compared with the average test coupons that failed at 100,000-psi and 0.012-in/in strain. For Mat 58, the model also predicted the initial stiffness of the test response well. Whereas the test response is linear elastic to failure, the Mat 58 predicted response deviates from linearity at approximately 60,000-psi, and eventually fails at a stress of 92,500-psi and a strain of 0.015-in/in. Note that the Mat 58 fabric model incorporates a much lower value of ERODS indicating that element deletion will occur at a lower value of strain.

4.1.6 Comparison of Compression Laminate Response with Simulation (Fabric)

The finite element model, shown in Figure 78, was modified to represent compressive loading of fabric coupons. The modifications included changing the total laminate thickness to 0.12-in., and changing the laminate stacking sequence to match the test specimen. Mat 54 and Mat 58 fabric material properties were used in the model. All other model details remained the same, as described in Section 4.1.4.

Predicted stress-strain results are shown in Figures 82(a) and (b) for Mat 54 and Mat 58, respectively, compared with the average compressive response of the fabric coupons. Both models exhibit a stiffer response than the test, which is linear elastic to failure. For the test

coupons, failure occurs at a stress of approximately 46,700-psi and a strain of 0.0064-in/in. The Mat 54 predicted curve fails at a stress of 91,000-psi and a strain of 0.01-in/in. Following failure, the laminate loses load-bearing capability. Conversely, the Mat 58 predicted curve reaches maximum strength at a stress of 57,000-psi and a strain of 0.0072-in/in. However, due to the SLIMC1 parameter, the compressive stress is reduced to 30,000-psi and elements continue to carry that load until the strain defined by ERODS is reached.

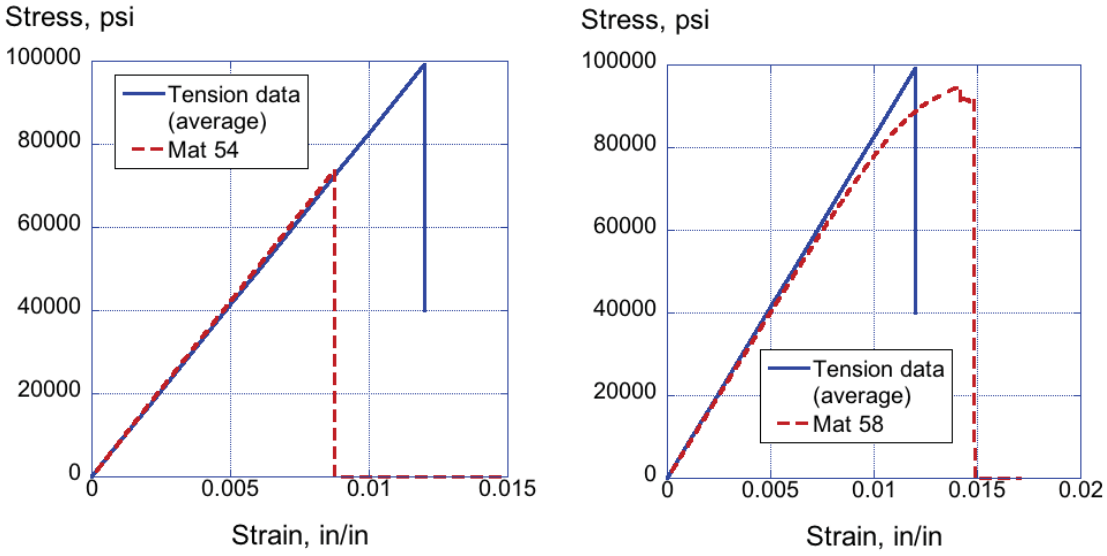

(a) Mat 54. (b) Mat 58.

Figure 81. Comparison of Mat 54 and Mat 58 predicted responses with average tensile response of fabric laminates.

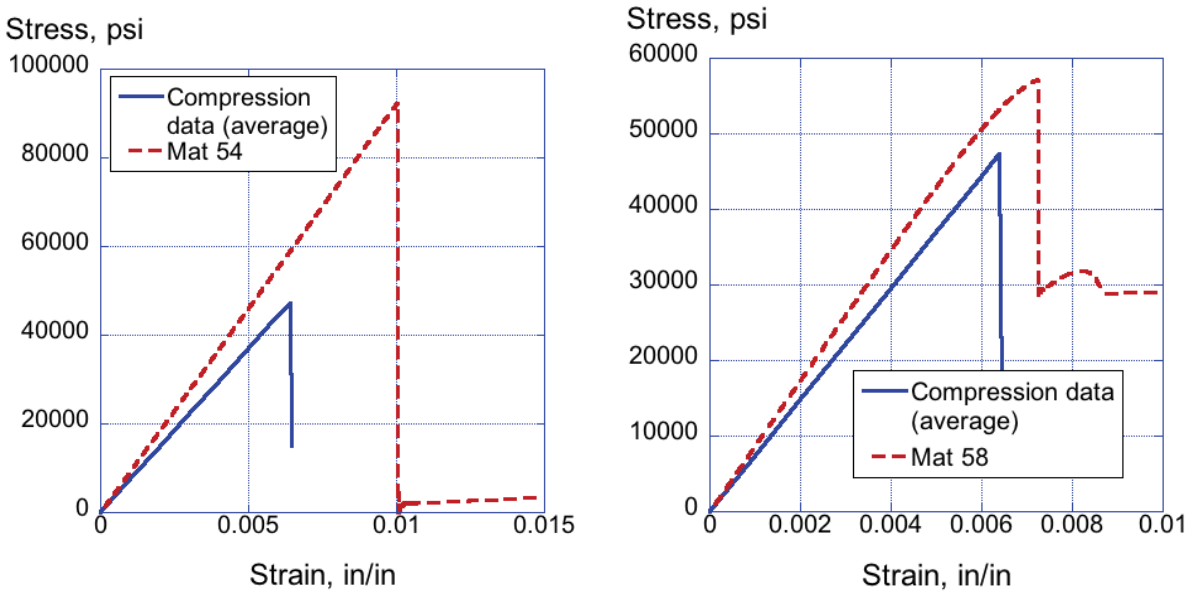

(a) Mat 54. (b) Mat 58.

Figure 82. Comparison of Mat 54 and Mat 58 predicted responses with average compression response of fabric laminates.

4.2 Simulation of Dynamic Crush Tests of Two I-Beam Specimens

4.2.1 Description of the Finite Element Model

A finite element model, depicted in Figure 83, was developed to simulate two dynamic crush tests of I-beam specimens. The model consisted of 24,300 nodes; 3,050 Belytschko-Tsay (ELFORM=Type 2) quadrilateral shell elements representing the I-beam with a nominal element edge length of 0.125-in.; and 16,400 solid elements representing the drop mass. Mat 54 or Mat 58 were assigned to the shell elements representing the I-beam, whereas Mat 20 (*MAT_RIGID) was assigned to the drop mass. The density of the rigid material was adjusted to ensure that the weight of the drop mass matched that of the test (204.8-lb). Seven different parts were used including one part for the drop mass, and six parts representing different regions of the I-beam. Several different PART_COMPOSITE cards were created to represent the upper edges of the I-beam flanges that incorporated ply drop-offs to mimic the reduced thicknesses produced by chamfering. I-beam models were executed using LS-DYNA SMP Version 971 R6.0.0 with double precision and required 5 hours and 51 minutes of CPU on four Linux-based processors for an end time of 0.02-s.

Two SPC definitions were used, one to fix the bottom nodes of the I-beam, and the second to ensure that the drop mass could move only in the vertical direction. Finally, the nodes forming the drop mass were assigned an initial velocity to match the two test conditions, 189.6- and 265.2-in/s. These two impact velocities correspond to the 4- and 8-ft drop heights used during the tests. As mentioned previously, both Mat 54 and Mat 58 material models were evaluated and input properties were based on unidirectional graphite tape composite material.

Output from the model included acceleration-, velocity-, and displacement-time histories of a central node on the drop mass, as well as pictures of model deformation. For the I-beam, T-section, and cruciform section component tests, acceleration data from the accelerometer(s) attached to the drop mass are compared with analytical predictions. Predicted velocity and displacement responses are also compared with experimental velocity and displacement data obtained from single- and double-integration of the acceleration data, respectively. In addition, displacement data obtained from photogrammetry were included for comparison.

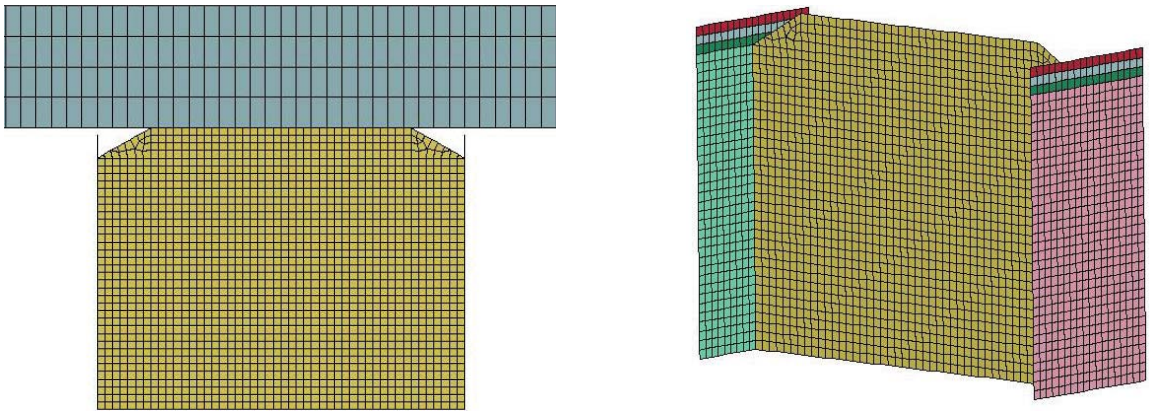

(a) Front view with drop mass. (b) Three-quarter view without drop mass.

Figure 83. LS-DYNA model of the I-beam component.

4.2.2 Mat 54 Predicted Responses Compared with 4-ft Test Data

Poor results were obtained using the Mat 54 material model. Essentially, the model failed in a brittle fashion, exhibiting very little energy absorption. Numerous parameter studies were conducted in an attempt to obtain stable crushing of the model. However, all models provided similar results to those shown in Figure 84. Predicted acceleration responses, shown in Figure 84(a), consisted of a series of spikes representing repeated contact and release of the drop mass onto the I-beam. These short-duration spikes occur early in the pulse. Only 50-in/s of velocity is removed during the simulation through failure of the I-beam, as shown in Figure 84(b). As indicated in Figure 84(c), the vertical displacement of the drop mass is not alleviated and it continues to displace linearly without abatement. The model fails catastrophically with no sign of stable crushing, as shown in Figure 85. The model loses the bottom nodal constraints, as elements are failed and removed.

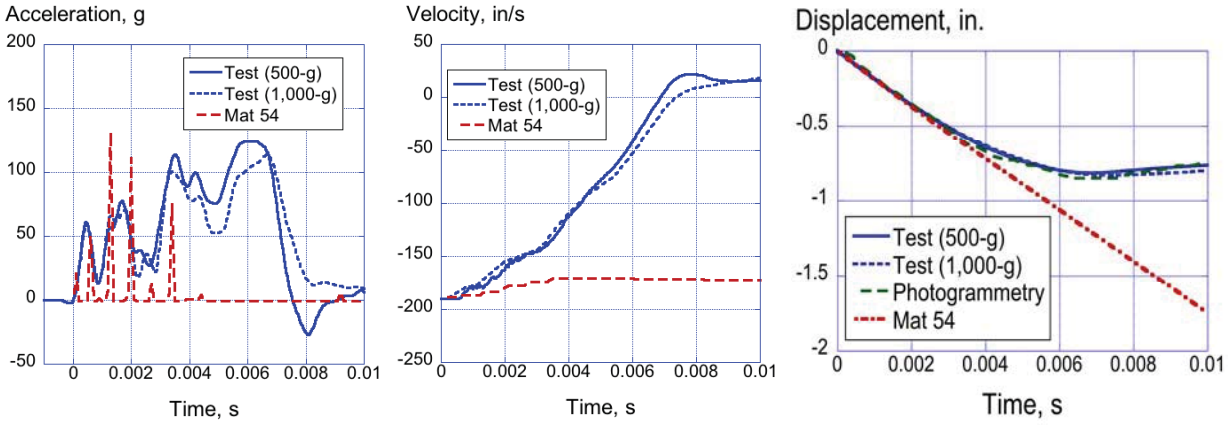

(a) Acceleration. (b) Velocity. (c) Displacement.

Figure 84. Experimental and Mat 54 analytical results for the I-beam crush test at 189.6-in/s.

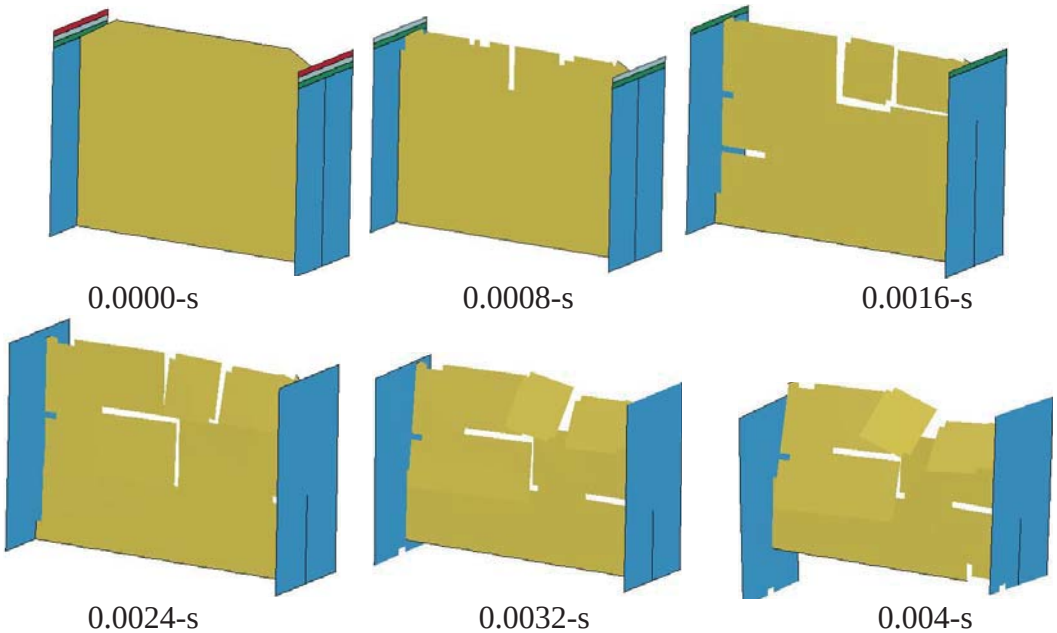

Figure 85. Mat 54 model predicted deformation pattern indicating complete specimen collapse.

4.2.3 Mat 58 Predicted Responses Compared with 4-ft Test Data

The baseline Mat 58 material model for unidirectional tape was used to represent the I-beam. The predicted responses show good agreement with the overall shapes, magnitudes, and pulse durations of the experimental curves, as shown in Figure 86. The experimental and predicted acceleration responses, shown in Figure 86(a), were filtered using a 1000-Hz Butterworth low-pass filter. The displacement results, shown in Figure 86(c), include the Mat 58 predicted response, the responses based on double integration of the acceleration data, and photogrammetry. The maximum crush displacement predicted by the model (0.85-in.) falls between the experimental results (0.82- to 0.86-in.). A sequence of model deformation is shown in Figure 87 for four time steps. These depictions show that the I-beam model exhibits stable crushing from the top edge, matching the deformation patterns of the test article, depicted in Figures 9 and 13. No global buckling is evident, though some folding of the webs is observed.

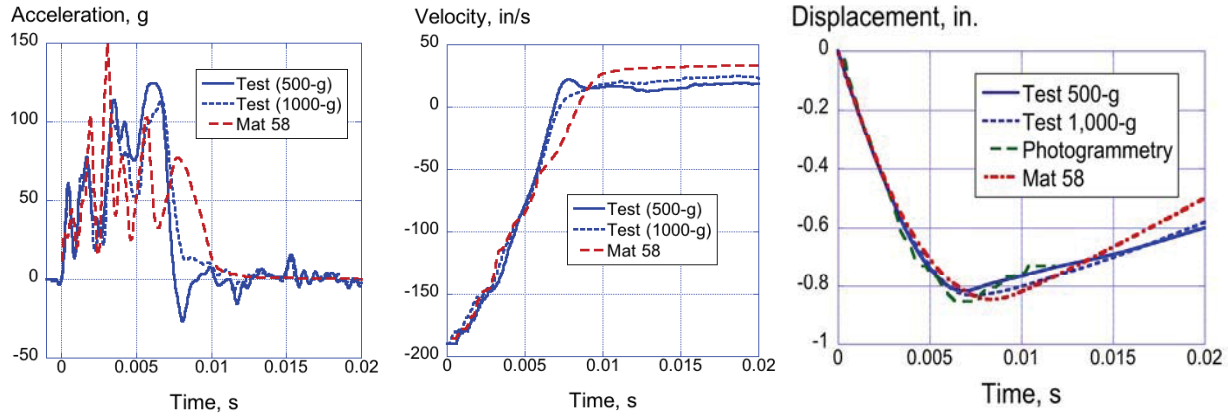

(a) Acceleration. (b) Velocity. (c) Displacement.

Figure 86. Experimental and Mat 58 analytical results for the I-beam 4-ft. drop test.

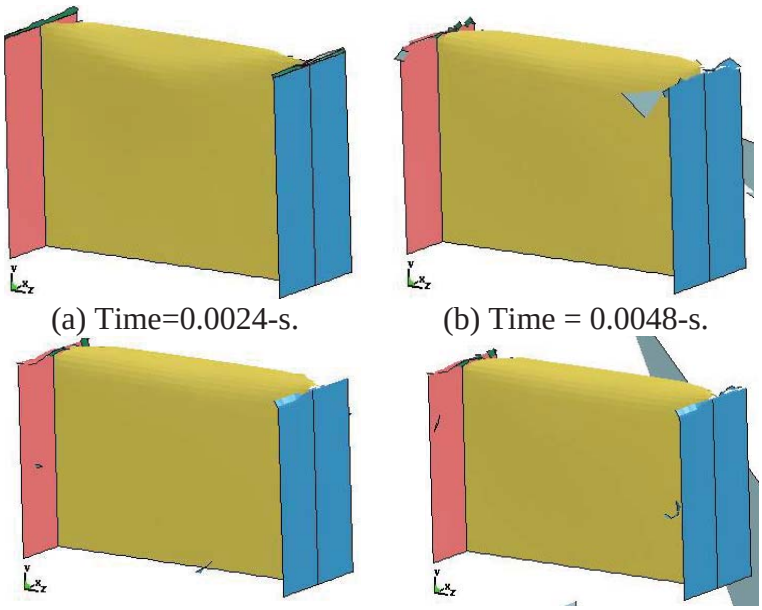

(a) Time=0.0024-s. (b) Time = 0.0048-s.

(c) Time=0.0072-s. (d) Time = 0.01-s.

Figure 87. Time sequence of I-beam model deformation for Mat 58.

As with the laminate characterization simulations, the I-beam model was executed using the reduced strength Mat 58 material model. In addition, a parameter study to evaluate the influence of ERODS was conducted. For this evaluation, ERODS was varied from 0.1 to 0.5 in increments of 0.1. Displacement-time history results for these two studies are shown in Figures 88(a) and (b), respectively. The reduced strength model resulted in over prediction of the maximum crush displacement by approximately 0.18-in., or 22.5%. The ERODS study indicates that a value of 0.5 provides best agreement with test data.

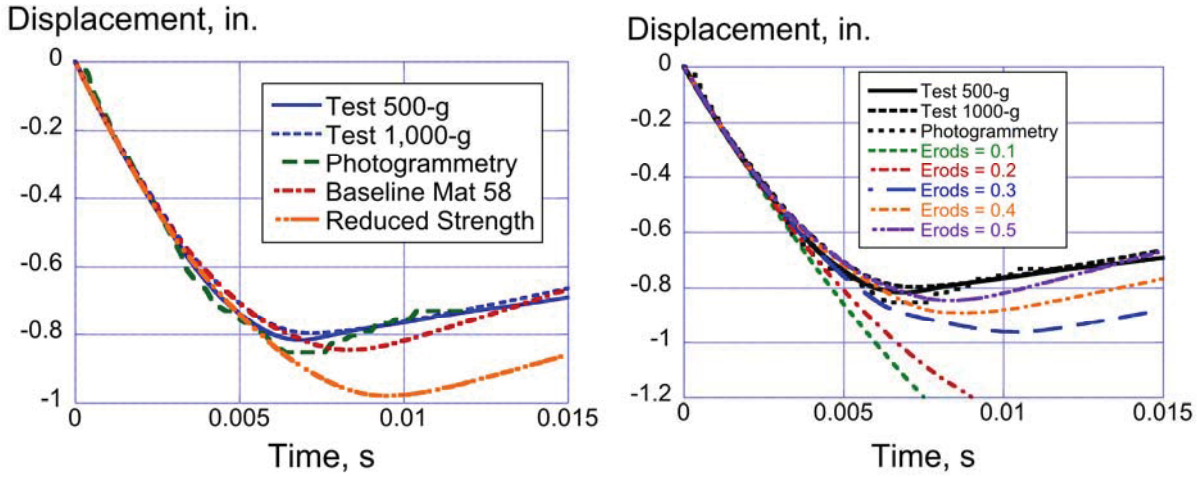

(a) Reduced strength model. (b) ERODS study.

Figure 88. Mat 58 parameter study results for the I-beam (189.6-in/s velocity).

4.2.4 Mat 54 Predicted Responses Compared with 8-ft Test Data

The finite element model of the I-beam, shown in Figure 83, was re-executed with a higher impact velocity of 265.2-in/s corresponding to the 8-ft drop test condition. All other model details were kept the same as for the lower velocity impact, including the Mat 54 autoclave material properties. Similar difficulties were found with the Mat 54 simulation at the higher impact velocity. The predicted acceleration responses consisted of a series of spikes representing repeated contact and release of the drop mass onto the I-beam as elements are deleted, until ultimate model collapse. Very little velocity is removed and the vertical displacement of the drop mass continues to increase linearly without abatement. As with the lower velocity case, many parametric simulations were executed in an unsuccessful attempt to generate a model that would predict stable crushing, rather than collapse. Consequently, no results are shown for the Mat 54 model.

4.2.5 Mat 58 Predicted Responses Compared with 8-ft Test Data

The I-beam model was executed with Mat 58 unidirectional tape properties for the higher velocity condition. Comparisons of predicted and experimental acceleration-, velocity- and displacement-time histories are shown in Figure 89. As before, the acceleration responses shown in Figure 89(a) were filtered using a 1000-Hz Butterworth low-pass filter. In addition, displacement data are shown based on double integration of the acceleration data and photogrammetry. The model generally exhibits a stiffer response than the experiment. For example, analytical acceleration peaks are higher than the experimental peaks, the predicted velocity curve is steeper than the test curve and crosses zero velocity earlier than the test, and the

model under predicts the maximum crush displacement (1.4-in. versus 1.78-in. for the test).

A sequence of model deformation is shown in Figure 90 for four time steps. These depictions show that the model I-beam web exhibits stable crushing from the top edge, thus mimicking the deformation behavior of the test article. No global buckling is evident, though some folding of the web section is observed. The predicted deformation simulates the observed test response, as shown in Figure 18.

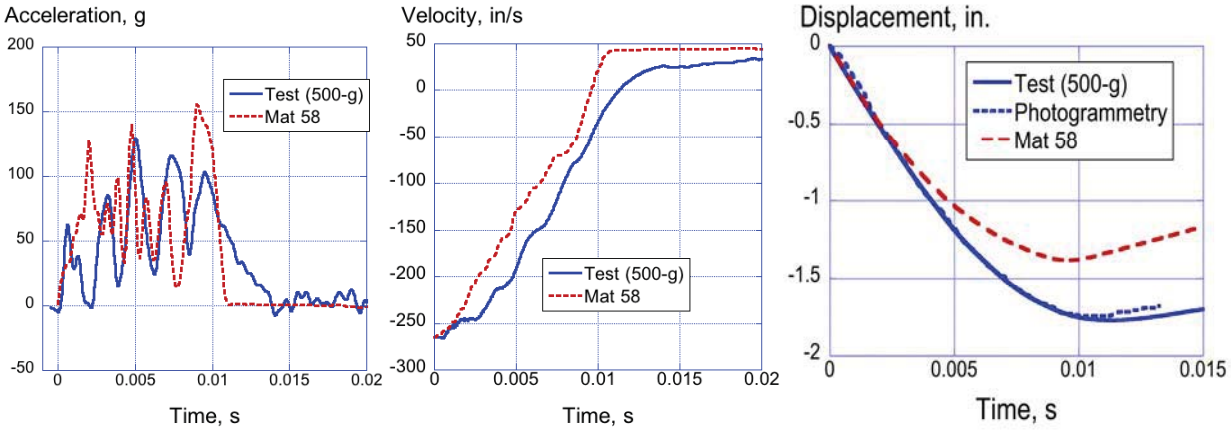

(a) Acceleration responses. (b) Velocity responses. (c) Displacement responses.

Figure 89. Experimental and Mat 58 analytical results for the I-beam 8-ft. drop test.

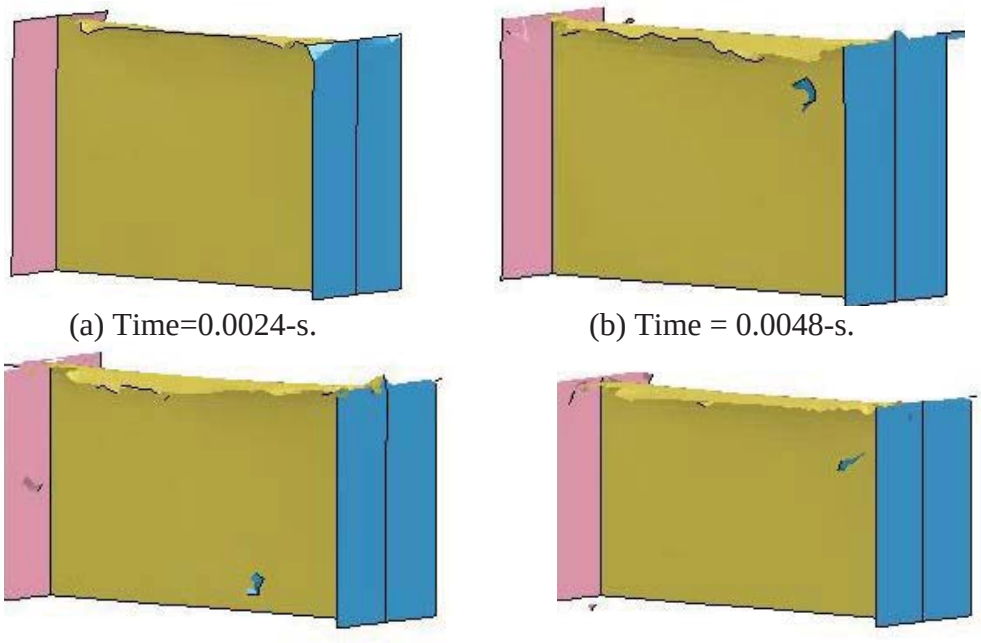

(a) Time=0.0024-s. (b) Time = 0.0048-s.

(c) Time=0.0072-s. (d) Time = 0.0096-s.

Figure 90. Time sequence of I-beam model deformation for Mat 58 simulation.

The I-beam model (velocity=265.2-in/s) was re-executed using the reduced strength Mat 58 material model. In addition, a parameter study to evaluate the influence of ERODS was

conducted. For this evaluation, ERODS was varied from 0.1 to 0.5 in increments of 0.1. Note that for the ERODS study, the baseline Mat 58 material properties were used. Displacement-time history results for these two studies are shown in Figures 91(a) and (b), respectively. The reduced strength model provided much better agreement with the experimental maximum crush displacement as compared with the original Mat 58 model. The reduced strength model predicted a crush displacement of 1.73-in. compared with 1.78-in. for the test. The ERODS study shows that a value of 0.3 provides best agreement with test data.

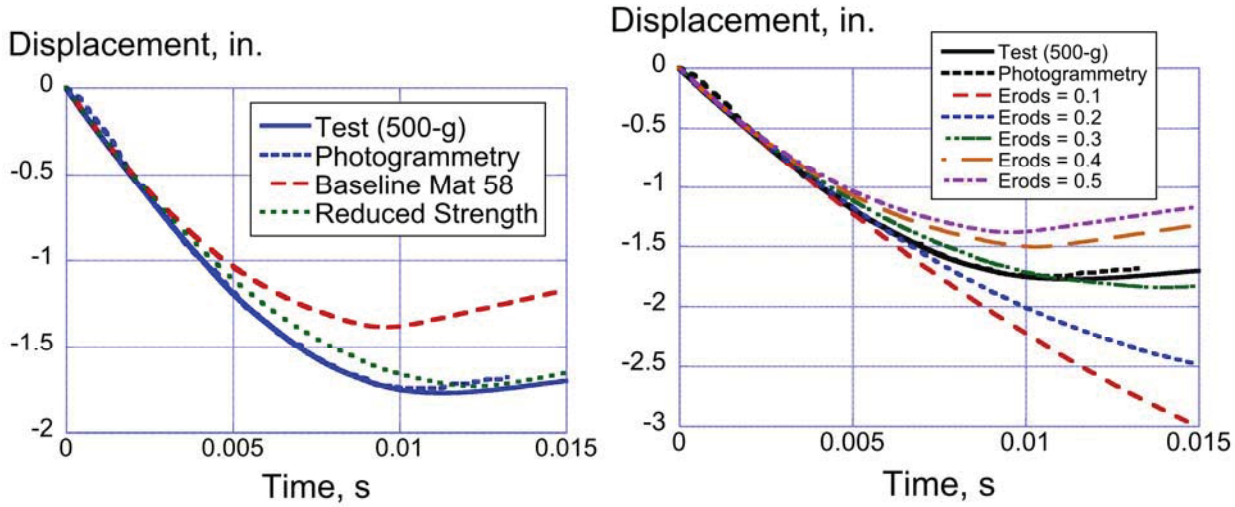

(a) Reduced strength model. (b) ERODS study

Figure 91. Mat 58 parameter study results for the I-beam (265.2-in/s velocity).

4.3 Simulation of Dynamic Crush Tests of Two T-Section Specimens

4.3.1 Description of the Finite Element Model

Finite element models, shown in Figure 92, were developed to represent the two dynamic impact tests of T-section components. Models were developed to represent two different configurations of the T-sections. For example, the 2-ft drop test was conducted on a T-section with two fillets only, whereas the higher velocity test (4-ft drop) was performed on a T-section with four fillets. The fillets are located at the intersection of the vertical and horizontal flanges. The 4-fillet model consists of: 15,367 nodes; 13,746 quadrilateral shell elements; 512 solid elements to represent the drop mass; 9 parts; 3 material models; 2 constraint definitions; and, one contact definition. Models were executed using both Mat 54 and Mat 58, in which material properties for unidirectional graphite tape were input. For all simulations, Belytscko-Tsay shell elements were used (ELFORM=Type 2). Mat 54 and Mat 58 were assigned to the shell elements representing the T-section, whereas Mat 20 (*MAT_RIGID) was assigned to the drop mass. The density of the rigid material was adjusted to ensure that the weight of the drop mass matched that of the test (204.8-lb).

Two SPC definitions were used, one to fix the bottom nodes of the horizontal I-beam flanges, and the second to ensure that the drop mass could move only in the vertical direction. Finally, the nodes forming the drop mass were assigned an initial velocity to match the two test conditions, 134.9- and 192-in/s. These two impact velocities correspond to the 2- and 4-ft drop

heights used during the tests. Output from the model included acceleration-, velocity-, and displacement-time histories of a central node on the drop mass, as well as pictures of model deformation. The nominal element edge length was 0.125-in. Simulations were executed for 0.04-s, which required 8 hours of CPU on four Linux-based processors.

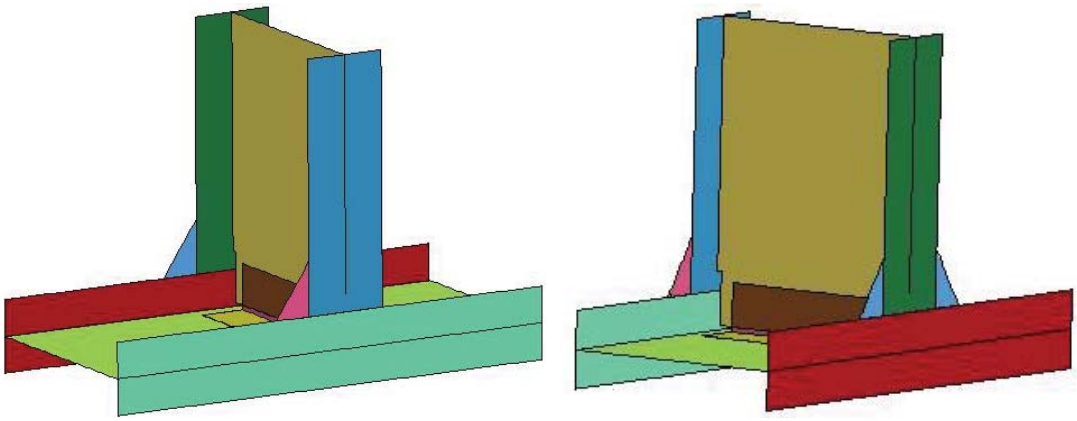

(a) 2-ft drop model (two fillets). (b) 4-ft drop model (four fillets).

Figure 92. T-section finite element models (drop mass not shown).

4.3.2 Mat 54 Predicted Responses Compared with 2-ft Drop Test Data

The model for the 2-ft drop test is shown in Figure 92(a). As observed in the test article, the fillets on the right side of the vertical flange have been cut off, leaving only the two fillets on the left side. Mat 54 properties representing unidirectional graphite tape composite material were assigned to shell elements representing the T-section. During the simulation, the model rapidly disintegrates as shown in Figure 93, which depicts the model deformation at time 0.017 seconds. Since the model does not represent the observed damage, no further test-analysis comparisons are presented.

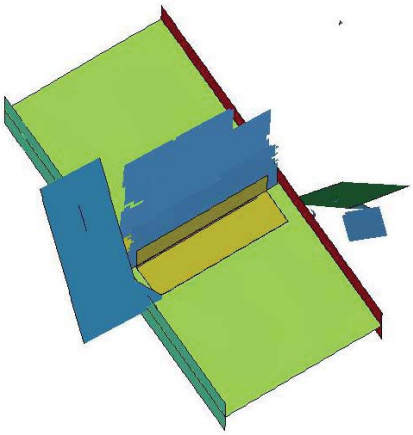

Figure 93. Mat 54 T-section model deformation at 0.017-s.

4.3.3 Mat 58 Predicted Responses Compared with 2-ft Drop Test Data

Comparisons of the measured acceleration- and displacement-time histories for the 2-ft drop test versus the Mat 58 simulation predictions are shown in Figures 94(a) and (b), respectively. The test and analysis acceleration curves, shown in Figure 94(a), were filtered using a low-pass Butterworth 1000-Hz digital filter. Test data shown in Figure 94(b) is from double integration of

the acceleration data and from photogrammetry. The initial peak accelerations are comparable at 270-g for the model and 320-g for the test, indicating that the initial stiffness, initial conditions, and mass of the model match those of the test article. However, after the initial spike, the model accelerations are higher than the test from 0.002- until 0.0075-s.

The damage observed from the 2-ft drop test indicated that both flanges on the vertical I-beam delaminated and buckled outward at the top of the fillets. The LS-DYNA model was not set up to account for ply delamination. Consequently, once delamination initiated, the actual test specimen became much weaker than the model and vertical displacement is greater in the test than in the model. From Figure 94(b), the maximum vertical test displacement from photogrammetry was measured to be 0.44-in. as compared to 0.27-in. in the LS-DYNA model.

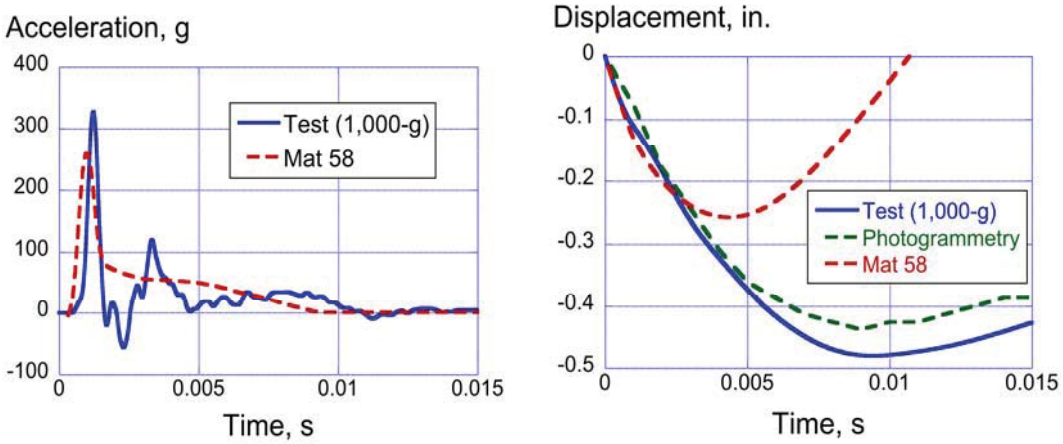

(a) Acceleration responses. (b) Displacement responses.

Figure 94. Comparisons of Mat 58 model predicted responses with test data for the 2-ft drop.

The deformed model of the T-section is shown in Figure 95 at 0.004-s. The figure indicates that a line of elements half way across the flange and located just above the fillet have failed and been deleted. However, other surrounding elements have not failed and these elements limit the amount of displacement. In the test, delamination and buckling allowed more deflection to occur, resulting in greater damage in the web than was seen in the model.

The same T-section model was re-executed with the reduced strength Mat 58 material model and test-analysis results are compared in Figure 96. The 1000-Hz low-pass filtered peak acceleration predicted by the model in Figure 96(a) is a little over 200 g's as compared to 320 g's from the test accelerometer. Thus, the peak acceleration of the reduced strength model does not compare as well as the baseline Mat 58 model. From Figure 96(b), the displacement for the reduced strength Mat 58 simulation is now closer to the test value. The final deformed plot looks very similar to Figure 95 and hence is not shown.

The T-section model representing the 2-ft drop test with baseline Mat 58 material properties was executed in which ERODS was varied from 0.1 to 0.5, in increments of 0.1. A depiction of model deformation is shown in Figure 97 for the Mat 58 simulation with ERODS = 0.1. Elements were deleted along the vertical flange and below the fillet for this small ERODS value. Comparisons of displacement-time histories for the different ERODS values are shown in Figure

98 along with data from the 2-ft drop test. Based on these results, an ERODS value between 0.3 and 0.4 shows best agreement with the test data.

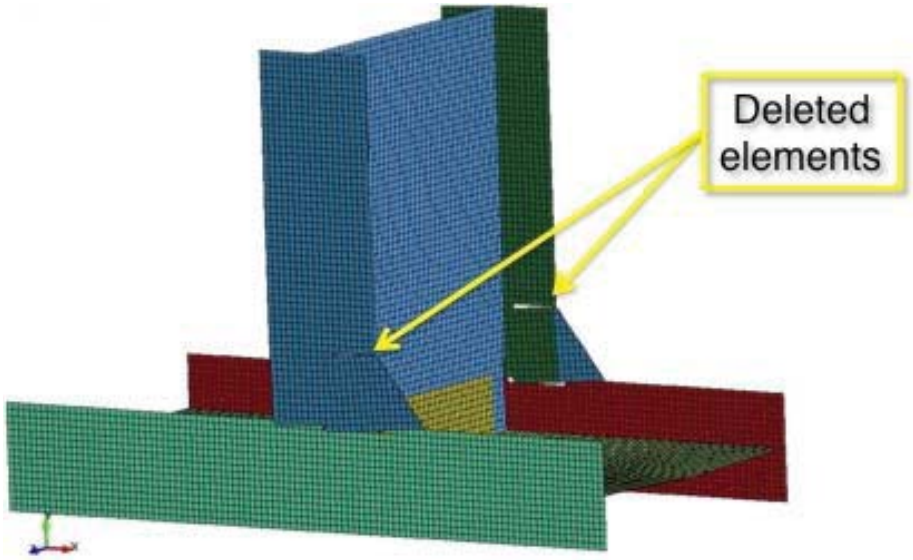

Figure 95. Maximum deformation of the Mat 58 T-section model at time 0.004-s after impact. Elements have been deleted where delamination occurred in the test.

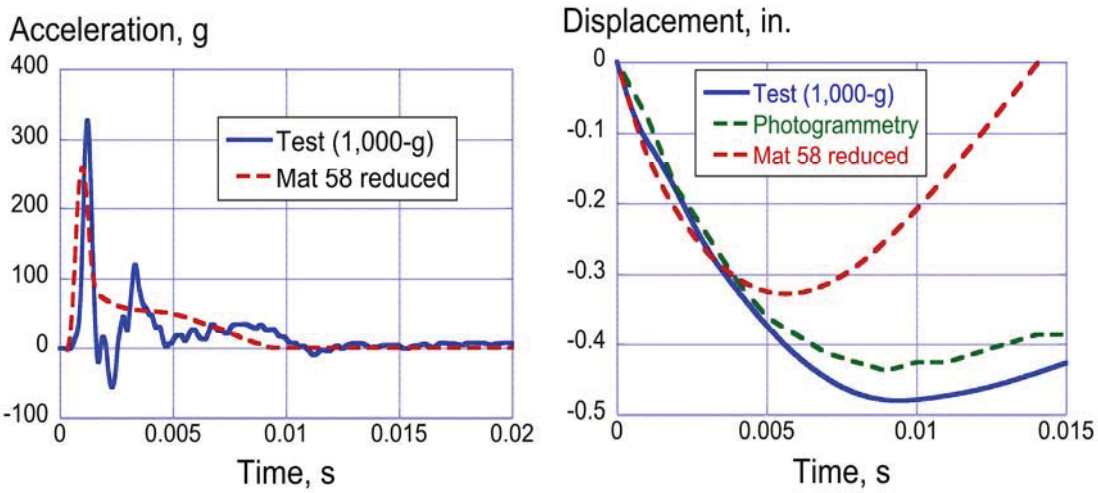

(a) Acceleration comparisons. (b) Displacement comparisons.

Figure 96. Comparison of reduced strength Mat 58 model with test for the 2-ft drop.

4.3.4 Mat 54 Predicted Responses Compared with 4-ft Test Data

The model representing the 4-ft drop test of the T-section is shown in Figure 92(b). Mat 54 material properties were assigned to shell elements representing the T-section. The model rapidly disintegrates as shown in Figure 99, which depicts model deformation at time 0.02 seconds. Multiple element failures are observed in different regions of the model, most of which do not match the test response. However, the simulation does capture the failure of the two vertical flanges above the fillets. The acceleration- and displacement-time histories of the drop-mass are compared with test data in Figure 100. The test-analysis comparisons are poor.

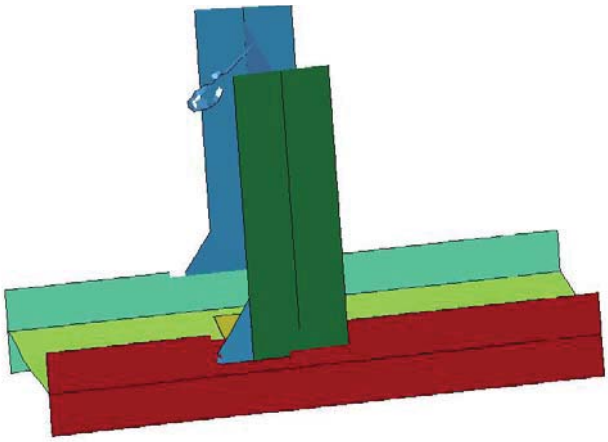

Figure 97. Mat 58 T-section model failure below the fillet for ERODS = 0.1.

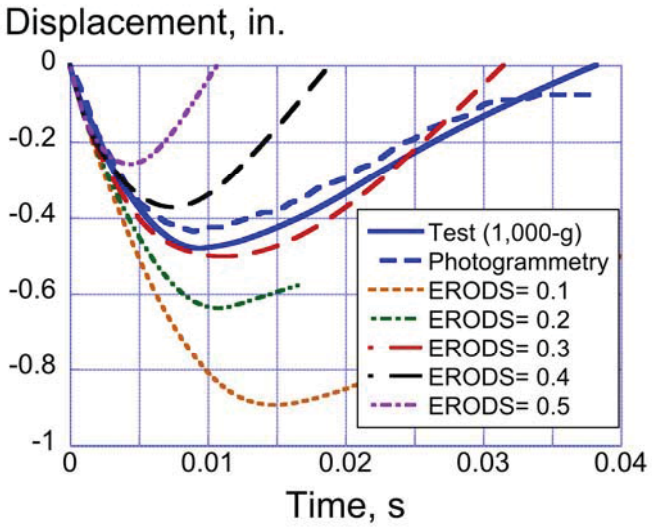

Figure 98. Comparison of displacement responses of the drop mass for the 2-ft T-section test with the Mat 58 models with only the ERODS parameter changed.

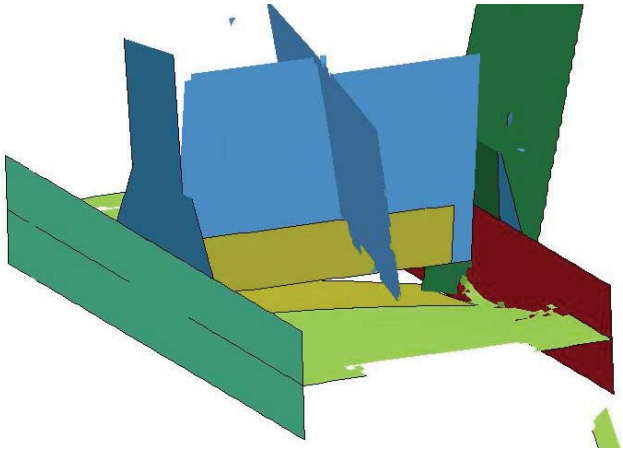

Figure 99. Mat 54 T-section model at time 0.02 seconds.

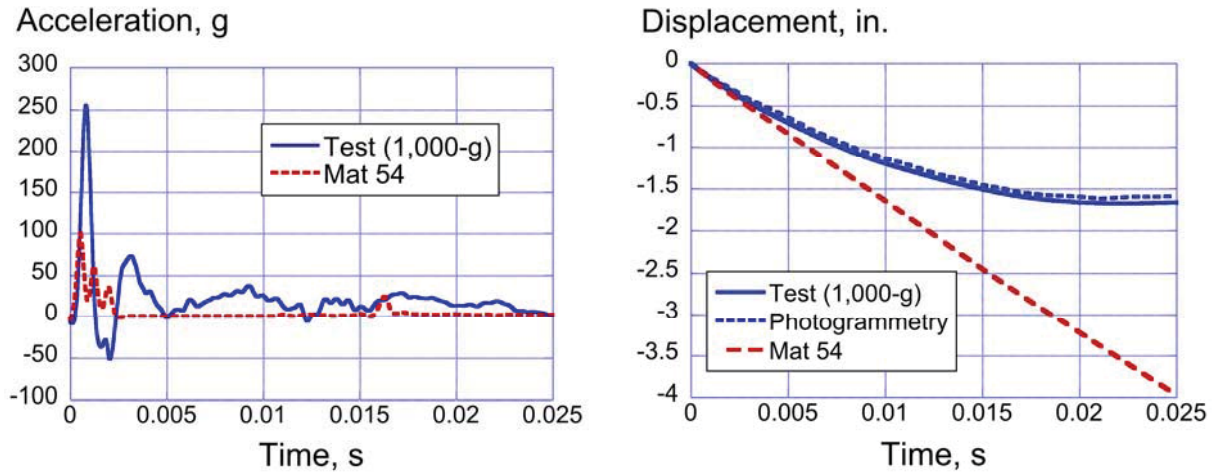

(a) Acceleration comparisons. (b) Displacement comparisons.

Figure 100. Comparisons of the 4-ft drop test data with the Mat 54 model predictions.

4.3.5 Mat 58 Predicted Responses Compared with 4-ft Test Data

The initiation of failure for the 4-ft drop test of the T-section occurred as buckling and delamination in the vertical I-beam flanges above the fillet. Delaminations caused complete failure of the flange, allowing the flanges on both sides above the fillets to become wedged inside the horizontal flanges below the fillets. Comparisons of the test and Mat 58 predicted acceleration, velocity, and displacement responses are shown in Figures 101(a), (b), and (c), respectively. Both test and analytical acceleration responses have been filtered using a 1000-Hz low-pass Butterworth filter. The Mat 58 model shows three peak accelerations whereas the test only shows two. However, the peak accelerations are comparable in magnitude to the test.

Again, the displacement is much lower for the model than the test as is evident in Figure 101(c). The displacement disparity can be explained by observing the failure mechanism in the test and comparing with the simulation. Although the vertical flanges in both the test and model completely failed above the fillet, in the test the vertical flanges wedged inside the horizontal flanges below the fillet. However, in the model (see Figure 102), the vertical flange rotated slightly after failing, which allowed edge-on-edge contact with the horizontal flange after failure. Since single surface contact was used, this contact allowed the upper flange to cut into the lower flange. The higher force generated prevented further displacement from occurring after 0.01 seconds, whereas the actual test specimen continued displacing up to 0.02 seconds. The final deformation pattern of the model is illustrated in Figure 102.

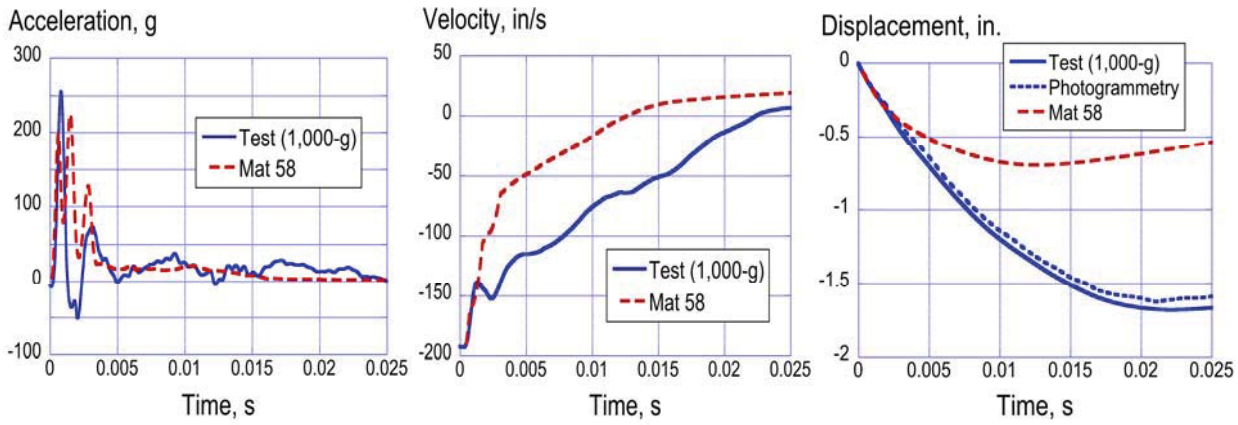

(a) Acceleration. (b) Velocity. (c) Displacement.

Figure 101. Comparisons of Mat 58 model predicted responses with 4-ft T-section test data.

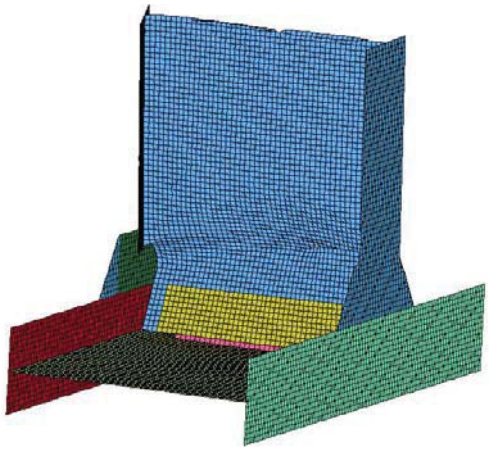

Figure 102. Mat 58 predicted damage of the T-section model at time 0.015 seconds after impact (4-ft drop test). The vertical flanges have delaminated and failed above the fillets.

The same T-section model was executed with the reduced strength Mat 58 material model and test-analysis results are compared in Figure 103. The acceleration peak predicted by the model in Figure 103(a) is less at 170 g's as compared to 250 g's for the test. From Figure 103(c), the displacement of the simulation is much greater than the test value. Both the photogrammetry data and the displacement data obtained from double integration of the acceleration data were used for comparison with predicted displacement. Photogrammetry provides direct displacement data and does not require careful reduction of accelerometer data required to account for zero offsets and constants of integration; however, both experimental displacement curves are similar.

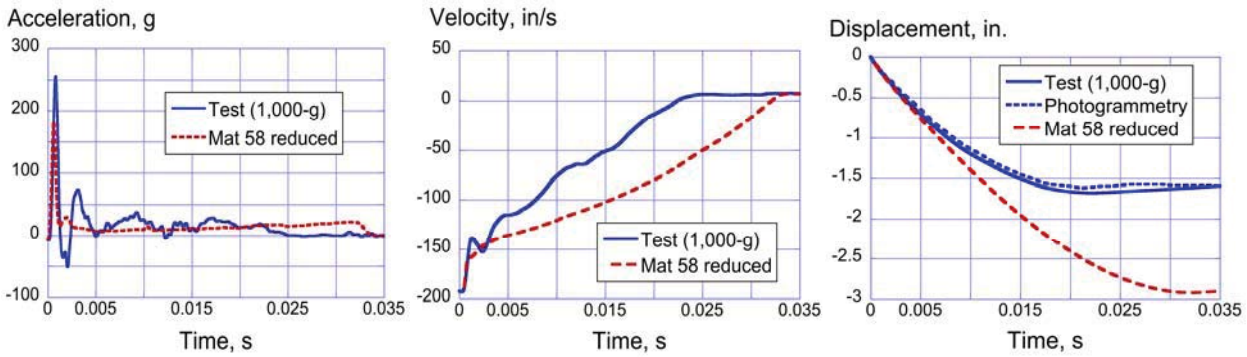

(a) Acceleration responses. (b) Velocity Responses. (c) Displacement responses.

Figure 103. Comparisons of test and Mat 58 reduced strength material model.

A picture of model deformation is shown along with a photograph of the post-test article, in Figures 104(a) and (b), respectively. The vertical flanges of the model break just above the fillet as can be seen in Figure 104(a). However, the upper flanges slide over the lower flanges instead of wedging inside as occurred during the test, see Figure 104(b). Also, the rivets were not included in the model. From Figure 104(b), rivet-on-rivet contact contributed to lowering the displacement of the test article.

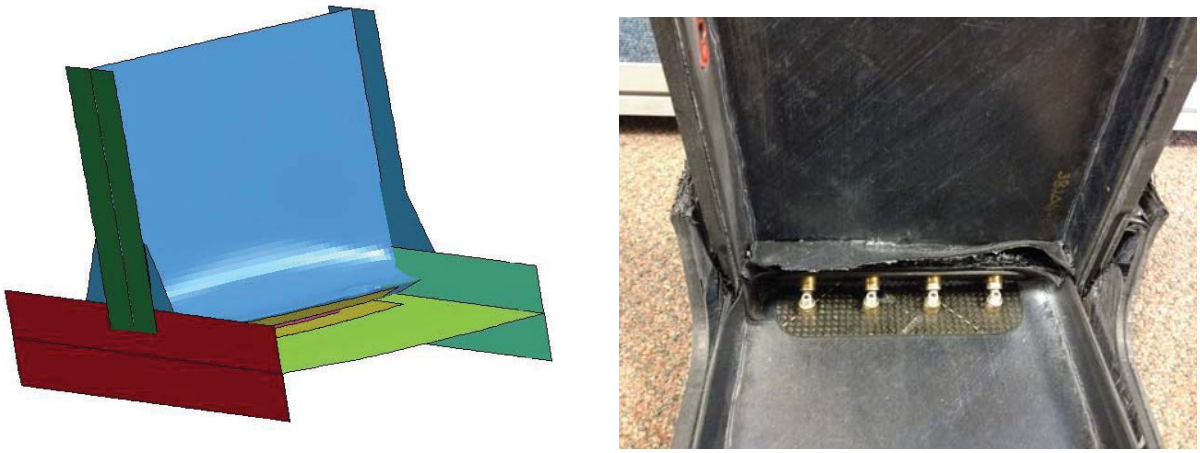

(a) Model deformation. (b) Post-test photograph.

Figure 104. Comparison of post-test picture with Mat 58 deformed plot.

The T-section model of the 4-ft drop test was executed with the baseline Mat 58 properties; however, the ERODS parameter was varied from 0.1 to 0.5 in increments of 0.1. The deformation and failure of the model varied considerably with the ERODS value. Consequently, there is no uniformity of results and there is no convergence, as shown in Figure 105. Although the displacement response for an ERODS value of 0.1 most closely matches the test data, the actual deformed model, shown in Figure 106(a), failed catastrophically and does not compare favorably with the post-test damage. The best deformation results are obtained with an ERODS of 0.2. The deformed shape shown in Figure 106(b) is similar to the observed damage with both vertical flanges failing above the fillets. However, the damage near the top of the vertical web did not occur in the test.

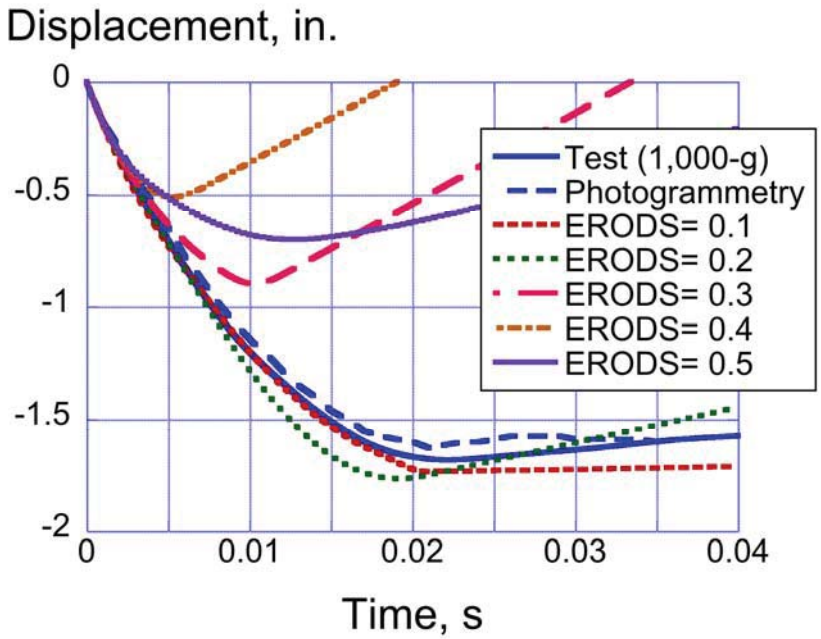

Figure 105. Displacement responses of the drop mass for the 4-ft T-section test and Mat 58 models with varying ERODS parameter.

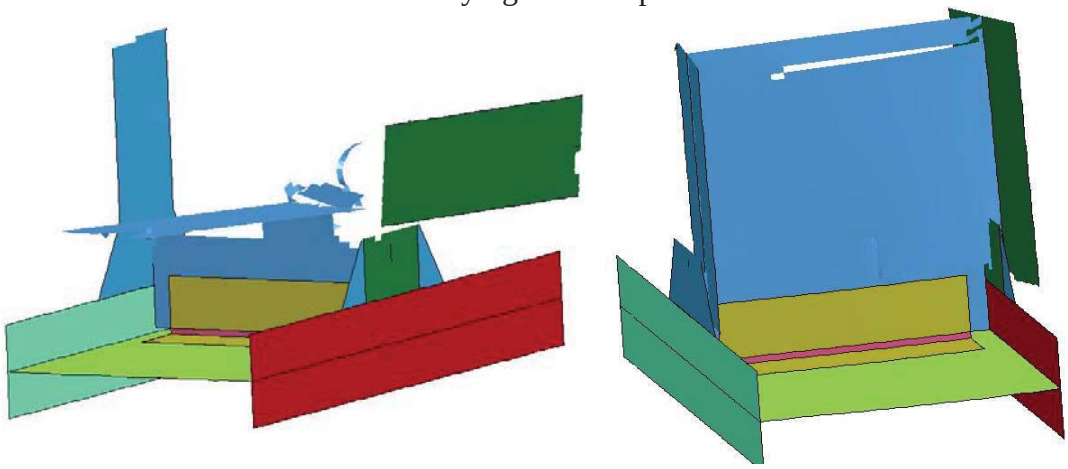

(a) Deformed model for ERODS = 0.1 (b) Deformed model for ERODS = 0.2

Figure 106. Mat 58 T-section model deformation for ERODS = 0.1 and 0.2.

4.4 Simulation of Dynamic Crush Tests of Two Cruciform Sections

4.4.1 Description of the Finite Element Model

Two views of the cruciform section model are depicted in Figure 107. The model consists of 16,916 nodes; 15,750 Belytschko-Tsay (ELFORM=Type 2) quadrilateral shell elements representing the cruciform; and, 512 solid elements representing the drop mass. Shell elements had a nominal element edge length of 0.125-in. Ten parts were defined, one part for the drop mass and nine parts for the cruciform, including four flange parts, two web parts, and three separate parts defining the center clips. Five material cards were defined including Mat 20 (MAT_RIGID) for the impact mass. Four different Mat 54 and Mat 58 cards were required to ensure consistent and correct local material axis directions. These were input by setting AOPT =

2.0, which specifies that the local material axis directions are defined using vector input [5]. The density of the rigid material was selected to match the weight (215-lb) of the experimental drop mass.

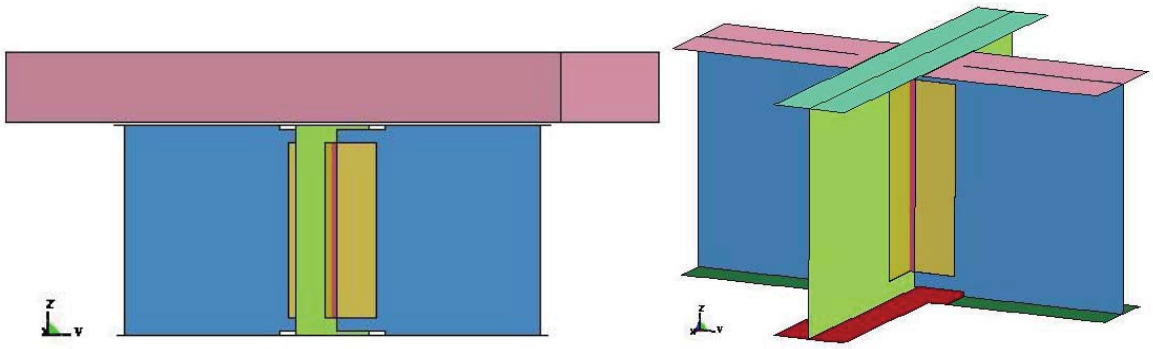

(a) Canted front view with drop mass. (b) View of the model without the drop mass.

Figure 107. Pictures of the cruciform model.

Two SPCs were defined, one to allow the drop mass to move in the vertical direction only and one to fix the nodes of the bottom flanges. Finally, the nodes forming the drop mass were assigned an initial velocity to match the two test conditions, 192.5- and 268.6-in/s. These two impact velocities correspond to the 4- and 8-ft drop heights used during the tests. Output from the model included acceleration-, velocity-, and displacement-time histories of a central node on the drop mass, as well as pictures of model deformation. Models were executed using LS-DYNA SMP Version 971 R6.0.0 with double precision and required up to 1 hour and 54 minutes of CPU on four processors for an end time of 0.02 seconds.

4.4.2 Mat 54 Predicted Responses Compared with 4-ft Drop Test Data

Results are shown in Figure 108 comparing the 192.5-in/s drop test data with the Mat 54 predicted responses. The experimental and analytical acceleration responses shown in Figure 108(a) were filtered using a low-pass Butterworth 1000-Hz filter. Also, displacement data are shown based on double integration of the acceleration response and photogrammetry. As with previous Mat 54 comparisons, the level of agreement between test and analysis for the Mat 54 predicted responses is poor. The velocity responses in Figure 108(b) indicate that the model is removing some kinetic energy during the simulation; however, the predicted response is not close to the test and it never reaches zero velocity during the 0.02-s simulation time. Likewise, the model never achieves a maximum crush displacement during the 0.02-s simulation time.

Deformation plots are illustrated in Figure 109 for the Mat 54 simulation for four time steps. The model fails in a brittle fashion, with no bending or plasticity shown in the webs. By 0.015-s, large pieces of the model including entire web sections have been separated from the upper and lower flanges. The predicted deformation pattern does not resemble the observed response, which is depicted in Figure 32. During the test, the webs exhibited bending and global bucking; however, no separations occurred between the flanges and webs.

4.4.3 Mat 58 Predicted Responses Compared with 4-ft Drop Test Data

Results are shown in Figure 110 comparing the 192.5-in/s drop test data with the Mat 58 predicted responses. The acceleration responses shown in Figure 110(a) have been filtered using

a Butterworth 1000-Hz low pass filter. Also, displacement data are shown in Figure 110(c) from double integration of the acceleration data, as well as direct photogrammetric measurements. The test accelerations exhibit an initial oscillatory response with a high-magnitude peak of approximately 540-g. The predicted response matches the timing of the initial test peak, but is much lower in magnitude (167-g). The velocity responses, shown in Figure 110(b), indicate that, after 0.004-s, the model is removing velocity more quickly than the test. The model response crosses zero velocity 0.0035-s sooner than the test response. A sudden dip in the velocity responses occurs in both traces and the analysis curve shows a marked change in slope during the same time period. In Figure 110(c), the test data indicate a maximum crush depth ranging between 0.97- and 1.02-inches that occurs at approximately 0.0127-s. Photogrammetric results show a slightly higher maximum displacement of 1.07-in. However, the model predicts a lower maximum crush displacement of 0.74-in. that occurs earlier in time at 0.0094-s.

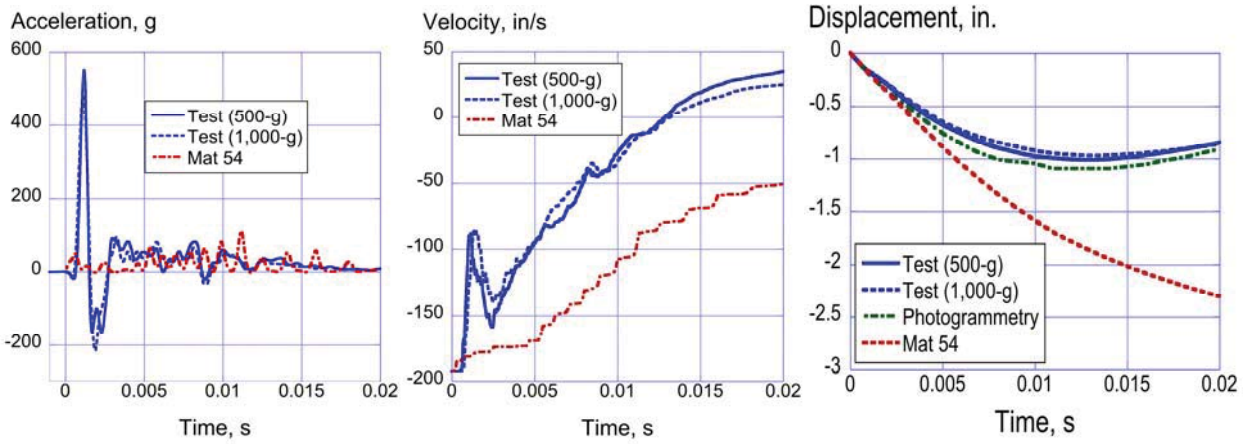

(a) Acceleration responses. (b) Velocity responses. (c) Displacement responses.

Figure 108. Experimental and Mat 54 analytical results for the cruciform 4-ft drop test.

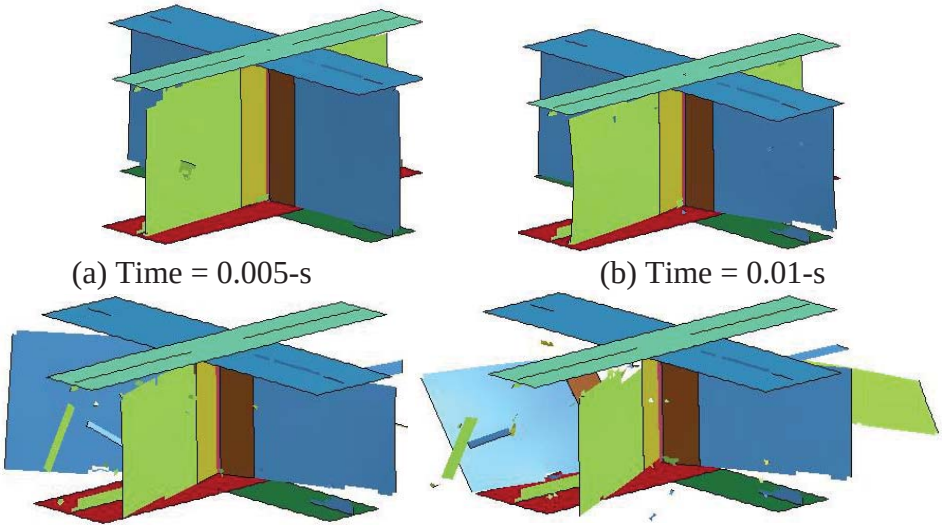

(a) Time = 0.005-s (b) Time = 0.01-s

(c) Time = 0.015-s (d) Time = 0.02-s

Figure 109. Mat 54 cruciform model deformation (velocity = 192.5-in/s).

A sequence of model deformation is shown in Figure 111 for five time steps. The cruciform webs in the model exhibit bending and buckling. Few element failures are observed, except at

the interface of the vertical webs and the lower flanges. Though not highly evident in this sequence, the web buckling behavior produces a slight rotation of the top flanges near the end of the pulse. The model deformation compares well with the test response, which is highlighted in Figure 32.

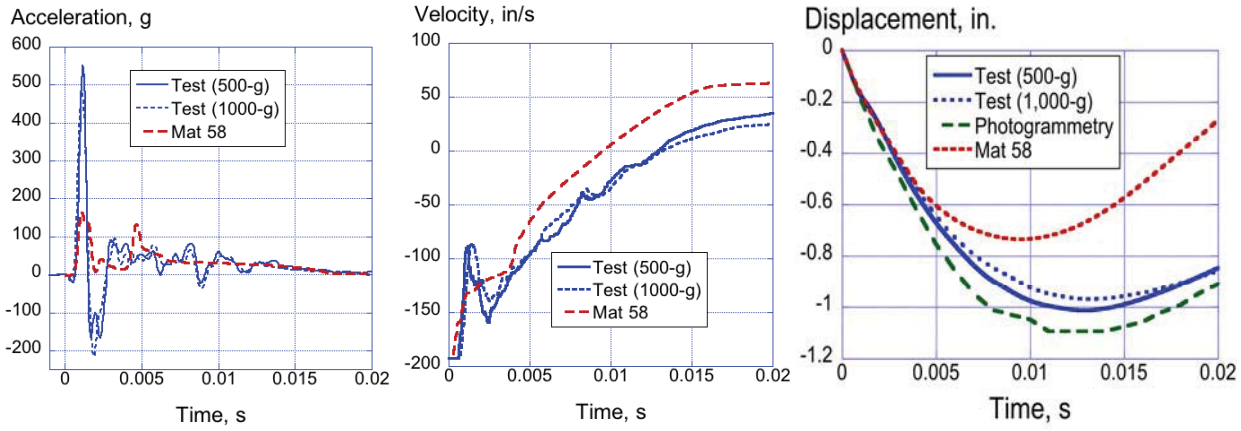

(a) Acceleration. (b) Velocity. (c) Displacement.

Figure 110. Experimental and Mat 58 analytical results for the cruciform 4-ft drop test.

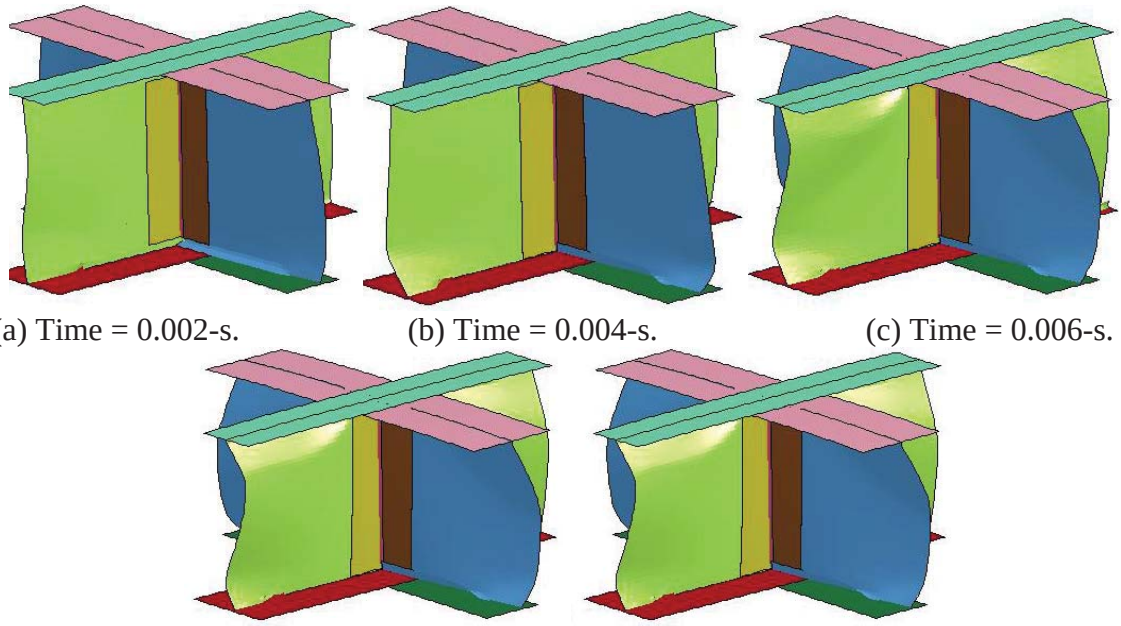

(a) Time = 0.002-s. (b) Time = 0.004-s. (c) Time = 0.006-s.

(d) Time = 0.008-s. (e) Time = 0.01-s

Figure 111. Mat 58 predicted cruciform model deformation sequence (velocity = 192.5-in/s).

The cruciform section model was re-executed using the reduced strength Mat 58 material properties to simulate the 4-ft drop test (velocity=192.5-in/s). In addition, an ERODS study was conducted in which ERODS was varied from 0.1 to 0.5 in increments of 0.1. The results for these two parametric studies are shown in Figure 112. The reduced strength model shows better agreement with the test maximum crush displacement, 0.98-in. for the model compared with 0.97- to 1.02-in. for the test, than the baseline Mat 58 material. The ERODS study indicates that a value of 0.4 provides the best agreement with test data.

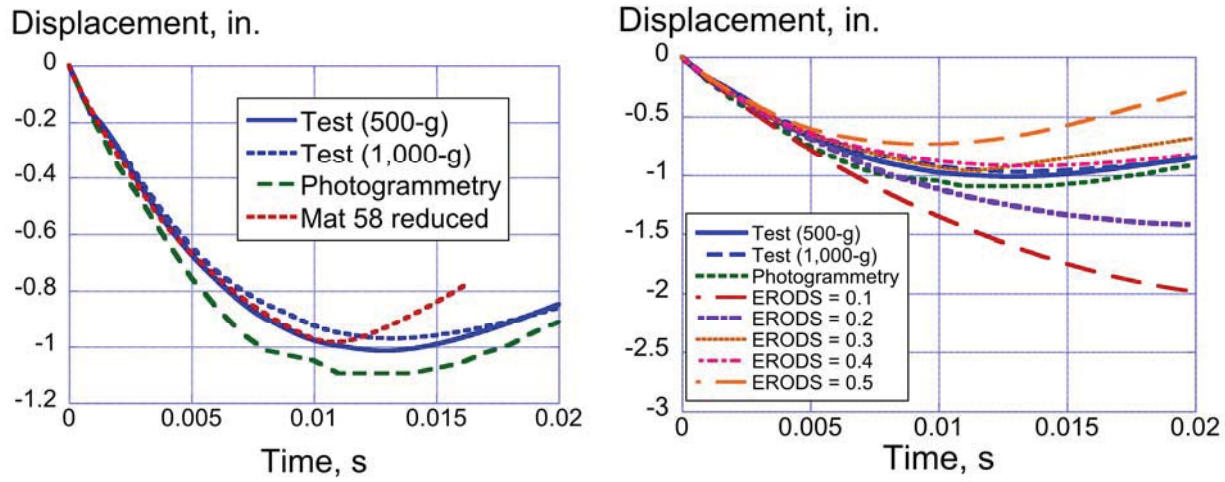

(a) Reduced strength model. (b) ERODS study.

Figure 112. Mat 58 parameter study results for the cruciform section (192.5-in/s velocity).

4.4.4 Mat 54 Predicted Responses Compared with 8-ft Drop Test Data

Results are shown in Figure 113 comparing the 268.6-in/s drop test data with the Mat 54 predicted responses. The acceleration responses shown in Figure 113(a) have been filtered using a Butterworth 1000-Hz low pass filter. Also, displacement data are shown in Figure 113(c) from double integration of the acceleration data, as well as direct photogrammetry measurements. As with the lower velocity test, the experimental acceleration response exhibits a high spike initially, followed by a somewhat stable crushing phase. However, the model is not able to capture any feature of the test response. The velocity comparison, shown in Figure 113(b), indicates that kinetic energy is removed from the test and the drop mass crosses zero velocity at 0.015-s. Conversely, the model shows that during the simulation time of 0.02-s, only 120-in/s of velocity was removed from the simulation. The displacement plot, shown in Figure 113(c) indicates that while the test curve exhibits a maximum crush stroke of 1.63-in., the predicted response continues to displacement vertically without abatement.

Four depictions of the Mat 54 model deformation are shown in Figure 114 for the simulation of the 268.6-in/s vertical drop test of a cruciform specimen. As was observed for the lower velocity condition, the model fails in a brittle fashion, with no evidence of bending or buckling. By 0.01-s, the interface elements between the web and flanges have failed and been removed from the simulation. These element failures allow the webs to separate from the flanges, and as the simulation continues, part-to-part contact forces the broken webs to rotate sideways. The predicted deformation pattern does not match the observed experimental results, which are depicted in Figure 37.

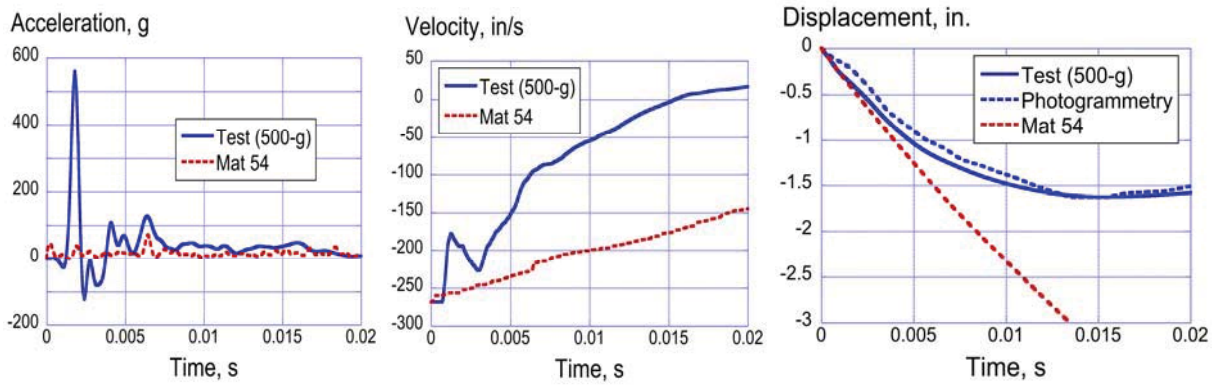

(a) Acceleration. (b) Velocity. (c) Displacement.

Figure 113. Experimental and Mat 54 analytical results for the cruciform 8-ft. drop test.

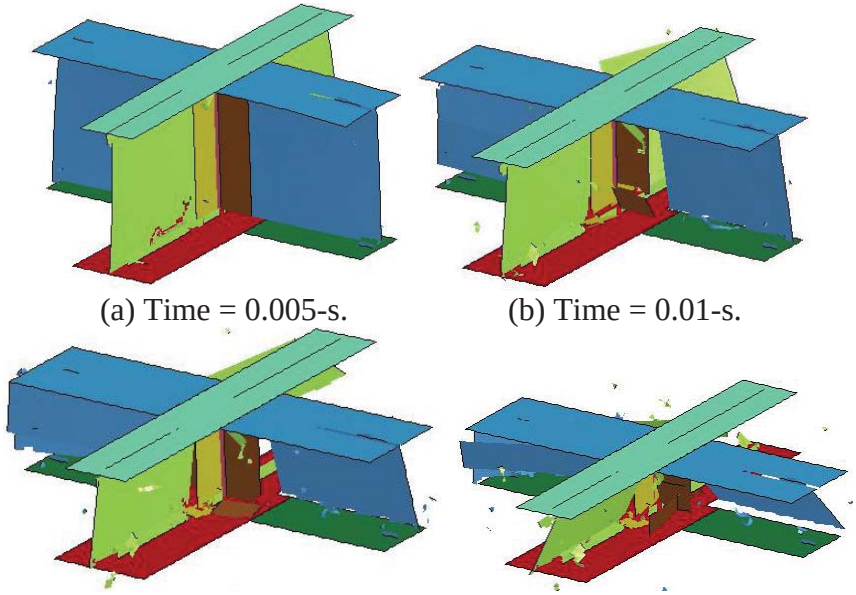

(a) Time = 0.005-s. (b) Time = 0.01-s.

(c) Time = 0.015-s. (d) Time = 0.02-s.

Figure 114. Mat 54 cruciform model deformation (velocity = 268.6-in/s).

4.4.5 Mat 58 Predicted Responses Compared with 8-ft Drop Test Data

The cruciform model (see Figure 107) was re-executed with Mat 58 material properties for the higher impact velocity of 268.6-in/s, representing the 8-ft drop test condition. All other model details remained the same as for the lower velocity simulation. Experimental and analytical acceleration-, velocity-, and displacement-time histories are compared in Figure 115. Note that the acceleration curves shown in Figure 115(a) were filtered using a Butterworth 1000-Hz low pass filter. As with the lower velocity case, the test acceleration exhibits an oscillatory response with a high initial peak acceleration of approximately 550-g. The predicted response also exhibits an initial peak acceleration (163-g), which is much lower in magnitude than the test response. Following the initial spike, the two curves are close in magnitude and duration. Further verification of the level of agreement is seen in the velocity and displacement responses, shown in Figures 115(b) and (c), respectively. The sudden dip that was observed in the velocity response of the 4-ft drop test is also seen here. Once again, the analytical curve exhibits a

significant change in slope early in the response and essentially averages the oscillations in the test response. The maximum predicted crush displacement is 1.68-in., which compares well with the test value of 1.63-in. Also, note that the photogrammetric results indicated a consistent maximum crush displacement of 1.63-in.

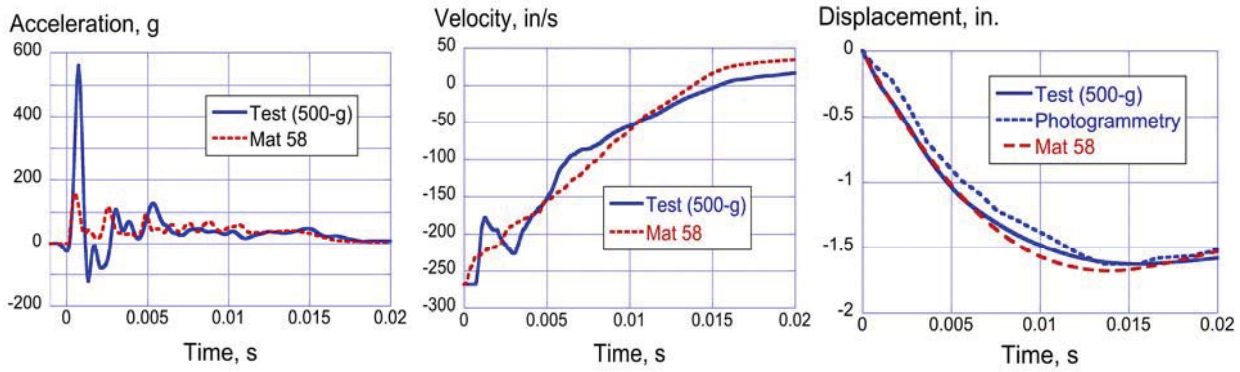

(a) Acceleration responses. (b) Velocity responses. (c) Displacement responses.

Figure 115. Experimental and Mat 58 analytical results for the cruciform 8-ft. drop test.

Model deformations are shown in Figure 116 for six time steps. These depictions indicate severe buckling and bending of the webs; however, few if any elements are removed from the model. Also, the integrity of the web-flange interface is maintained. The predicted deformation pattern is a reasonably good match to the test response, which is shown in Figure 37.

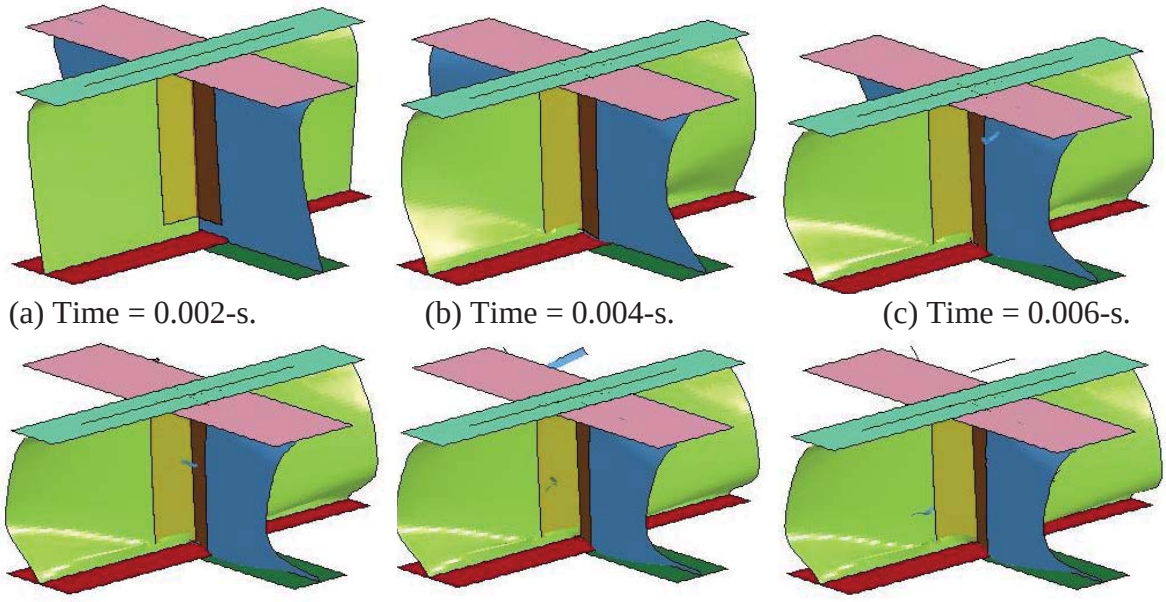

(a) Time = 0.002-s. (b) Time = 0.004-s. (c) Time = 0.006-s.

(d) Time = 0.008-s. (e) Time = 0.01-s. (f) Time = 0.012-s.

Figure 116. Mat 58 cruciform model deformation sequence (velocity = 268.6-in/s).

The cruciform section model was re-executed using the reduced strength Mat 58 material properties to simulate the 8-ft drop test (velocity=268.6-in/s). In addition, an ERODS study was conducted in which ERODS was varied from 0.1 to 0.5 in increments of 0.1. The results for

these two parameter studies are shown in Figures 117(a) and (b), respectively. In this case, the reduced strength material shows a much higher maximum crush displacement than the test, e.g. 2.25-in. for the model compared with 1.63-in. for the test. The ERODS study indicates that a value of 0.5 provides the best agreement with test data.

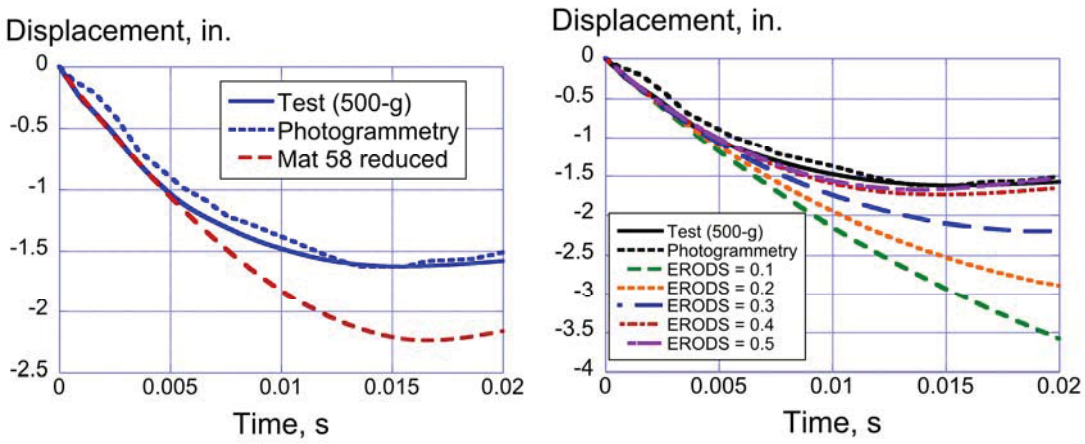

(a) Reduced strength model. (b) ERODS study.

Figure 117. Mat 58 parameter study results for the cruciform section (268.6-in/s velocity).

4.5 Simulation of the Longitudinal Impact of a Subfloor Section

4.5.1 Description of the Finite Element Model

Pictures of the finite element model of the subfloor section are shown in Figure 118. The model consists of 109,393 quadrilateral shell elements; 1,500 solid elements; 111,607 nodes; 15 parts; and, 5 material cards. A single contact definition was used to define contact between the impact mass and the subfloor, and self-contact within the subfloor, which is designated CONTACT_AUTOMATIC_SINGLE_SURFACE. Of the 15 parts specified in the model, all but two were defined as PART_COMPOSITE, which allows input of ply orientations, thicknesses, and material designations for each layer in a multi-layered composite laminate. A Mat 20 (MAT_RIGID) card was used for the impact drop mass and a Mat 24 (MAT_PIECEWISE_LINEAR_PLASTICITY) card was used for the upper and lower aluminum support plates. All other parts were assigned either Mat 54 or Mat 58 material properties. For Mat 54 and Mat 58, autoclave material properties for unidirectional graphite tape were evaluated. Both models were executed using the fully integrated shell element formulation (ELFORM=Type 16). Models were executed using LS-DYNA SMP Version 971 R6.0.0 with double precision and required up to 129 minutes of CPU on four processors for an end time of 0.1 seconds. The nominal element edge length is 0.25-inch.

Nodes forming the drop mass were assigned an initial velocity of 264-in/s, matching the test condition. Two SPCs were defined, one to fix the bottom nodes of the lower support plate and a second to ensure that the drop mass could only move in the vertical direction. Model output included acceleration-, velocity-, and displacement-time histories of a center node on the drop mass, as well as pictures of model deformations. As indicated in Section 3.7.2, the only reliable data collected for the subfloor drop test was from photogrammetry of the base skinned panel, including vertical velocity and displacement responses.

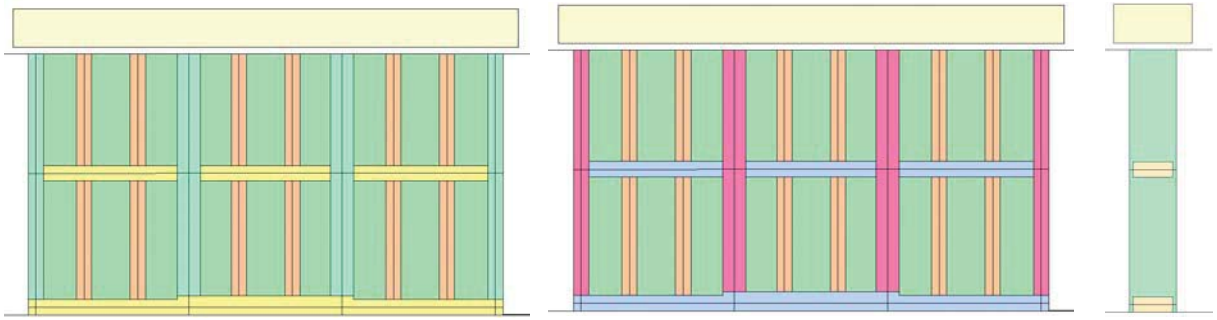

(a) Front view. (b) Rear view. (c) Side view.

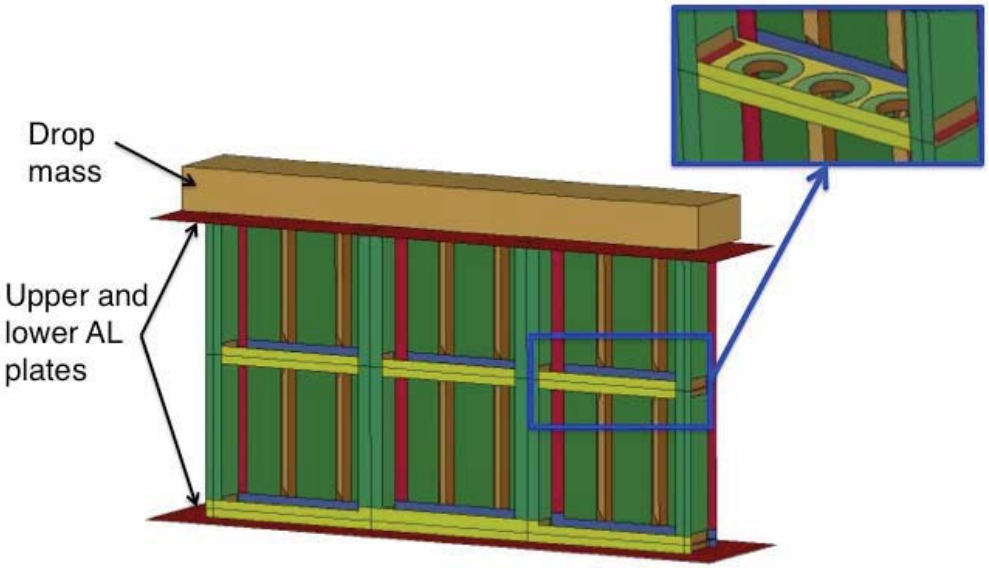

(d) Canted view.

Figure 118. Pictures of the subfloor section model.

4.5.2 Mat 54 Predicted Responses Compared with Test Data

Comparisons of the Mat 54 predicted velocity- and displacement-time history responses with photogrammetric data obtained during the subfloor section impact test are shown in Figure 119. The photogrammetric velocity response, shown in Figure 119(a), was filtered using an SAE CFC60 low-pass filter. The Mat 54 analysis indicates that only a small amount of kinetic energy is removed during the simulation. The predicted response started at a velocity of -264-in/s and ended at a velocity of -200-in/s. Likewise, the predicted vertical displacement increases in a linear fashion, without abatement, throughout the duration of the simulation.

The predicted deformation pattern of the subfloor model that was executed with Mat 54 material properties is shown in Figure 120. As with previous simulations conducted using the Mat 54 material model, failure occurs in a brittle fashion, with large pieces of the structure breaking away as the model shatters like glass. The test article failed catastrophically through debonding of the T-stiffeners, tearing of the rear skin, and crushing of the I-beams, as described in Section 3.7.2. However, in the test, sufficient energy absorption occurred to limit the displacement of the upper mass to approximately 13-inches by the time of contact with the honeycomb stops (0.071-s). In the simulation, the drop mass displaced approximately 17-inches by 0.071-s. The

honeycomb stops were not included in the model and the drop mass continued to displace vertically with no abatement, as brittle failure of the structure continued.

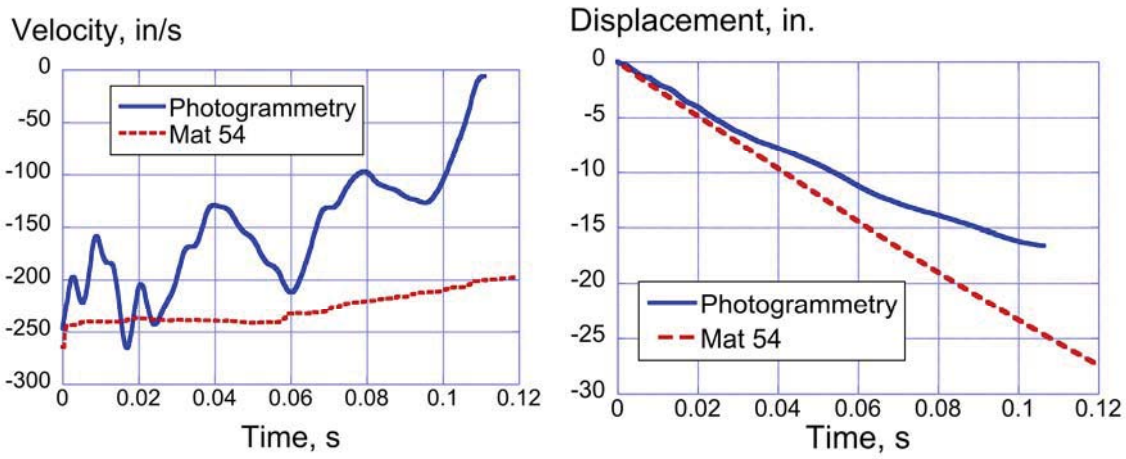

(a) Velocity responses. (b) Displacement responses.

Figure 119. Comparisons of Mat 54 predicted velocity and displacement responses with PG.

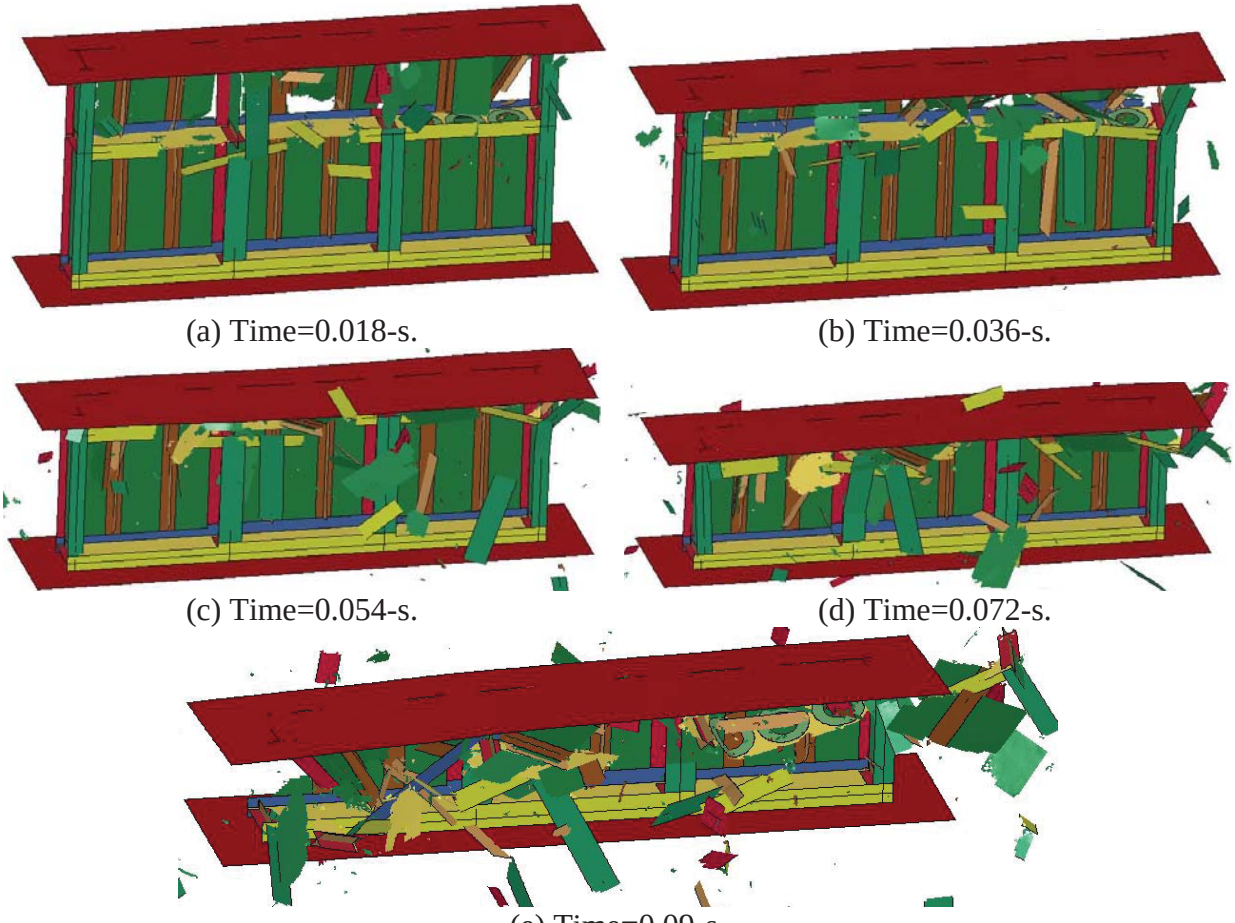

(a) Time=0.018-s. (b) Time=0.036-s.

(c) Time=0.054-s. (d) Time=0.072-s.

(e) Time=0.09-s.

Figure 120. Pictures of Mat 54 subfloor model deformation.

4.5.3 Mat 58 Predicted Responses Compared with Impact Test Data

Comparisons of Mat 58 pre-test predicted velocity- and displacement-time histories with photogrammetric test data are shown in Figure 121. The predicted velocity response indicates that the model is too stiff and removes velocity much more quickly than the test. Likewise, the model predicts a maximum crush displacement of only 7-inches. Conversely, the test article displaces 13-inches, at which point the honeycomb stops are contacted. The pre-test simulation was executed using the baseline material properties for unidirectional graphite tape. The value of ERODS used in this material model proved to be too high to match the experimental deformations and failures. Pictures of model deformations are shown in Figure 122.

Whereas the Mat 54 simulation predicted too much damage to the subfloor, the pre-test Mat 58 simulation predicts too little damage. In addition, the type of predicted damage, which is mostly uniform crushing, does not match the test. The rear skin, I-beams, and T-stiffeners in the upper half of the section exhibit some out-of-plane bending and localized crushing; however, the lower half of the section remains undamaged.

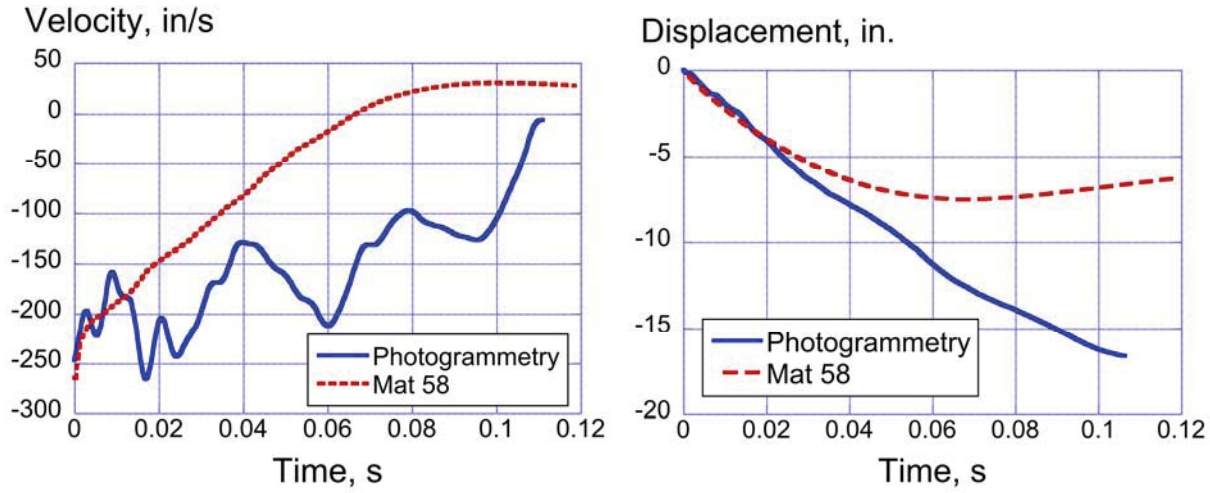

(a) Velocity-time history. (b) Displacement-time history.

Figure 121. Comparison of experimental and Mat 58 analytical responses for the subfloor test.

As with previous simulations, two parametric studies were conducted. The first involved re-executing the simulation using the reduced strength Mat 58 material model in which XC, XT, and E11T were lowered. As a reminder, XC was reduced by 25%; XT was reduced by 25%; and, E11T was reduced by 35%. Next, a study was conducted using the baseline Mat 58 material properties in which the ERODS parameter was varied from 0.1 to 0.5 in increments of 0.1. The results of these two studies are shown in Figures 123 and 124.

The reduced strength model was not successful in generating improved prediction of the velocity response or the maximum crush displacement, as shown in Figures 123(a) and (b). The results, shown in Figure 124, indicate that ERODS values of 0.5, 0.4, and 0.3 provide similar velocity and displacement responses with maximum displacement values ranging from 7- to 8-inches. However, the model executed with ERODS=0.1 shows excellent agreement with test data up to a crush displacement of 10-inches.

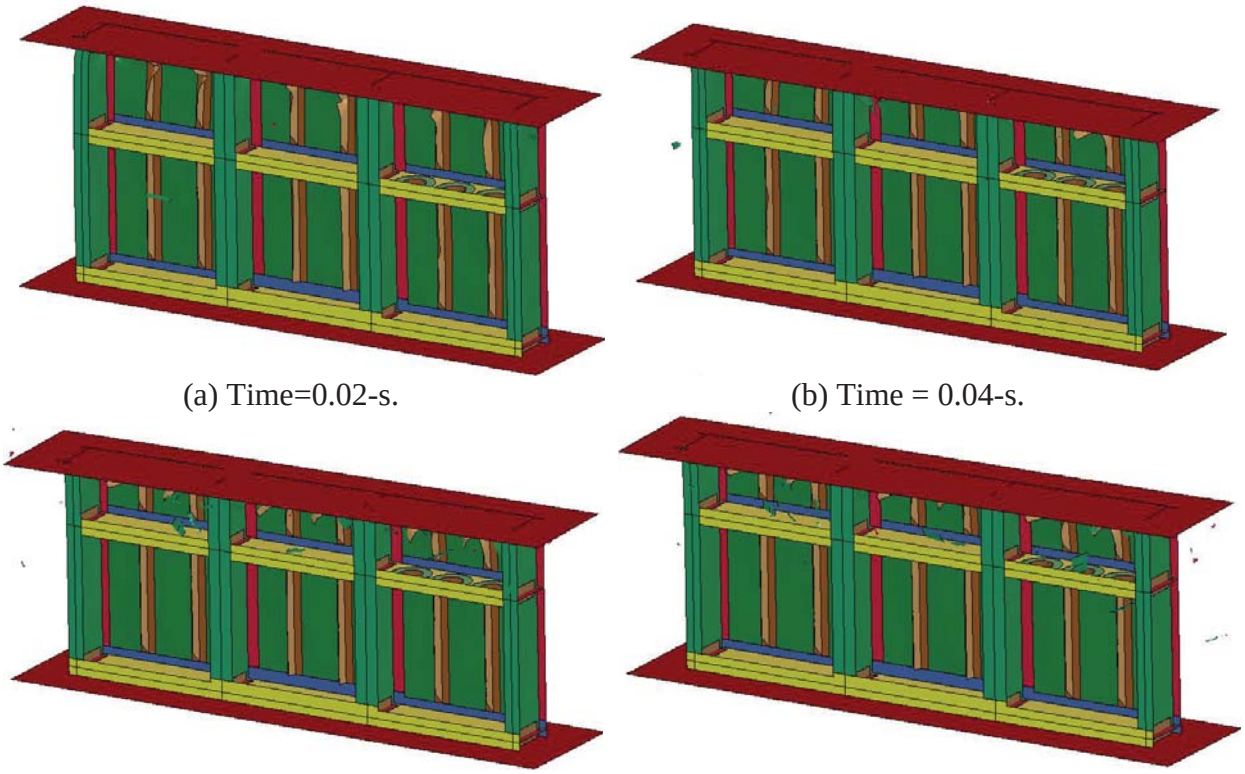

(a) Time=0.02-s. (b) Time = 0.04-s.

(c) Time=0.06-s. (d) Time = 0.08-s.

Figure 122. Pictures of Mat 58 subfloor model deformation.

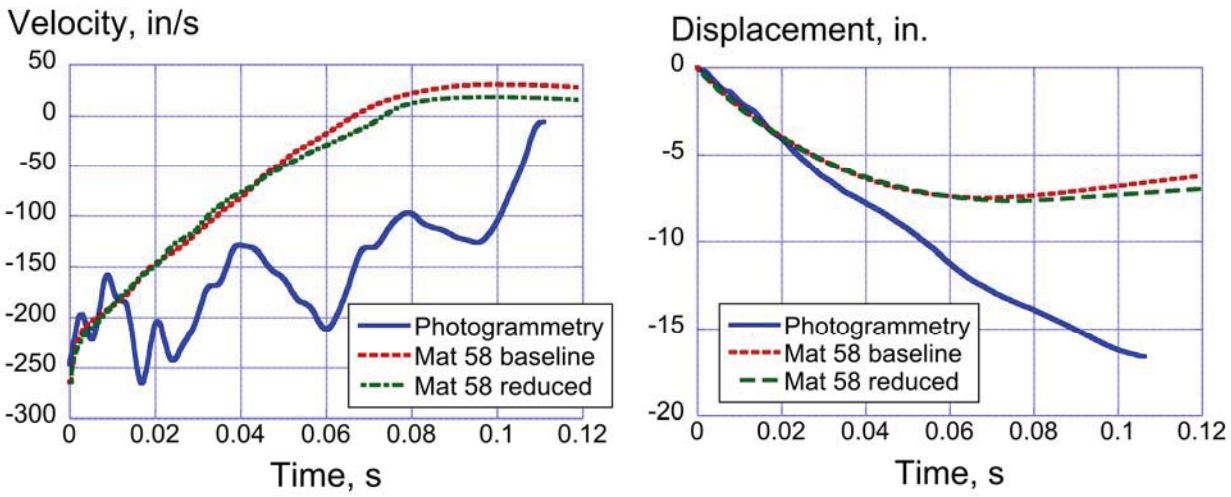

(a) Velocity-time history. (b) Displacement-time history.

Figure 123. Mat 58 reduced strength parameter study results for the subfloor section.

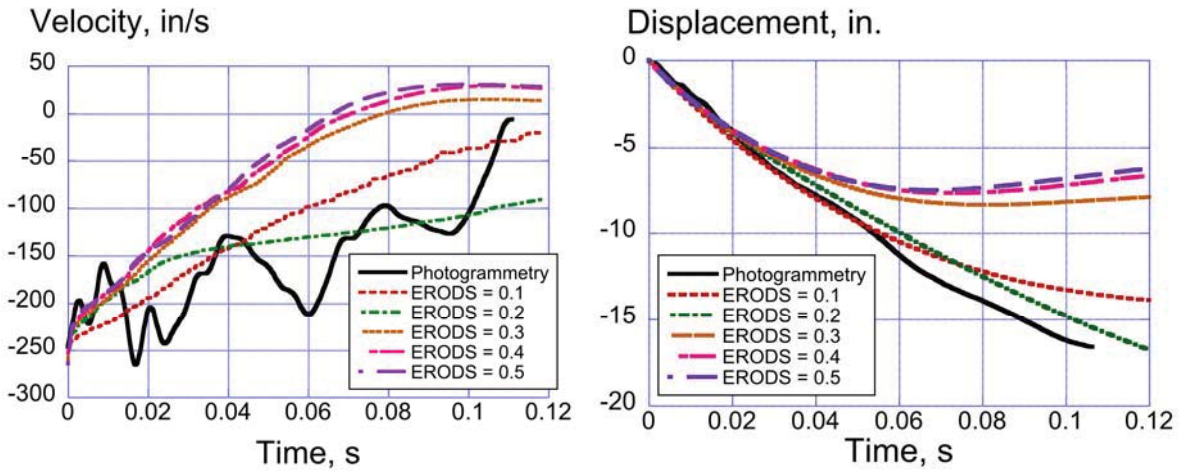

(a) Velocity-time history. (b) Displacement-time history.

Figure 124. Mat 58 ERODS parameter study results for the subfloor section.

Since the Mat 58 model with ERODS=0.1 gave much improved prediction of both the velocity- and displacement-time history responses obtained during the subfloor impact test, the deformation pattern for this simulation is shown in Figure 125. This simulation exhibits considerably more damage than the model that was executed with baseline properties that include a relatively high value of ERODS (see Figure 122). Pieces of the model are failed and separated from the main model, as crushing initiates from the upper edge. Damage appears to progress from the upper edge of the subfloor to the mid-section in a stable and fairly uniform fashion. By 0.1-s, the upper half of the section has been completely removed from the model.

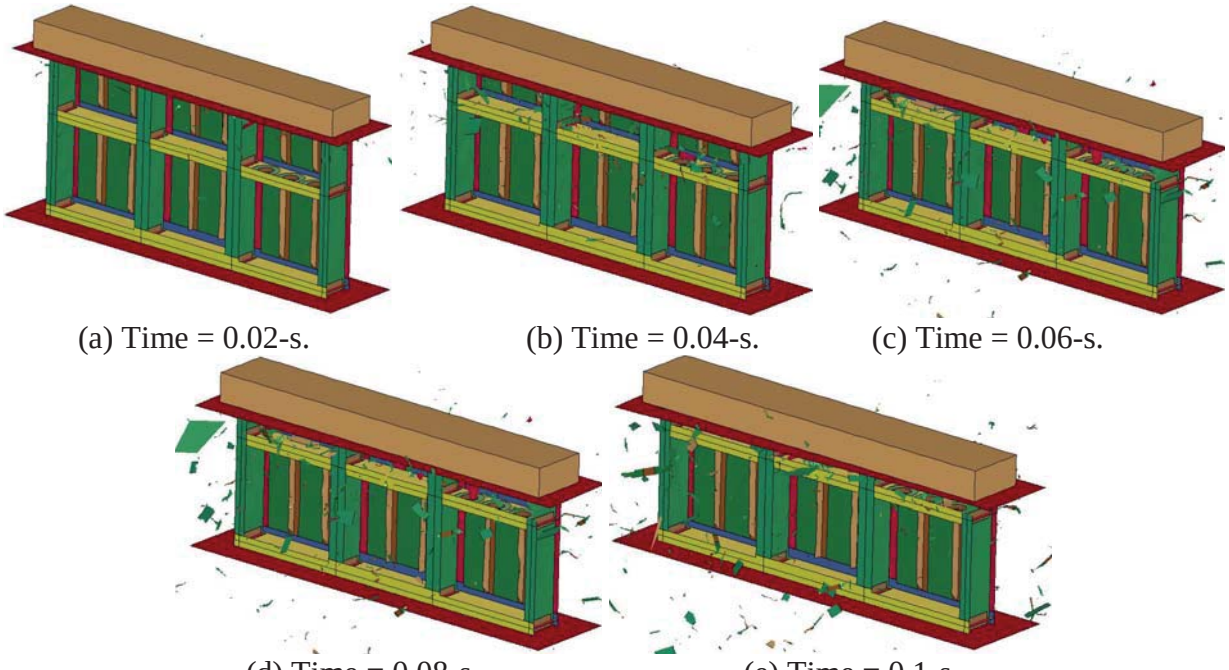

(a) Time = 0.02-s. (b) Time = 0.04-s. (c) Time = 0.06-s.

(d) Time = 0.08-s. (e) Time = 0.1-s.

Figure 125. Pictures of Mat 58 (ERODS=0.1) subfloor model deformation.

Once again, the predicted behavior is not truly representative of the damage seen during the test, though this model (Mat 58 with ERODS=0.1) comes as close as any subfloor simulation that was executed. Part of the explanation is that neither the Mat 54 or Mat 58 models were setup to capture debonding or delamination. One of the first events that occurred during the test is that the T-stiffeners debonded from the base skin. These parts were almost completely undamaged, as they popped off of the subfloor. Other localized areas of delamination were noted. In general, the effect of debonding and delamination is to lower the stiffness of the structure in either a global or localized manner. For example, the loss of the T-stiffeners reduced the overall longitudinal stiffness of the subfloor, while delaminations reduce the stiffness and strength of parts in the localized region where they occur. While T-stiffener debonding could be simulated fairly easily through model modifications, it is a much more challenging task to prepare the model to accurately represent the location and amount of delamination. Note that stiffener debonding simulations were not attempted due to constraints on time and resources.

4.5.4 Multi-Dimensional Model Calibration

One of the research areas pursued under the SRW Rotorcraft Crashworthiness program has been multi-dimensional model calibration [28-31]. The process of model calibration involves reconciling differences between test and analysis. Most calibration efforts combine both heuristics and quantitative methods to assess model deficiencies, to consider uncertainty, to evaluate parameter importance, and to compute required model changes. Calibration of large structural models presents particular challenges because the computational burden limits the number of solutions obtainable in a timely manner. Oftentimes, efforts are focused on predicting responses at critical locations as opposed to assessing the overall adequacy of the model. As documented in this report thus far, calibration efforts typically rely on scalar deterministic metrics, such as test-analysis comparison of acceleration-, velocity-, and displacement-time history responses.

Multi-dimensional calibration of the subfloor model concentrated in two areas: 1) processing of photogrammetric images to augment the number of evaluation points for model calibration, and 2) conducting parametric studies of the LS-DYNA subfloor model. As a reminder, all accelerometer data from the test were lost, as well as the photogrammetric data from the camera covering the open side of the subfloor. Consequently, only photogrammetric data from cameras viewing the base skinned side of the subfloor were collected. As noted previously, Mat 58 pre-test simulations grossly under predicted the vertical crushing of the impact mass and the amount of damage seen in the test. Consequently, this model was a prime candidate for application of multi-dimensional model calibration.

One complication with calibration efforts of nonlinear models in general is the lack of universally accepted metrics to judge model adequacy. References 32 and 33 are two noteworthy efforts that provide users with metrics to evaluate nonlinear time histories. However, these metrics are seldom used to assess model adequacy. In addition, the metrics, as stated in References 32 and 33, do not consider the multi-dimensional aspect of the problem explicitly. A more suitable metric for multi-dimensional calibration used in the present work exploits the concept of impact shapes, as proposed in Reference 34 and demonstrated in Reference 35. The approach used to perform subfloor model calibration focused on parameter uncertainty propagation and quantification.

For calibration purposes, certain parameters are assumed to be uncertain and are arbitrarily assigned a uniform distribution function. This uncertainty model is used to create a family of *N* equally probable parameter vectors, where *N* is arbitrarily selected. The analyst needs to know the probability of being able to reconcile measured data with predictions, given a particular model for the structure and parameter uncertainty. To this end, let $Q(t,p) = \|v(t,p)\|_2$ be a scalar time varying function, in which the response vector *v* is used to compute the 2-norm at time *t*, using parameter vector *p*. Furthermore, let $\underline{\sigma} = min_{\forall p} Q(t,p)$be the minimum value over all parameter variations, and let $\overline{\sigma} = max_{\forall p} Q(t,p)$ be the maximum value. Using these definitions and *N* LS-DYNA solutions corresponding to equally probable parameter vectors, a calibration metric is established to bound the probability of predicting different values of $Q(t,p)$ as;

$$M_1(t) = Prob\left(\underline{\sigma} < Q(t) < \overline{\sigma}\right) \gg \frac{N-1}{N} \tag{1}$$

A corollary to this probability statement indicates that the probability of the model to explain experimental observations $Q_e(t)$ (in terms of 2-norm of responses) outside the analysis range is that less than 1/*N*. Note that *N* controls the tightness of the bounds and also the number of LS-DYNA solutions required.

The use of norms, although convenient, tends to hide the spatial relationships that exist between responses at different locations in the model. In order to study this spatial multi-dimensional dependency explicitly, a different metric must be established.

Spatial multi-dimensional dependency of models has been studied in classical linear dynamic problems in terms of mode shapes or eigenvectors resulting from a solution to an eigenvalue problem. An efficient and compact way to study the spatial relationship is by using a set of orthogonal basis vectors. These basis vectors, referred to as impact shapes, are computed by decomposing the time histories using singular value decomposition (SVD). For example, time histories from analyses and experiments are decomposed using SVD as:

$$y(x,t) = \sum_{i=1}^{n} \sigma_i \varphi_i g_i(t) \tag{2}$$

In this form, the impact shape vector φ_i sized *m* x 1, contains the spatial distribution information for *m* sensors, *g*(t) contains the time modulation information, σ contains scalar values with shape participation factors, and *n* is the number of impact shapes to be included in the decomposition, often truncated based on allowable reconstruction error. Although Eq. (2) is written in continuous time form, for most applications, time is sampled at fixed intervals such that $t = k\Delta T$ where the integer k=0,…,L and $\Delta T$is the sample time. From Eq.(2), the fractional contribution of the i^{th} impact shape to the total response is proportional to δ_i, defined as:

$$\delta_i = \sigma_i / \sum_{i=1}^{n} \sigma_i \tag{3}$$

Similar to the approach used in classical dynamic problems, impact shapes can now be used to compare models using orthogonality. Orthogonality, computed as the dot product operation of vectors (or matrices), quantifies the similarities or projection between two vectors. If the projection is zero, vectors are orthogonal, i.e., dissimilar. This same idea applies when

comparing test and analysis impact shapes. Numerically, the orthogonality metric is computed as:

$$M_2 = \breve{\Phi}^T \breve{\Psi} \tag{4}$$

where $\breve{\Phi}$ is sized *m* x *l* with *l* impact shapes at *m* locations computed from test data and $\breve{\Psi}$, sized *m* x *l*, are shapes computed using simulation data. Note that both $\breve{\Phi}$ and $\breve{\Psi}$ are normalized matrices such that $\breve{\Phi}^T \breve{\Phi} = I$ and $\breve{\Psi}^T \breve{\Psi} = I$, where I is the identity matrix. Because individual impact shape vectors are stacked column-wise, metric M_2 is a matrix sized *l* x *l* with diagonal values corresponding to the vector projection numerical value. If vectors are identical then their projection equals 1. Consequently, when evaluating models, multi-dimensional closeness with experiment is judged based on similarity of impact shapes and shape contributions. Application of multi-dimensional calibration techniques to the subfloor is discussed next.

Based on previous efforts, it was concluded that using a limited number of target points (25 targets) from photogrammetry was not sufficient to understand the behavior of the subfloor. Because the entire back panel of the subfloor was measured using photogrammetry, a task was undertaken to process the images to produce a large subset of measured points. This process evaluated images and removed targets that were not in all images throughout the time span needed, transformed the photogrammetric data into the LS-DYNA coordinate system, conducted interpolation of time histories to correct for anomalies due to photogrammetric drop-outs, and mapped the resulting target displacements to nodes in the LS-DYNA model. A y-z grid overlay is shown in Figure 126 of the subfloor back panel photogrammetry targets (dot-blue) versus LS-DYNA evaluation nodes in (+ red). The algorithm to map targets to LS-DYNA nodes only kept photogrammetric targets within 1 inch of LS-DYNA node locations. Voids in the images showed up as white spaces in Figure 126. After the mapping process was completed, the photogrammetric displacement time histories had to be screened for anomalies manually. When the processing was completed, 3.6-ms of data was retained for 214 targets. This expanded data set allowed for a significantly better understanding of the panel behavior.

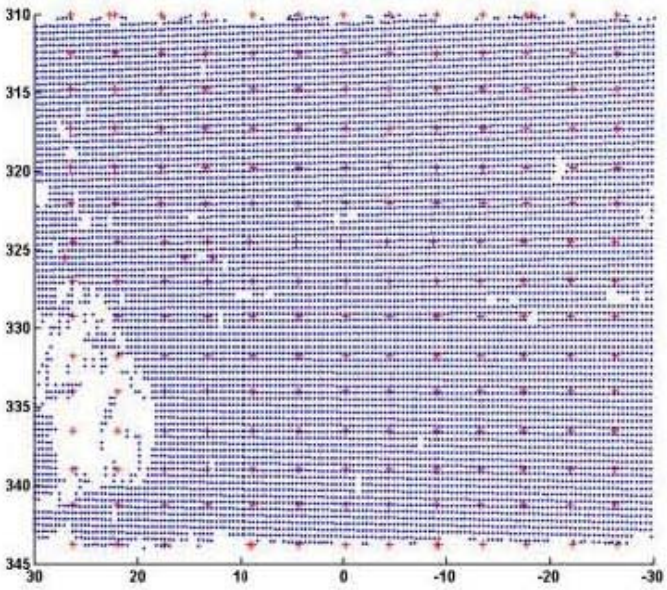

Figure 126. Photogrammetric targets and LS-DYNA evaluation nodes.

With the expanded photogrammetric data set at hand, calibration of the subfloor model proceeded by conducting parametric studies of the subfloor model to determine parameters to reconcile model with test. As discussed previously, this process uses bounds of the subfloor displacement response as a metric to assess the ability to reconcile the model. Many parametric studies were completed to evaluate the effect of varying thicknesses of several components, impact angles, and longitudinal/transverse modulus. The latest set of parameters, shown in Table 7, included thicknesses of various parts, longitudinal and transverse moduli, and the pitch angle. These parameters are assumed to be equally valid within the bounds defined in the table. Combinations of these parameters were used to conduct 40 LS-DYNA runs, using Mat 58 baseline material properties for unidirectional graphite tape. For each LS-DYNA run, the displacement magnitude norm was computed for the 214 targets matched from the photogrammetric data. The upper and lower displacement bounds are shown in Figure 127 from 40 LS-DYNA runs (dashed blue) plotted along with the displacement magnitude computed from photogrammetric data (solid red). For regions where the analysis bounds encompass the test there is a probability greater than 1/40 that a parameter set exists that would reconcile test with analysis. However, finding such set is a very difficult task that requires optimization.

Table 7. Parameters Used in Uncertainty Studies of the Subfloor Model.

Variable Number	Parameter Description	Nominal Value	Lower Bound	Upper Bound	Calibrated Value
1	EA (psi)	19,000,000	14,000,000	19,000,000	17,792,075.6
2	EB and EC (psi)	1,400,000	840,000	1,400,000	1,042,798.33
3	Thickness of beam cap and T-stiffener (in.)	0.006	0.004	0.007	0.004
4	Thickness of beam web, frame (in.)	0.006	0.004	0.007	0.006
5	Pitch angle, (degree)	0	-0.8	-0.3	-0.7

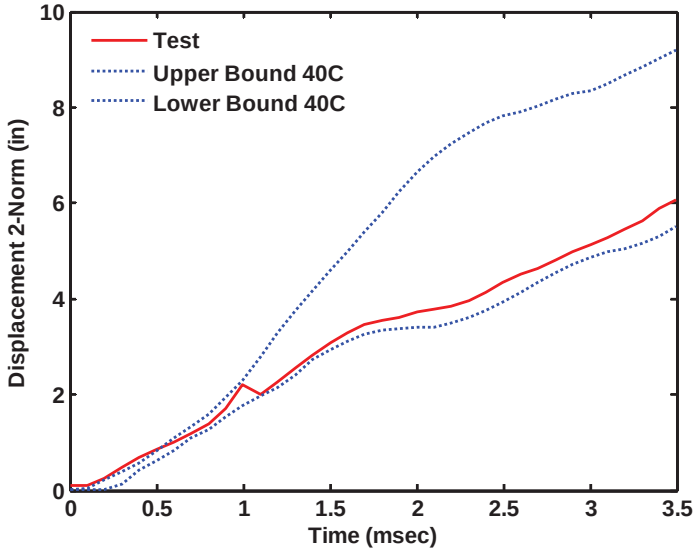

Figure 127. Displacement bounds metric M_2 from 40 LS-DYNA runs and photogrammetric test data.

To evaluate metric M_2 for the subfloor, the orthogonality is computed based on the magnitude-normalized impact shape vectors from test and analysis. For the subfloor problem, each impact shape vector is sized 642 x 1, which corresponds to data from 214 target locations in 3 directions. Orthogonality values computed for the first 10 impact shapes for both test and the nominal model are shown in Figure 128. Along the abscissa are values corresponding to test impact shapes, top labels are the individual shape contribution to the response, whereas the ordinate shows the corresponding predicted analysis contribution. The numerical values for the colors used are shown on the color bar to the right with the highest orthogonality value less than 0.6. For the case shown, the 1st impact shape predicted using LS-DYNA explains 58% of the data whereas for test, the 1st impact shape explains 45%. Although the orthogonality values are low, these results are significantly better than previous results. In particular, with the addition of more photogrammetric targets the dominant impact shape appears first in both LS-DYNA and test. The next step in the calibration process is to use optimization.

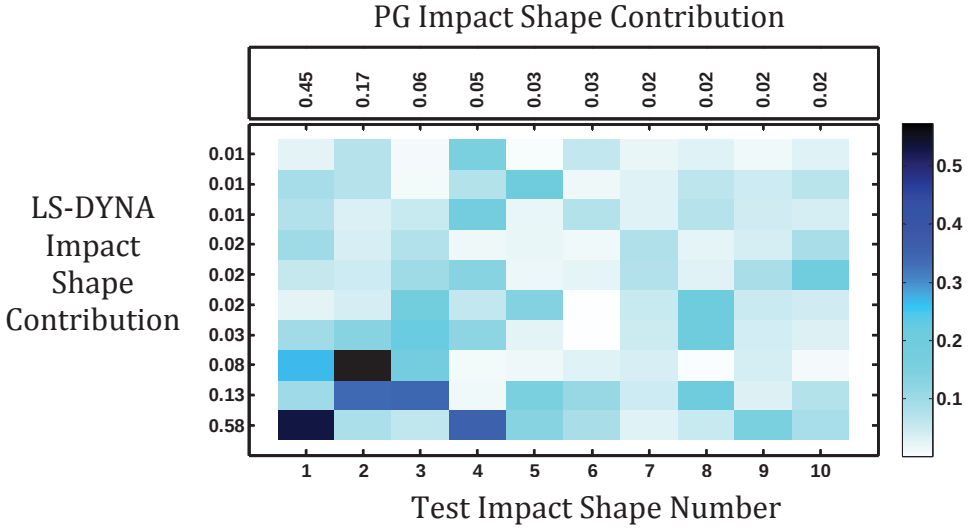

Figure 128. Orthogonality of impact shapes from the PG data and the Mat 58 model using the baseline parameter set.

Before proceeding with the optimization, it is important to understand and quantify the contribution from each parameter to the displacement variance. To judge parameter importance, a sensitivity analysis was conducted, using a variance-based approach, which produced the results shown in Figure 129. Parameter variance contributions are shown at each time step for 3-ms of simulation. Parameters labeled P1-P5 in Figure 129 correspond to those listed in Table 7. At each time, the sum total of the parameter variance contribution adds up to a value near 1. From Figure 129, note that P5 (pitch angle) had the highest contribution to the variance followed by the longitudinal modulus EA.

Optimization of the subfloor model proceeded by using the five parameters in Table 7 to search for a reconciling solution. The optimizer sought to minimize the prediction error between displacements from LS-DYNA and test. Because execution time of LS-DYNA models is large, the optimizer was only allowed to compute 25 additional runs. Parameters for the best solution

are also listed in Table 7. In addition, a comparison of the norm magnitude using calibrated model parameters versus test is plotted in Figure 130. Although a region still exists where the calibrated model over predicts the measured values, results are significantly better than when using the baseline parameters. Note that the norm values for the 214 targets compared indicate that the largest error within the first 3-ms is less than 1-in., which is the maximum difference between the curves shown in Figure 130. On the other hand, the orthogonality of the impact shapes using the calibrated parameter set is shown in Figure 131. When compared to Figure 128, orthogonality values are higher for the dominant impact shapes. Furthermore, the 1st impact shape from LS-DYNA explains 50% of the response as compared to 45% from test, as shown in Figure 131.

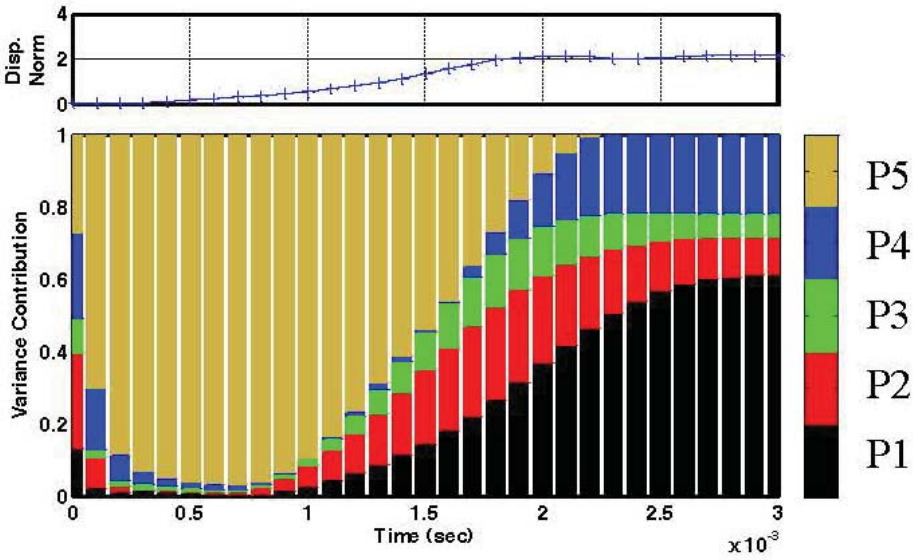

Figure 129. Sensitivity analysis of the subfloor model.

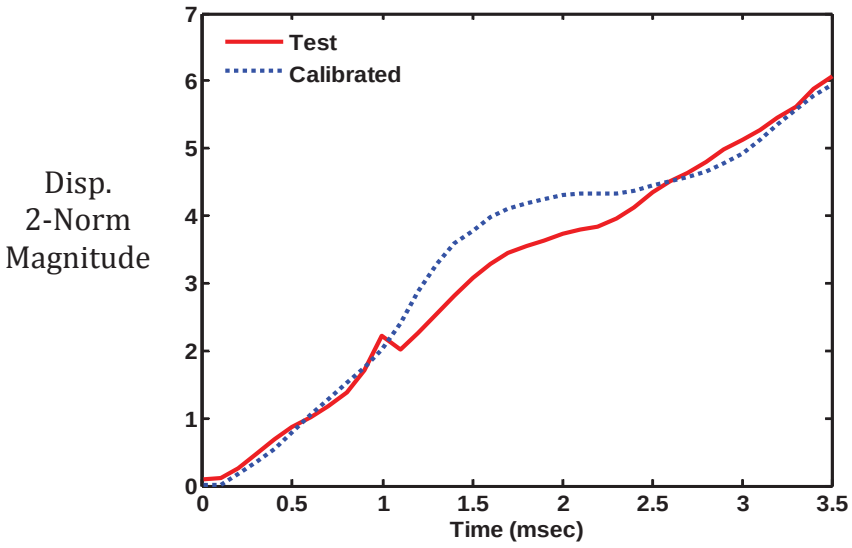

Figure 130. Norm magnitude comparison of test versus calibrated model.

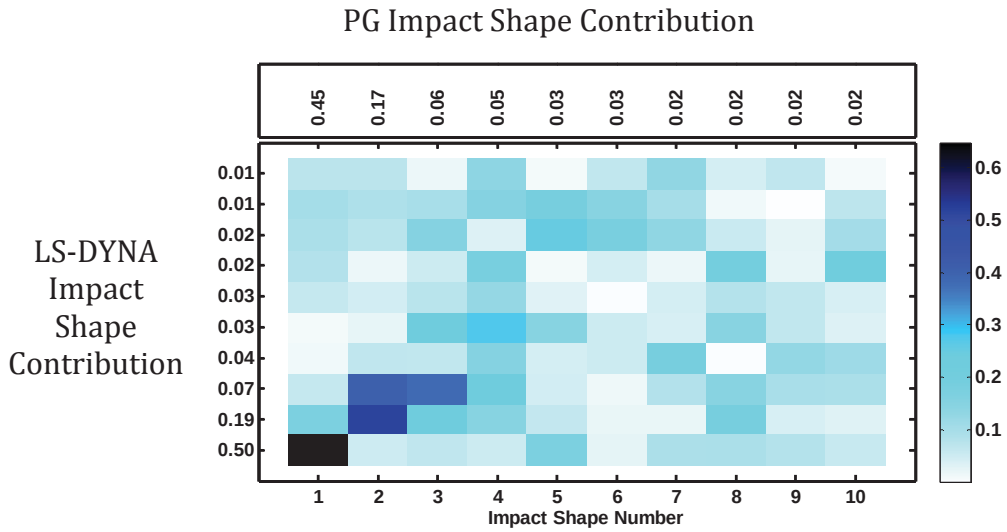

Figure 131. Orthogonality of impact shapes from photogrammetry and LS-DYNA model data using calibrated parameter set.

4.6 Simulation of a Framed Fuselage Section

4.6.1 Description of the Finite Element Model

Sikorsky provided an updated 2-frame fuselage model to NASA in September 2012 that is illustrated in Figure 132. Although some of the test article was constructed of unidirectional tape, the primary material used for construction of the framed fuselage sections and subfloor was a plain weave thermoset graphite fabric. The finite element model consisted of two frames plus associated skin and beam structure in the upper and lower frame sections. The actual section was cut from the forward end of the post-test SARAP TVA that was drop tested at NASA Langley in 2008 (see Figure 2).

Sixty-nine PART_COMPOSITE cards were used to define the layer-by-layer thickness, orientation, and material assigned to plies within each composite laminate in the model. Some of the composite layups had over 100 plies. The light green solid volume attached to the top of the upper fuselage structure is intended to simulate the entirety of the upper loading mass (~5100 lbs.) and facility hardware (portal frame). This part was originally connected to the upper fuselage structure using CONTACT_TIEBREAK_SURFACE_TO_SURFACE. The empty weight of the fuselage was 368 pounds. An illustration is provided in Figure 133 showing the individual parts that are assigned to the material models (unidirectional tape and fabric) used in the framed fuselage section.

In order to securely attach the fuselage structure to the portal frame, aluminum blocks were machined to fit the contour of the upper surface along the front and rear cross member. These aluminum fixtures are shown in Figure 134 prior to and during the bonding process. High-strength adhesive was used as the bonding agent. Due to the existence of the Hy-Lok fasteners protruding from the top of the fuselage structure a series of spot-face reliefs (holes) were made in the aluminum beams to accommodate the rivet heads. These reliefs were intended to provide for

a more direct contact path between the aluminum assembly and the fuselage structure. Images of the raised fasteners and spot-face reliefs are shown in Figures 135(a) and (b), respectively.

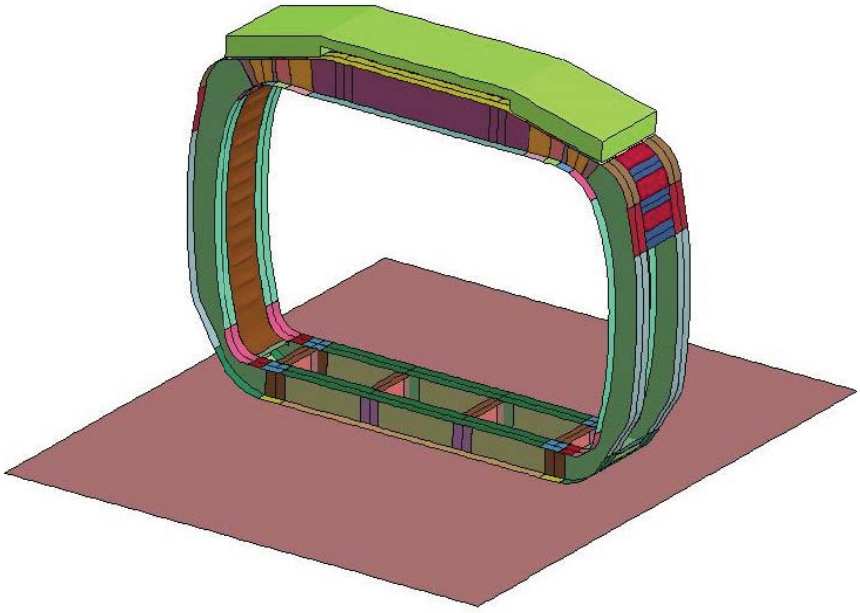

Figure 132. Sikorsky two-frame fuselage model with impact plane.

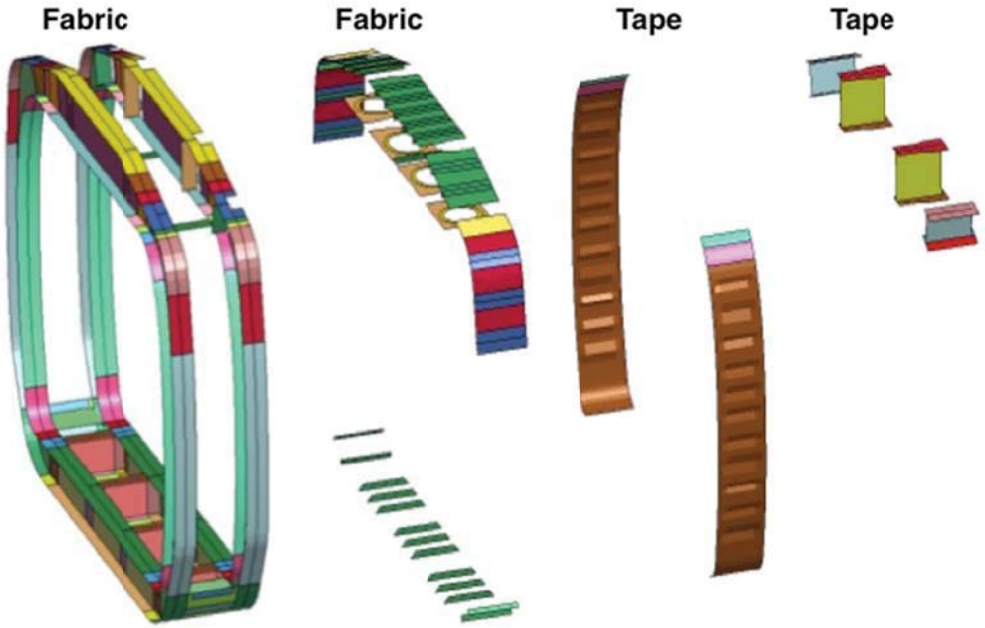

Figure 133. Sikorsky two-frame fuselage model separated by material type.

Once the actual attachment hardware was constructed, the upper ballast mass was removed from the original Sikorsky finite element model and replaced with a more appropriate geometry. The revised geometry better reflected the current upper mass configuration of the test article and included increased height and line-on-line matching of the upper fuselage section profile. This approach provided a convenient means to use shared nodes between the fuselage section and the

ballast mass (see Figure 136) as opposed to tied-contact definitions. Four lead masses of approximately 100 pounds each were added to the floor and the volumes were discretized using solid elements. These lead weights are shown in Figure 137. By removing the contact definitions between the upper mass and the roof, and between the lead blocks and the floor, noisy chatter due to contact was reduced. The upper mass shown in Figure 136 represents the mass of the drop portal frame plus attachment hardware.

Figure 134. Photographs of aluminum blocks used to properly orient the upper mass on the fuselage section.

(a) Raised fasteners. (b) Spot face reliefs.

Figure 135. Photographs of raised fasteners and spot face reliefs.

A substantial number of Hy-Lok fasteners were used in the fuselage. The mass of these fasteners was missing from the original simulation model as delivered by Sikorsky. A discrepancy between the weight of the fuselage section and the model was determined when the physical test hardware was weighed. The test article was found to be approximately 70-lb heavier than the analytical model. Consequently, the missing 70-lb mass was included in the model as 2,200 lumped masses representing the Hy-Lok fasteners at nodes corresponding approximately to each fastener location. Two images of the fuselage structure and Hy-Lok fasteners are shown in Figure 138, along with corresponding images of the fuselage simulation model and the spatial

location of the added fastener masses. As shown, the locations are not exact but the nodal spacing in the simulation model provides for adequate mass placement.

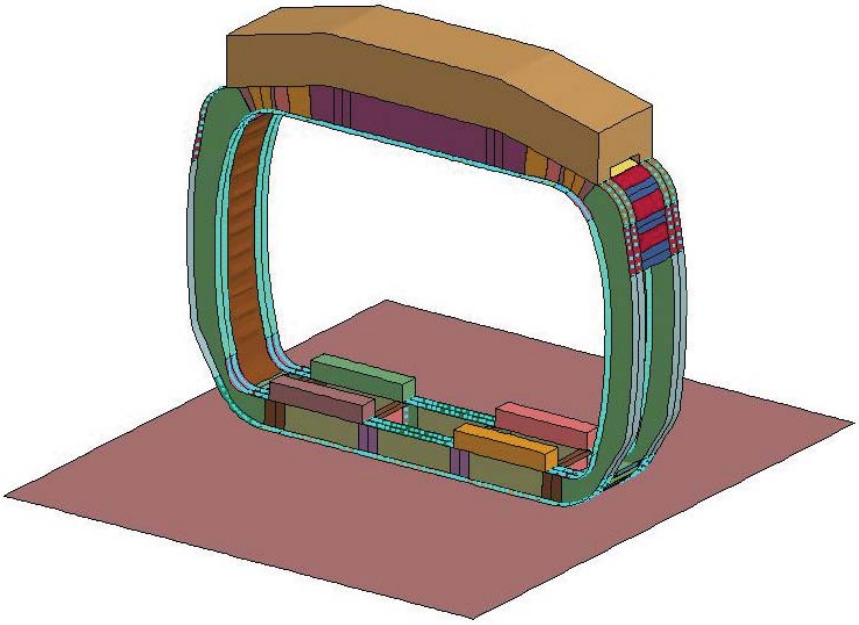

Figure 136. Revised fuselage model updated with 4 lead blocks on the floor plus a modified upper loading mass that correctly represents the upper mass and contact area of the test article.

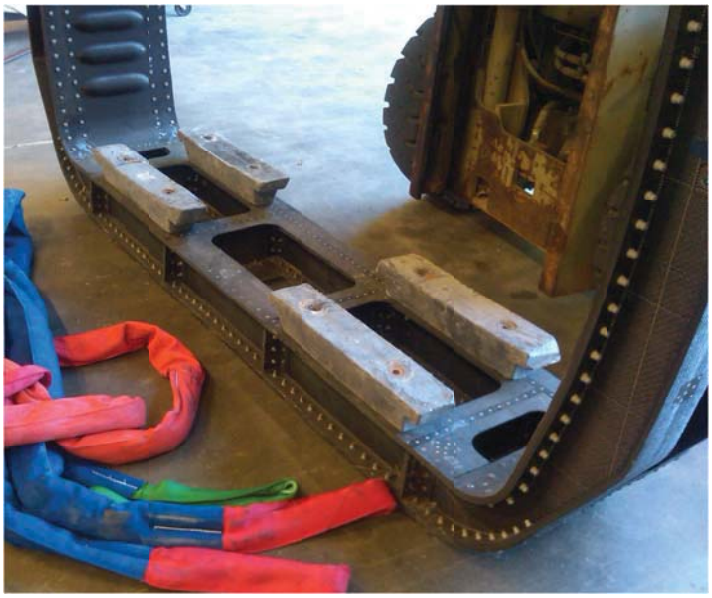

Figure 137. Photograph of the lead masses added to the floor of the fuselage section.

The revised simulation model contained: 37,111 nodes; 17,216 Belytschko-Tsay (ELFORM = Type 2) shell elements; 8,300 solid elements; and 2,200 concentrated masses. The nominal element edge length varied between 0.5- and 1.0-in. One SPC was defined to fully constrain the nodes used in the model to represent the impact surface. An automatic single surface contact was specified. Pre-test predictions were made with the revised LS-DYNA model shown in

Figure 136 using Mat 54 or Mat 58 properties for the composite unidirectional tape and fabric layups. A perfectly flat impact was assumed. Gravity loading and an initial velocity of 21-ft/s (252-in/s) were applied. The model was executed for a termination time of 0.12-seconds, which required 10 hours and 15 minutes of CPU to execute to normal completion on a Linux-based workstation computer with four processors, running LS-DYNA SMP version 971 R6.0.0.

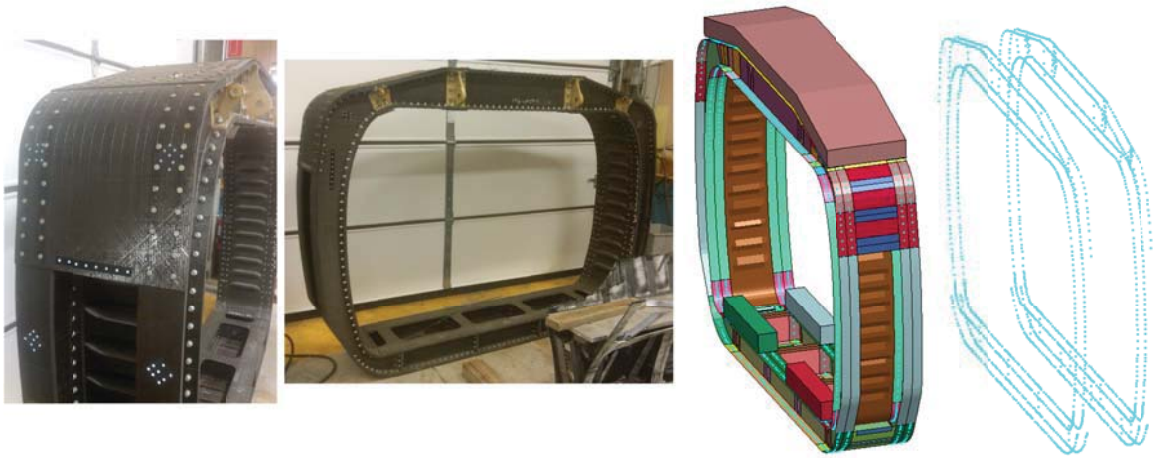

Figure 138. Fastener and nodal mass locations on the framed fuselage section.

4.6.2 Analysis of the Static Load Test Data

The revised fuselage section model with Mat 54 material properties was executed to simulate the static loading conditions, described in Section 3.8.2. The model was executed by applying gravitational loading slowly, over a period of time, in which the magnitude was ramped up from 0- to 1.0-g. The displacement of the upper mass is shown in Figure 139(a). The upper mass moves downward a maximum of 13 mils, whereas photogrammetric data collected during the test indicated about 60 mils. The frequency of the oscillations produced by applying the gravitational loading is about 31-Hz. This frequency is close to the value found in vibration testing to be a fundamental mode. However, the displacement is not well predicted and indicates that the model is too stiff.

As a result of the poor level of correlation, the photogrammetric data from the static test was re-analyzed by processing the images to map targets to LS-DYNA nodes. From the data collected, it was apparent that the geometry recovered by photogrammetry for the un-deformed fuselage was tilted about 0.5 degrees from the vertical y-z plane in LS-DYNA. Consequently, to line up the targets with the LS-DYNA nodes, the photogrammetric data was rotated about the reference coordinate system origin at the bottom of the fuselage by 0.5 degrees. After this rotation, a search algorithm was used to find photogrammetric targets that corresponded to nodes in the LS-DYNA model. A target was said to coincide with a node if it was within a 1-inch radius. This process successfully mapped 539 photogrammetric targets to LS-DYNA nodes, while rejecting 21,483 targets. A side-view of the 539 photogrammetric targets un-deformed (red circles), the locations of the photogrammetric targets under static load (green squares), and the LS-DYNA un-deformed geometry (blue cross) are shown in Figure 139(b).

Comparing the deformed with the un-deformed initial geometry, it was apparent that the fuselage motion under a static load was primarily a rotation of the entire fuselage about the y-axis. As

noted previously, a strip of material was discovered on the bottom of the fuselage section that was located on one side only. This extra material caused asymmetry of the fuselage section and may have contributed to the rigid body rotation observed in the static test results. From the data, the rotation angle was computed to be 0.44 degrees. If, in fact, the measured deformation was due to rigid body rotation, the elongation computed between any two points on the fuselage should be within the photogrammetric variability. To evaluate the amount of fuselage elongation, all 539 targets were used to compute elongation values between any two points. From the photogrammetric data, the mean elongation value across any two pair of targets was 0.0184-inches and the maximum value was 0.0635-inches. Because no rotation of the fuselage under static load was predicted, it is suspected that differences in the boundary conditions between test and analysis caused the fuselage to rotate. In particular, if the fuselage was loaded while initially tilted, as the photogrammetric data seems to suggest, a static load would cause an additional rotation. Without further analysis, data from the static test cannot be used to estimate fuselage stiffness. As a result, the static test was not simulated using the Mat 58 material model.

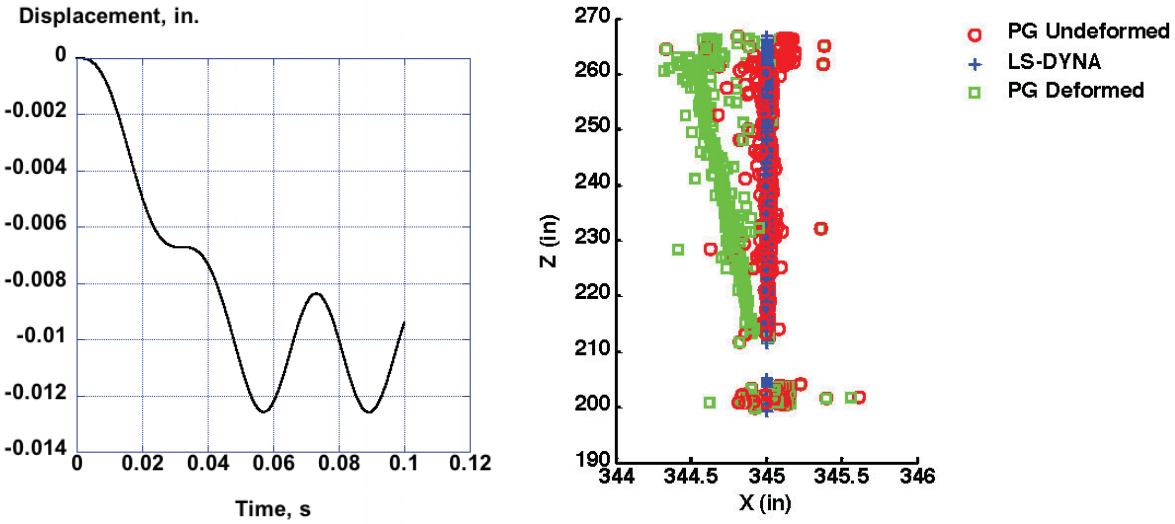

(a) Predicted displacement. (b) Side view of PG data.

Figure 139. Mat 54 predicted displacement of the upper portal mass for a slowly applied gravity loading and side view of photogrammetric data from the static test.

4.6.3 Comparison of Modal Test Results with Analysis

As described in Section 3.8.1, modal vibration tests were performed on the fuselage section prior to impact testing. Test-analysis results are shown in Figure 140 as orthogonality between the identified vibration mode shapes and the LS-DYNA predicted mode shapes. Readers should note that although orthogonality is used again, in this case the model comparisons are in terms of vibration modes and not impact shapes, as described earlier. This comparison is a validation of the linear behavior of the fuselage when using Mat 58 material properties. No results for Mat 54 are shown. Listed along the ordinate of Figure 140 are the frequencies for the identified modes and along the top abscissa are the predicted frequencies using the baseline model parameters. Circled in red are the two target modes based on pre-test predictions. All orthogonality results are weighted using the reduced mass matrix *M* such that the orthogonality matrix is computed as $O = \Phi_d^T M \Phi_t$, where $\Phi_d$are the mode shapes from an explicit solution from LS-DYNA and Φ_t are the mode shapes from the modal test. Pairing of test and analysis modes was done based on

orthogonality values (e.g. modes with orthogonality values near 1 are similar). In some cases, a single analytical mode matched several experimental modes. This finding is often due to too small a sensor count or problems with the data processing. For this case, if an analysis mode is paired to an identified mode(s), the analytical mode exists but perhaps was not well identified.

As shown in Figure 140, the first analysis target mode at 73-Hz appears to be similar (i.e. high orthogonality value) to identified modes 39.32- and 39.78-Hz. Furthermore, the LS-DYNA predicted mode at 408-Hz appears to be similar to identified modes in the 220-230-Hz range. Similarly, the second target mode at 144-Hz appears to be similar to an identified mode at 74.5-Hz. Based on these results, it should be clear that the LS-DYNA model is consistently over-predicting the frequencies of the fuselage vibration modes and therefore changes to the model should seek to reduce all predicted frequencies. One obvious choice to reduce the model frequencies is to reduce the modulus of the material.

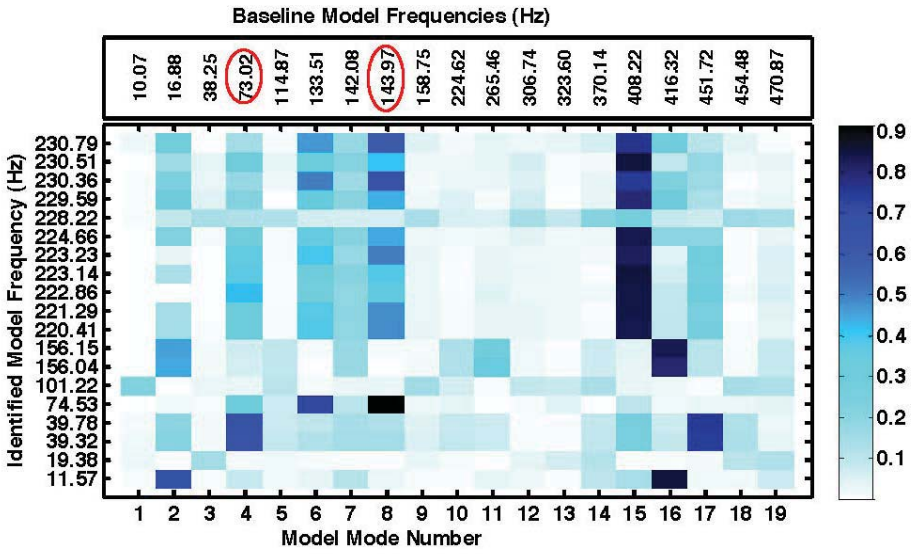

Figure 140. Orthogonality of test versus LS-DYNA predicted modes.

Because the second target mode had the highest orthogonality value, it was used as a reference to estimate changes required to get the frequencies to agree. Specifically, to get a frequency reduction from 144- to 74.5-Hz (~ 52%) one would need to reduce the modulus to about 27% of its original value. To test this assumption, the Mat 58 unidirectional tape and fabric material properties EA, EB, GAB, GBC, and GCA were all adjusted accordingly based on the required values. The orthogonality results using modes predicted with the updated LS-DYNA model versus test are shown in Figure 141. With this modulus adjustment, the first analysis target mode is now at 43.4-Hz as compared to the measured modes in the 39.32- to 39.78-Hz range. Similarly, the second target mode is now at 80.3-Hz as compared to a measured mode at 74.5-Hz. Interestingly, the LS-DYNA mode at 230.9-Hz appears to be similar to modes in the 220- to 230-Hz range. Consequently, a modulus reduction as initially suggested will greatly improve frequency agreement not only for the target modes but also for other system modes. Certainly, the modulus can be tweaked again to get a better frequency matching; however, that was not the objective of this exercise. Although the orthogonality values with the reduced stiffness are

slightly smaller than those from the baseline model, frequency agreement is significantly better and thus provides a good starting point for model calibration.

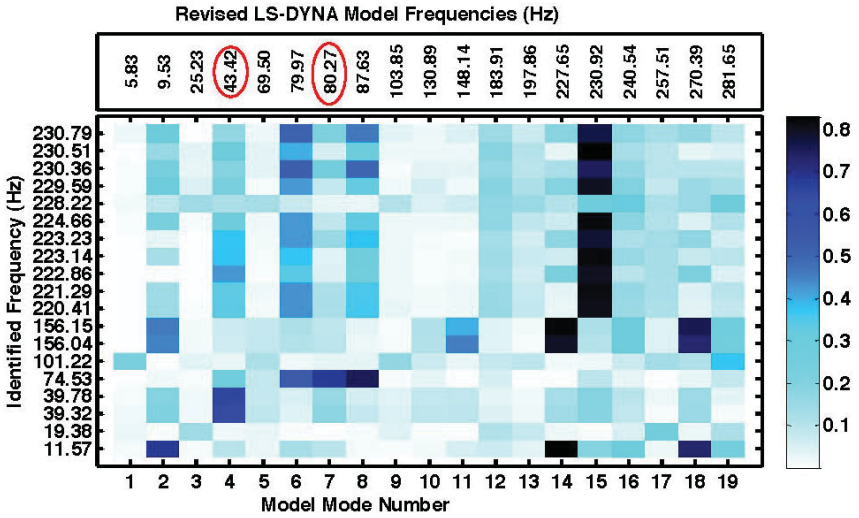

Figure 141. Orthogonality of test versus updated LS-DYNA predicted results.

4.6.4 Mat 54 Predicted Responses Compared with Impact Test Data

The Mat 54 predicted acceleration of a typical node on the upper mass, shown in Figure 142(a), exhibits very high amplitude, high-frequency oscillations even when filtered with a 300-Hz low-pass Butterworth filter. The acceleration response from an accelerometer located on the portal is plotted in Figure 142(a) for comparison. The magnitudes of the initial peaks are comparable. Likewise, the Mat 54 predicted acceleration of a node located on a 100-lb lead block is shown in Figure 142(b) along with data from an accelerometer mounted to the floor mass. The simulation overpredicts the magnitude of the initial peak acceleration; however generally good agreement is shown after the initial peak.

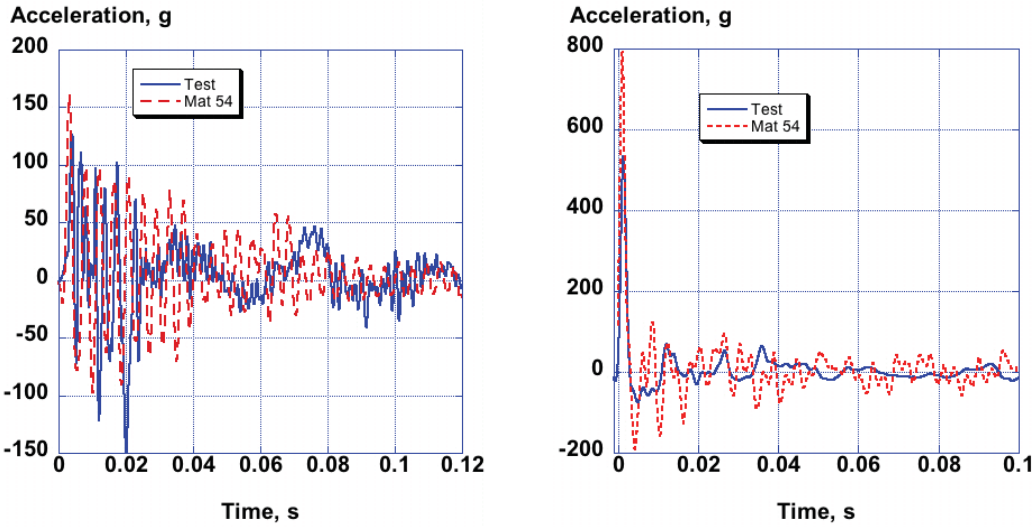

(a) Upper mass. (b) Lead block.

Figure 142. Comparisons of predicted accelaration responses of the upper loading frame mass and a floor-mounted lead block from the Mat 54 fuselage section model with test.

The velocity and displacement curves are much easier to compare as low-pass filtering is not required. The velocity response obtained by integrating the acceleration data from an accelerometer mounted on the upper mass is compared with the computed velocity from the Mat 54 simulation in Figure 143(a). Unfortunately, the integrated velocity is hard to interpret as a small drift or offset in acceleration can produce a very large difference in the integrated response. Consequently, it is instructive to compare with velocity that is obtained by differentiating full-field photogrammetric displacement data. However, since differentiation of digital data can produce large oscillations, it is best to smooth the curve before differentiating. A comparison of the predicted velocity from the Mat 54 fuselage section model with differentiated photogrammetric displacement data (velocity) is shown in Figure 143(b). In general, the Mat 54 predicted velocity response agrees well with the test data and tends to fair through the test ocsillations. Note that the analysis was conducted to 0.12-seconds termination time.

The static displacement of the portal frame was measured post-test to be approximately 7.25 inches. As illustrated in Figure 144, the Mat 54 model predicted that the maximum dynamic displacement of the portal was slightly over 8.5 inches. A possible explanation for the difference is that there was likely some rebound of the portal from the maximum. In addition, the rollers may have bound slightly causing energy loss. However, the results shown in Figure 144 indicate that the model was more flexible and weaker than the test article.

Finally, some qualitative assessments can be performed by comparing photographs and motion picture analysis with predictions of model kinematic behavior. A photograph that was captured from a high-speed video is shown in Figure 145(a). This picture shows the rebound of the floor section after it had completely broken loose from the fuselage. The Mat 54 predicted fuselage damage at a time slightly over 100-ms after impact is shown in Figure 145(b). The kinematic motion ans structural deformations of the test and analysis are nearly identical.

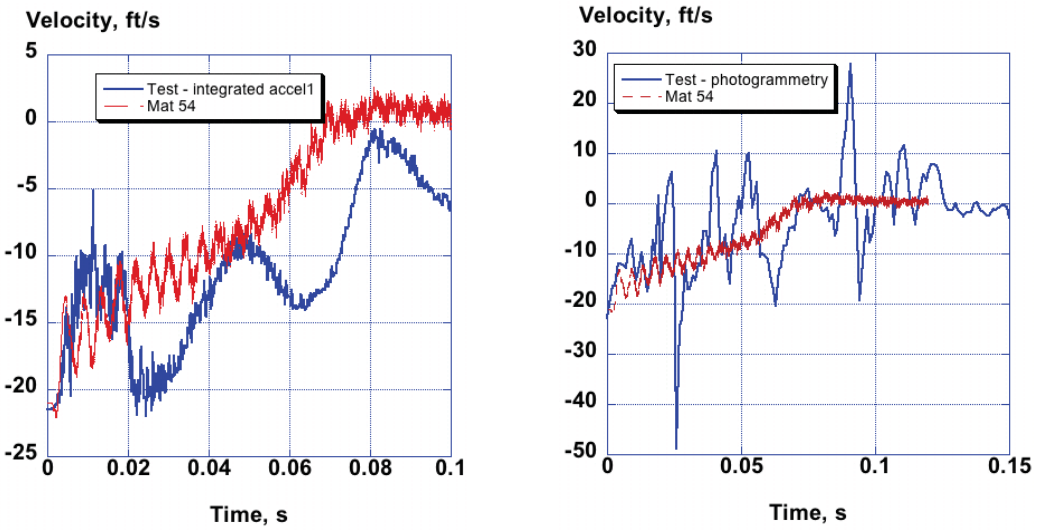

(a) Data from integrated accelerometer. (b) Data from differentiated photogrammetry.

Figure 143. Comparison of Mat 54 predicted velocity of the upper mass with test data.

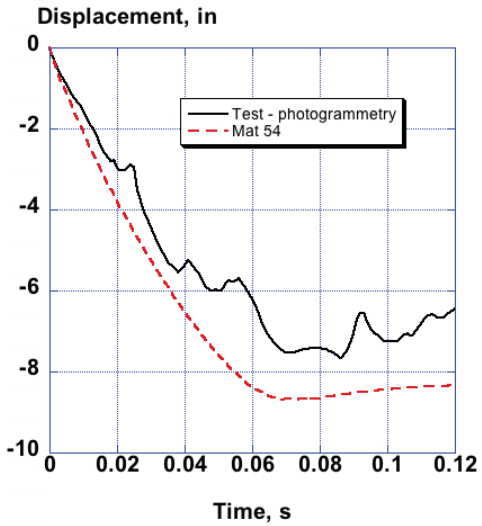

Figure 144. Mat 54 predicted time history of the displacement of the upper mass test portal.

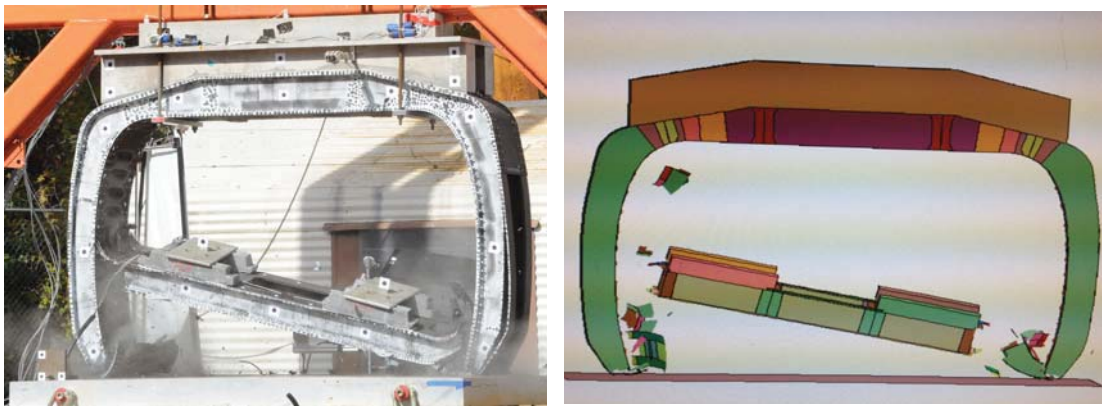

(a) Film-capture photo. (b) Mat 54 model prediction.

Figure 145. Test and analysis deformations of the fuselage section at time=0.1-s.

4.6.5 Mat 58 Predicted Responses Compared with Impact Test Data

The fuselage section model, shown in Figure 136, was modified by changing the unidirectional tape and fabric material properties from Mat 54 to Mat 58, and the model was re-executed. A low value of ERODS (0.06) was used in the baseline model for both material types. A picture of the deformed fuselage model at a time of 0.15 seconds after impact is shown in Figure 146(a). This figure shows that the deformation and rebound of the floor closely match the actual test scenario, shown in Figure 146(b).

The maximum displacement of the upper mass predicted by the Mat 58 model with ERODS=0.06 is slightly over 9 inches, which is greater than the displacement of 7.25 inches measured after the test. Consequently, a parametric study was performed to determine the influence of ERODS on the displacement of the upper mass. The results are shown in Figure 147. ERODS was varied from a high of 0.1 to a low of 0.06. The results show that the displacement of the upper mass is bounded by ERODS values of 0.06 and 0.09. The value of 0.075 provided the best match to photogrammetric displacement data. The displacement of the upper mass was measured post-test to be 7.25 inches. However, there is always some rebound

and settling of a structure after an impact. Note that the photogrammetry data was collected from target number 1200, which is shown in Figure 148.

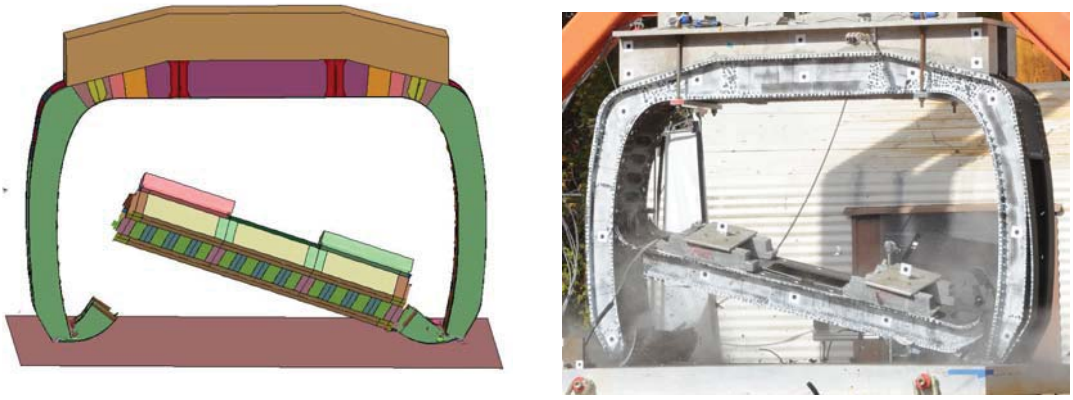

(a) Mat 58 model prediction. (b) Film-capture photograph.

Figure 146. Mat 58 (ERODS=0.06) simulation of the fuselage drop test at a time 0.1 seconds after impact compared with test.

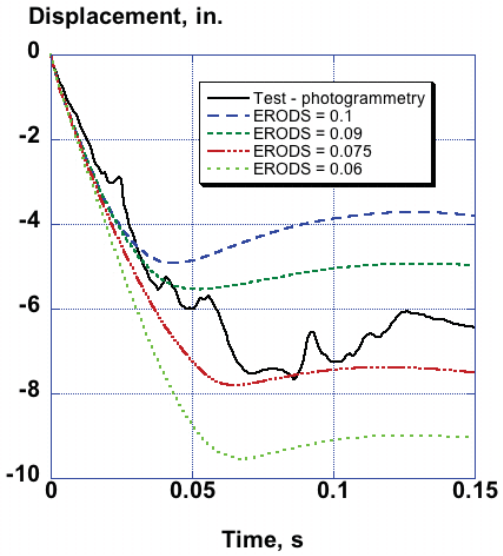

Figure 147. ERODS study on the effect of upper mass displacement versus time.

As a result of the ERODS study, the fuselage model was re-executed in which the only change was to increase ERODS from 0.06 to 0.075. The predicted displacement of the upper mass now agrees better with photogrammetric data, as shown in Figure 149. In addition, comparisons of predicted velocity with test data based on differentiated photogrammetric data and with the integrated accelerometer data are shown in Figures 150(a) and (b), respectively. The differentiated displacement (velocity) response in Figure 150(a) is for the target 1200 shown in Figure 148 at the upper left. Differentiation of the photogrammetric displacement to produce a velocity plot does produce considerable oscillations in the velocity. It is better to first smooth the photogrammetric displacement before differentiating. However, the velocity produced from photogrammetric data analysis is typically more accurate than the velocity produced from integrating accelerometer data due to large offsets or drifts that can occur. An acceleration offset

or drift greatly alters the velocity. The initial acceleration peak is often correct, but offsets can occur shortly afterwards due to damping, filtering, and electronic biases. This problem is illustrated by the comparison of integrated acceleration with photogrammetric velocity in Figure 150 where the integrated acceleration is too low after 0.02-seconds.

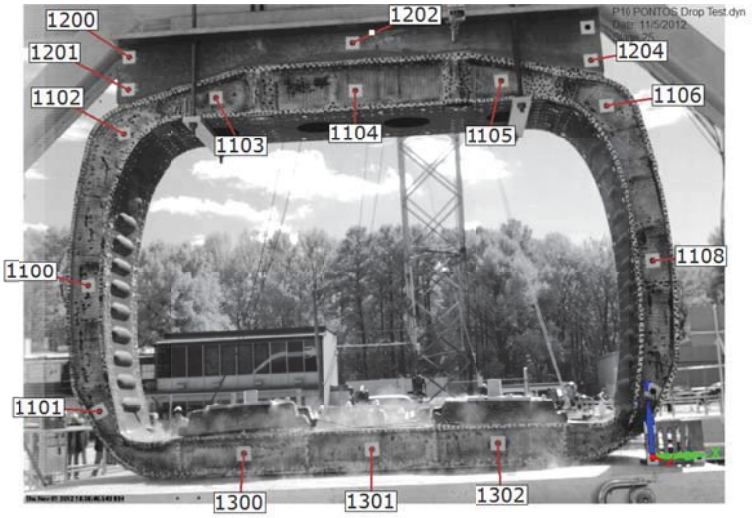

Figure 148. Photogrammetric data was collected for target 1200, shown in the upper left corner.

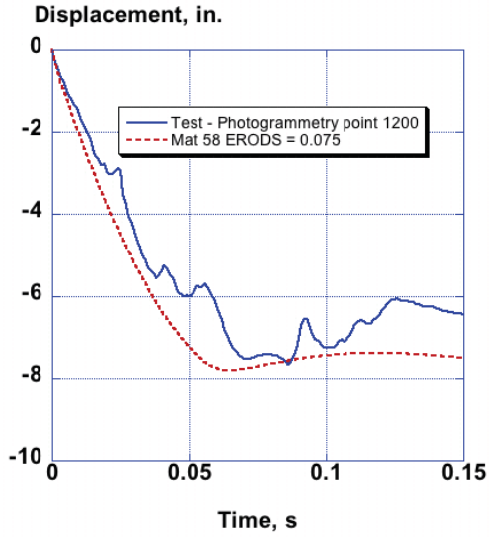

Figure 149. Comparison of upper mass displacement predicted with Mat 58 (ERODS=0.075) with photogrammetry of target 1200.

Although the Mat 58 fuselage model with ERODS=0.075 provided the best agreement with test displacement from the upper mass, the model with ERODS=0.06 showed the best match in predicting model kinematic behavior, including rebound of the floor, as can be seen by comparing Figure 145(b) and Figure 151. These two figures show Mat 58 model deformation at a time of 0.1-s for ERODS=0.06 and 0.075, respectively. In Figure 145(b), there is complete separation of the floor on one side. In Figure 151, neither side of the floor completely broke

free. Note that, since the floor does not completely break away, the amount of rebound for the ERODS=0.075 model is not as great as for the model with ERODS=0.06.

A comparison of Mat 58 (ERODS=0.075) predicted and test acceleration-time histories for the upper mass and for a lead block mounted to the floor are shown in Figures 152(a) and (b), respectively. All acceleration curves were filtered using a 300-Hz Butterworth low-pass filter. As shown in Figure 152(a), the predicted and experimental acceleration responses of the upper mass are highly oscillatory from initial impact through 0.03-s. The Mat 58 simulation slightly over predicted the initial acceleration spike, but generally matched the test response quite well. Likewise, the initial peak acceleration of the lead mass response was slightly over predicted, as shown in Figure 152(b).

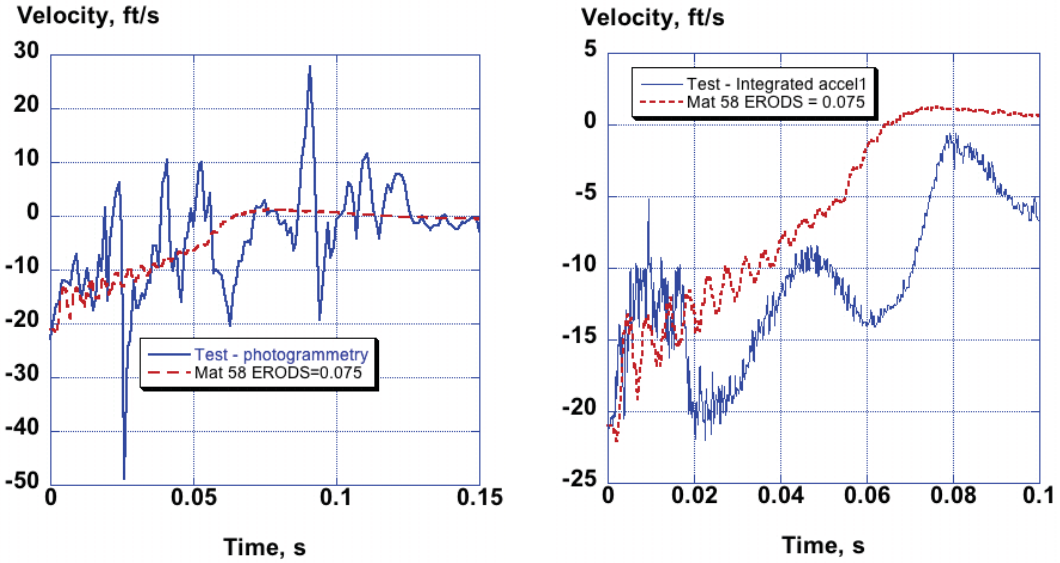

(a) Data from photogrammetry. (b) Data from integrated acceleration.

Figure 150. Test-analysis velocity comparisons.

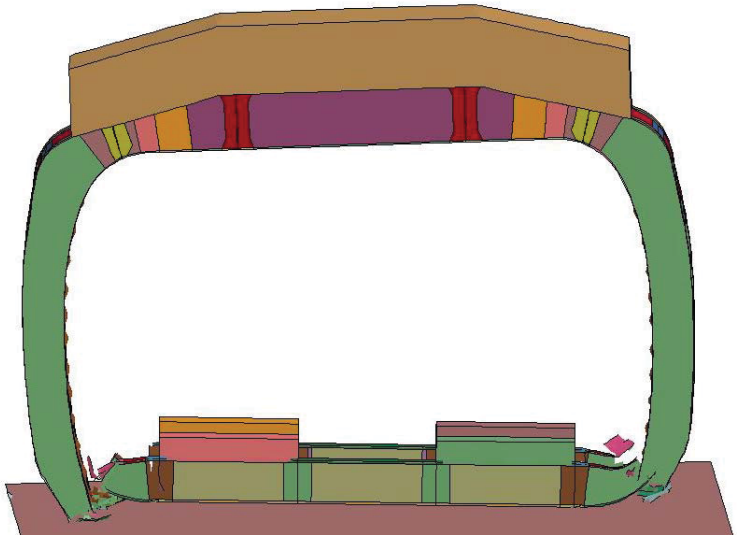

Figure 151. Deformed plot for Mat 58 fuselage model (ERODS=0.075) at 0.1-s.

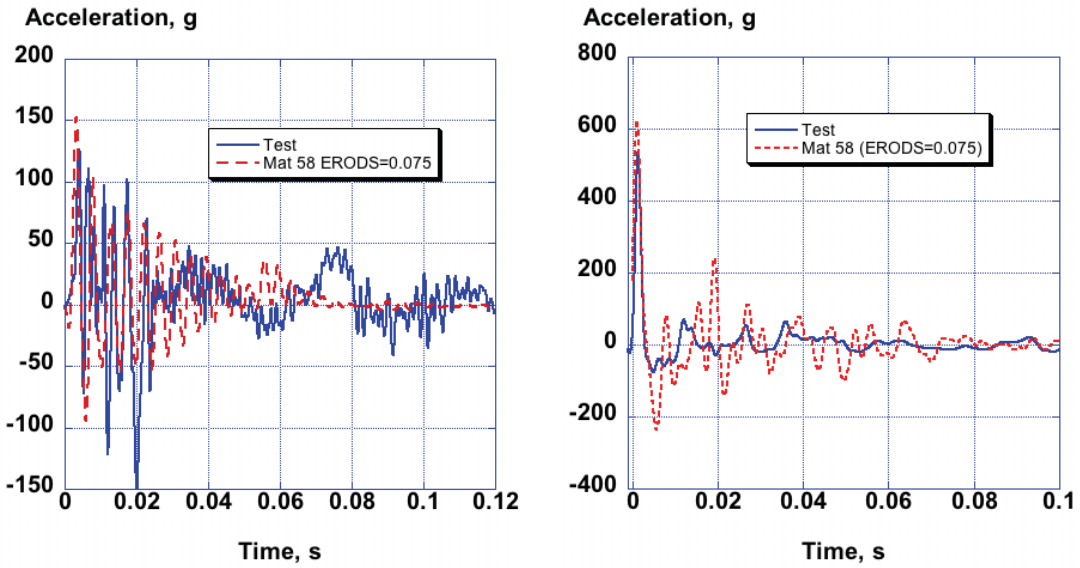

(a) Upper mass location. (b) Lead block on the floor.

Figure 152. Comparison of test accelerations with Mat 58 (ERODS=0.075) predictions.

4.6.6 Multi-Dimensional Calibration of the Mat 58 Impact Model

Multi-dimensional model calibration was used exclusively with photogrammetric data to get a broad perspective of the overall behavior of the system. This work concentrated in three areas: 1) processing of photogrammetry images to map targets to LS-DYNA, 2) conducting parametric studies of the LS-DYNA model to evaluate metrics M_1 and M_2, and 3) to determine a parameter set to reconcile impact model predictions with test. Although the number of photogrammetric targets collected was large, not all targets mapped to LS-DYNA nodes. In addition, not all targets were tracked during the entire test. For model multi-dimensional calibration, only the first 9-ms of data were selected, since the floor was completely attached during this time period. Note that this time window is significantly shorter than the 100-ms of test data that was compared with simulation results in the previous section. Processing of the photogrammetric images required removal of targets that were not in all images throughout the time span needed, transforming the photogrammetric data into the LS-DYNA coordinate system, conducting interpolation of time histories to correct for anomalies due to dropouts, and mapping the resulting target displacements to nodes in the LS-DYNA model. A *y*-*z* grid overlay of the LS-DYNA nodes (dot-blue) versus photogrammetric targets in (o red) is shown in Figure 153. The algorithm mapped photogrammetric targets to LS-DYNA nodes within 2-in. of each other.

With the photogrammetric data set in hand, calibration of the fuselage model proceeded by conducting parametric studies to determine parameters to reconcile the model with test. Instead of looking at individual target displacements, the process used the displacement metric M_1 to assess the ability to reconcile the model. Specifically, the reconciliation distance between the model and test is gaged using a vector 2-norm. Simply stated, displacements from 584 targets in 3 directions are used to construct a response vector with 1752 entries corresponding to the *x*, *y*, *z* displacements as a function of time, i.e, $Q(t,p)$. At each time step, differences between photogrammetry and LS-DYNA model predictions were compared in terms of a vector 2-norm.

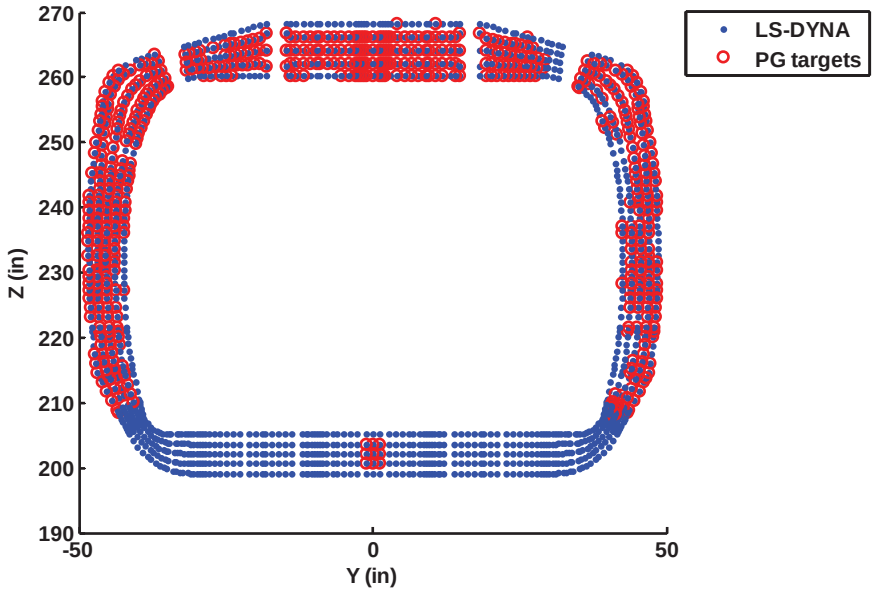

Figure 153. Photogrametry targets mapped to LS-DYNA nodes.

The first step in the calibration process was to determine a parameter set that when adjusted would reconcile the model with test observations. To find such a set, many parametric studies were completed which included the effects of varying the longitudinal modulus, transverse modulus, shear modulus, impact angles, impact velocity, and ERODS parameters. The final parameter set used in the study is shown in Table 8. Parameters were assumed to be uniformly distributed within the bounds defined in the table. A random sampling of these parameters was used to execute 120 LS-DYNA runs. For each LS-DYNA run, the displacement magnitude norm was computed for all 584 targets. Figure 154 shows the displacement upper and lower bounds from 120 LS-DYNA runs (dashed blue) plotted along with the displacement norm computed with photogrammetric data (solid red). Test and analysis reconciliation is only probable if the analysis bounds encompass the measured data.

At this point, although the bounds are reasonably close, they do not encompass the entire measured data set. A parameter set to fully encompass the test results has not been found. Nonetheless, because the bounds are relatively close to the measured data, a reconciling solution using optimization was computed and reported in Table 8 under "Cal Solution". Additionally, the displacement 2-norms are shown in Figure 155 for test (solid red), the baseline model (dashed-dot black), and the calibrated solution (dashed blue). At any point in time the maximum displacement error in *x*, *y*, or *z* is less than or equal to the difference in the norm between test and analysis.

A final check of the model examined the orthogonality metric M_2 (see Eq. 4) to assess model similarity in terms of impact shapes from test and analysis. A plot is shown in Figure 156 of the metric M_2 using 5 impact shapes computed using photogrammetric data and those corresponding to the analysis when using the baseline parameters. The ordinate shows the fractional shape contributions for analysis, as defined by Eq. 3, and the test results are shown across the top. Note that the 1st impact shape from test contributes 73% to the response in contrast to 87% for

the analysis. Similarly, the orthogonality results are shown in Figure 157 using the calibrated parameters instead. It should be apparent that differences between the two models, i.e., baseline versus calibrated, are small indicating that the relative contribution of the impact shapes is not improved. More importantly, the model was only able to predict the dominant impact shape. Therefore, the more complex structural behavior measured by photogrammetry was not well predicted.

Table 8. Parameters Used in Uncertainty Studies of the Fuselage Section Model.

Param. No.	Properties	Nominal	Lower Bound	Upper Bound	Cal Solution
1	EA (lb/in^2)	1.00E+07	5.00E+06	2.50E+07	1.64E+07
2	EB (lb/in^2)	1.00E+07	3.00E+05	2.50E+07	3.00E+05
3	GAB, GBC, GCA (lb/in^2)	7.40E+05	1.90E+05	1.05E+06	2.73E+05
4	ERODS	0.15	0.02	0.60	0.56
5	θ_x roll (degrees)	0.00	-0.50	0.00	-0.10
6	θ_y pitch (degrees)	0.00	0.00	0.50	0.00

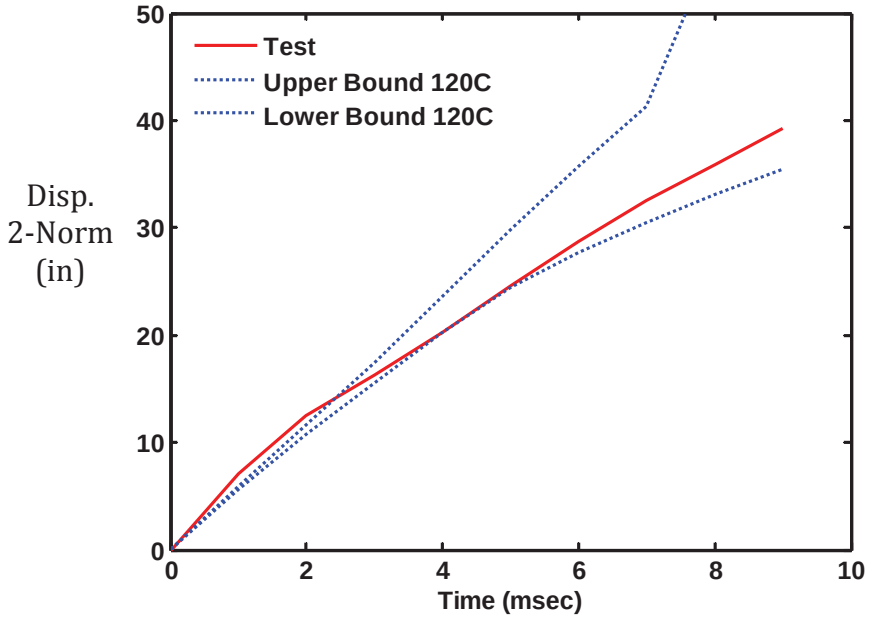

Figure 154. Displacement 2-norm for test and 120 LS-DYNA runs.

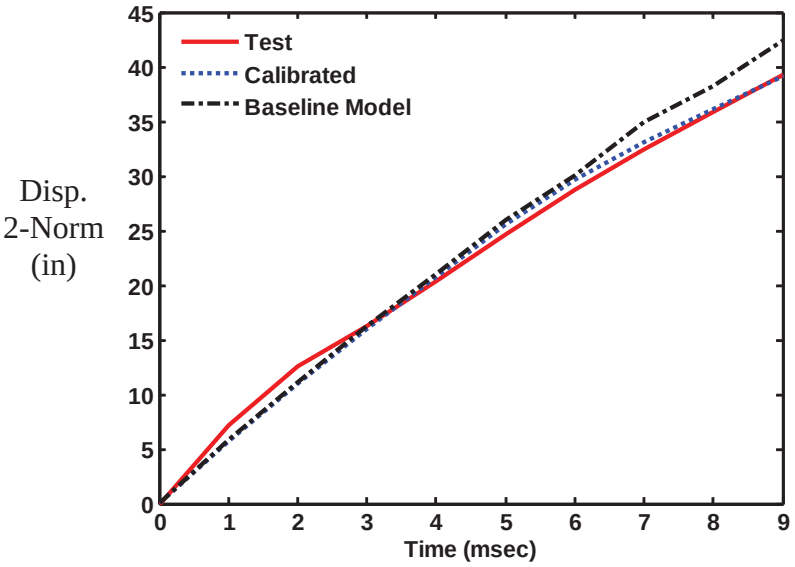

Figure 155. Displacement 2-norm for test, baseline, and calibrated model.

Figure 156. Orthogonality of impact shapes: baseline model versus test.

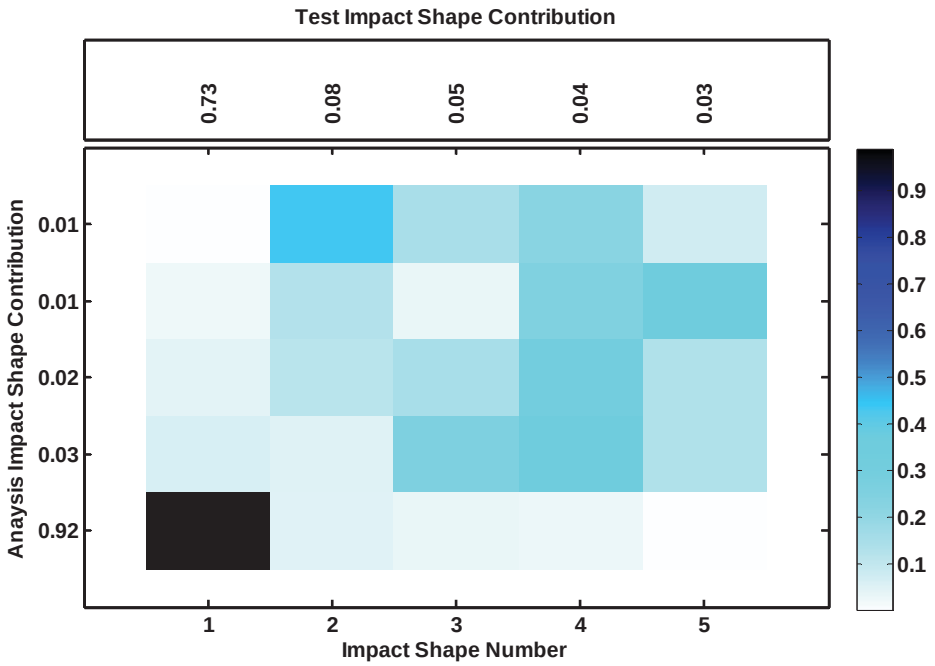

Figure 157. Orthogonality of impact shapes: calibrated model versus test.

5.0 DISCUSSION OF RESULTS

5.1 Experimental Program

One of the realities of conducting impact tests is that repeated tests on the same type of specimen are rarely possible. Consequently, most tests are a one-time only event, making quantification of experimental uncertainties difficult. As reported in this document, the only opportunity for repeated tests were using the laminated coupons, as described in Section 3.3, in which as many as seven coupons were tested. For the component tests, photogrammetric measurements assisted in bounding the uncertainty in the experimental responses. For example, target-tracking measurements enabled accurate determination of the velocity and attitude of the drop mass or the test article at the moment of impact. In addition, photogrammetric techniques were used to collect full-field strain contour plots, when strain gages failed. In the case of the subfloor test, all data were lost except for photogrammetric data from the skinned side of the subfloor. Fortunately, that information provided accurate velocity- and displacement-time histories that were used in conducting test-analysis comparisons. Finally, full-field strain and out-of-plane displacement data generated using photogrammetric techniques were able to capture localized regions of high strain and oil-canning modes of failure.

A variety of composite failure modes were evident during testing including brittle fracture, crushing of the material, ply delamination, layer splitting, and localized bending. The I-beam specimens exhibited uniform crushing of the material from the top edge that was aided by the presence of a crush initiator. Conversely, the T-section components exhibited delamination and localized brittle fracture, with very little crushing of the material. In addition to material failures, structural failures occurred such as stiffener debonding and global/local buckling. As an

example, the T-stiffeners that were bonded onto the base of the subfloor separated almost immediately upon impact of the specimen. Likewise, the cruciform webs exhibited global buckling and crushing under impact loading. The ability to accurately model so many different structural deformation and composite failure modes is a major challenge for the current generation of nonlinear, explicit transient dynamic finite element codes.

5.2 Analytical Program

One great disadvantage in conducting the analytical simulations was the lack of a complete set of material property data. Laminate characterization tests were performed using coupons that were cut from the SARAP hardware. Typically, the longitudinal modulus (EA) of a composite material is determined from tensile tests on 0° unidirectional tape coupons. Likewise, the transverse modulus (EB) is determined from tensile tests on 90° unidirectional tape coupons. For this research effort, the procedure used to determine Mat 58 material properties involved assessment of literature data, comparison with similar Mat 54 properties, and a trial and error process in which laminated coupons were tested and simulated under both tensile and compressive loading. Reverse engineering had to be used to derive fundamental material property values from tests on laminates. Often, one set of material properties that provided excellent comparison with coupon test data was too weak or perhaps too stiff when simulating more complex structures. Consequently, an iterative process was required. However, once a baseline set of material properties was established, the properties were fixed. Thus, the Mat 58 material properties represent compromises, meaning that they are not optimized for any one simulation. In the end, the lack of complete material property data remains a major source of modeling uncertainty.

Tests of all of the SARAP components were simulated using LS-DYNA shell-based finite element models. The shell elements were assigned either Mat 54 or Mat 58 material models to represent the behavior of the composite structure. In general, poor levels of agreement were seen when the Mat 54 material was used. Models that were assigned Mat 54 tended to fail catastrophically in a brittle fashion, absorbing little kinetic energy. As mentioned previously, many parametric studies were conducted to find a set of parameters that would predict stable crushing, as opposed to brittle failure and structural collapse.

Reference 22 describes the application of Mat 54 in modeling the quasi-static crushing response of a composite sinusoidal-shaped component. The authors of Reference 22 demonstrate excellent prediction of composite crushing. Consequently, the Mat 54 model that was reported in Reference 22 was incorporated into the I-beam model and executed. This Mat 54 model had the DFAILM, DFAILS, DFAILT, and DFAILC parameters specified, as well as the TFAIL, SOFT, ALPH, FBRT, YCFAC, and BETA parameters. Unfortunately, even this Mat 54 simulation failed to produce stable crushing of the I-beam component under dynamic compressive loading.

All attempts to modify the Mat 54 material model to improve the crushing behavior failed, with one exception. An I-beam model was executed using Mat 54 autoclave properties, except that all failure strain inputs (DFAILM, DFAILS, DFAILT, and DFAILC) were undefined. The parameter EFS (Effective Failure Strain) was varied from 0.01 to 0.06 in increments of 0.01.

The EFS parameter can be used instead of DFAILT, DFAILC, DFAILS and DFAILM. At each time step, LS-DYNA calculates an effective scalar strain for each integration point within an element and then compares the scalar strain to the EFS value. If the scalar strain is higher than EFS, then the integration point is deleted, regardless of loading condition. When all integration points have failed, the element is removed. Thus, EFS controls element erosion/deletion, and does not represent progressive failure as is governed by Chang-Chang in Mat 54. Using Chang-Chang, the elastic properties of plies within the laminate stacking sequence are degraded as part of the ply-by-ply failure process. When all plies within an element are deleted, then the element is removed from the simulation.

Predicted acceleration-, velocity, and displacement-time history responses are compared with test data in Figure 158 for the I-beam model executed with EFS=0.06. The impact velocity for this simulation was 189.6-in/s. This model was able to generate predicted responses that matched the test data reasonably well, especially when compared with the original Mat 54 results, shown in Figure 84. The experimental and predicted acceleration responses, shown in Figure 158(a), were filtered using a 1000-Hz Butterworth low-pass filter.

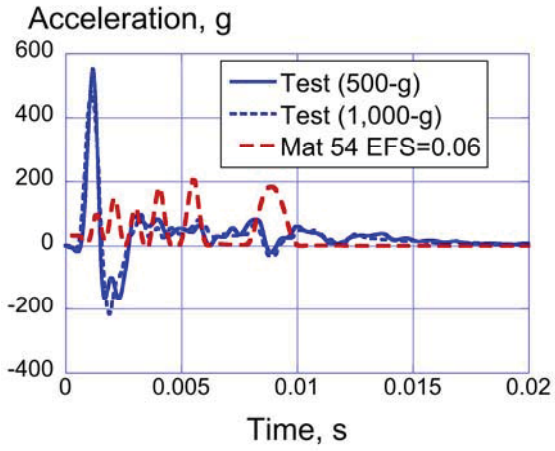

(a) Acceleration.

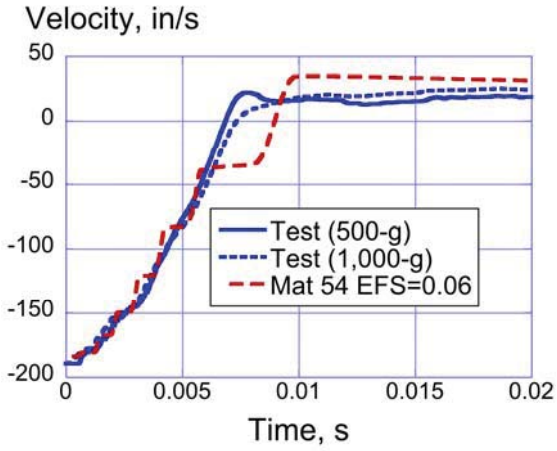

(b) Velocity.

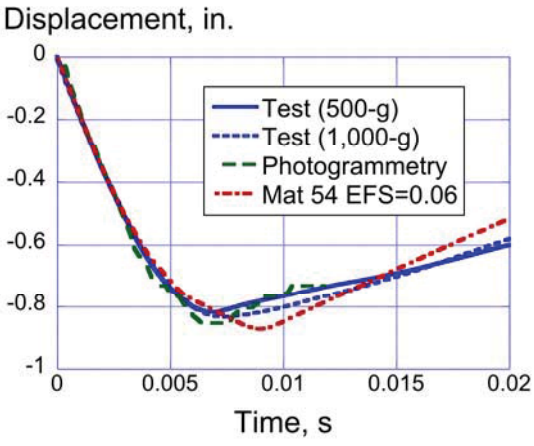

(c) Displacement.

Figure 158. Experimental and Mat 54 analytical results for the I-beam 4-ft drop (velocity=189.6-in/s) with EFS=0.06.

However, despite the reasonably good comparison with time history responses, the predicted deformation pattern, shown in Figure 159, does not match the test. The model begins to crush initially from the top edge. By 0.0064-s, elements have failed along the web-flange intersection almost completely separating these two parts on both sides. Also, a large "crack" has opened running from the middle of the top edge of the web to the side flange, which separates a large chunk of the web from the specimen. By 0.024-s the failed portion of the web is removed from the model and no additional damage is seen. Conversely, the test article exhibits fairly uniform crushing of the specimen from the top edge, as shown in Figure 13.

As described in Reference 22, the success of the analytical predictions using Mat 54 were based on utilizing a contact definition called CONTACT_RIGID_NODES_TO_RIGID_BODY. This contact allows direct input of a load versus penetration curve. The user-defined load-penetration curve can be adjusted to provide improved predictive responses. In discussions with the authors of Reference 22, they recommended selecting the rigid nodes to rigid body contact, and then conducting a parameter study using SOFT in the Mat 54 material model. The I-beam model was modified to include the new contact definition with input of a load-penetration curve similar to the one described in Reference 22. Unfortunately, no improvement in the predicted response was obtained and a SOFT parameter study was not attempted.

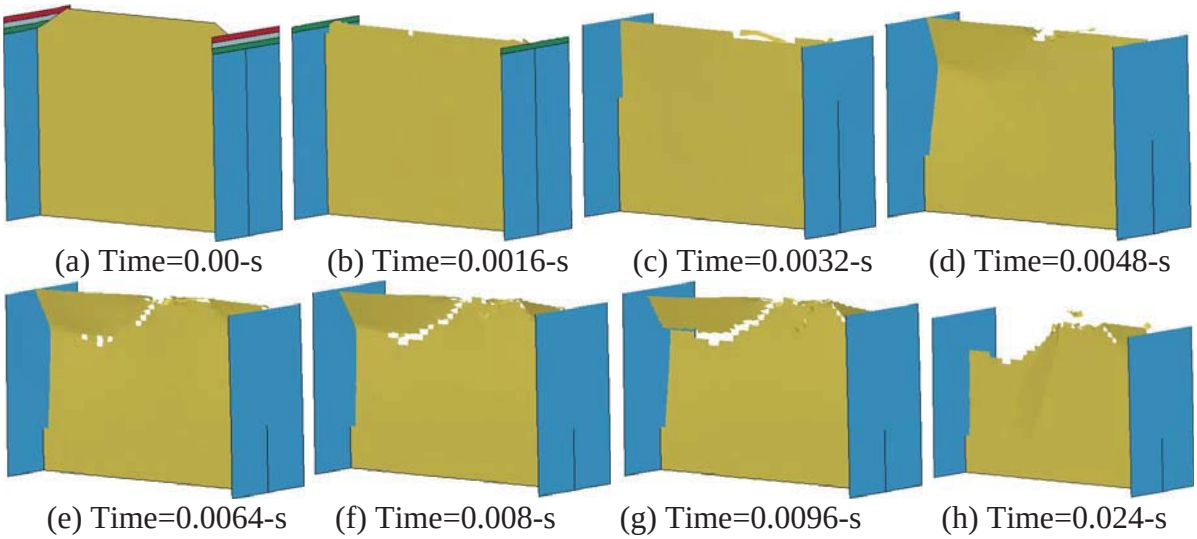

(a) Time=0.00-s (b) Time=0.0016-s (c) Time=0.0032-s (d) Time=0.0048-s

(e) Time=0.0064-s (f) Time=0.008-s (g) Time=0.0096-s (h) Time=0.024-s

Figure 159. Deformation pattern of I-beam model executed with Mat 54 (EFS=0.06).

Unlike Mat 54, Mat 58 incorporates parameters such as SLIMs and ERODS, which allow the analyst to incorporate some degree of plastic-like behavior into the model. This feature allows failed elements to carry small stresses, yet remain in the model. As seen when using Mat 54, once elements are removed from the simulation, holes are created in the model, resulting in stress concentrations. The model can quickly collapse. The only case in which the brittle failure predicted by Mat 54 matched the test response was for the fuselage section vertical drop test. The fuselage section failed catastrophically in the lower corners, which allowed the floor to completely separate from the sidewalls, as shown in Figure 145(a). The fuselage model with Mat 54 was successful in predicting this response.

In general, the capability of LS-DYNA to accurately predict all of the composite failure modes is inconsistent. Material crushing of the I-beam components was successfully simulated; however, debonding and delamination were not predicted. Current composite material models such as Mat 54 and Mat 55 are not capable of predicting delamination based on either fracture mechanics or energy–based approaches. However, if the location of a potential delamination or debond is known, a model could be modified to account for this failure mode using either tiebreak contact definitions or spot weld connections [36, 37].

Within LS-DYNA, Mat 54 and Mat 58 offer opportunities to view "hot spots" in the model through output of history variables. In general, the history variables are calculated as the simulation progresses and are typically associated with a particular failure mode. The values can range from 0 (no failure) to 1 (imminent failure). Mat 54 allows output of 16 history variables and Mat 58 allows for 15. As an example, a fringe plot of History Variable 3 is shown in Figure 160 for the T-section model that was executed with Mat 58 material properties. History Variable 3 is an interactional strain based on maximum values of two in-plane strains and the shear strain.

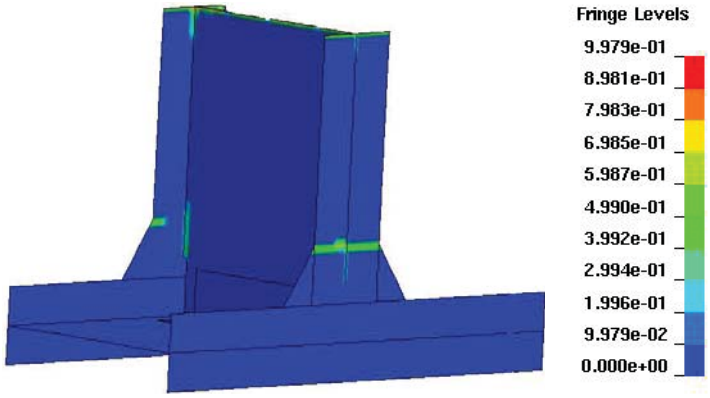

Figure 160. Fringe plot of History Variable 3 of the T-section model shown just prior to failure of the vertical flanges (t=0.001).

Three "hot spots" shown in the plot of Figure 160 indicate the locations of imminent failure, which are the vertical flanges just above the fillets and the top edge of the vertical web. This plot was taken from a d3plot file using LS-Prepost. The very next d3plot file showed that element failures had occurred across the vertical flanges on both sides. In the future, using the History Variable plots as a guide, the hot spot regions could be modified to incorporate delamination.

Recent advances in composite material model development have focused on three-dimensional ply failure models that utilize solid element representations of composite materials, as described in Reference 21. Also, Livermore Software Technology Corporation (LSTC), the company that markets LS-DYNA, has recently incorporated a user-defined material model (Mat 162) that can be purchased and used in LS-DYNA to represent composite materials as solid elements [38]. While these approaches were not evaluated in the present study, they offer some potential for future simulations. In addition, a joint ASU-FAA-LSTC-NASA-GWU research project was initiated in 2012 with the goal of producing a new material model in LS-DYNA that has the flexibility to simulate a wide range of properties, accumulated damage behavior, and different types of failure, which exist in composite materials. This model should successfully predict

aircraft turbine engine containment threshold velocities based upon mechanical property tests, without relying on post-test correlation to large-scale system tests [39].

Both Mat 54 and Mat 58 contain parameters that cannot be measured in the laboratory. These parameters must be tuned through repeated test-analysis comparisons. Over time, an analyst may gain experience in selecting these parameters based on prior simulations. However, without relying on test data for comparison, it can be difficult to choose the correct values. For example, pre-test simulations for the subfloor longitudinal impact were executed using the baseline Mat 58 material model. However, the baseline ERODS parameter for unidirectional tape was set at a relatively high value (close to 1.0), meaning that elements would not be removed until a high value of strain had been achieved. Consequently, the pre-test simulation of the subfloor impact predicted only 7-in. of vertical displacement of the drop mass, whereas the actual displacement was 13-in. The value of ERODS was too high, and a post-test parameter study was performed. The actual value that gave best correlation with test was ERODS=0.1. Consequently, it is fair to say that, while the capabilities of the current generation of explicit transient dynamic codes, such as LS-DYNA, may not always provide accurate pre-test predictions of the impact response of composite airframe structures, the test response can be bounded using analysis.

Finally, multi-dimensional calibration techniques were applied to both the composite subfloor and fuselage section models in an attempt to assess model deficiencies and uncertainties, to evaluate parameter importance, and to compute required model changes needed to better reconcile test and predictions. The need for additional subsystem tests to reduce the uncertainty in joints, aggregate material properties, and geometry is extremely important if model validation is required for more than just one test condition. As an example, the fuselage section was tested under quasi-static loading, modal vibration, and vertical drop test conditions. These tests were conducted to provide additional opportunities for calibration of the global model. While results from the static test proved to be unusable, results from the vibration test of the composite fuselage indicated that the model needed to have the modulus reduced by 27% from the baseline value. However, results using impact data suggested an increase in modulus. Clearly, these two requirements are inconsistent; however, both are supported by experimental data. These conflicting results highlight the inadequacy of the existing model to be predictive under different loading conditions. Although, comparisons of the observed global behavior with analytical predictions are reasonable, attempts to use the analytical model to predict other tests conditions will likely fail.

6.0 CONCLUDING REMARKS

This report documents a research study to assess the capabilities of a nonlinear, explicit transient dynamic code, LS-DYNA, for predicting the impact response of composite airframe structures. The test specimens were extracted from a previously tested composite prototype fuselage section developed and manufactured by Sikorsky Aircraft Corporation under the US Army's Survivable Affordable Repairable Airframe Program (SARAP). Laminate characterization testing was conducted in tension and compression. In addition, dynamic impact tests were performed on several components, including I-beams, T-sections, and cruciform sections. Finally, tests were conducted on two full-scale components including a subfloor section and a framed fuselage section. These tests included a modal vibration and longitudinal impact test of the subfloor

section and a quasi-static, modal vibration, and vertical drop test of the framed fuselage section. Most of the test articles were manufactured of graphite unidirectional tape composite with a thermoplastic resin system. However, the framed fuselage section was constructed primarily of a plain weave graphite fabric material with a thermoset resin system.

Due to the varying complexity of the test articles, several different composite failure modes were evident during testing including brittle fracture, delamination, material crushing, and localized bending. In addition, structural failure modes occurred such as stiffener debonding and global/local buckling. The ability to accurately simulate so many different failure responses is a major challenge for the current generation of nonlinear, explicit transient dynamic finite element codes.

Typically, the test articles were instrumented with accelerometers and strain gages. Based on the results of the test program, strain gages tended to separate from the specimens immediately following impact and provided no information. In the longitudinal impact test of the subfloor, which was a severe impact event, even the accelerometers failed. In addition to more traditional instrumentation, all of the test articles were sprayed with a stochastic speckle pattern that was used in conjunction with photogrammetric techniques to capture full-field strain contour plots. During the subfloor test, all data were lost except for photogrammetric data from the skinned side of the subfloor. Fortunately, that information provided accurate velocity- and displacement-time histories that were used in conducting test-analysis comparisons. Photogrammetry was also able to provide accurate information on impact conditions, such as drop mass velocity and off-nominal attitudes. Thus, photogrammetry proved to be an invaluable tool for this test program.

Finite element models were developed to represent the laminate characterization tests; the impact tests of I-beam, T-section, and cruciform components; the longitudinal impact test of the subfloor; and the vertical drop test of the framed fuselage section. Sikorsky Aircraft Corporation, the manufacturer of the SARAP hardware, provided most of the models to NASA as part of a cooperative research agreement. Once received, the models were updated and modified to best represent the test conditions. Simulations were conducted using LS-DYNA version 971 R6.0.0. Within LS-DYNA, two composite material models were evaluated: Mat 54 and Mat 58. Mat 54 is a progressive failure model that uses the Chang-Chang failure criterion to simulate ply-by-ply failure and property degradation, while Mat 58 is a continuum damage mechanics model for representing unidirectional tape and fabric composite materials. Mat 54 material properties were provided by Sikorsky, whereas material properties for Mat 58 were determined by assessing literature data, comparing with similar Mat 54 property values, and using a trial and error process in which laminated coupons were simulated under both tensile and compressive loading.

In general, the Mat 54 simulations did a poor job in simulating the impact responses of the components and the subfloor. These models tended to fail catastrophically in a brittle fashion, absorbing little kinetic energy. Numerous parametric studies were conducted to find a set of parameters that would predict stable crushing, as opposed to brittle failure and structural collapse. None of these attempts were successful. The only case in which the brittle failure predicted by Mat 54 matched the test response was for the fuselage section vertical drop test. The fuselage section failed catastrophically in the lower corners, which allowed the floor to

completely separate from the sidewalls. The fuselage model with Mat 54 was successful in predicting the location and amount of damage to the fuselage section, even matching the kinematics of the floor following separation from the sides of the fuselage structure.

Unlike Mat 54, Mat 58 includes parameters, which allow the analyst to incorporate plastic-like behavior into the model. This feature allows failed elements to carry small stresses, yet remain in the model. As seen when using Mat 54, once elements are removed from the simulation, holes are created and stress concentrations are generated, leading to numerical instabilities and element failures. The model can quickly collapse. Mat 58 models of the I-beam were able to accurately predict material crushing. Likewise, Mat 58 models of the cruciform sections predicted global buckling behavior of the webs under dynamic loading. Consequently, excellent agreement was seen for the Mat 58 model predictions with the I-beam and cruciform responses.

However, during the impact test, the T-section component failed primarily through delamination. Likewise, the first failure event that occurred with the subfloor longitudinal impact test was debonding of the T-stiffeners from the base. Current composite material models such as Mat 54 and Mat 55 cannot predict delamination or debonding without *a priori* knowledge of where it will occur. If the location of a potential delamination or debond is known, the model can be modified to account for this failure mode using tiebreak contact or spot welds. Whether this is a reasonable or practical approach for modeling debonding or delamination was not evaluated in this study.

Because both Mat 54 and Mat 58 contain parameters that cannot be measured in the laboratory these parameters must be tuned through repeated test-analysis comparisons. Over time, an analyst may gain experience in selecting these parameters based on prior simulations. However, without relying on test data for comparison, it can be difficult to choose the correct values. As a result, these analysis methods cannot be considered truly predictive. However, it is fair to say that, while the capabilities of the current generation of explicit transient dynamic codes such as LS-DYNA may not provide accurate pre-test predictions of the impact response of composite airframe structures, the test response can be bounded using analysis.

Finally, in this report, model calibration efforts relied primarily on scalar deterministic metrics, such as test-analysis comparisons of acceleration, velocity-, and displacement time-histories at critical locations (e.g. comparisons of test-analysis acceleration responses of the drop mass during a component impact test). In addition, multi-dimensional model calibration techniques were applied to the subfloor and fuselage section models in an attempt to reconcile differences between test (photogrammetry data) and analytical predictions. Two metrics were evaluated for both simulations including the displacement 2-norm and the orthogonality of impact shapes. These techniques were successful in assessing the overall adequacy of the model based on parameter uncertainty propagation and quantification, and in generating a calibrated model that minimized differences in test and predicted responses.

7.0 ACKNOWLEDGEMENTS

The authors of this report gratefully acknowledge Charles Clarke, Brian Wilson, and Joe Shen of Sikorsky, who helped establish the Space Act Agreement between NASA and Sikorsky,

provided finite element models, and offered invaluable assistance in planning and executing the test and simulation program. We also recognize the work of Michael A. Polanco, who performed many preliminary simulations. In addition, we thank the NASA Aeronautics Rotary Wing Program Office for supporting this work financially. Also, Joe Zalameda, Jim Bly, and Pat Johnston of the Nondestructive Evaluation Sciences Branch of NASA Langley performed the Non Destructive Evaluation. Finally, we would like to acknowledge the team of technicians and contractors at the LandIR Facility who provided technical support for conducting the tests, mounting instrumentation and operating the data acquisition system, and setting up cameras and high-speed video systems. These technicians included: Pat Quander-Haas, Doug Prochnow, Paul Bagby, Nelson Seabolt, Richard Wheeler, Dave White, and Steve Sieder.

8.0 REFERENCES

1. Cartensen T. A., Townsend W., and Goodworth A., "Development and Validation of a Virtual Prototype Airframe Design as Part of the Survivable Affordable Repairable Airframe Program," Proceedings of the 64th American Helicopter Society Forum, Montreal, Canada, April 29-May 1, 2008.

2. Non-Reimbursable Space Act Agreement between Sikorsky Aircraft Corporation and NASA Langley Research Center for Collaborative Research Regarding Impact Testing and Simulation of Composite Airframe Structures, SAA1-1122, signed May 5, 2011.

3. Jackson K.E., Fuchs Y. T., and Kellas S., "Overview of the NASA Subsonic Rotary Wing Aeronautics Research Program in Rotorcraft Crashworthiness," ***Journal of Aerospace Engineering***, Special Issue on Ballistic Impact and Crashworthiness of Aerospace Structures, Volume 22, No. 3, July 2009, pp. 229-239.

4. Hallquist J. Q., "LS-DYNA Keyword User's Manual," Volume I, Version 971, Livermore Software Technology Company, Livermore, CA, August 2006.

5. Hallquist J. Q., "LS-DYNA Keyword User's Manual," Volume II Material Models, Version 971, Livermore Software Technology Company, Livermore, CA, August 2006.

6. ASTM Standard D3039, "Standard Test Method for Tensile Properties of Polymer Matrix Composite Materials," ASTM International, West Conshohocken, PA, 2008, DOI: 10.1520/D3039_D3039M-08, www.astm.org.

7. ASTM Standard D3410, "Standard Test Method for Compressive Properties of Polymer Matrix Composite Materials with Unsupported Gage Section by Shear Loading," ASTM International, West Conshohocken, PA, 2008, DOI: 10.1520/D3410_D3410M-03R08, www.astm.org.

8. Military Standard, MIL-STD1290A(AV),Light Fixed- and Rotary-Wing Aircraft Crash Resistance, Department of Defense, Washington D.C., 20301, September 26, 1988.

9. Juang, J.-N., Horta, L.G., and Phan, M.: System/Observer/Controller Identification Toolbox. NASA TM 107566, February 1992.

10. Horta, L.G., Juang, J.-N., Chen, C-W: Frequency Domain Identification Toolbox. NASA TM 109039, Sept. 1996.

11. Mongiardini M., Ray M.H., Anghileri M., "Development of a Software for the Comparison of Curves During the Verification and Validation of Numerical Models," Proceedings of the 7th European LS-DYNA Conference, Salzburg, Austria, May 14-15, 2009.

12. Marzougui D., Kan C-D., and Opiela K. S., "Comparison of the Crash Test and Simulation of an Angle Impact of a 2007 Chevrolet Silverado Pick-Up Truck into a New Jersey-Shaped Concrete Barrier for MASH Conditions," National Crash Analysis Center NACA 2010-W-001 Working Paper, July 2012.

13. Jackson K. E., Fasanella E. L., Annett M. S., and Polanco M. P., "Material Model Evaluation of a Composite Honeycomb Energy Absorber," Proceedings of the 12th International LS-DYNA Users Conference, Dearborn, MI, June 3-5, 2012.

14. Sprague M.A., and Geers T. L., "Spectral Elements and Field Separation for an Acoustic Fluid Subject to Cavitation," Journal of Computational Physics, Vol. 184, 2003, pp: 149-162.

15. Schwer L.E., "Validation Metrics for Response Histories: Perspectives and Case Studies." Engineering with Computers," Engineering with Computers (2007), 23:295-309.

16. Chang, Fu-Kuo, and Chang, Kuo-Yen, "Post-Failure Analysis of Bolted Composite Joints in Tension or Shear-out Mode Failure Mode," ***Journal of Composite Materials***, Vol. 21, No. 9, September 1987, pp. 809-833.

17. Chang, Fu-Kuo, and Chang, Kuo-Yen, "A Progressive Damage Model for Laminated Composites Stress Concentrations," ***Journal of Composite Materials***, Vol. 21, No. 9, September 1987, pp. 834-855.

18. Tsai, S. W. and Wu, E. M., "A General Theory of Strength for Anisotropic Materials," ***Journal of Composite Materials***, Vol. 5, 1971, pp. 58–80.

19. Hahn H., and Tsai S.W., "Nonlinear Elastic Behavior of Unidirectional Composite Laminate," ***Journal of Composite Materials***, Vol. 7, 1973, pp. 102–110.

20. Hahn H., and Tsai S.W., "Nonlinear Behavior of Laminated Composites," ***Journal of Composite Materials***, Vol. 7, 1973, pp. 257–271.

21. Donadon M.V., de Almeida S.F.M., Arbelo M.A., and de Faria A.R., "A Three-Dimensional Ply Failure Model for Composite Structures, ***International Journal of Aerospace Engineering***, Vol. 2009, Article ID 486063, 2009.

22. Feraboli P., Wade B., Deleo F., Rassaian M., Byar A., "LS-DYNA MAT54 Modeling of the Axial Crushing of a Composite Tape Sinusoidal Specimen," ***Composites: Part A***, Vol. 42 (2011), pp. 1809-1825.

23. Matzenmiller A., Lubliner J., and Taylor R. L., "A Constitutive Model for Anisotropic Damage in Fiber Composites," ***Mechanica of Materials***, Vol. 20, 1995, pp. 125-152.

24. Xiao X., "Modeling Energy Absorption with a Damage Mechanics Based Composite Material Model," ***Journal of Composite Materials***, Vol. 43, No. 5, 2009, pp. 427-444.

25. Maekawa Z., Hamada H., Lee K., and Kitagawa T., "Reliability Evaluation of Mechanical Properties of AS4/PEEK Composites," *Composites*, Vol. 25, No. 1, 1994, pp. 37-45.

26. Sun C. T., and Rui Y., "Orthotropic Elasto-Plastic Behavior of AS4/PEEK Thermoplastic Composite in Compression," ***Mechanics of Materials***, Vol. 10, 1990, pp. 117-125.

27. Hsu S. Y., Vogler T. J., Kyriakides S., "Inelastic behavior of an AS4/PEEK Composite Under Combined Transverse Compression and Shear. Part II: Model," ***International Journal of Plasticity***, Vol. 15, No. 8, 1999, pp. 807-836.

28. Horta, L. G., Jackson, K. E., and Kellas, S., "A Computational Approach for Model Update of an LS-DYNA Energy Absorbing Cell," ***Journal of the American Helicopter Society***, Vol. 55, No. 3, July 2010, pp. 032011-1 – 032011-8.

29. Horta, L.G., Mason, B.H., Lyle, K.H., "A computational approach for probabilistic analysis of water impact simulations," ***International Journal of Crashworthiness***, 1753-2111, Vol. 15, Issue 6, 2010, pp. 649-665.

30. Horta L.G., Reaves M.C, Annett M.S., and Jackson K.E.: "Multi-Dimensional Calibration of Impact Models," ***Aeronautics and Astronautics***, edited by Max Mulder, ISBN 978-953-307-473-3, Chapter 15, pp. 441-457, September 2011.

31. Horta, L. G., Reaves, M. C., Annett, M. S., and Jackson, K. E., "Multi-Dimensional Correlation of Impact Dynamic Models," Proceedings of the IMAC-XXIX Conference & Exposition on Structural Dynamics, Jacksonville, Florida, January 31 - February 3, 2011.

32. Oberkampf, W.L. and Barone, M.F.: "Measures of Agreement Between Computation and Experiment: Validation Metrics." Journal of Computational Physics, 217 (2001) 5-56, www.elvevier.com/locate/jcp

33. Schwer, L.E., "Validation Metrics for response Histories: Perspectives and Case Studies." Engineering with Computers." Engineering with Computers (2007), 23:295-309.

34. Anderson M.C., Gan W., and Haselman T.K., "Statistical Analysis of Modeling Uncertainty and Predictive Accuracy for Nonlinear Finite Element Models," Proceedings of the 69th Shock and Vibration Symposium, Minneapolis/St. Paul, MN, 1998.

35. Horta L.G., Lyle K.H., and Lessard W.B., “Evaluation of Singular Value Decomposition Approach for Impact Dynamic Data Correlation.” NASA TM 2003-212657, Oct. 2003.

36. Fleming, D. C., “Modeling Delamination Growth in Composites using MSC.Dytran,” *Proceedings of the 2nd Worldwide Automotive Conference*, Dearborn, MI, Oct. 9-11, 2000.

37. Fleming D.C., Morrow C., Clarke C. W., Bird C. E., “Finite Element Simulation of Delamination with Application to Crashworthy Design,” ***Journal of the American Helicopter Society***, Volume 53, Number 3, July 2008, pp. 267-281.

38. Anon., “User’s Manual for LS-DYNA Mat162 Unidirectional and Plain Weave Composite Progressive Failure Models,” http://www.ccm.udel.edu/Tech/MAT162/MAT162Manual_v3.pdf, December 2011.

39. Rajan S., Altobelli D., Emmerling W., Carney K., Goldberg R., Blankenhorn G., and DuBois P., “Joint ASU-FAA-LSTC-NASA GRC-GWU Research Technical Plan Composite Material for Impact Analysis, 2012.

9.0 APPENDIX A - NON DESTRUCTIVE EVALUATION

Non Destructive Evaluation (NDE) methods including transmission flash thermography and ultrasonic C-scans were used to determine the integrity of the SARAP residual hardware. This evaluation was considered extremely important given the fact that the SARAP hardware was obtained from a fuselage section that had already experienced a severe impact test. The Nondestructive Evaluation Services Branch of NASA Langley Research Center conducted the tests and their contributions are gratefully acknowledged. Only the smaller sized specimens were evaluated such as the laminate tension and compression coupons, the I-beams, the T-beams, and the cruciform sections. No NDE was performed on the larger subfloor section or the framed fuselage section.

Results are divided into two categories based on evaluation method. For the first category, results are shown for the baseline ultrasonic NDE, which were conducted using 2.25 MHz. For the second, results are shown for flash thermography.

A-1. Baseline Ultrasonic NDE

Ultrasonic C-scan images of the laminate coupons, including back wall reflections, are shown in Figure A-1. These scans indicate no flaws present in the coupons.

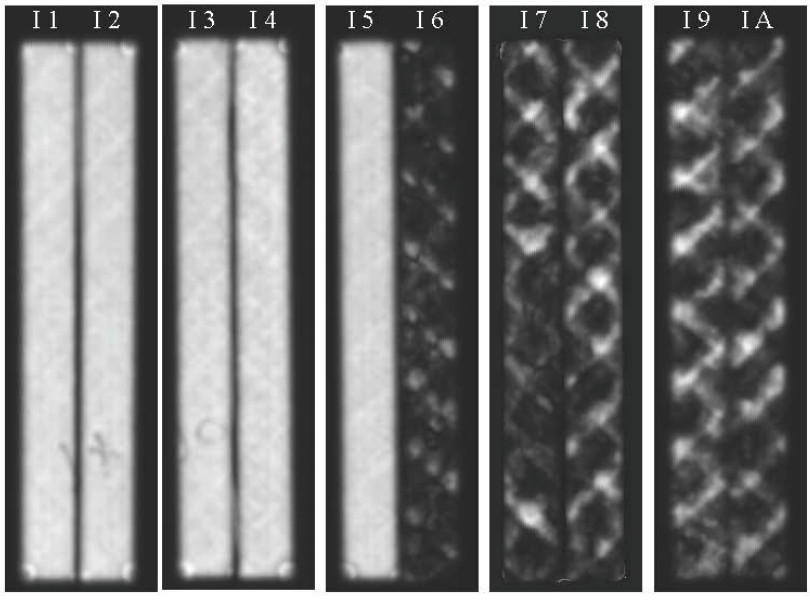

Figure A-1. Ultrasonic C-scan and back wall reflection of laminate coupons.

Next, the flanges of the I-beam specimens were examined, as shown in Figure A-2. Both ultrasonic C-scan images and back wall reflections are shown. Once again, no indications of flaws are seen, except possibly in the F D area.

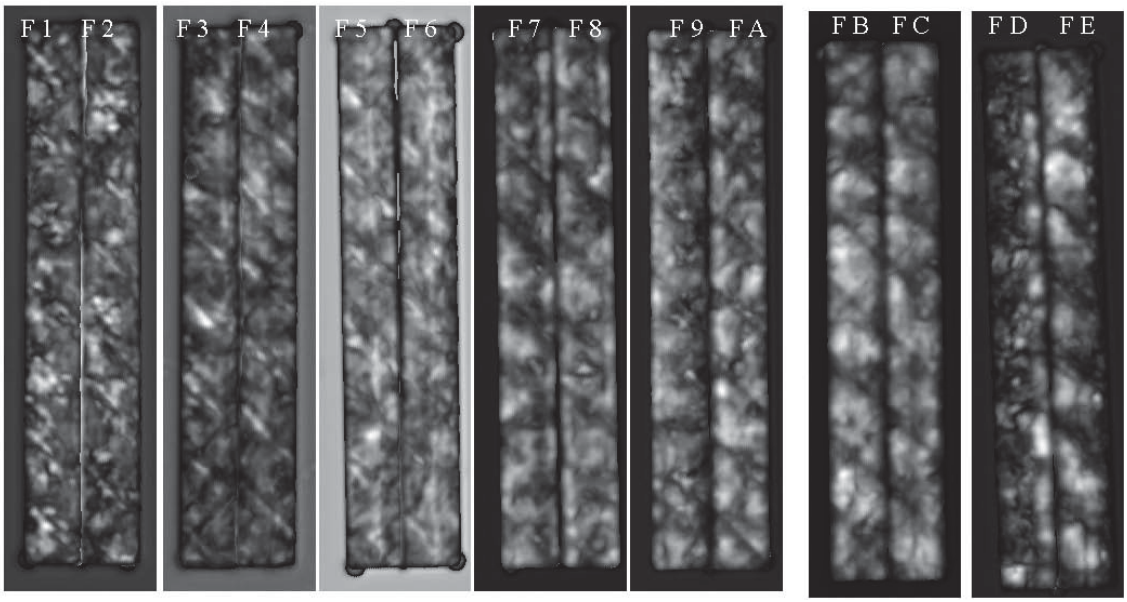

Figure A-2. Ultrasonic C-scans of the I-beam flanges.

The I-beam webs were also scanned and the images and back-wall reflections are shown in Figure A-3. Most of these images indicate that flaws are present near the ends of the specimens. However, the nature of the flaws is not determined.

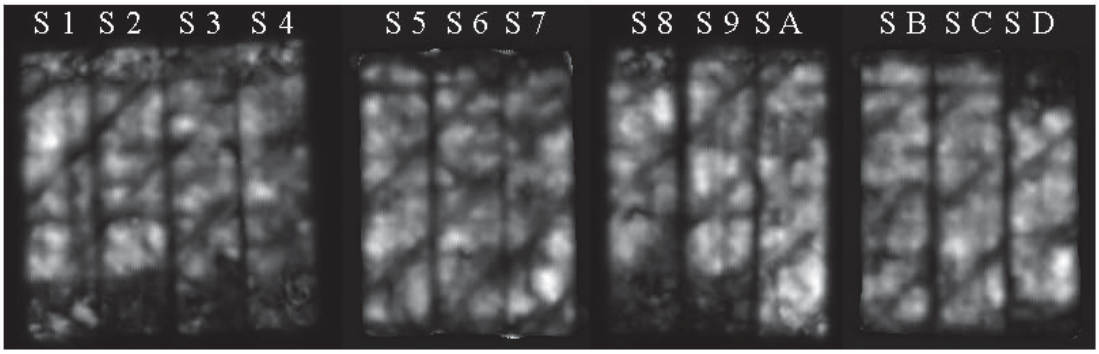

Figure A-3. Ultrasonic C-scans of the I-beam webs, indicating flaws near the ends of the specimens.

Ultrasonic C-scans were performed on the bottom and top of cruciform 1's flanges, as well as its four webs. These scans are shown in Figures A-4 through A-6, respectively. These images show no strong indication of any damage.

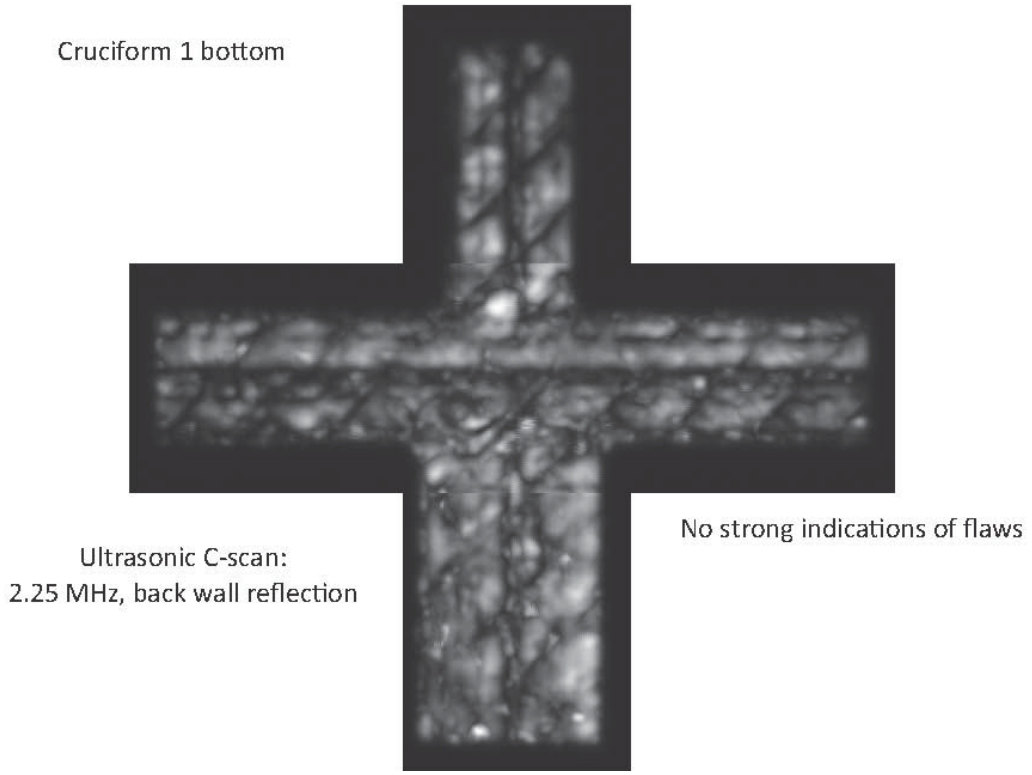

Figure A-4. Ultrasonic C-scale of the bottom flanges of cruciform 1.

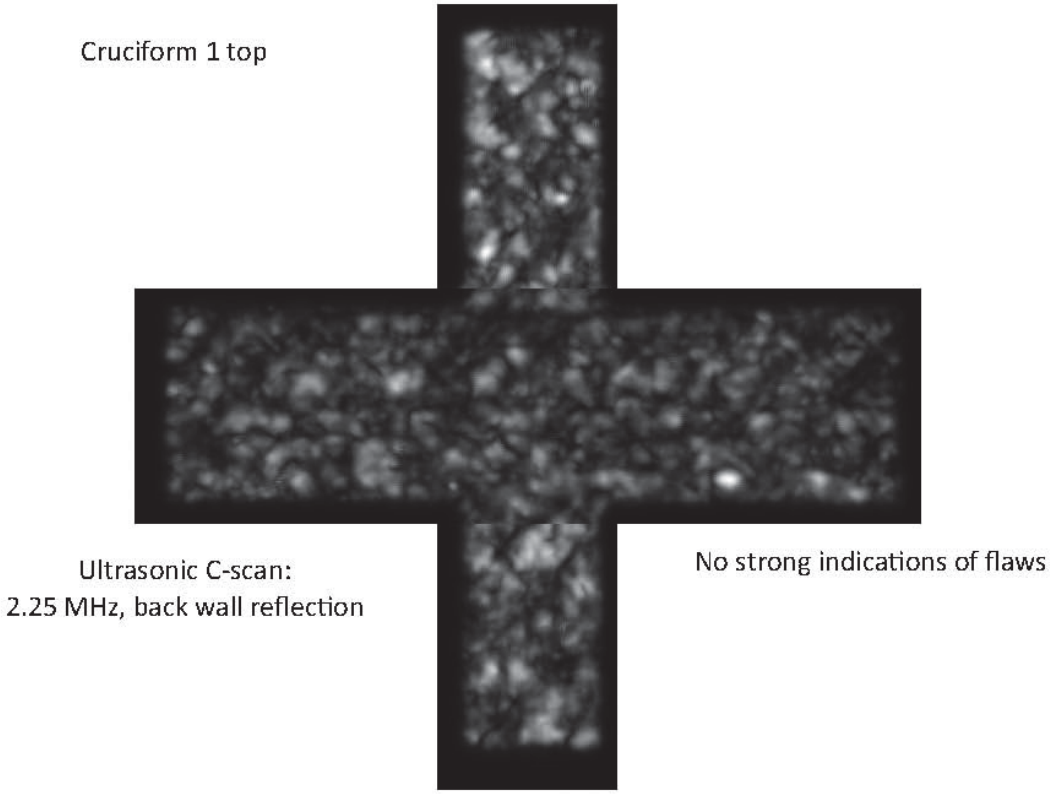

Figure A-5. Ultrasonic C-scan of the top flanges of cruciform 1.

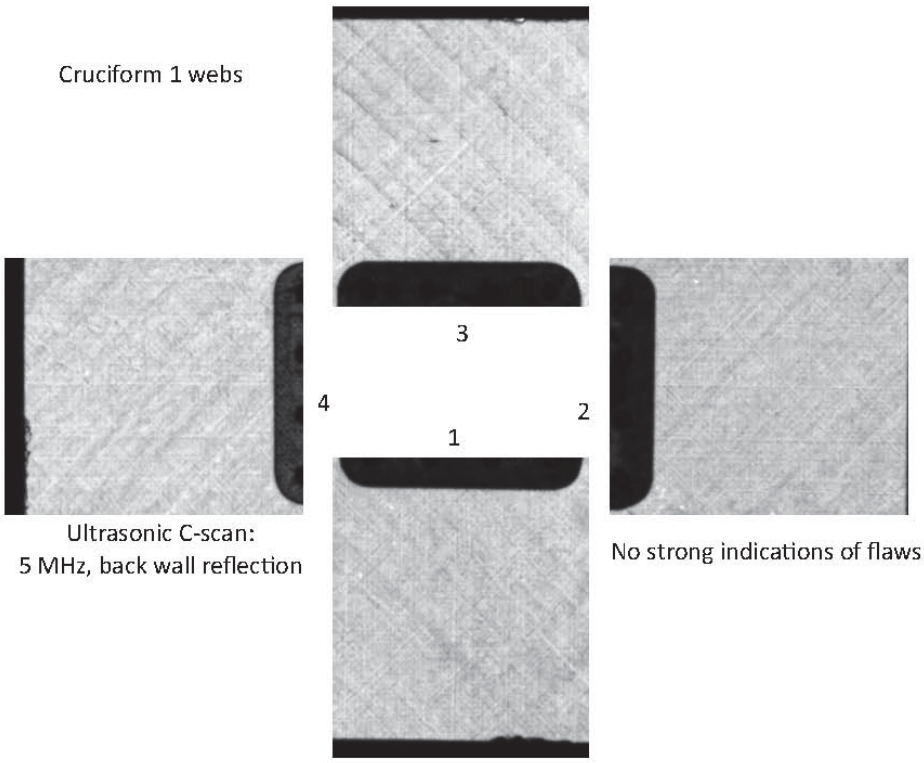

Figure A-6. Ultrasonic C-scan of the webs of cruciform 1.

Ultrasonic C-scans were performed on the bottom and top of cruciform 2's flanges, as well as its four webs. These scans are shown in Figures A-7 through A-9, respectively. These images show no strong indication of any damage.

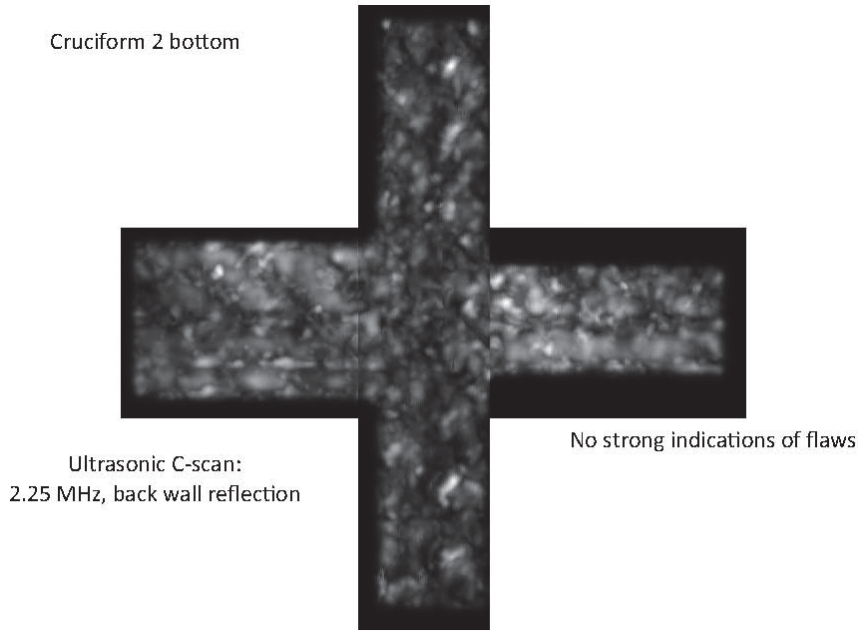

Figure A-7. Ultrasonic C-scan of the bottom flanges of cruciform 2.

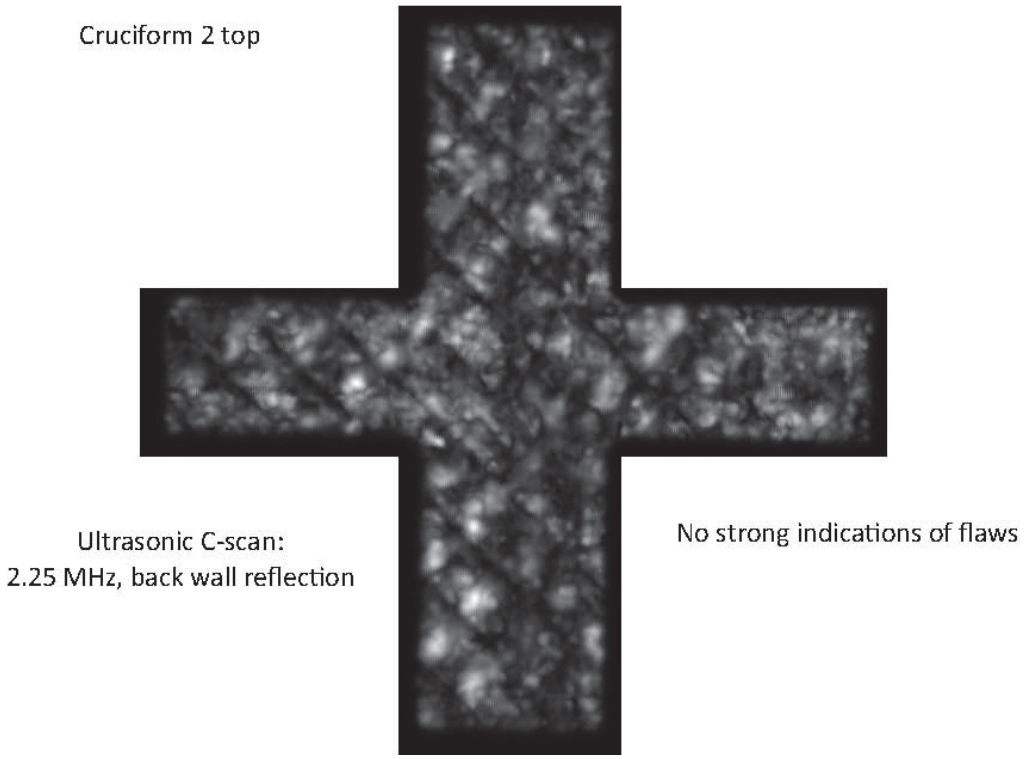

Figure A-8. Ultrasonic C-scan of the top flanges of cruciform 2.

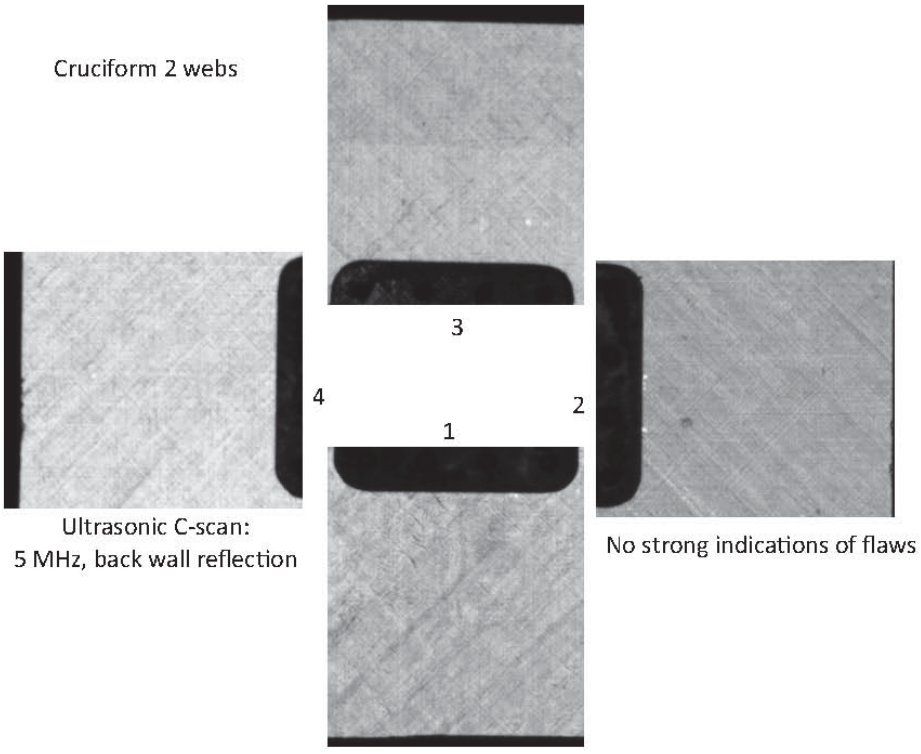

Figure A-8. Ultrasonic C-scan of the webs of cruciform 2.

A-2. Flash Thermography Inspection

Single-sided flash thermography was used to conduct follow-on inspections of the cruciform specimens. The test set-up is depicted in Figure A-9. Thermal Wave Imaging, Inc. developed the system that was used for the evaluation, which incorporates a 3-5 micron infrared camera with a sample rate of 60 Hz. Data acquisition time is approximately 10 seconds (600-720 frames).

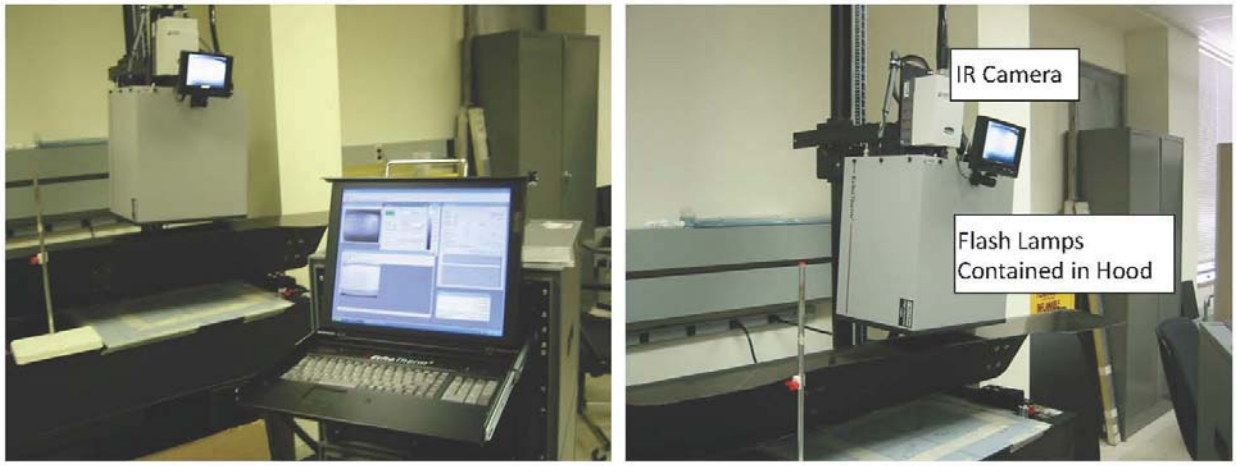

(a) Thermal inspection system photo. (b) Close up of the thermal hood.

Figure A-9. Photographs of the thermal inspection system.

Thermal inspection photographs of cruciform 1 are shown in Figures A-10 through A-37. Areas of possible damage are highlighted in red circles.

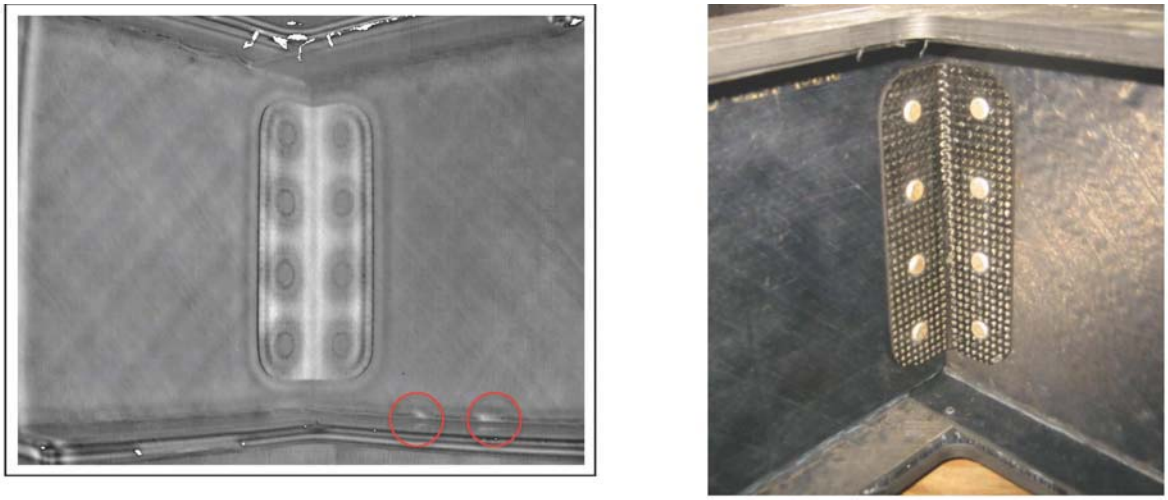

Figure A-10. Thermal inspection results for cruciform 1, rivet 1.

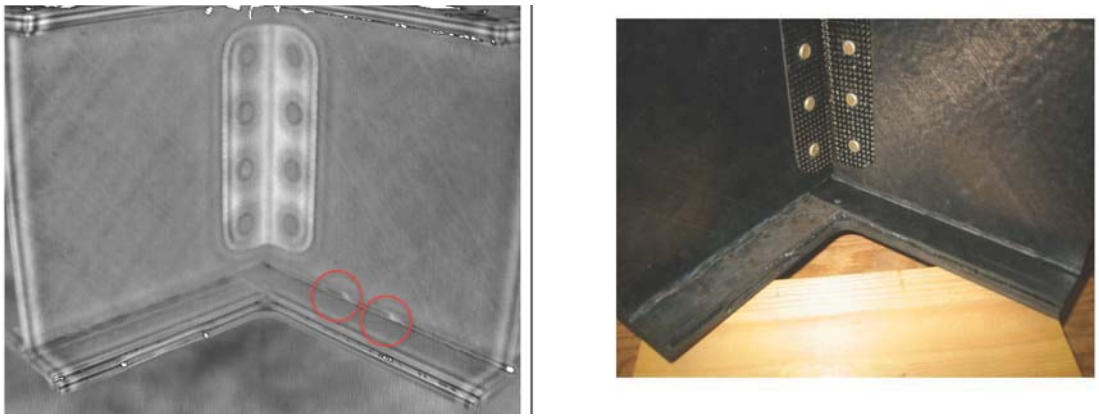

Figure A-11. Thermal inspection results for cruciform 1, rivet 1 bottom.

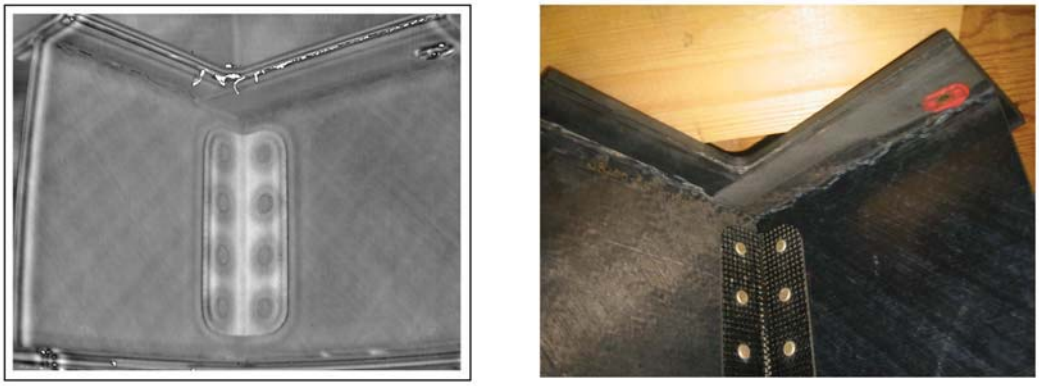

Figure A-12. Thermal inspection results for cruciform 1, rivet 1 top.

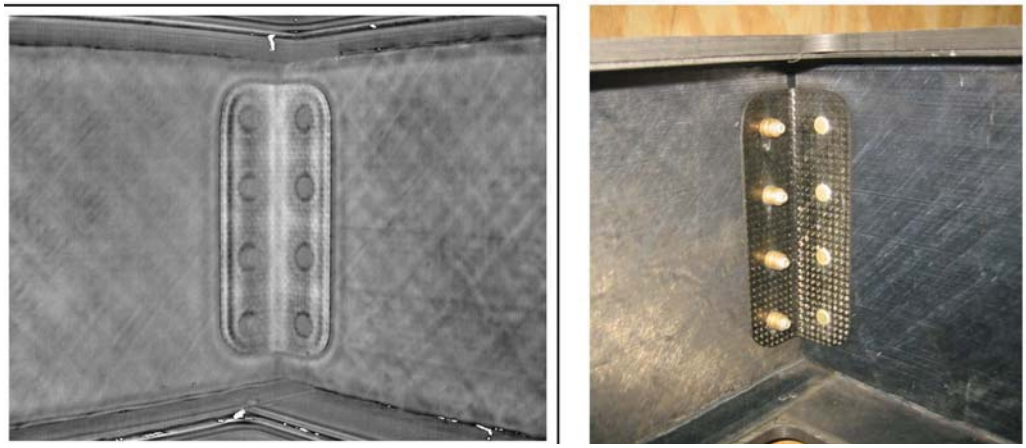

Figure A-13. Thermal inspection results for cruciform 1, rivet 2.

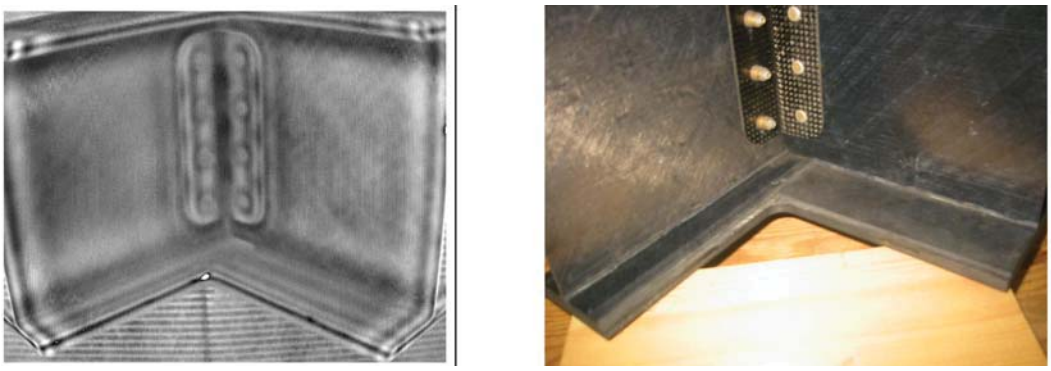

Figure A-14. Thermal inspection results for cruciform 1, rivet 2 bottom.

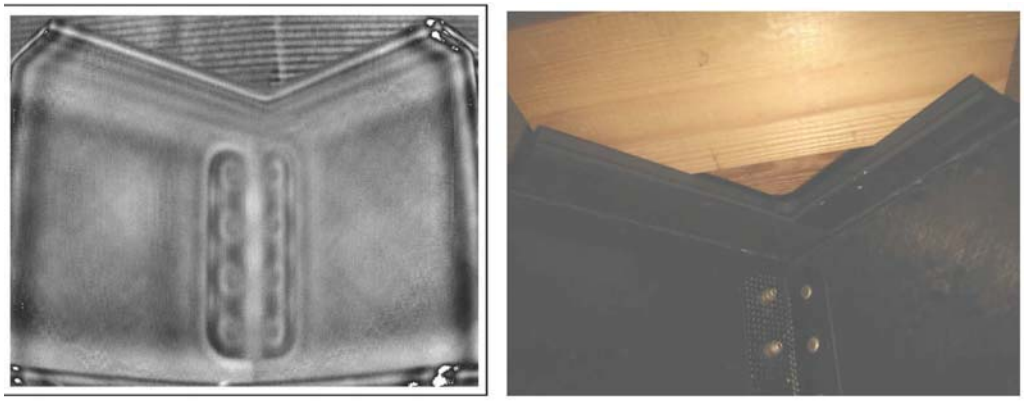

Figure A-15. Thermal inspection results for cruciform 1, rivet 2 top.

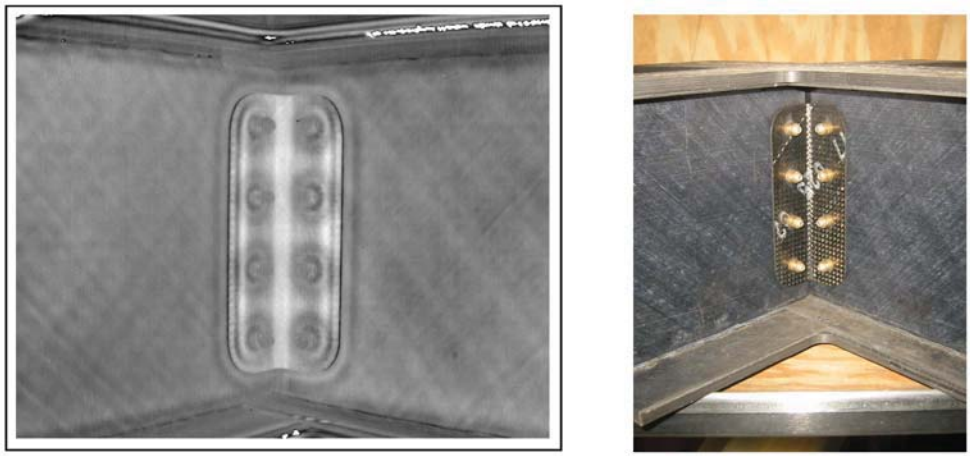

Figure A-16. Thermal inspection results for cruciform 1, rivet 3.

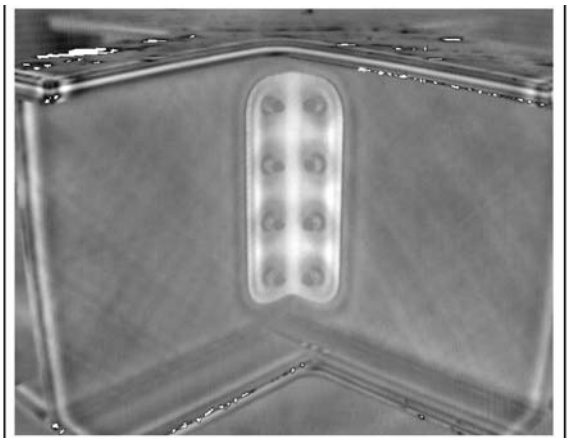

Figure A-17. Thermal inspection results for cruciform 1, rivet 3 bottom.

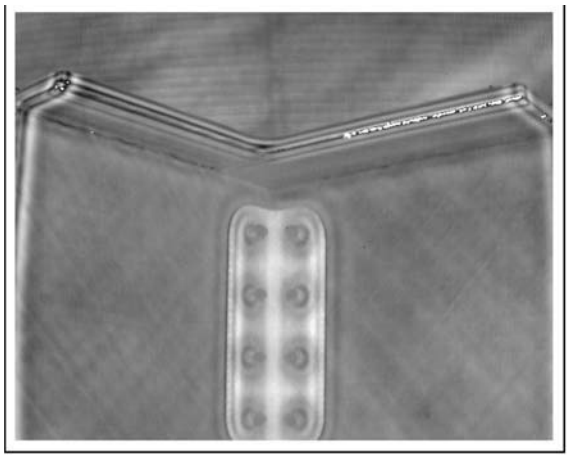

Figure A-18. Thermal inspection results for cruciform 1, rivet 3 top.

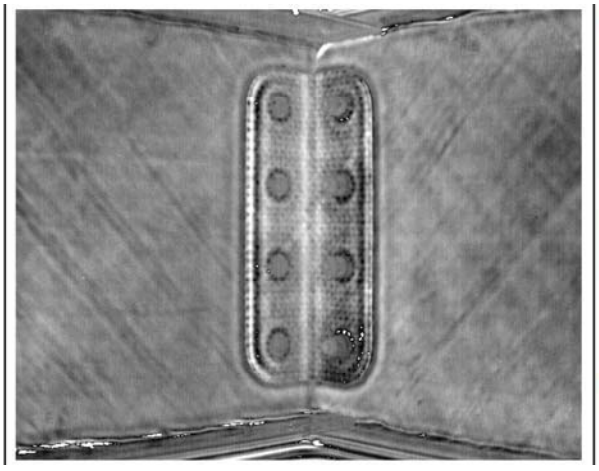

Figure A-19. Thermal inspection results for cruciform 1, rivet 4.

Figure A-20. Thermal inspection results for cruciform 1, rivet 4 bottom.

Figure A-21. Thermal inspection results for cruciform 1, rivet 4 top.

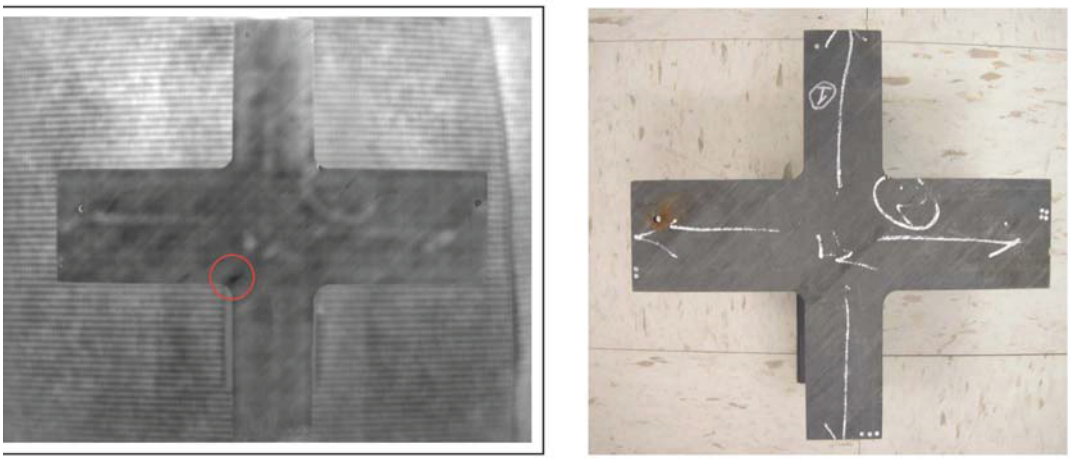

Figure A-22. Thermal inspection results for cruciform 1 top.

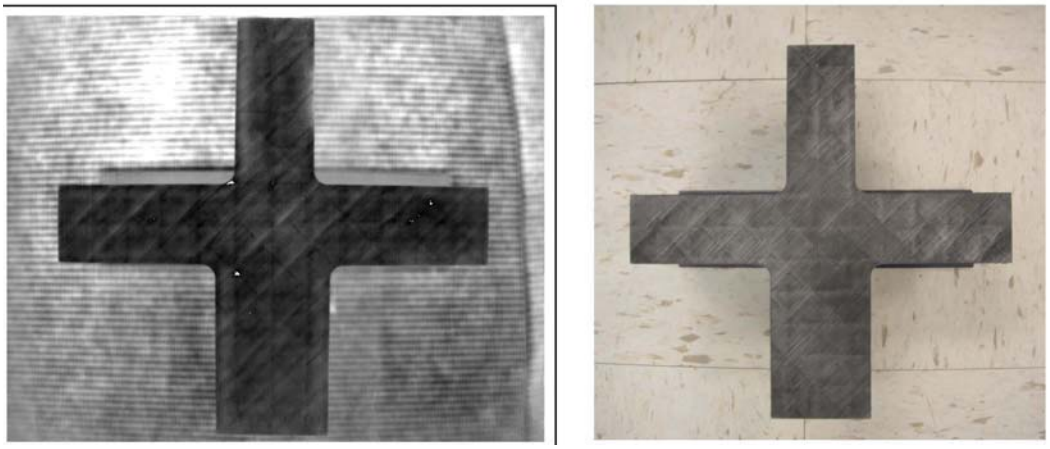

Figure A-23. Thermal inspection results for cruciform 1 bottom.

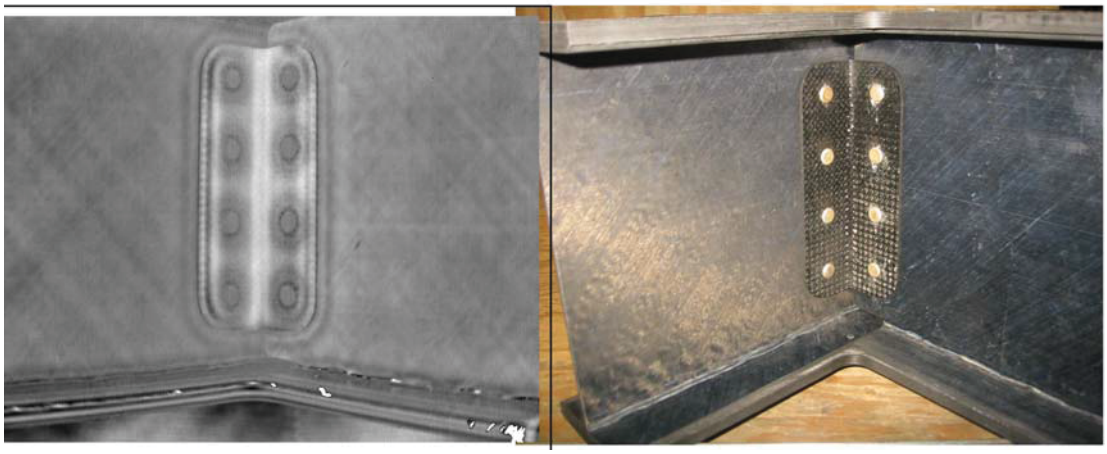

Figure A-24. Thermal inspection results for cruciform 2, rivet 1.

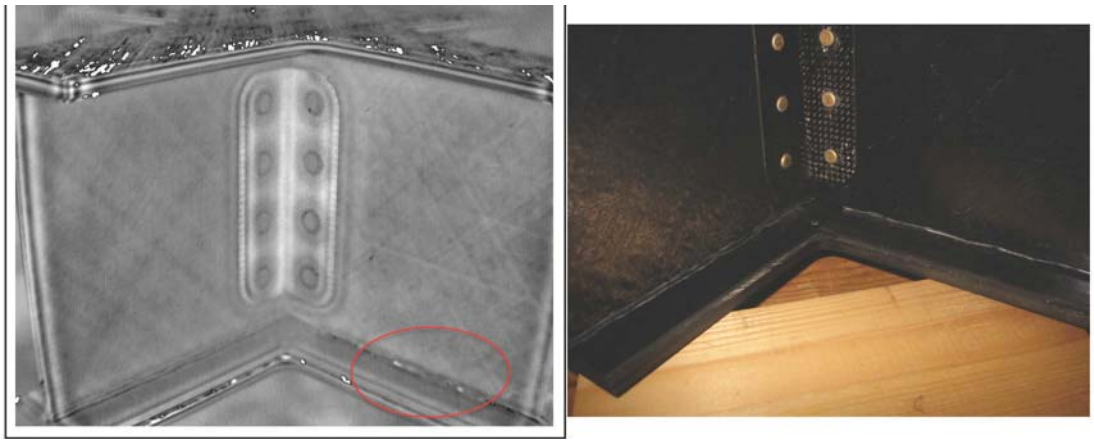

Figure A-25. Thermal inspection results for cruciform 2, rivet 1 bottom.

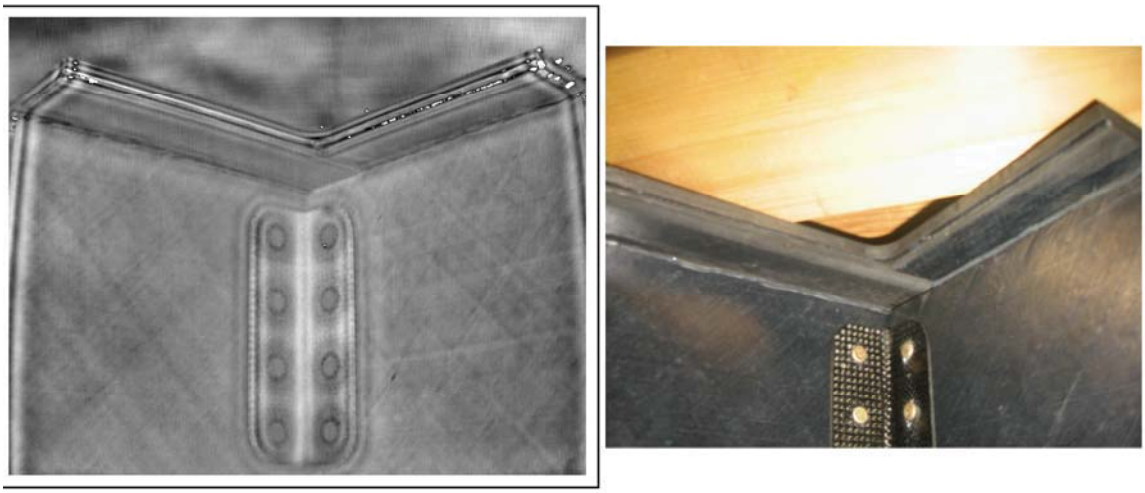

Figure A-26. Thermal inspection results for cruciform 2, rivet 1 top.

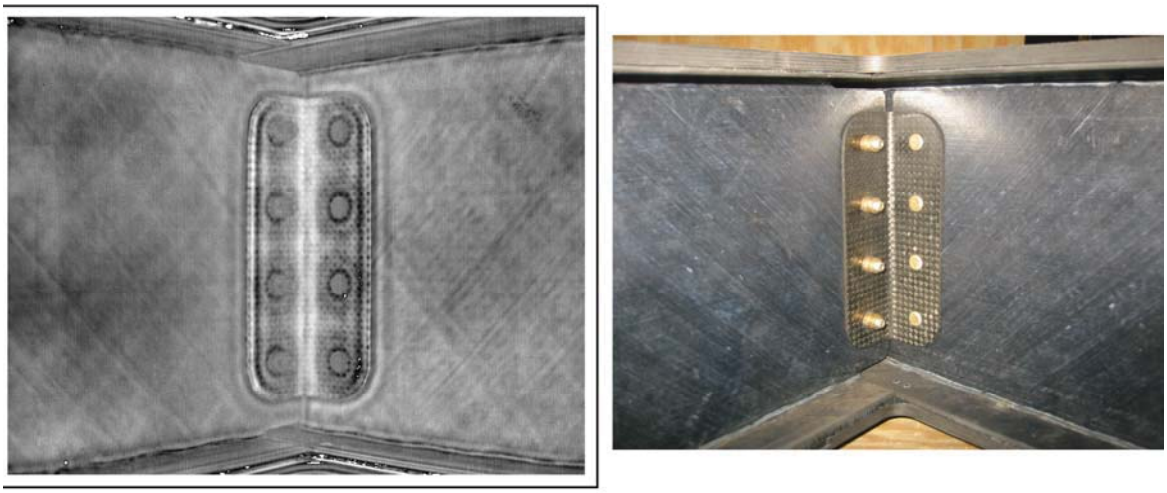

Figure A-27. Thermal inspection results for cruciform 2, rivet 2.

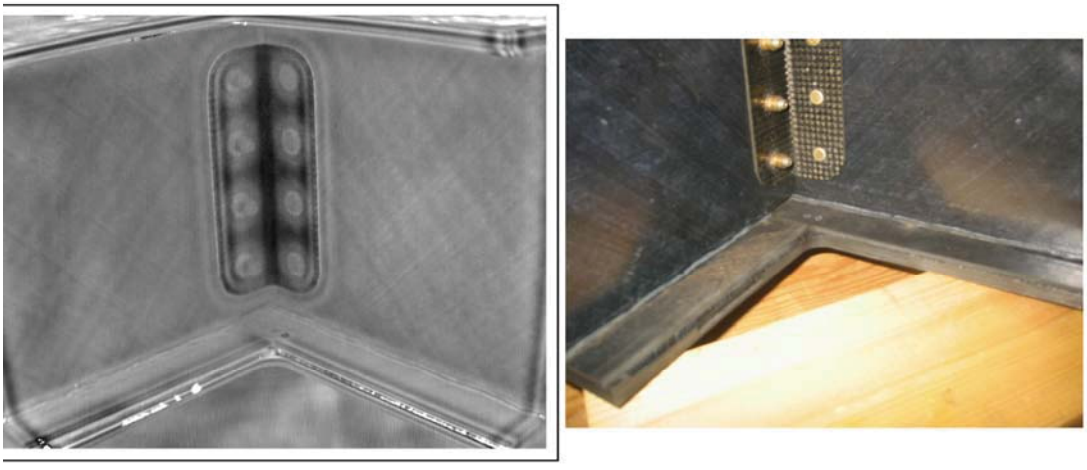

Figure A-28. Thermal inspection results for cruciform 2, rivet 2 bottom.

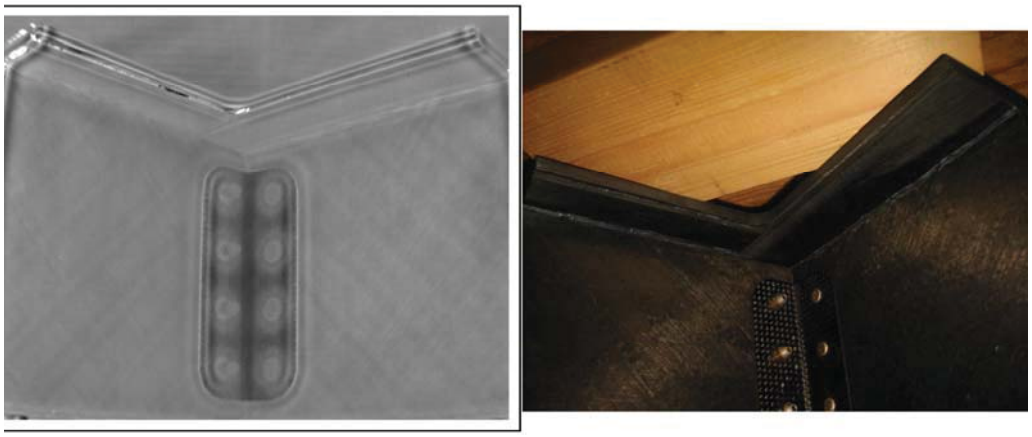

Figure A-29. Thermal inspection results for cruciform 2, rivet 2 top.

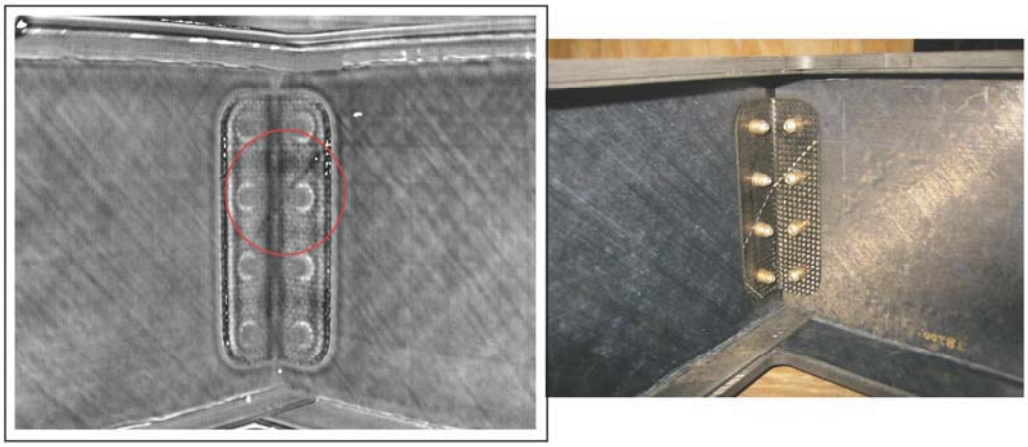

Figure A-30. Thermal inspection results for cruciform 2, rivet 3.

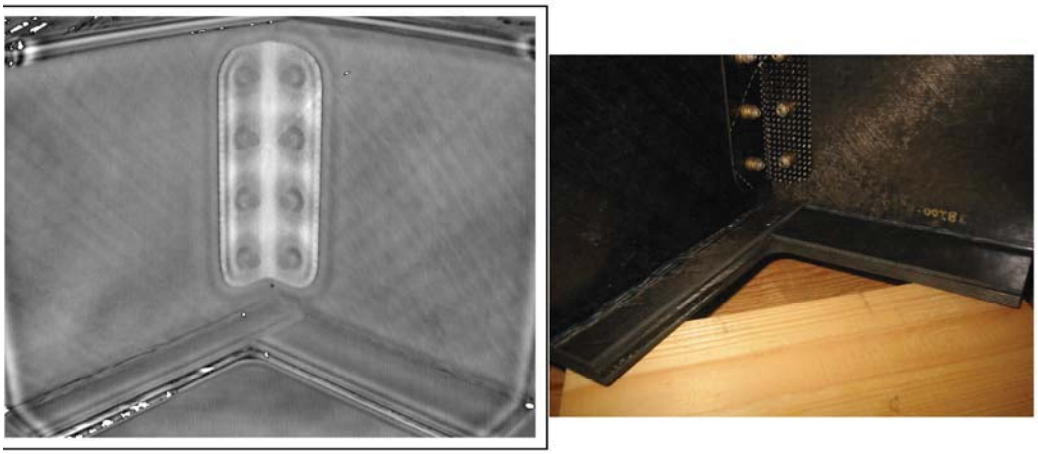

Figure A-31. Thermal inspection results for cruciform 2, rivet 3 bottom.

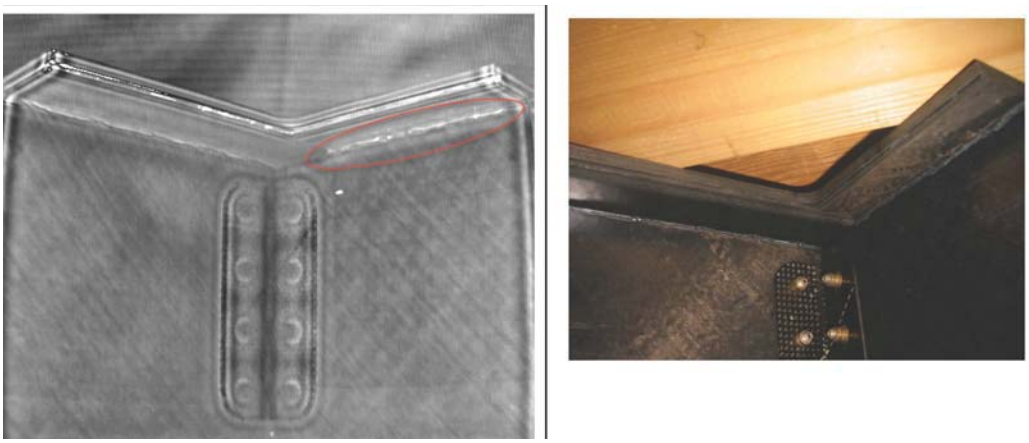

Figure A-32. Thermal inspection results for cruciform 2, rivet 3 top.

Figure A-33. Thermal inspection results for cruciform 2, rivet 4.

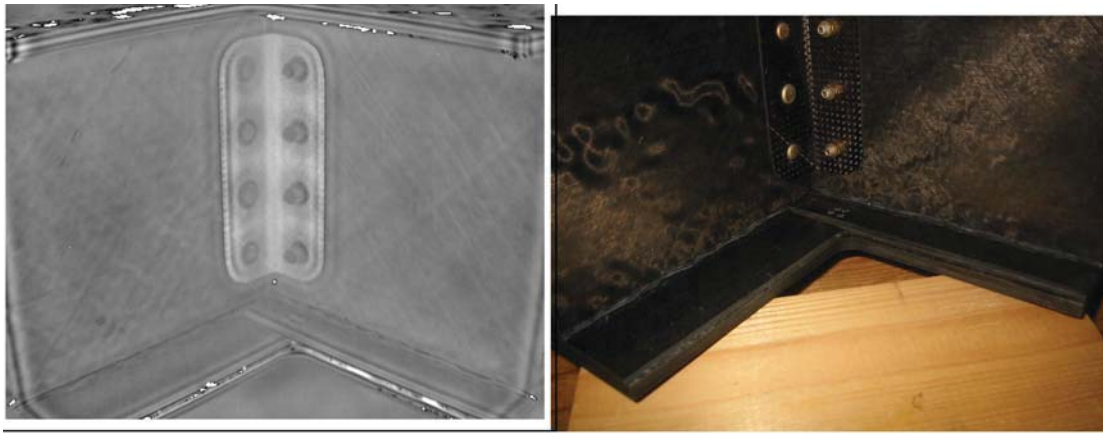

Figure A-34. Thermal inspection results for cruciform 2, rivet 4 bottom.

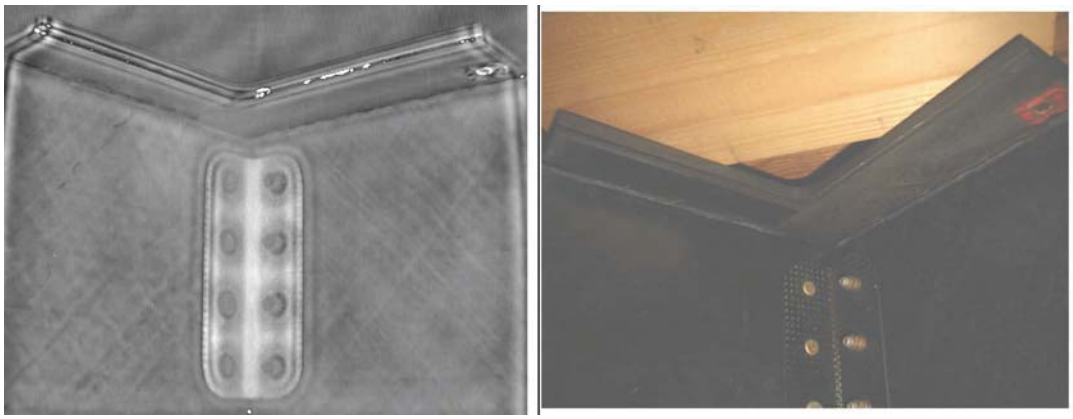

Figure A-35. Thermal inspection results for cruciform 2, rivet 4 top.

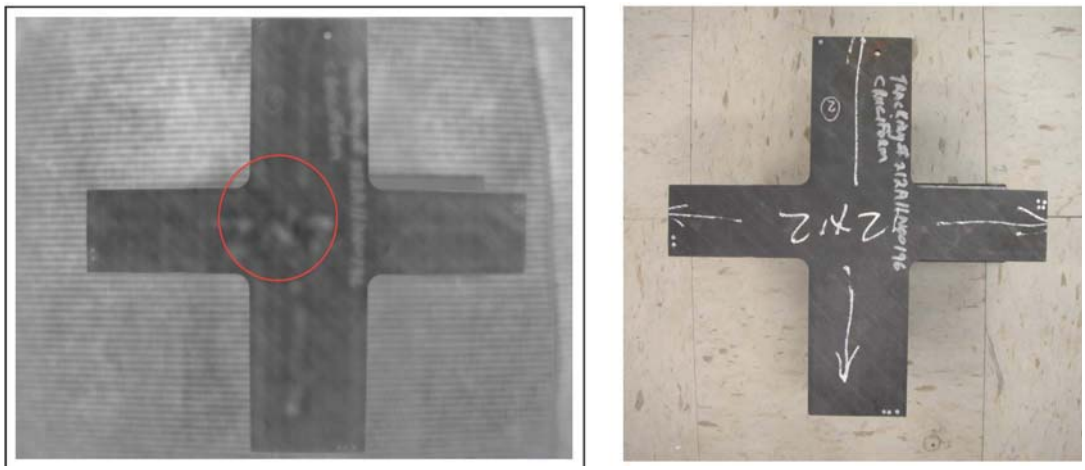

Figure A-36. Thermal inspection results for cruciform 2, top.

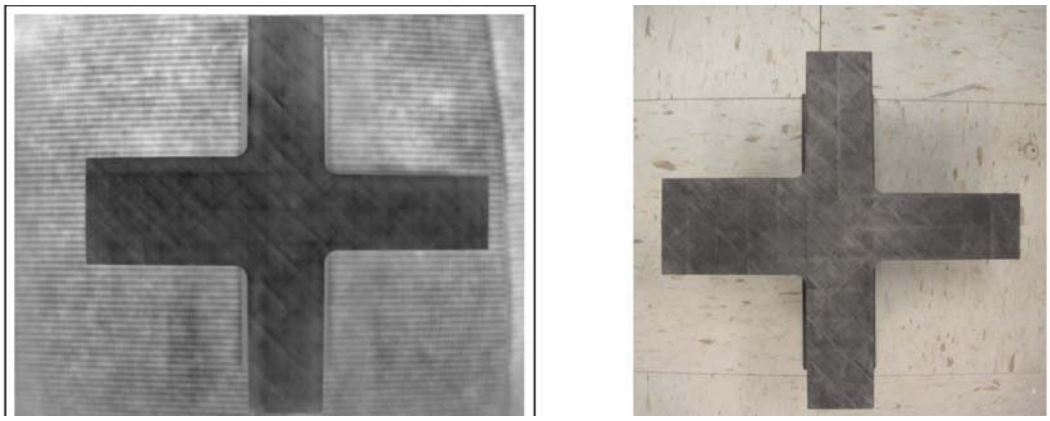

Figure A-37. Thermal inspection results for cruciform 2, bottom.

REPORT DOCUMENTATION PAGE

Form Approved
OMB No. 0704-0188

1. REPORT DATE *(DD-MM-YYYY)*	2. REPORT TYPE	3. DATES COVERED *(From - To)*
01-02-2014	Technical Memorandum	

4. TITLE AND SUBTITLE

Impact Testing and Simulation of Composite Airframe Structures

5a. CONTRACT NUMBER

5b. GRANT NUMBER

5c. PROGRAM ELEMENT NUMBER

6. AUTHOR(S)

Jackson, Karen E.; Littel, Justin D.; Horta, Lucas G.; Annett, Martin S.; Fasanella, Edwin L.; Seal, Michael D., II

5d. PROJECT NUMBER

5e. TASK NUMBER

5f. WORK UNIT NUMBER

380046.02.07.04.01.04

7. PERFORMING ORGANIZATION NAME(S) AND ADDRESS(ES)

NASA Langley Research Center
Hampton, VA 23681-2199

8. PERFORMING ORGANIZATION REPORT NUMBER

L-20373

9. SPONSORING/MONITORING AGENCY NAME(S) AND ADDRESS(ES)

National Aeronautics and Space Administration
Washington, DC 20546-0001

10. SPONSOR/MONITOR'S ACRONYM(S)

NASA

11. SPONSOR/MONITOR'S REPORT NUMBER(S)

NASA/TM-2014-218169

12. DISTRIBUTION/AVAILABILITY STATEMENT

Unclassified - Unlimited
Subject Category 39
Availability: NASA CASI (443) 757-5802

13. SUPPLEMENTARY NOTES

14. ABSTRACT

Dynamic tests were performed at NASA Langley Research Center on composite airframe components of increasing complexity to evaluate their energy absorption behavior when subjected to impact loading. A second objective was to assess the capabilities of predicting the dynamic response of composite airframe structures, including damage initiation and progression, using a state-of-the-art nonlinear, explicit transient dynamic finite element code, LS-DYNA. Specimens were extracted from a composite prototype fuselage section manufactured by Sikorsky Aircraft under the US Army's Survivable Affordable Repairable Airframe Program (SARAP). Laminate characterization testing was conducted and dynamic impact tests were performed on I-beam, T-section, and cruciform section components. Full-scale tests were conducted including a longitudinal impact test of a subfloor section and a vertical drop test of a framed fuselage section. Most of the test articles were manufactured of graphite tape composite with a thermoplastic resin. However, the framed fuselage section was constructed of a plain weave graphite fabric with a thermoset resin. Finite element models were developed and impact simulations were executed. The composite materials were represented using both a progressive in-plane damage model and a continuum damage mechanics model. Test-analysis comparisons of time history responses and structural damage development are presented for each test article.

15. SUBJECT TERMS

Aircraft structures; Airframes; Composite structures; Finite element method; element modeling; impact tests; nonlinearity

16. SECURITY CLASSIFICATION OF:			17. LIMITATION OF ABSTRACT	18. NUMBER OF PAGES	19a. NAME OF RESPONSIBLE PERSON
a. REPORT	b. ABSTRACT	c. THIS PAGE			STI Help Desk (email: help@sti.nasa.gov)
					19b. TELEPHONE NUMBER *(Include area code)*
U	U	U	UU	156	(443) 757-5802